Design, Implementation and Control of a Sparse Aperture Imaging Satellite

by

Soon-Jo Chung

B.Sc., Aerospace Engineering
Korea Advanced Institute of Science and Technology, 1998

SUBMITTED TO THE DEPARTMENT OF AERONAUTICS AND ASTRONAUTICS
IN PARTIAL FULFILLMENT OF THE DEGREE OF

MASTER OF SCIENCE

at the

MASSACHUSETTS INSTITUTE OF TECHNOLOGY

September 2002

Signature of Author . . . . . .
Department of Aeronautics and Astronautics
August 20, 2002

Certified by . . . . . .
David W. Miller
Professor of Aeronautics and Astronautics
Thesis Supervisor

Accepted by . . . . . .
Edward M. Greitzer
Professor of Aeronautics and Astronautics
Chair, Committee on Graduate Students

Design, Implementation and Control of a Sparse Aperture Imaging Satellite

by

SOON-JO CHUNG

Submitted to the Department of Aeronautics and Astronautics
on Ausgust 20, 2002 in Partial Fulfillment of the
Requirements for the Degree of Master of Science
at the Massachusetts Institute of Technology

The quest for higher angular resolution in astronomy will inevitably lead to larger and larger apertures. Unfortunately, the diameter size of primary mirrors for space telescopes is limited by the volume and mass constraints of current launch vehicles as well as the scaling laws of manufacturing costs. Efforts are ongoing to break this trend by employing exotic technologies such as deployed segmented mirror telescopes, and sparse aperture optics using interferometry. In order to better understand the technological difficulties involved in designing and building a sparse aperture array, the challenge of building a white light Golay-3 telescope was undertaken. The MIT Adaptive Reconnaissance Golay-3 Optical Satellite (ARGOS) project exploits wide-angle Fizeau interferometer technology with an emphasis on modularity in the optics and spacecraft subsystems. Unique design procedures encompassing the nature of coherent wavefront sensing, control and combining as well as various systems engineering aspects to achieve cost effectiveness, are developed. To demonstrate a complete spacecraft in a 1-g environment, the ARGOS system is mounted on a frictionless air-bearing, and has the ability to track fast orbiting satellites like the ISS or the planets. Wavefront sensing techniques are explored to mit-igate initial misalignment and to feed back real-time aberrations into the optical control loop. This paper presents the results and the lessons learned from the conceive, design and implementation phases of ARGOS. A preliminary assessment shows that the beam combining problem is the most challenging aspect of sparse optical arrays. The need for optical control is paramount due to tight beam combining tolerances. The wavefront sensing/control requirements appear to be a major technology and cost driver.

Thesis Supervisor:
Professor David W. Miller
Dept. of Aeronautics and Astronautics

ACKNOWLEDGMENTS

Firstly, I wish to thank my academic and research advisor, Professor David Miller for his incessant encouragement and invaluable inspiration for the research. Thank you, Dave. Your professionalism always motivates me. I have been very fortunate enough to spend time with three wonderful officemates. My first officemate, Olivier de Weck, now a professor at MIT, has been a mentor, role-model and great friend throughout my life at MIT since he picked me up at the airport. The second officemate, Cyrus Jilla has taught me a lot about how to manage myself physically and mentally to become a super efficient person (I am still far away from one). I have been getting a lot of help from my current officemate, Scott Uebelhart. Scott was also kind enough to review my thesis.

Without the helps and encouragements from the fellow graduate students in the Space Systems Lab, it would have been impossible to finish this work. I am enormously grateful to the following SSLers: Alice Liu for her academic and personal advice, Becky Masterson for her advice and help in this research, Edmund Kong for his previous work and advice throughout the research, also for reviewing my thesis, Alvar Saenz-Otero for helpful inputs and advice as the first CDIO class TA, Mark Hilstad for his computer administrative support and his kindness, Laila Elias for her advice and help, Karen Marais for her kindness to let me read her qualifying exam materials, and Seung Chung for being such a cool Korean friend in the lab,

I appreciate greatly the helps from the staff members of the SSL: Dr. Raymond Sedwick for being a role model with his passion for the research and also for reviewing my thesis, Paul Bauer for his enormous help and advice in the electronic devices and the purchases, SharonLeah Brown for her talks with me and financial support, Marilyn Good and Peggy Edwards for their administrative supports.

This thesis is completed as I TAed the Department's three-semester long CDIO class. I really enjoyed interacting with the students and the staffs. I thank enormously Col. John Keesee and Dr. Carl Blaurock for their technical advice and devotions to the class. I was very lucky to work with Erik Iglesias and Abran Alaniz. Their hard work made everything possible in the Optics subsystems team. Most of Chapter 4 is excerpted from the ARGOS design document. I especially appreciate the hardwork of the following wonderful students, Dustin Berkovitz of the Power subsystem, Chris Rakowski of the avionics, Marc dos Santos of the structure subsystem.

I also would like to appreciate the helps from Korean students here at MIT: Kyungyeol Song, Sanghyuk Park, Seonghwan Cho, and Chulmin Joo.

Most of all, I cannot thank enough my parents for their love and support.

CONTENTS

Acknowledgments **5**

List of Figures **11**

List of Tables **17**

Chapter 1. Introduction **19**

1.1 Motivation 19

1.2 Previous and Current Related Projects 23

1.3 Thesis Objectives 28

1.4 Thesis Outline 28

Chapter 2. Sparse Aperture Imaging Array **31**

2.1 SOCS Framework Overview 31

2.1.1 Motivation and Objective 31

2.1.2 Benefits of Modular Architecture 32

2.1.3 Procedures 34

2.2 Fundamentals of Interferometry 36

2.2.1 Single Telescope (Diffraction) 36

2.2.2 Two Telescope Interferometry 38

2.3 Determination of Array Configuration 38

2.3.1 Optics Performance Requirements 39

2.3.2 Point Spread Functions vs. Modulation Transfer Function 43

2.3.3 Determining the Angular Resolution of a Sparse Array 46

2.4 Beam Combining Errors and Error Budget Table 52

2.4.1 Piston Error 53

2.4.2 Tip/Tilt Errors 56

2.4.3 Pupil Mapping Error 59

2.4.4 Wavefront Error Budget 69

2.5 Chapter Summary 71

Chapter 3. Description of ARGOS Testbed **75**

3.1 ARGOS Overview 75

3.1.1 Project Objective 75

3.1.2 Overview of Mission Requirements . . . 77
3.1.3 Final Design . . . 78
3.2 Attitude Control System . . . 81
3.2.1 ACS Sensor Suite . . . 82
3.2.2 Active Balancing System . . . 84
3.2.3 Reaction Wheels . . . 88
3.2.4 General Control System Design . . . 90
3.3 Structure . . . 96
3.3.1 Aperture Alignment System . . . 96
3.3.2 Other Structure Requirements . . . 99
3.3.3 Final Design . . . 100
3.4 Power . . . 103
3.4.1 Continuous autonomous operation for up to one hour: . . . 103
3.4.2 Simple and Standard Interfaces: . . . 108
3.4.3 Automatic Health Status (Telemetry) Data Reports: . . . 109
3.4.4 Automatic Control in response to Ground Commands and Manual Control: 112
3.4.5 Other Design Points . . . 113
3.5 Avionics . . . 113
3.5.1 Software . . . 113
3.5.2 Avionics Hardware . . . 116
3.6 Chapter Summary . . . 119

Chapter 4. Optics component design and integration . . . 121

4.1 Sub-Aperture Telescope . . . 123
4.1.1 Image Aberrations . . . 123
4.1.2 Two-Mirror Telescope . . . 126
4.1.3 Collimating Lens . . . 129
4.2 Relay Optics . . . 134
4.2.1 Optical Delay Line (ODL) Design . . . 134
4.2.2 OPD and FSM Coupled Design . . . 139
4.2.3 Final ODL-FSM design . . . 142
4.2.4 Pyramidal Mirror . . . 148
4.3 Beam Combiner . . . 150
4.4 Structural Misalignment Tolerancing . . . 152
4.4.1 Tolerancing Based on OPD Change . . . 152
4.4.2 Tolerancing Using NSC Ray-Tracing . . . 154

4.5 CCD System . . . 157
4.5.1 CCD Metrics . . . 157
4.5.2 CCD Design From FOV Requirement . . . 159
4.5.3 CCD Design From SNR Requirement . . . 161
4.6 Chapter Summary . . . 167

Chapter 5. Wavefront Sensing and Control . . . 169
5.1 Wavefront Sensing . . . 169
5.1.1 Shack-Hartmann vs. Phase Diversity . . . 170
5.2 Coarse Optics Control of ARGOS . . . 173
5.2.1 Method of Increasing Image Sampling Rate . . . 173
5.2.2 Elliptical Spot Based Sensing . . . 174
5.2.3 Controller Design . . . 177
5.3 Chapter Summary . . . 179

Chapter 6. Cost Analysis on Sparse Aperture Array . . . 181
6.1 Introduction to Cost Analysis . . . 181
6.1.1 Objective . . . 181
6.1.2 Categories of Life-Cycle Cost . . . 182
6.1.3 Cost Modeling Approach for Sparse Aperture Payload . . . 183
6.2 Telescope Cost Modeling . . . 184
6.3 Relay Optics Cost Modeling . . . 186
6.4 Quantitative Life-Cycle System Analysis . . . 192
6.4.1 Cost Modeling of ACS . . . 194
6.4.2 Subsystem Cost Tables . . . 196
6.4.3 Labor Cost Table . . . 198
6.4.4 Results . . . 199
6.5 Chapter Summary . . . 204

Chapter 7. Conclusion . . . 205
7.1 Thesis Summary . . . 205
7.2 Contributions . . . 210
7.3 Recommendations for Future Work . . . 210

References . . . 213

Appendix A. ARGOS Requirements Document . . . 219

A.1 Introduction 219
A.2 Customer Requirements 220
A.3 ARGOS Proposed Approach 220
A.4 Flight Article Description 221
A.5 Mission Statement 221
A.6 Constraints 222
A.7 Systems Engineering Requirements 223
A.8 Subsystem Requirements 224
A.9 Guidelines 226

Appendix B. OPD Sensitivity Analysis of Optics Structures 227

Appendix C. ARGOS Cost and Mass Table 231

LIST OF FIGURES

Figure 1.1 The plot of price vs. primary diameter of small amateur telescopes . . 20

Figure 1.2 The motivation of the future space interferometers projects 20

Figure 1.3 Pupil-plane interferometry (Michelson interferometry) 21

Figure 1.4 Two types of Fizeau interferometers: The common secondary mirror array (left) and the phased telescope array (right) 23

Figure 1.5 The Multiple Mirror Telescope (top picture) and The Multipurpose Multiple Telescope Testbed (MMTT) of the Air Force Research Lab (AFRL) (bottom picture) 25

Figure 1.6 Optical layout of the Multi Aperture Imaging Array (top) and the laboratory setup (bottom) 26

Figure 1.7 Large Binocular Telescope (LBT) 27

Figure 1.8 Thesis outline 29

Figure 2.1 The four major cost savings from modular architecture 33

Figure 2.2 Sparse Aperture Optics/Control System (SOCS) design and implementation framework 34

Figure 2.3 Diffraction pattern from a single telescope as a function of the direction q 36

Figure 2.4 Two aperture interferometry vs. one aperture intensity plot 39

Figure 2.5 Encircled energy plot of one ARGOS sub-aperture (Mewlon 210). Each color indicates a different field angle in degrees 41

Figure 2.6 Definitions for spacecraft/telescope pointing requirements. Note that the desired target direction is given in terms of a (right ascension) and d (declination) 42

Figure 2.7 The relationship between the PSF and OTF. The absolute value of OTF is MTF. 43

Figure 2.8 PSF plot of Golay-3 sparse array (ARGOS): 2D plot (left) and 3D plot (right) 44

Figure 2.9 MTF plot of a Golay-3 array (ARGOS configuration) 45

Figure 2.10 MTF plot of ARGOS sparse array with color lines indicating the field angles 45

Figure 2.11 MTF plot of one ARGOS sub-aperture telescope 46

Figure 2.12 PSF and MTF plots when D=0.21m and L = 0.12m (blue), 0.19m (red), 0.3m (black). The corresponding array configurations are shown below the PSF-MTF plot. The black-yellow figure is a MTF plot. Yellow circles indicate the practical cut-off frequency. 47

Figure 2.13 Final array configuration of ARGOS 48

Figure 2.14 Calculation of Ruv and the effective diameter 50

Figure 2.15 Iso-effective-diameter plot as a function of L and D. Two black lines indicate the constraints in Equation 2.21 51

Figure 2.16 Three primary beam combining errors 52

Figure 2.17 Notations for Menneson's Interferometric equation. 53

Figure 2.18 2-dimensional PSF plot using Equation Increment 1/10 λ 55

Figure 2.19 3D PSF plot of Golay-3 array with a piston error of +/- 0.2 λ with respect to other apertures 56

Figure 2.20 PSF plot of Golay-3 array with zero OPD, 0.5 l OPD , and 1.0 l OPD, from the left to the right. 57

Figure 2.21 The single aperture of D=0.21 m is segmented into a FEM model with 100 elements. The "*" point at the middle of each element indicates the central point, and the phase error of each element is calculated at the central point. 58

Figure 2.22 PSF plot under the following tilt errors: Aperture 1: X, Y Tilt =0, Aperture 2: X tilt=1.0e-4 degrees, Ytilt=0, Aperture 3: Xtilt=0,Ytilt= -1.0e-4 degrees. 59

Figure 2.23 Graphical setup for two aperture interferometric array to analyze pupil mapping 61

Figure 2.24 FOV vs. tolerable shear error for different magnification factors 63

Figure 2.25 FOV vs. Pupil mapping tolerances for ARGOS (m=10) with different FOVs 65

Figure 2.26 FOV vs. Pupil mapping tolerances for ARGOS with achievable magnification tolerance 66

Figure 2.27 Magnification vs. shear tolerance with magnification error =0.0095 . . 67

Figure 2.28 Magnification vs. shear tolerance with magnification error =0.001 . . 68

Figure 2.29 Error budget tree for a general optical system 69

Figure 2.30 Wavefront error propagation 70

Figure 2.31 The ARGOS WFE budget tree for 0.8 Strehl Ratio (0.075l RMS WFE) 71

Figure 3.1 Functional and operational objectives of ARGOS 79

Figure 3.2 The final ARGOS system with the three ACS sensors shown in the bottom 81
Figure 3.3 Multi-staged ACS Sensors 84
Figure 3.4 Schematic of Center of Rotation, Center of Gravity Offset, and Gravitational Torque 85
Figure 3.5 Active Balancing System Schematic 86
Figure 3.6 Single-axis linear motion slide 87
Figure 3.7 ISS Tracking Operation 89
Figure 3.8 Reaction wheel mounting method 90
Figure 3.9 General Control System Design 91
Figure 3.10 Sensor Input Diagram 92
Figure 3.11 Motor Controller Design 94
Figure 3.12 Angular separation error between the line of site of ISS and ARGOS . 95
Figure 3.13 Zoomed-out view of angular separation error between the line of site of ISS and ARGOS 96
Figure 3.14 Maximum Alignment Requirements: q =1 deg, d=30 mm, y=3.39 mm Resolution Requirements: q=15 arc sec, y=15 mm 97
Figure 3.15 FEM Analysis of aperture collar 98
Figure 3.16 Aperture module (left) and RWA module (right) 100
Figure 3.17 Center Combiner Module 101
Figure 3.18 Assembled aperture mode and swing arm design 102
Figure 3.19 Fully Assembled Satellite 103
Figure 3.20 Schematic of Power Supply 106
Figure 3.21 ISS Tracking and Power System 107
Figure 3.22 ARGOS battery pack and charger 109
Figure 3.23 ARGOS power telemetry circuit and the case with LED 111
Figure 3.24 28V Bus Power Layout 114
Figure 3.25 Cyclic Executive Model 115
Figure 3.26 Priority Driven CPU Example 116
Figure 3.27 ARGOSVIEW- the ARGOS PC GUI controller 117
Figure 3.28 Avionics Hardware Schematic 118
Figure 4.1 Step 4, Step 5, Step 6 and Step 7 of the Sparse aperture Optics/Control System design 121

Figure 4.2 Optical layout of ARGOS (Zemax nonsequential modeling) 122
Figure 4.3 The first eight Zernike polynomials 127
Figure 4.4 Takahashi Mewlon-210 , 8 inch Dall-Kirkham telescope 128
Figure 4.5 Spot diagrams of Mewlon-210, The circles indicate the diffraction-limited airy disk 129
Figure 4.6 Options for location of collimating lens. FM=fold mirror, CL=collimating lens 130
Figure 4.7 Baffle of Mewlon-210 131
Figure 4.8 Cemented doublet (left) and air-spaced doublet (right) 132
Figure 4.9 Chromatic focal shift of the FK51-BaK2 collimating doublet 134
Figure 4.10 Final ARGOS collimating doublet. The numbers in mm 135
Figure 4.11 The real interferograms for the three ARGOS sub-apertures with the collimating lens installed. 135
Figure 4.13 ODL control 136
Figure 4.12 ODL designs 136
Figure 4.14 Optical sensitivity. A region: UV, B region: visible (color), C region: quasi-monochromatic 138
Figure 4.15 Perpendicular ODL deisign coupled with FSM 140
Figure 4.16 Parallel ODL design coupled with FSM 141
Figure 4.17 FSM control laws from the geometry. 142
Figure 4.18 FSM and its mount 143
Figure 4.19 FSM amplifier circuit 144
Figure 4.20 Printed circuit board design using Orcad Layout. Three coaxial inputs on the bottom and three LEMO outputs on the top. 145
Figure 4.21 Zoom of PCB shows filter locations and orientation. 146
Figure 4.22 Filter transfer function 147
Figure 4.23 Pyramidal mirror and its mount combo 148
Figure 4.24 The PSF simulation of the ARGOS with 3 arcsec tilt error of the pyramidal mirror (SR=0.444, Left). The PSF with FSM correction (SR=0.960, Right) 149
Figure 4.25 Two-mirror (Cassegrain) type beam combiner. The secondary mirror of the beam combining telescope partially blocks the incoming beams. . . . 150
Figure 4.26 The refractive beam combiner of the ARGOS testbed 151

Figure 4.27 The final layout of the ARGOS optical train (only one aperture shown) 1-subaperture, 2- collimating lens, 3-FSM/ODL actuator, 4-pyramidal mirror, 5-beam combiner, 6-CCD 151

Figure 4.28 OPD tolerancing of a single arm relay optics 152

Figure 4.29 OPD Sensitivity analysis of each optics component 153

Figure 4.30 Rotation of FSM 154

Figure 4.31 0.01 degree tilt error of a sub-aperture (SR=0.064), left, FSM compensation (SR=0.604), middle, OPD correction as well as FSM (SR=0.859), right . . 156

Figure 4.32 The PSF plots when the beam combiner has tilt errors. From left to right, (1) X tilt: 0.2, Y tilt: 0.4 , (2) X: 0.3 Y: 0.3, (3) X: 0.25 Y: 0.25 [degrees] . 157

Figure 4.33 Quantum efficiency of CCD systems to different illumination methods. Source: http://www.ccd.com (CCD University) 158

Figure 4.34 ISS image taken by a 12" Schmidt-Cassegrain Telescope at f/30. ARGOS has an effective diameter =0.4 meter so our goal is to achieve a better resolution than this image 161

Figure 4.35 SNR plots for two different CCDs: DALSA (low sensitivity with faster frame rate) and AP (high sensitivity with slower frame rate) 166

Figure 5.1 Shack-Hartmann sensor of Adaptive Optics Associates (AOA), Cambridge, MA. 171

Figure 5.2 Phase Diversity concept [Paxman, 2000] 172

Figure 5.3 Imaging processing loops 173

Figure 5.4 Elliptical spot based sensing 174

Figure 5.6 Code finds area of circumscribed circle to determine direction of actuation 176

Figure 5.5 MinX, MinY, MaxX, and MaxY values drawn as tangent and moved toward CCD's centroid 176

Figure 5.7 : Each FSM is actuated until the MinX value is no longer changed by any FSM (first row), Once the points are vertically aligned, the FSM actuate vertically until one point is achieved (second row). 177

Figure 5.8 Simulink diagram of two-aperture FSM controller 178

Figure 6.1 Cost modeling approach for sparse apertures 183

Figure 6.2 Telescope cost CER using small amateur telescopes in Figure 1.1 . . . 185

Figure 6.3 Cost of OTA’s telescope systems (http:www.opticalguidancesystems.com) 186

Figure 6.4 Tip/Tilt Error 189

Figure 6.5 Control cost vs. subaperture diameter for different array compactness . 190
Figure 6.6 Control cost vs. magnification 191
Figure 6.7 Control cost vs. array compactness (D/L) 193
Figure 6.8 Regression curve fitting of momentum Capacity and mass of RWA . . 194
Figure 6.9 Subsystem cost estimates for different array configurations 200
Figure 6.10 Array configurations used for cost estimates- monolith, Golay-3, Golay-6, Golay-9 and Golay-12. EE is a corresponding encircled energy within the mainlobe of a point spread function. 200
Figure 6.11 Ground-based Golay arrays vs. monolith hardware cost 201
Figure 6.12 Ground based Golay arrays vs. monolith hardware and labor costs . . 201
Figure 6.13 Compact Golay-3 arrays with their u-v plots and PSFs. 202
Figure 6.14 Cost of telescopes for three-aperture array 203
Figure 6.15 System cost of three aperture array spacecraft 203

LIST OF TABLES

TABLE 1.1 Summary of Fizeau Interferometry vs. Michelson Interferometry . . . 22
TABLE 2.1 Strehl Ratio variations under the tip/tilt errors of ARGOS 60
TABLE 3.1 Power System Requirement 104
TABLE 3.2 Loads on 56V bus and 28V bus 106
TABLE 4.1 The first eight Zernike polynomials 126
TABLE 4.2 Mewlon-210 specification 128
TABLE 4.3 Evaluation of collimating lens location options 130
TABLE 4.4 Optical Delay Line Specifications 139
TABLE 4.5 Optical Delay Line Downselect 139
TABLE 4.6 FSM and FSM mount specifications 143
TABLE 4.7 Flat mirror specifications 146
TABLE 4.8 Pyramidal mount combo specifications 149
TABLE 4.9 Sub-aperture tip/tilt tolerancing 155
TABLE 4.10 Magnitudes of various targets at brightest 163
TABLE 6.1 Cost estimate table for passive optics and active optics sub-systems . 196
TABLE 6.2 Cost estimate table for the ACS, Structure, Science, Operation, Communications subsystems 197
TABLE 6.3 Cost estimate table for Power, Avionics and Software subsystem and miscellaneous costs 198
TABLE 6.4 Labor cost estimates table 199

Chapter 1

INTRODUCTION

1.1 Motivation

The quest for finer angular resolution in astronomy will inevitably lead to larger apertures- we can recall the Rayleigh criterion for angular resolution. Unfortunately, the primary mirror diameter for space telescopes is limited by the volume and mass constraints of current launch vehicles as well as the scaling laws of manufacturing costs [Meinel, 1979]. Meinel predicted that the manufacturing cost of an aperture increases in proportion to $D^{2.58}$.

A survey plot of Figure 1.1 indicates that the manufacturing cost of small amateur telescopes increase proportionally to $D^{2.76}$. Since the cost of monolithic optics increases faster than the diameter squared, and mirrors such as the Hubble Space Telescope's are already at the edge of what is financially feasible, efforts are ongoing to break this trend by employing exotic technologies such as deployed segmented mirror telescopes, and sparse aperture optics using interferometry.

Similiar to the ground-based Multiple Mirror Telescope (MMT), space based imaging can be accomplished with a segmented monolithic mirror. NASA's Next Generation Space Telescope (NGST) features a 6.5-meter monolithic mirror with deployable lightweight filled apertures [Redding, 1998]. Another breakthrough technology is space interferometry. Numerous NASA future telescope missions such as the Space Interferometry Mission

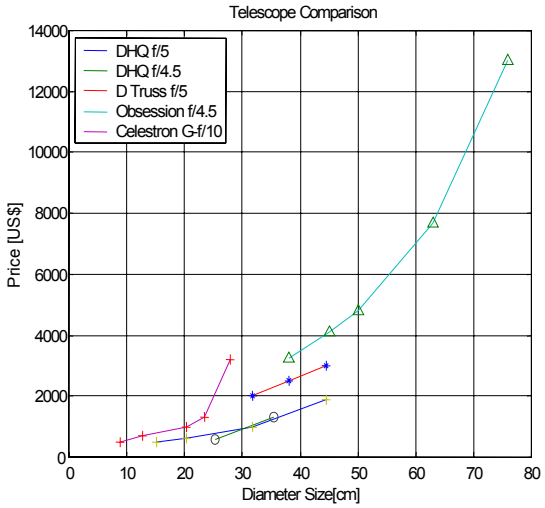

Figure 1.1 The plot of price vs. primary diameter of small amateur telescopes

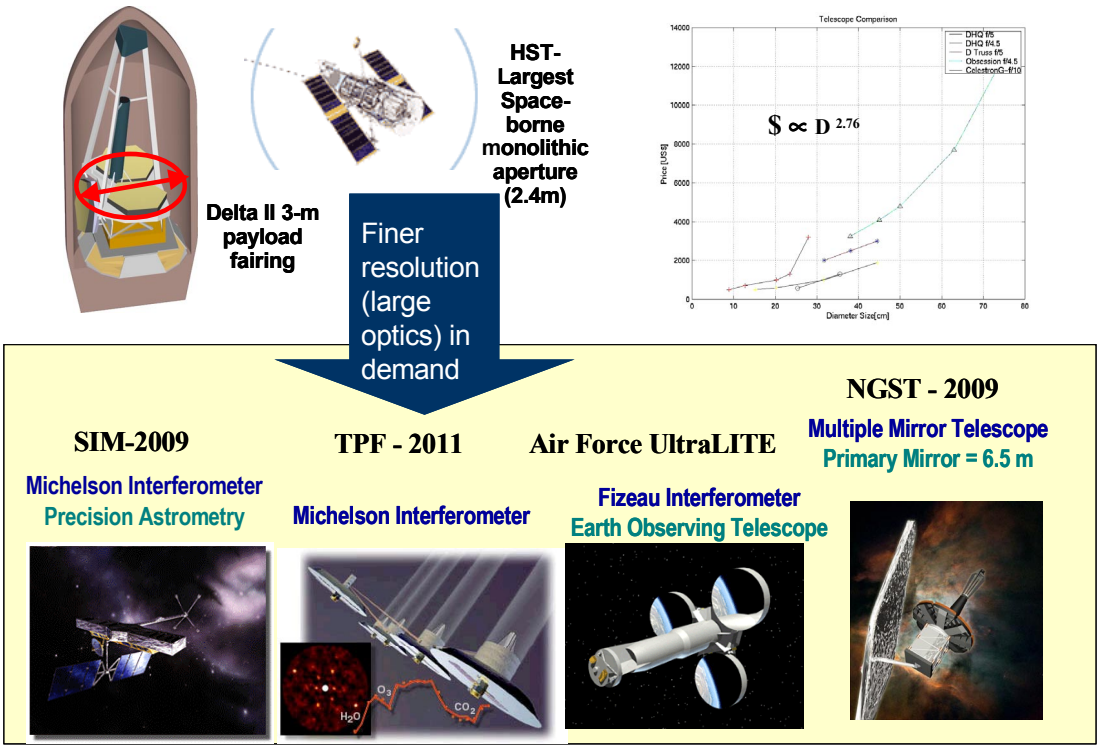

Figure 1.2 The motivation of the future space interferometers projects

(SIM) and the Terrestrial Planet Finder (TPF) are based on Michelson interferometer technology.

Basically, stellar interferometers deploy two or more than two apertures and combine multiple beams to achieve higher angular resolution, astrometry and nulling depending on the mission requirements.

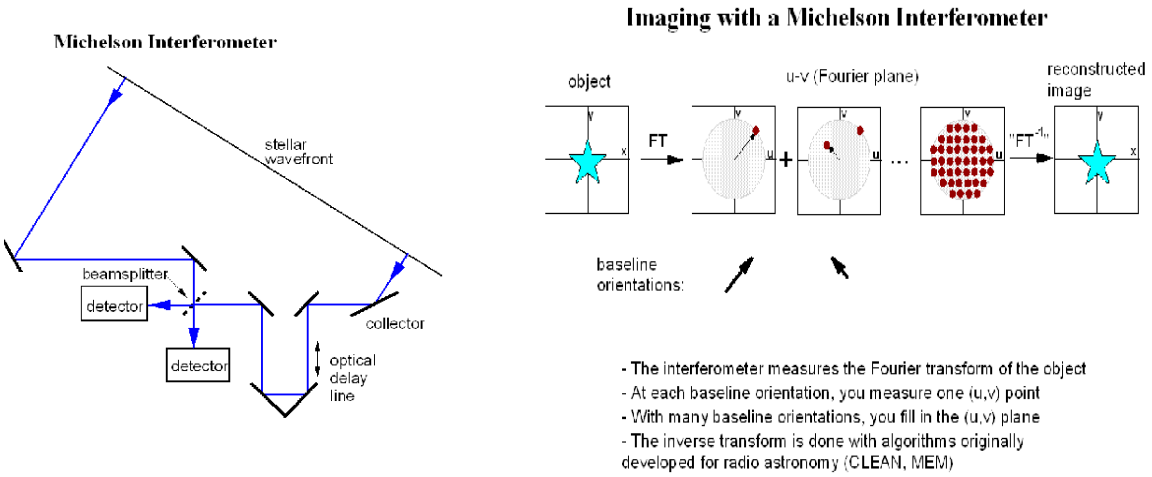

Figure 1.3 Pupil-plane interferometry (Michelson interferometry)

There are two fundamentally different ways beams are combined in an interferometer. Pupil-plane interferometry is the method of combining two beams in which parallel beams are superimposed using a half-silvered mirror or equivalent, and the two resulting output beams are each focused on detector pixels. This is commonly called Michelson interferometry as shown in Figure 1.3. The interferometer measures the spatial Fourier transform of the objects. At each baseline orientation, one (u,v)[1] point is measured, and the (u,v) plane is filled in with many different baseline orientations. The inverse transform is computed to reconstruct an image with algorithms originally developed for radio astronomy.

1. u and v represent spatial frequencies in convenient astronomical coordinates like right ascension and declination. $u = B_x/\lambda$, $v = B_y/\lambda$, where λ is the wavelength and B_x, B_y are the baseline lengths in x and y coordinates respectively.

Whereas Michelson interferometers feed beams from independent collectors to a prism-type beam combiner to obtain interfered fringes over a period of time (the time it takes to rotate the baseline and fill the u-v plane), Fizeau interferometers produce direct images with full instant u-v coverage. Hence, the Fizeau is suitable for optical imaging of extended objects and rapidly changing targets. In contrast to the long baselines of Michelson interferometers, Fizeau interferometry systems tend to have compact telescope arrays. Fizeau inteferometry is also called Image-plane interferometry because it is the method of combining multiple beams, each focused to make an image of the sky. Fizeau originally suggested using a two-slit mask across the aperture of a conventional telescope to resolve stellar diameters. This is also the method used by Michelson in his stellar interferometer. Table 1.1 highlights the differences between the two interferometry types.

TABLE 1.1 Summary of Fizeau Interferometry vs. Michelson Interferometry

Fizeau Interferometry (Image-Plane Interferometry)	**Michelson Interferometry (Pupil-Plane Interferometry)**
Produce a direct image of its target (Full Instant u-v coverage provided)	Takes a subset of u-v points obtained a period of time
Wide angle(field) of view imaging applications	Astrometry, Nulling Interferometry
Rapidly changing targets(Terrestrial, Earth Objects)	Target unchanged(Astronomical Objects)
Takes the combined science light from all the apertures and focuses it into a CCD	Measures points in Fourier transform of images => Inverse FFT needed
U-V resolution depends on both the separation and the size of apertures	Angular resolution depends solely on the separation of apertures
Optimal Configuration: Golay (minimum aperture size)	The angular resolution improves as the separation increases

Two types of optical Fizeau interferometers are shown in Figure 1.4. The common secondary array type shares one common secondary mirror, thus giving little or zero central obstruction. The second type, the phased telescope array (sparse array) is chosen for the MIT Adaptive Reconnaissance Golay-3 Optical Satellite (ARGOS) over the common sec-

ondary because it allows the system to utilize off-the-shelf telescopes providing more opportunity to explore modularity than the common secondary array. More complicated relay optics and beam combining are however expected.

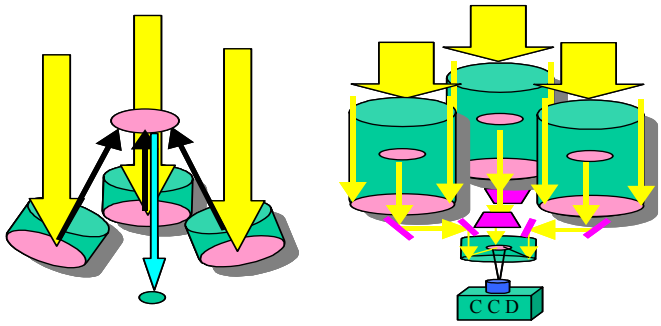

Figure 1.4 Two types of Fizeau interferometers: The common secondary mirror array (left) and the phased telescope array (right)

An optimal imaging configuration designed for sparse arrays was first proposed by Golay[Golay, 1971]. Sparse arrays are promising for applications that do not require extremely high sensitivity (a bright source is present) and allow for a rather limited field-of-view (FOV) [Harvey, 1985;Faucherre, 1989;Harvey, 1995].

In order to better understand the technological difficulties involved in designing and building a sparse aperture array, the challenge of building a white light Golay-3 telescope was undertaken. The MIT Adaptive Reconnaissance Golay-3 Optical Satellite (ARGOS) project exploits wide-angle Fizeau interferometer technology with an emphasis on modularity in the optics and spacecraft subsystems. This thesis is detailed elaboration on the design and implementation methodologies of the ARGOS testbed.

1.2 Previous and Current Related Projects

There are many past and ongoing long baseline ground-based Michelson interferometer projects including the Keck interferometer and Palomar Testbed Interferometer (PTI)

[Colavita, 1999]. In addition, NASA is planning to launch innovative space-based interferometers, e.g. SIM, TPF. However, successful sparse aperture telescope projects using Fizeau beam combining are rare due to the technical challenges involving phased telescope arrays as will be discussed in Chapter 2 and Chapter 4.

The pioneering Multiple Mirror Telescope (MMT) on Mount Hopkins in Arizona, had six 1.82 m individual telescopes to achieve an effective diameter of 4.45 m, but the MMT is now being converted to a monolithic aperture telescope with a 6.5 m diameter. The old MMT had a 30 arcsec field of view, but had been phased only for a small part of that field of view, and only to an accuracy of several waves. Additionally, a skilled human operator was needed to control manual adjustments[Hege, 1985].

A notable project in the area of phased telescope arrays is the Multipurpose Multiple Telescope Testbed (MMTT) [De Hainaut, 1995] by the Air Force Research Laboratory (AFRL) shown in Figure 1.5. The MMTT project was inspired by the success of a three-telescope transmitting phased array called Phasar [Fender, 1988]. Phasar showed that the first-order wavefront aberrations of wavefront tilt and piston can be removed by actuated mirrors in a feedback control loop. If the telescope optics are of high quality, these aberrations are the dominant errors that reduce the system's Strehl ratio [Gonglewski, 1988]. The MMTT consists of four 20-cm-aperture telescopes phased together with a 15-arcmin field-of-view (FOV). As opposed to the MIT ARGOS testbed, which operates in a real environment tracking celestial objects, the MMTT is built for laboratory use only using laser point sources. The MMTT is the first wide FOV phased array telescope measuring a combined point spread function (PSF). The Air Force is also developing the UltraLITE Earth imaging satellite using a Golay-6 array Fizeau interferometry [Powers, 1997].

To achieve coherent phased beam combining, the images should be superimposed on a CCD with an accuracy of a fraction of the operating wavelengths. We can infer that high precision wavefront error (WFE) sensing is critical to accomplish this goal. The MMTT employs a complex laser interferometer metrology system to sense WFE [De Hainaut,

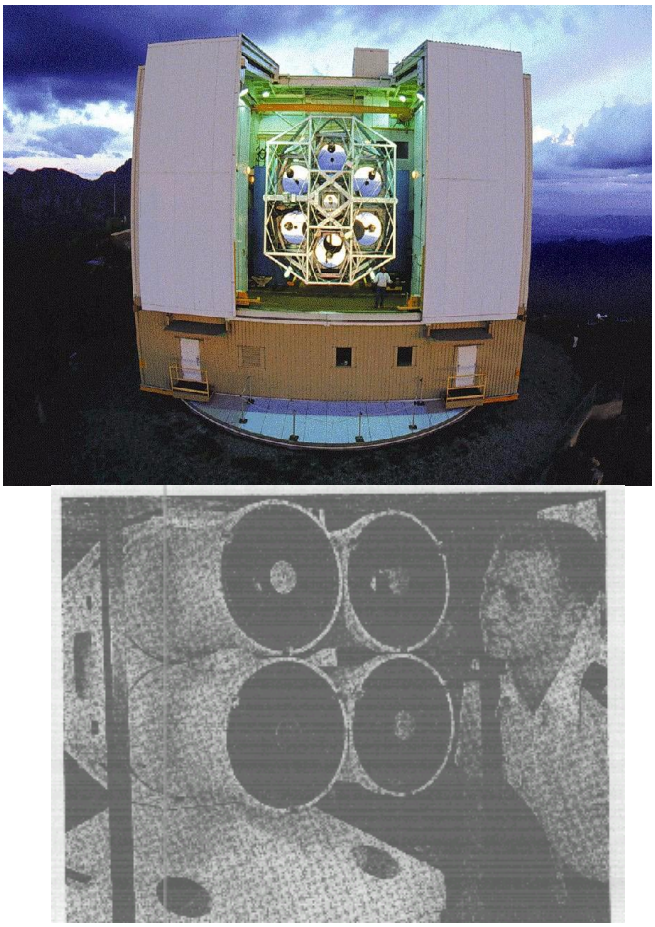

Figure 1.5 The Multiple Mirror Telescope (top picture) and The Multipurpose Multiple Telescope Testbed (MMTT) of the Air Force Research Lab (AFRL) (bottom picture)

1988;Hentz, 1988]. The cost of the complicated optics in the MMT sensor system is prohibitively high, and it occupies more space than would be available for compact space-borne observatories.

The Multi Aperture Imaging Array in Figure 1.6, built by Lockheed Martin, demonstrated phase diversity computation techniques for WFE sensing [Zarifis, 1999]. This sparse array consists of nine 10-cm afocal telescopes arranged in a Y-formation whose beams are combined to a common focus in a Fizeau interferometer configuration. The individual telescopes have a magnification of 10, and a set of fold flats adjust the outgoing beams to the common refractive beam combining telescope for correct optical pathlength difference

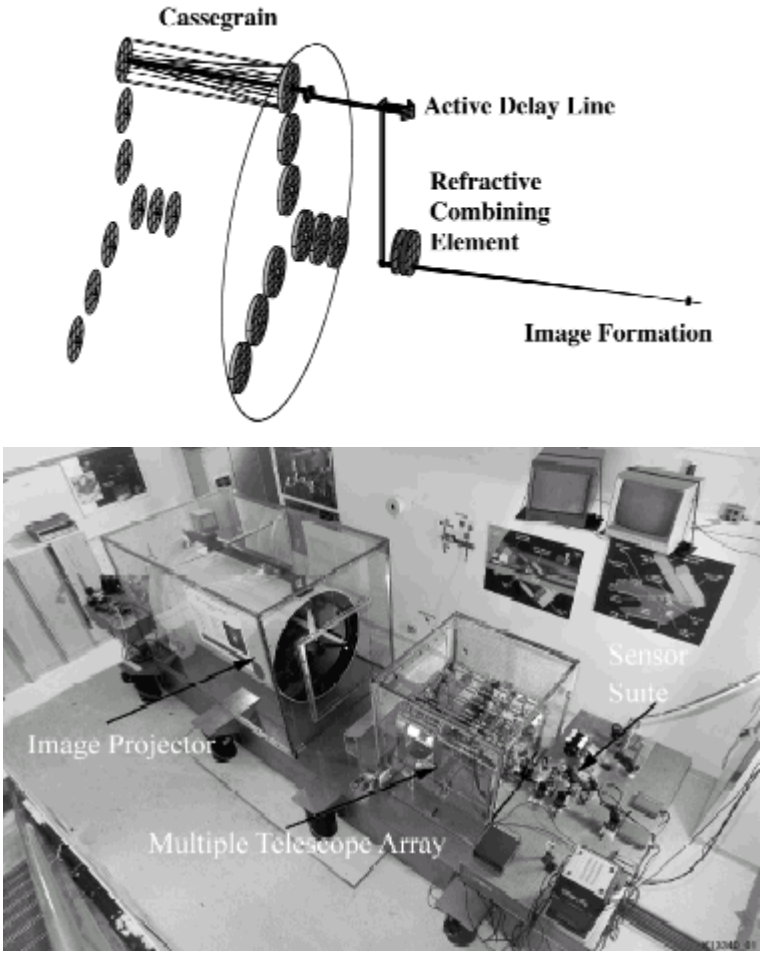

Figure 1.6 Optical layout of the Multi Aperture Imaging Array (top) and the laboratory setup (bottom)

and pupil mapping maintenance. It demonstrated the first results of a broad band multiple telescope imaging array phased over a significant field of view using the extended image projector in the lab.

The Large Binocular Telescope (LBT) in Figure 1.7 is being built by the University of Arizona along with several international institutions [Hill, 2000;Bonaccini, 2001]. The LBT telescope will have two 8.4 m diameter primary mirrors phased on a common mounting with a 22.8 meter baseline. Both apertures will be mounted on the same structure, resulting in a system more compact than other current ground-based interferometers. The

LBT optical layout has a T configuration in which flat mirror actuators control the collimated beams on their way to the refractive beam combiner.

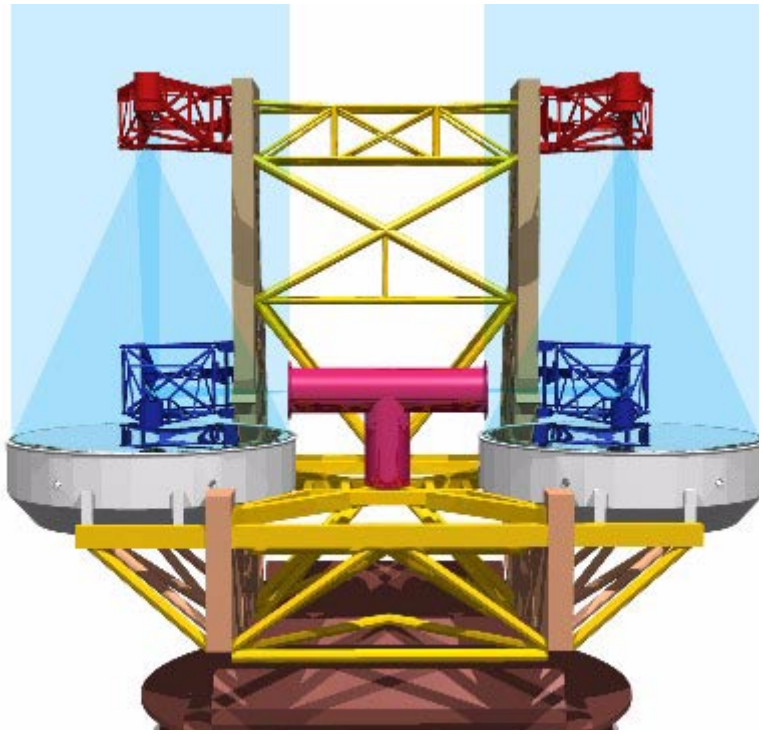

Figure 1.7 Large Binocular Telescope (LBT)

The ARGOS testbed is the first in-flight sparse aperture array simulating an imaging space-borne observatory in a 1-g environment. Most of the previous sparse aperture array systems do not deal with real world problems such as the vibrational coupling between a spacecraft structure and the wavefront errors propagating through the whole system. If ARGOS succeeds in coherent phased beam combining, it will be the first sparse aperture array to obtain a phased image of a real target in the sky.

1.3 Thesis Objectives

The main objective of this thesis is to validate the systems engineering approach to the design and implementation of sparse aperture interferometric array imaging spacecrafts.

- To understand the fundamental nature of imaging interferometric arrays by properly understanding and analyzing the physics behind them.
- To develop the design methodologies in order to correctly flow down the system and science requirements to each design stage for coherent phased beam combining.
- To develop a schematic framework for a sparse interferometric array with the aim of disseminating systems engineering practices emphasizing cost-effectiveness by exploring modular architecture in spacecraft systems.
- To produce a good reference for designing similar sparse aperture array telescope projects.

1.4 Thesis Outline

The structure of this thesis follows the step by step procedures of the Sparse-Aperture Optics/Control System (SOCS) design/implementation framework, which is described in detail in Chapter 2.

Chapter 2 details how we can achieve the goals suggested previously by the SOCS framework. The highlight of this framework is that complete design and implementation of sparse aperture arrays or interferometric array systems are performed with balanced attention to both the physics of interferometry and a system engineering mind.

The first half of Chapter 2 describes the fundamental physics and the characteristics of the interferometric arrays, and analyzes the effects of different array configurations on the performance of an interferometer. The second half is devoted to discussions on coherent beam combining errors. These tolerancing errors form a central basis for the rest of the design procedures.

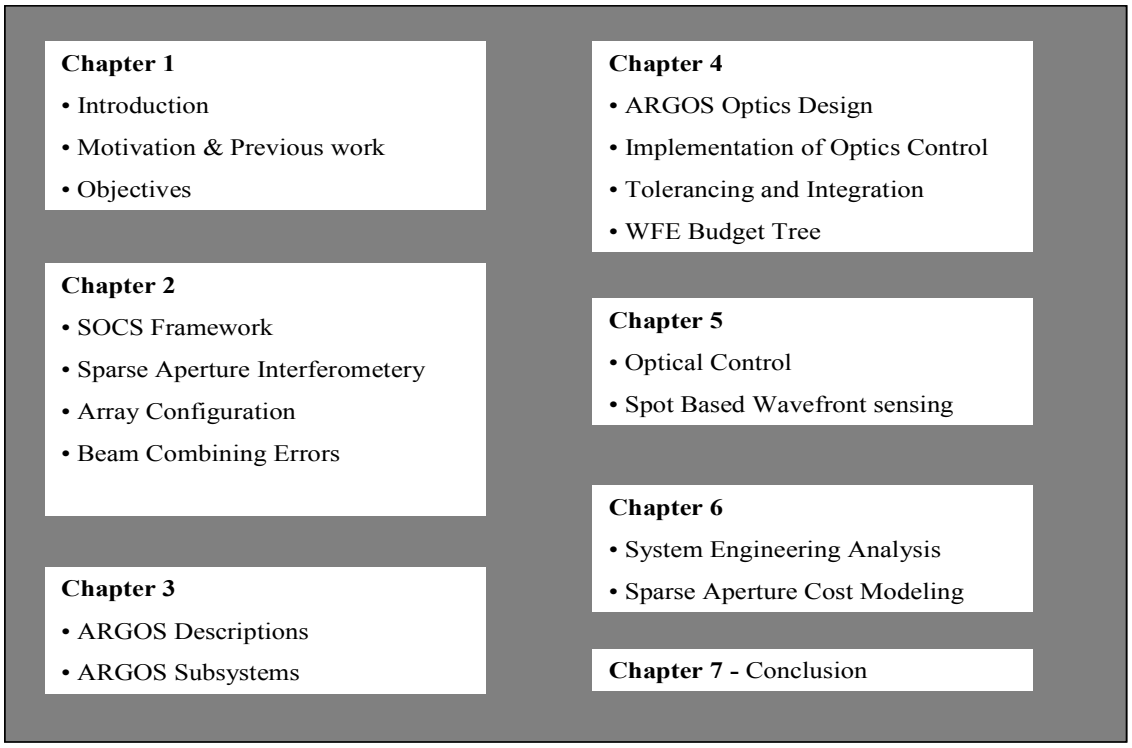

Figure 1.8 Thesis outline

Chapter 3 introduces the ARGOS testbed considering all other spacecraft subsystems including the Attitude Control System (ACS), Avionics, Structures and Power systems. Active and passive optics design for ARGOS is discussed in Chapter 4.

Chapter 4 expands upon the design and implementation procedures of sub-apertures and relay optics including a beam combiner. Optical design using professional ray tracing software is introduced and the trades in determining the shape of the relay optics are discussed. The final assembly will follow the design and manufacture of all the optical and structural components of the sparse aperture array. In Chapter 4, the guidelines of assembling all the optics are also discussed based on the calculation of allowable structural misalignments and the specifications of the mounts.

Development of wavefront sensors is one of the most important part of SOCS development procedures. Various wavefront sensing techniques are explored in Chapter 5. Chapter 5 also presents optical control methodologies developed for the ARGOS testbed.

Chapter 6 introduces the cost models developed through the experience of building the ARGOS testbed, and attempts to capture the impact of different array configurations on the life-cycle system cost.

Chapter 7 summarizes this thesis and suggests future work recommendations.

Chapter 2

SPARSE APERTURE IMAGING ARRAY

The Sparse Aperture Optics/Control System (SOCS) framework is a system engineering design tool as well as a manufacturing guideline for sparse aperture interferometric arrays. The SOCS was developed while building the MIT Adaptive Reconnaissance Golay-3 Optical Satellite (ARGOS) [16.684 CDIO; 16.685 CDIO; 16.686 CDIO]. The ARGOS testbed employs a sparse aperture imaging array using Fizeau interferometry, thus the SOCS framework is primarily geared toward space-based Fizeau interferometry. However, this framework can be applied to a Michelson interferometer with a few modifications of design parameters and requirements. Ground-based interferometers can also benefit from the SOCS approach. Usually, the requirements for space-based imaging systems are more stringent than for ground-based systems. In this chapter, the SOCS framework is introduced, and the fundamental characteristics of interferometric arrays are discussed.

2.1 SOCS Framework Overview

2.1.1 Motivation and Objective

The SOCS framework was developed from the following observations:

1. There have been many interferometric array projects around the world. However, there have been few projects that emphasize cost effective designs

using a system engineering approach. Both cost and risk are critical factors, particularly for space-based imaging systems.

2. Lack of a systems engineering mind set in rapid technological advances of astronomical interferometry, adaptive optics and sparse aperture arrays, caused confusions in identifying key elements and their mutual relations to avoid high-cost systems.
3. The control engineer and the optics designers must communicate with each other from the early stage of design through the actual implementation to achieve coherent beam combining with an interferometric array.

The objective of SOCS is, in each design step, to facilitate identification and correlation procedures of design parameters in order to get an optimum cost-effective performance design.

What is unique about this framework is that it explores the benefits of modular architecture in space-borne imaging systems. In other words, the design philosophy of cost-effectiveness and manufacturability throughout the design and implementation process so as to better understand the impact of systems engineering methodologies on the development of space interferometric arrays.

2.1.2 Benefits of Modular Architecture

Figure 2.1 epitomizes how the modular architecture influences the system costs in developing space-based interferometric arrays.

Stellar interferometry inherently makes use of the philosophy of modular architecture design because its concept is based on the fact that a better angular resolution can be achieved by combining multiple beams from the replicated apertures together. We explore the benefits of modularity in the designs of subsystem components as well.

Modular architecture implies assembling the system out of modules (identical, similar or dissimilar) that facilitate fabrication, integration, and testing. The design should maximize the simplicity of interfaces and the standardization of its components.

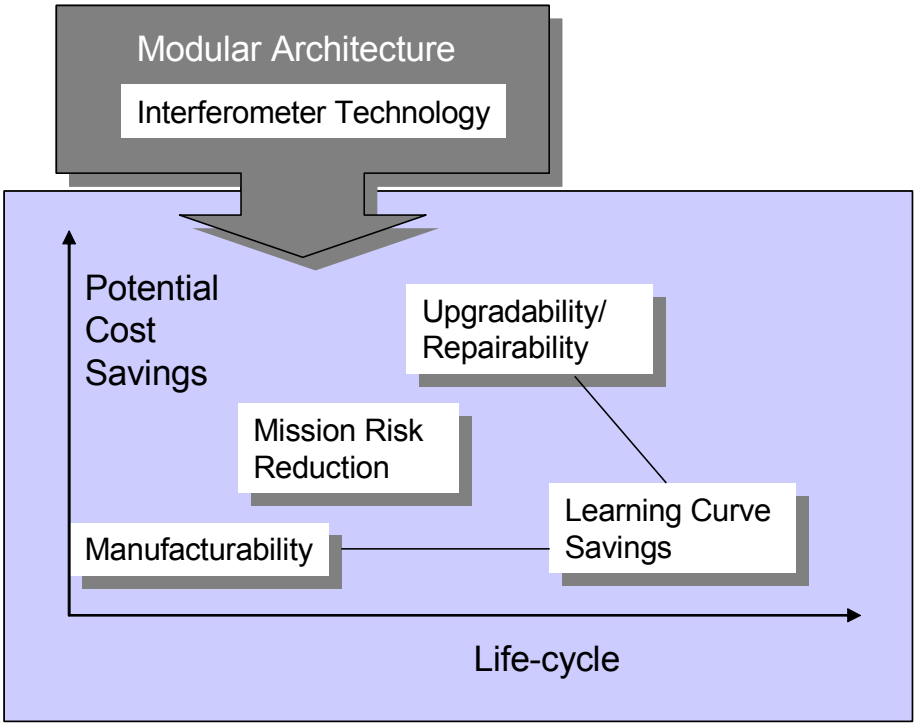

Figure 2.1 The four major cost savings from modular architecture

The two most important factors in deciding the available technologies and components are their cost-effectiveness and manufacturability. The ARGOS project maximized the usage of commercially-off-the-shelf (COTS) products, thereby greatly reducing the production costs. For example, instead of custom building high precision telescopes for three identical sub-apertures, one of the highest precision telescopes available in the market was selected, and an collimating double was installed to convert it to an afocal telescope. This is explained in detail in Chapter 4.

As opposed to the production cost and manufacturability, cost drivers such as upgradability, repairability, risk reduction effects, and learning curve savings are not easily observed in the early stage of design and fabrication. One of the objectives of the SOCS framework is to identify those potential cost drivers in the design, and to strive to maximize the benefits.

2.1.3 Procedures

We will briefly go over each step in the SOCS framework.

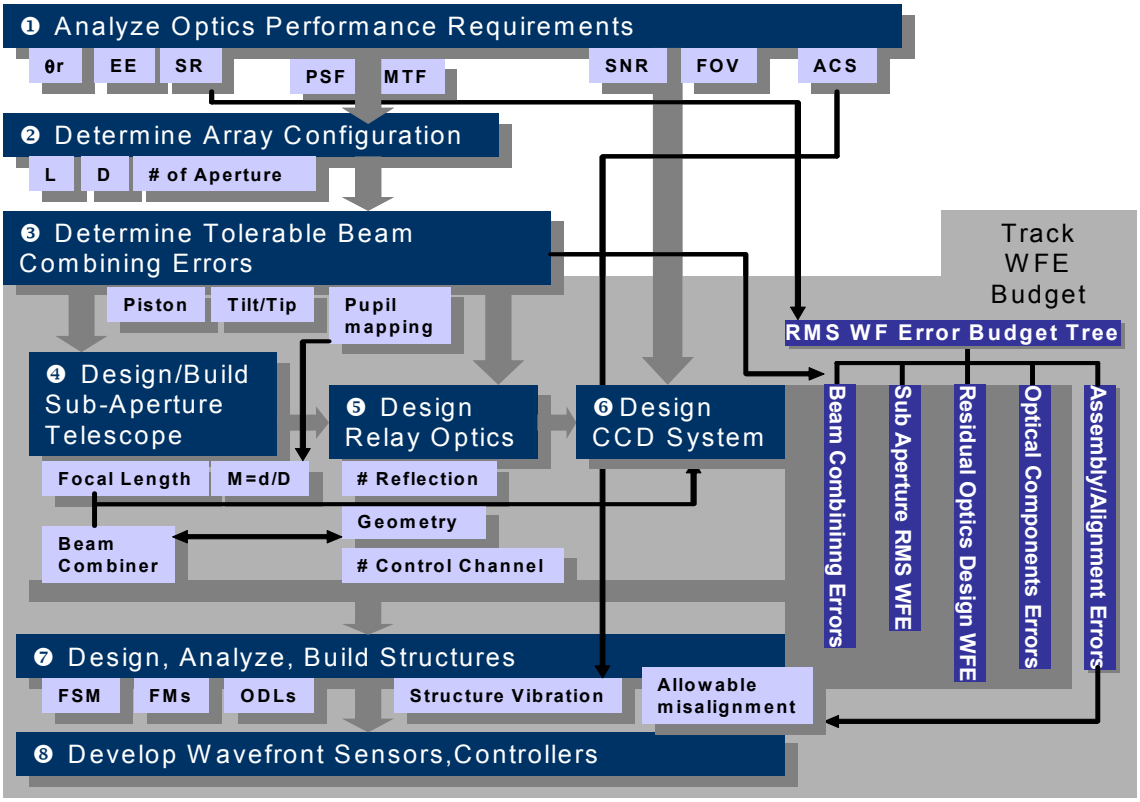

Figure 2.2 Sparse Aperture Optics/Control System (SOCS) design and implementation framework

(Step 1) Analyze optics performance requirements - define and interpret customer requirements such as angular resolution, Strehl Ratio (SR) and encircled energy (EE).

(Step 2) Determine an array configuration- determine a sub-aperture diameter (D) and the array radius (L) by looking at the point spread functions (PSF) and modulation transfer functions (MTF).

(Step 3) Analyze tolerable beam combining errors and begin to keep track of the wavefront error budget tree. Using the array configuration from step 2, determine the beam

combining tolerances. This analysis is fundamental in understanding the nature of interferometric arrays. Also, construct and update the wavefront error budget trees.

(Step 4) Design a sub-aperture with an optical precision that meets the wavefront error (WFE) budget tree specifications.

(Step 5) Design and build relay optics- determine how many optical reflections will be incorporated into the relay optics. The geometry and the shape of the optics controllers are defined. In addition, explore the various methods of beam combining.

(Step 6) Design the CCD systems. The relationships between spare aperture array and Signal to Noise Ratio (SNR) are discussed in Chapter 4.

(Step 7) Design/ Analyze/ Build Structures. According to the remaining WFE budgets, calculate the maximum allowable misalignment for each structure (sub-aperture, FSM and ODL actuators, and beam combiner). Also, design the structures to meet the optics requirements (precision stages, precision mounts). Perform finite element model (FEM) analysis.

(Step 8) Implement the wavefront sensors and controllers- Develop the wavefront sensors and control logics to achieve coherent beam combining.

We can re-iterate Step 1 to Step 6 to come up with a better design. Usually, calculating and selecting each design parameter outlined in Figure 2.2 requires the knowledge of the previous design parameters in the prior steps. Step 1,2,3 are elaborated upon in this chapter, and Step 4,5,6 are explained in detail in Chapter 4. The structural design for optical components such optical actuator mounts is described in Chapter 4, while the overall spacecraft structure is discussed in Chapter 3. Chapter 6 will elucidate wavefront sensing and control.

2.2 Fundamentals of Interferometry

The fundamental interferometry equations are developed in this section.

2.2.1 Single Telescope (Diffraction)

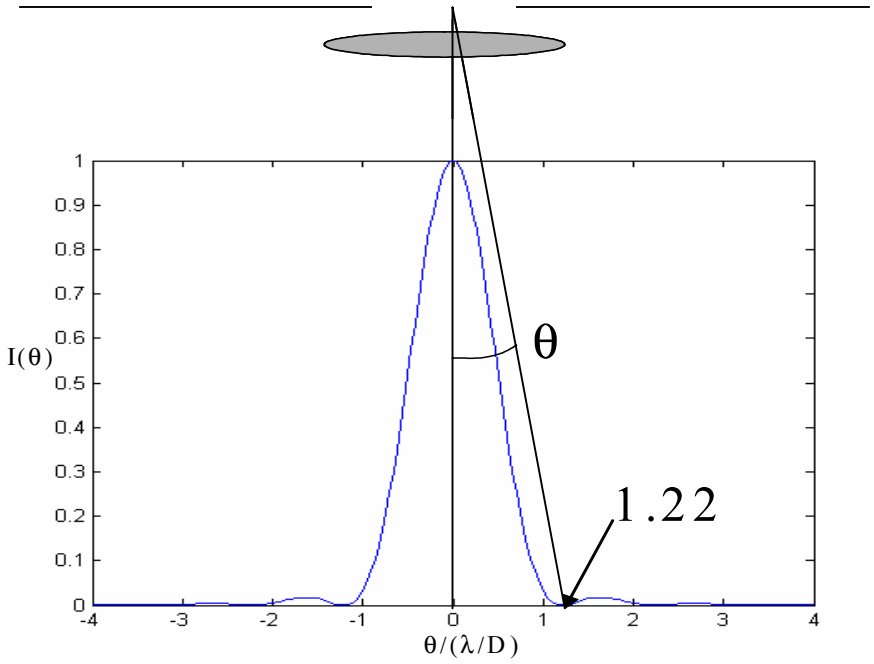

Figure 2.3 Diffraction pattern from a single telescope as a function of the direction θ

The wave amplitude measurement from a single telescope can be calculated as the algebraic sum of all wavelets across the telescope pupil.

$$A_{one}(\theta) = \sum(wavelets) \tag{2.1}$$

In case of a one dimensional aperture, the amplitude is calculated as a fourier transform of a pupil function (see Figure 2.7).

$$A_{one}(\theta) = \int_{-D/2}^{+D/2} e^{i(2\pi x\theta/\lambda)} dx \tag{2.2}$$

$$= \frac{\lambda}{2\pi i\theta}\left[e^{+i\pi\theta D/\lambda)} - e^{-i\pi\theta D/\lambda)}\right] \tag{2.3}$$

$$= \frac{\sin(\pi\theta D/\lambda)}{\pi\theta D/\lambda} D \tag{2.4}$$

The measured intensity *I* is the squared magnitude of the amplitude,

$$I_{one}(\theta) = \left[\frac{\sin(\pi\theta D/\lambda)}{\pi\theta D/\lambda}\right]^2 D^2 \tag{2.5}$$

For a two dimensional aperture, the sine function in equation 2.5 is replaced by J_1, a Bessel function of the first kind, order one.

$$I_{one}(\theta) = \left[\frac{2J_1(\pi\theta D/\lambda)}{\pi\theta D/\lambda}\right]^2 D^2 \tag{2.6}$$

The intensity in Equation 2.6 is plotted in Figure 2.3. The first null point is approximately at 1.22, and that gives an angular resolution θ_r.

$$\theta_r = 1.22\frac{\lambda}{D} \tag{2.7}$$

The full-width at half maximum (FWHM) method of defining the angular resolution of a telescope is approximated by this value. Equation 2.7 is often referred to as Rayleigh angular resolution criterion[Hecht, 2001].

2.2.2 Two Telescope Interferometry

From the previous discussion, we can simply add one more aperture and sum two amplitude functions for the case of two telescope interferometry. For the baseline length, B, the amplitude is determined as follows:

$$A_{two}(\theta) = \sum (wavelets) \tag{2.8}$$

$$= \int_{+B/2-D/2}^{+B/2+D/2} e^{i(2\pi x\theta/\lambda)} dx + \int_{-B/2-D/2}^{-B/2+D/2} e^{i(2\pi x\theta/\lambda)} dx \tag{2.9}$$

$$= \frac{\sin(\pi\theta D/\lambda)}{\pi\theta D/\lambda} \cos(\pi\theta B/\lambda) 2D \tag{2.10}$$

Accordingly, we can derive the intensity of a two-aperture interferometer.

$$I_{two}(\theta) = 2I_{one}(\theta)\left[1 + \cos(2\pi\theta B/\lambda)\right] \tag{2.11}$$

This result is plotted in Figure 2.4. The blue line corresponds to the intensity pattern of a two aperture interferometer with B=3D. The peak intensity of a two aperture interferometer is four times higher than that of the one aperture diffraction pattern (red line in Figure 2.4). It can be observed that the broad envelope of the interference pattern is produced by a single aperture whereas the rapidly oscillating interference pattern depends on the baseline length, B.

2.3 Determination of Array Configuration

This chapter is an elaboration on Step 1 and Step 2 of the SOCS framework.

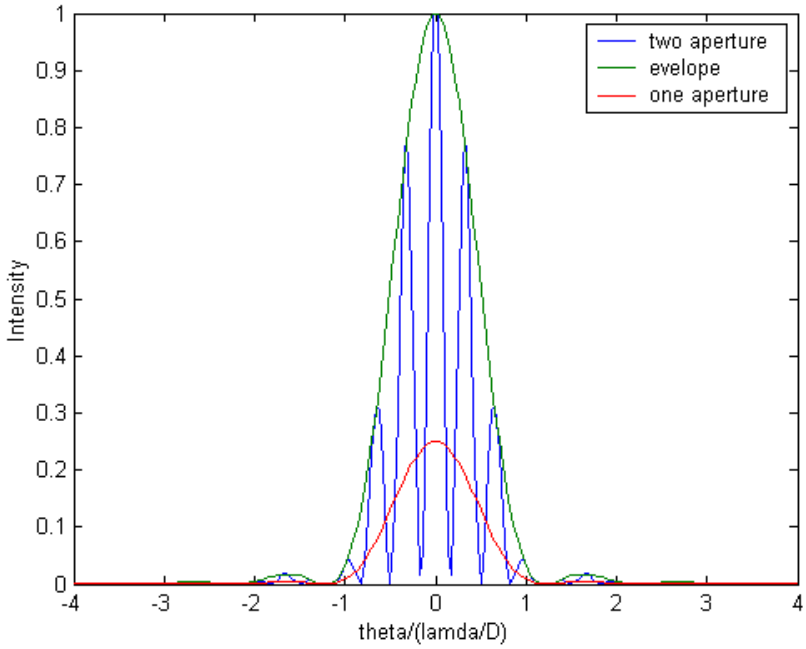

Figure 2.4 Two aperture interferometry vs. one aperture intensity plot

2.3.1 Optics Performance Requirements

Angular Resolution

The angular resolution predicts how crisply an optical system is able to resolve an observing target. The smaller the angular resolution, the more graphical features a telescope system can extract from an image.

In Section 2.2, the definition of angular resolution is given by reading the first null point of an intensity plot (point spread function) or FWHM. For the case of a two aperture interferometer, the angular resolution given by the FWHM or the first null point is:

$$\theta_r = \frac{\lambda}{2B} \tag{2.12}$$

This result is applicable to a Michelson type interferometer with a long baseline since the visibility loss is compensated by a series of measurements with different orientations of the baseline. However, for a Fizeau interferometer with instant imaging, determining angular resolution is more complex than Equation 2.12. It will be discussed in detail in the following sections.

Encircled Energy

The encircled Energy $E_e(q)$ is a monotonically increasing function of the off-axis angle as follows:

$$E_e(\theta_o) = \frac{A_{array}}{\lambda^2} \int_0^{\theta_o} \int_0^{2\pi} I(\theta,\phi)\theta d\phi d\theta \tag{2.13}$$

where A_{array} is the total area of the 3 apertures, θ is the off-axis angle; ϕ is the azimuth angle and $I(\theta,\phi)$ is the multi-aperture point-spread-function (PSF). The factor in front of the integral comes from the total flux entering the system at the input pupil and is used to normalize E_e to 1. We are interested in the encircled energy, when θ_o is equal to the angular resolution θ_r set forth in the requirements. Our purpose in using encircled energy is to measure the relative size between the mainlobe and sidelobes of the Point Spread Function (PSF). So our encircled energy will be the encircled energy within the first minima (mainlobe) of a point spread function. The encircled energy of the unaberrated airy disk is 84%.

Figure 2.5 shows a diffraction encircled energy plot of one ARGOS sub-aperture.

Strehl Ratio

As shown in Figure 2.2, it is necessary to calculate the beam combining errors, which mean the maximum allowable piston, tip/tilt and pupil mapping errors at the entrance pupil of the system beam combiner. Since a real optical system consists of additional surfaces such as mirrors, and refractive surfaces in the relay optics, more rigorous calculation for each optical component is required.

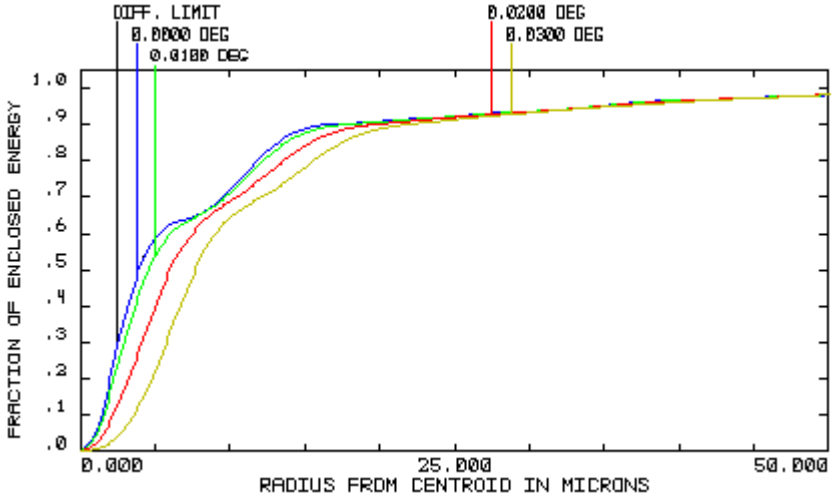

Figure 2.5 Encircled energy plot of one ARGOS sub-aperture (Mewlon 210). Each color indicates a different field angle in degrees

When we calculate these errors, we standardize our merit function to the Strehl ratio, which is the ratio between the intensity on-axis of an aberrated beam and the intensity on-axis of an unaberrated beam. We set the minimum allowable Strehl ratio to 80% of an unaberrated beam, which means that the system is near-diffraction limited.

Minimum Intensity peak = 80% of unaberrated beam

Strehl ratio = 0.8 (SR >0.8 means diffraction-limited)

When we express OPD errors, it usually means P-V (Peak to Valley) OPD or P-V wave-front error. RMS(Root Mean Square) OPD or wavefront error is the square root of the average of the squares of all the OPD errors sampled over the full aperture of the system.

$$\text{RMS OPD} = \text{P-V OPD} / 3.5 \tag{2.14}$$

The relationship between the Strehl ration and the RMS OPD is approximated by

$$\text{Strehl Ratio} = e^{-\left(2\pi\frac{\sigma}{\lambda}\right)^2} \tag{2.15}$$

where σ is RMS Wavefront error in λ.

To achieve a Strehl Ratio of 0.8, $\sigma = 0.075\ \lambda$ is the maximum allowable RMS error. This corresponds to 0.25 λ OPD error.

Signal-to-Noise Ratio (SNR)

A sparse aperture array causes a substantial depression in the modulation transfer function (MTF). As an interferometric array becomes more sparse, we will achieve a finer angular resolution at the expense of increased noise in the image. The signal-to-noise ratio (SNR) can be increased by longer integration time, but it levies a pointing stability requirement on the whole control system. SNR is discussed in detail in Chapter 4.

Pointing Stability and Pointing Accuracy

Figure 2.6 shows how pointing stability and pointing accuracy are defined for an imaging

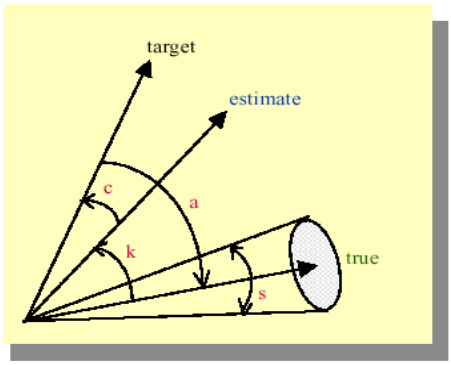

target	desired pointing direction (α,δ)
true	actual pointing direction (mean)
estimate	estimate of true (instantaneous)
a	pointing accuracy (long-term)
s	stability (peak-peak motion)
k	knowledge error
c	control error

(Source: Gary Mosier, NASA GSFC)

Figure 2.6 Definitions for spacecraft/telescope pointing requirements. Note that the desired target direction is given in terms of α (right ascension) and δ (declination)

spacecraft system. These pointing requirements are considered as attitude control system (ACS) requirements, but these ACS requirements bear some relationships with an optical payload. For example, a pointing stability of a tenth of the angular resolution of a telescope is usually required.

2.3.2 Point Spread Functions vs. Modulation Transfer Function

Traditional image quality criteria such as resolution and encircled energy (EE) are inade-

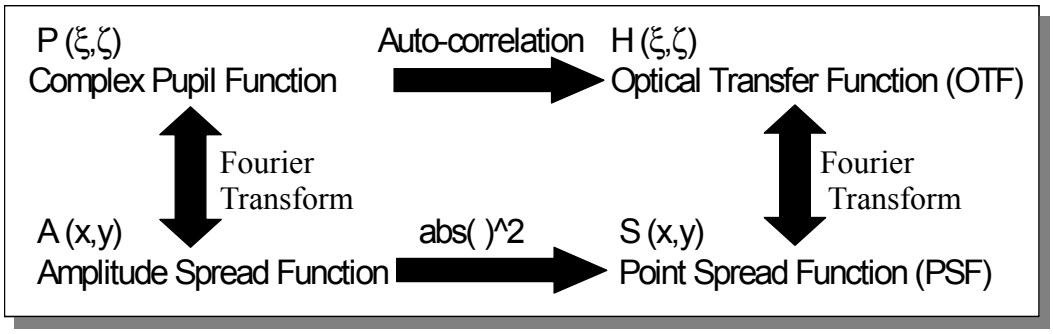

Figure 2.7 The relationship between the PSF and OTF. The absolute value of OTF is MTF.

quate for many sparse aperture or interferometric array applications[Harvey, 1988]. Given the angular resolution and encircled energy specifications from the optics requirements, the designers should use the optical performance evaluation tools such as point spread functions (PSF) and modulation transfer functions (MTF).

Figure 2.7 shows the crucial relationship between the two most common image quality criteria - PSF and MTF. The point spread function (PSF) is the squared modulus of the Fourier transform of the complex pupil function. OTF is a Fourier transform of PSF. MTF is an absolute value (magnitude) of OTF.

Point Spread Function (PSF)

A PSF is an irradiance distribution representing the image of an ideal point source. Namely, a PSF is a diffraction limited intensity distribution in response to a point source such as a very distant star. The intensity plots shown in Figure 2.3 and Figure 2.4 are the PSF plots. Figure 2.8 shows the Zemax-generated PSF plots of the ARGOS Nonsequential ray tracing model using the Huygens integration method.

We can derive the Strehl ratio, encircled energy and angular resolution from the PSF. The

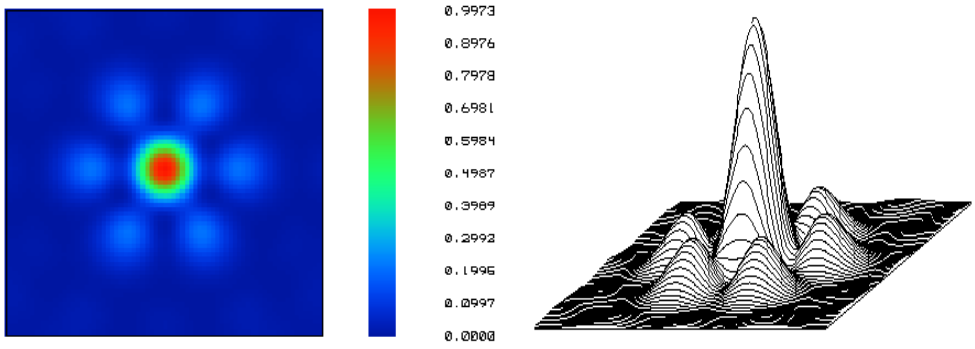

Figure 2.8 PSF plot of Golay-3 sparse array (ARGOS): 2D plot (left) and 3D plot (right)

Strehl ratio is the ratio between the on-axis intensity of an aberrated beam and the on-axis intensity of an unaberrated beam. Encircled energy is defined as the intensity energy enclosed under the PSF envelope as a function of off-axis angle.

Modulation Transfer Function (MTF)

When we look at an extended objects such as the Moon and a faint distant nebula, evaluation of an optical system is far more complex than by simply looking at a point source response (PSF). MTF is a better metric to evaluate the contrast (modulation) transfer characteristic of an extended object.

A perfect monolithic array, free of optical aberrations, has a monotonically decreasing MTF contrast characteristic as shown in Figure 2.11. In case of a sparse array, the MTF suffers a contrast loss in the mid spatial frequency range as shown in Figure 2.10. This characteristic of a sparse array interferometer is also observed in Figure 2.12, where the PSF and MTF plots of D=0.21m (ARGOS sub-aperture diameter) and L=0.12m (blue), 0.19m (red), 0.3m (black) are shown. The blue MTF line of Figure 2.12 resembles a monolithic aperture showing a linearly decreasing contrast. More sparse arrays (red and black lines in Figure 2.12) indicate a contrast loss in the mid spatial frequency range.

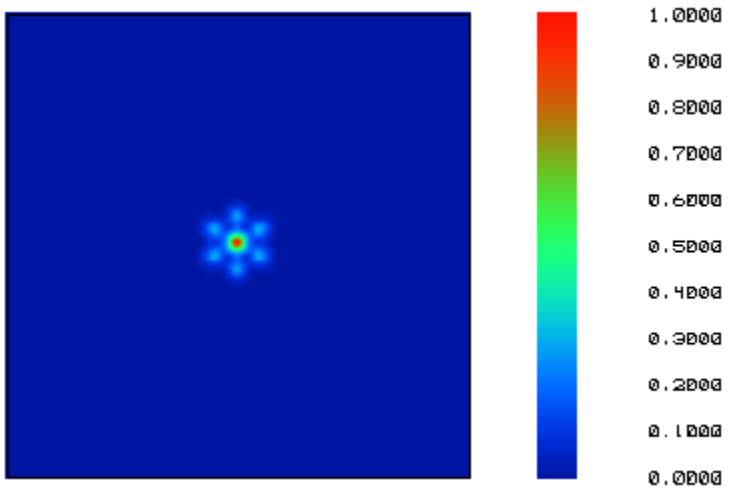

Figure 2.9 MTF plot of a Golay-3 array (ARGOS configuration)

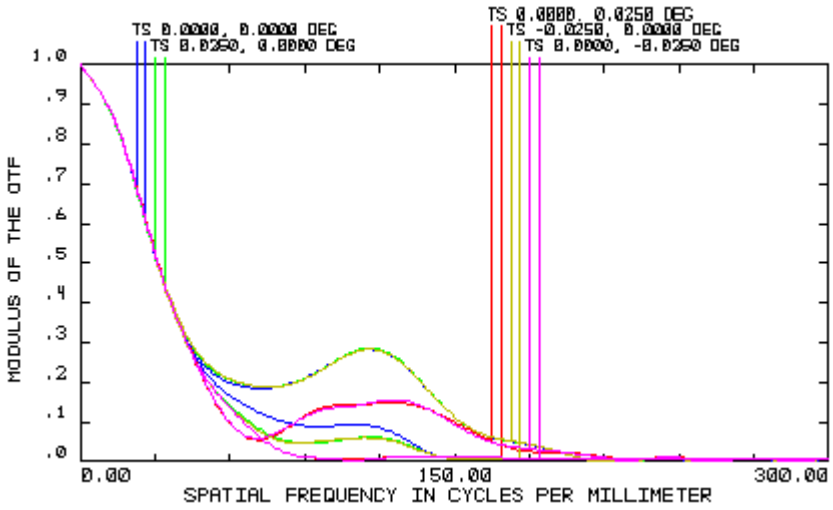

Figure 2.10 MTF plot of ARGOS sparse array with color lines indicating the field angles

MTF is also an important evaluation criterion for determining the angular resolution of the system. We can see that the MTF plot with L=0.3m exhibits two zero values rather than one. The first zero denoted by Fr is the practical spatial cut-off frequency, and defines the "practical resolution limit". The Fc is the cut-off frequency, whose inverse indicates an angular resolution under the normal condition that there is no Fr (another zero region)

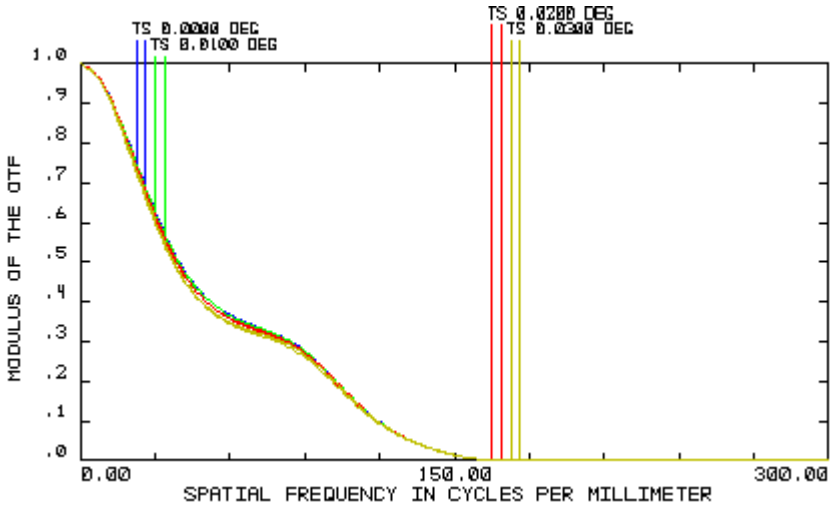

Figure 2.11 MTF plot of one ARGOS sub-aperture telescope

before Fc. So the larger Fc or Fr is, the better angular resolution a sparse array will achieve.

2.3.3 Determining the Angular Resolution of a Sparse Array

As opposed to a monolithic aperture, the method of Full-Width-Half-Maximum (FWHM) or reading the first minima of a PSF plot is not sufficient to determine the angular resolution. Assuming that angular resolution is fully determined by the array size, the PSF can reveal the highest achievable angular resolution. This assumption holds especially for very large baseline Michelson interferometers. We can observe in Figure 2.12, that the main-lobe size of the PSF plot is getting smaller, indicating improved angular resolution as we increase the array size L. The Fizeau interferometer, however, requires an instant full u-v coverage, which limits our practical resolution. In addition, as discussed above, the contrast loss of mid-spatial frequency range should be avoided. So if the practical cut-off frequency(Fr) is less than the normal cut-off frequency(Fc), Fr determines the limiting angular resolution. In other words, there should be no zero region before the MTF reaches Fc.

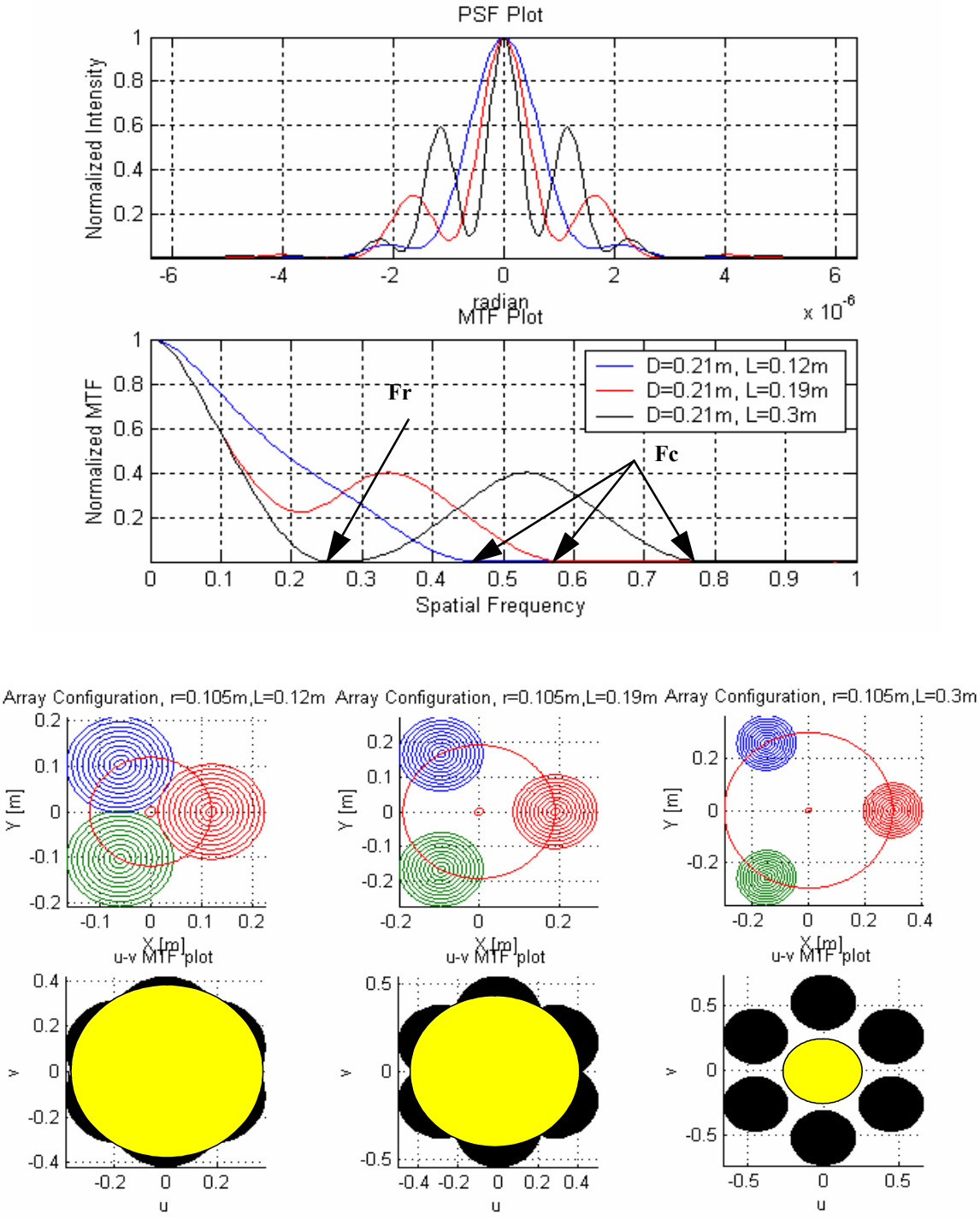

Figure 2.12 PSF and MTF plots when D=0.21m and L = 0.12m (blue), 0.19m (red), 0.3m (black). The corresponding array configurations are shown below the PSF-MTF plot. The black-yellow figure is a MTF plot. Yellow circles indicate the practical cut-off frequency.

As we increase L, the array becomes more sparse, which, as a result, boosts the heights of the sidelobes on the PSF plots. The MTF plot of L=0.3m (black in Figure 2.12) has two zeros while others have only one. It means the resolution is limited not by Fc but Fr, whose inverse is an angular resolution of one single aperture (1.22 * wavelength/D). So the sparse array has no advantage over one sub-telescope. As L decreases further from L=0.3m, the Fr becomes equal to Fc and no more singular point exists between zero spatial frequency and Fc as we can see in the uv-MTF plots of Figure 4.

When L=0.12m, the three apertures touch each other, the MTF plot almost resembles that of one monolithic aperture, which is very desirable. But such an array results in no more than a Multiple Mirror Telescope(MMT) sacrificing the possibility of achieving a better angular resolution. The array configuration of the ARGOS (see Figure 2.13) is selected to L = 0.19185 m for D=0.21 m (8 inch) sub-telescopes, and it gives a better theoretical angular resolution of 0.35 arcsec rather than 0.55 arcsec of a single aperture, as well as a reasonable MTF characteristic (see Figure 2.10).

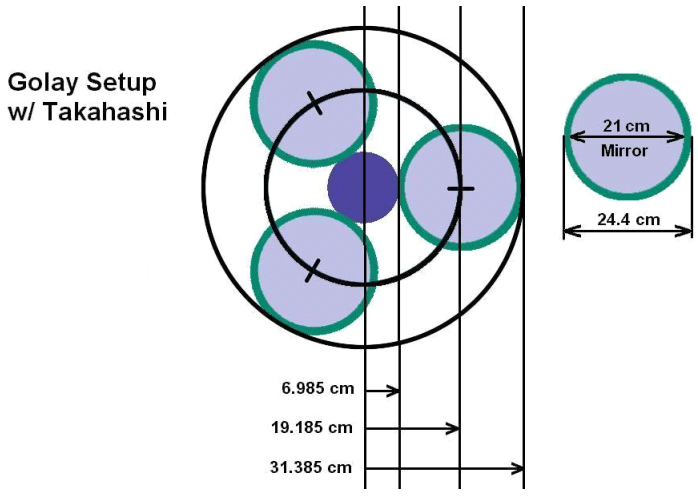

Figure 2.13 Final array configuration of ARGOS

Development of Angular Resolution Equation for Golay-3 Array

The deterministic relationship between the effective diameter of an array and its configuration (L and D) is developed in this section. According to the previous discussions, finding the practical cut-off frequency from a MTF plot should be performed in order to find the angular resolution. From the relationship between PSF and MTF in Figure 2.7, we can derive the MTF by Fourier transforming the PSF. However, we can also derive MTF by performing an auto-correlation procedure of a pupil function. This is the same as generating a uv plot of an array. In Figure 2.12, the yellow circles in the 2D MTF plot indicate the practical cutoff frequency. R_{uv} is the radius of a yellow circle.

u,v spatial frequencies are defined as follows:

$$u = \pm\frac{x_2 - x_1}{\lambda} \qquad v = \pm\frac{y_2 - y_1}{\lambda} \tag{2.16}$$

where x,y points are at any point in the telescope pupil planes.

So, when we generate a uv-MTF plot, we can ignore the wavelength, λ, making the unit of a uv plot the same as the array configuration factors such as L (array radius) and D (aperture diameter).

By the geometry in Figure 2.14, R_{uv} can be derived as follows.

p is the distance between the center of a uv plot and the center of six symmetric uv circles, and q is the radius of those six symmetric circles highlighted by green color. From the inspection, p and q are given as:

$$q = D \qquad p = \sqrt{3}L \tag{2.17}$$

Applying the cosine rule into the triangle with p, q and R_{uv}:

$$R_{uv}^{\ 2} - 2p\cos 30 R_{uv} + p^2 - q^2 = 0 \tag{2.18}$$

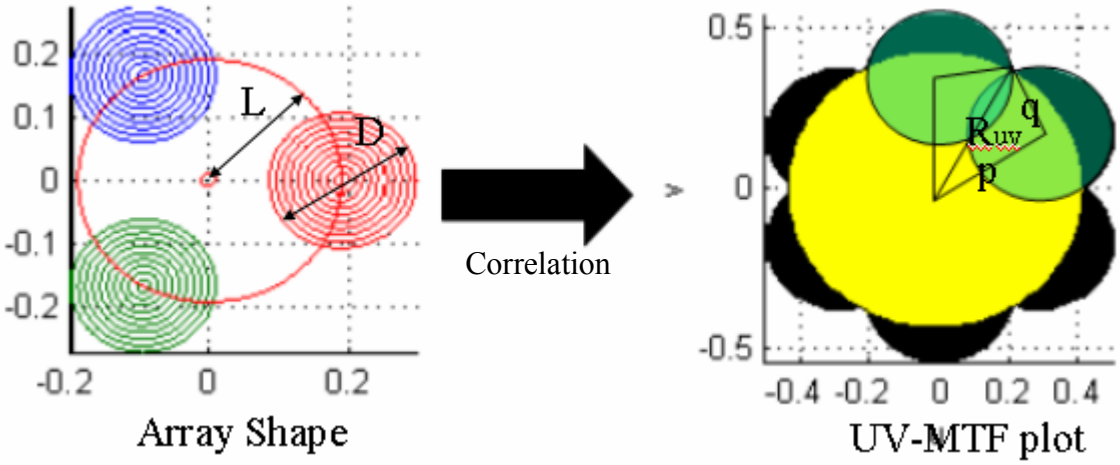

Figure 2.14 Calculation of Ruv and the effective diameter

We can solve this equation for R_{uv} :

$$R_{uv} = \frac{\sqrt{3}p + \sqrt{4q^2 - p^2}}{2} \tag{2.19}$$

Since the effective diameter of an array equals R_{uv} ,

$$D_{eff} = 2R_{eff} = R_{uv} = \frac{3L + \sqrt{4D^2 - 3L^2}}{2} \tag{2.20}$$

According to Equation 2.20, L=2/$\sqrt{3}$ D appears to be the maximum array size resulting in a real solution with no imaginary part. However, L=D (the original Golay-3 configuration[Kong, 1998;Golay, 1971]) is the maximum L, with no singular points inside the uv plot region. From the geometry of three aperture array, when L=D/ $\sqrt{3}$, each aperture touches each other, restricting the minimum size of L. Thus, L of a three aperture array should be within these values:

$$\frac{D}{\sqrt{3}} \le L \le D \tag{2.21}$$

Equation 2.20 is plotted in Figure 2.15 with the constraint (Equation 2.21). We can clearly

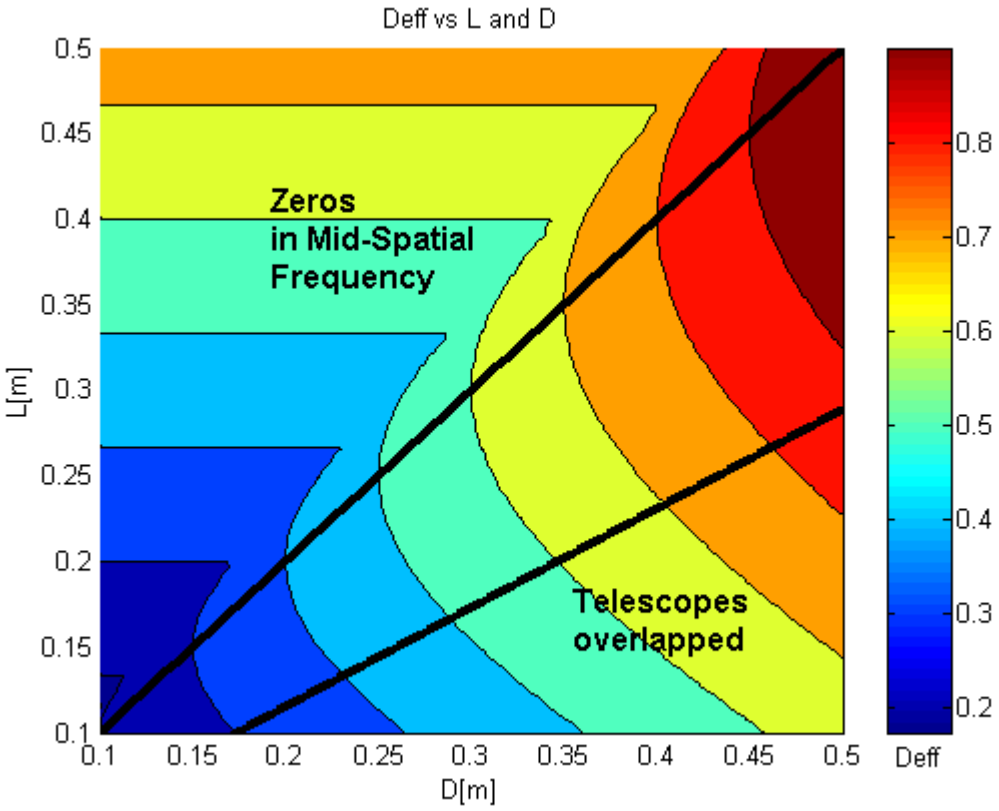

Figure 2.15 Iso-effective-diameter plot as a function of L and D. Two black lines indicate the constraints in Equation 2.21

see that increasing the diameter, D, or the array size, L, results in a larger effective diameter (better angular resolution). It is interesting to note that we can achieve a larger effective diameter by increasing L and decreasing D (or increasing D and decreasing L).

Finally, the angular resolution of a Golay-3 type sparse imaging array is given by:

$$\theta_r = 1.22\frac{\lambda}{D_{eff}} = 2.44\frac{\lambda}{3L + \sqrt{4D^2 - 3L^2}} \tag{2.22}$$

2.4 Beam Combining Errors and Error Budget Table

This section corresponds to SOCS framework step 3.

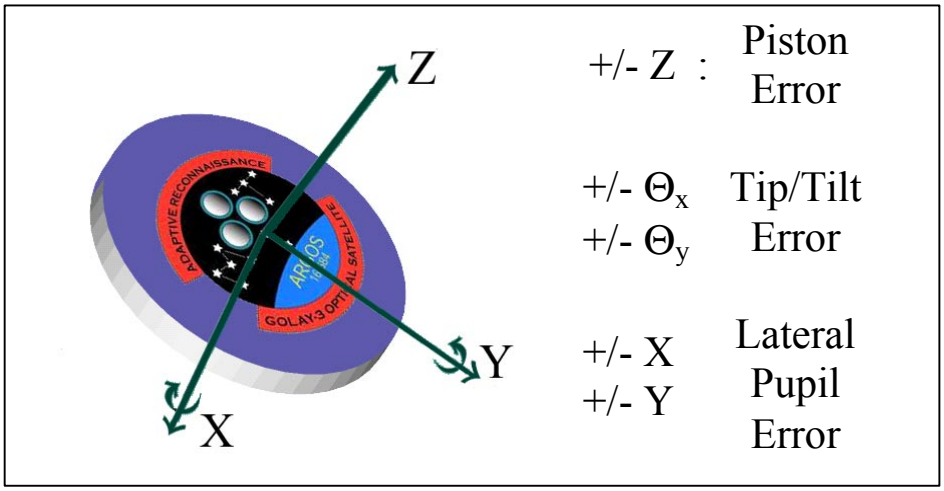

Figure 2.16 Three primary beam combining errors

There are three beam combining errors as shown in Figure 2.16 that need to be kept within certain tolerance values for a sparse interferometric array to achieve coherent phased beam combining.

Piston Error: This error results from Optical Path Difference (OPD) along the Z-axis of the exit pupil plane and is only relevant for multiple beams. OPD misalignments between the sub-apertures can degrade the Point Spread Function (PSF) to that of a monolithic system. The maximum tolerable piston error is roughly l/10λ or 55 nanometers for the 550nm wavelength. Optical delay lines (ODL) will be used to control OPD and minimize this type of error.

Tip/Tilt Error: Tip/Tilt error is a result of rotations in the X and Y-axis of the compressed pupil plane. Tilt error analysis predicts a maximum allowable tolerance of 0.35 μrad. A fast steering mirror (FSM) will be used to correct this error.

Pupil Mapping Error: Lateral pupil mapping error is also known as shear error. The shearing comes from the image being moved along the X-Y plane. The allowable tolerance for pupil error is estimated to be roughly 12 μm. A modified optical delay line or movable fold mirror will be used to control lateral pupil error. In addition, the magnification errors between the subapertures must be kept within a certain tolerance value.

The following sections will detail an analysis on these beam combining errors.

2.4.1 Piston Error

Development of Golay-3 Interference Equation

The intensity of a multiple aperture array is given by [Mennesson, 1997]:

$$I \propto \left|\frac{\pi D(1+\cos(r))}{\lambda}\right|^2 \left|\frac{J_1(\pi D \sin r/\lambda)}{\pi D \sin r/\lambda}\right|^2 \left|\sum_{k=1}^{n} e^{j2\pi(L_k r/\lambda)\cos(\delta_k-\theta)} e^{j\phi_k}\right|^2 \tag{2.23}$$

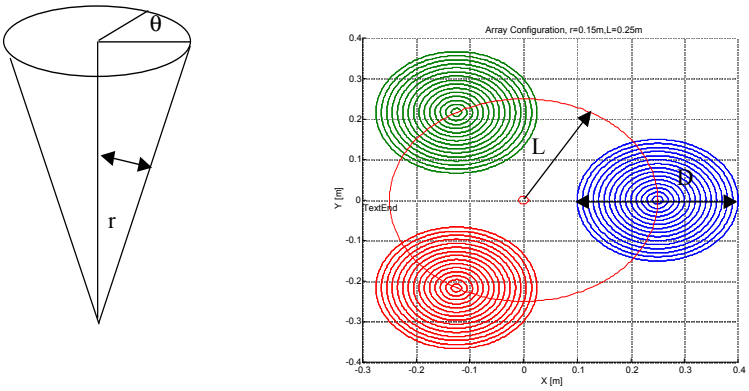

Figure 2.17 Notations for Menneson's Interferometric equation.

The first term of Equation 2.23 is practically constant over a small range of r. The second term is the intensity pattern of a single aperture and the third term is an array interference factor. Equation 2.23 looks similar to the two aperture interference Equation 2.11, but

Equation 2.23 adds a phase difference into an individual aperture. This phase information is denoted by ϕ_k. Since we are interested in the effect of the OPD errors on the PSF of a Golay-3 type array, a simplification of Equation 2.23 is performed to derive the interference term for a Golay-3 sparse array.

$$I_{Interference} = \left| \sum_{k=1}^{n} e^{j2\pi(L_k r/\lambda)\cos(\delta_k - \theta)} e^{j\phi_k} \right|^2 \tag{2.24}$$

With n=3,

$$I_{Interference} = \left| e^{j2\pi(Lr/\lambda)\cos(\theta)} e^{j\phi_1} + e^{j2\pi(Lr/\lambda)\cos(2\pi/3-\theta)} e^{j\phi_2} + e^{j2\pi(Lr/\lambda)\cos(4\pi/3-\theta)} e^{j\phi_3} \right|^2 \tag{2.25}$$

$$\begin{aligned} &= (e^{j2\pi(Lr/\lambda)\cos(\theta)} e^{j\phi_1} + e^{j2\pi(Lr/\lambda)\cos(2\pi/3-\theta)} e^{j\phi_2} + e^{j2\pi(Lr/\lambda)\cos(4\pi/3-\theta)} e^{j\phi_3}) \\ &\bullet (e^{-j2\pi(Lr/\lambda)\cos(\theta)} e^{-j\phi_1} + e^{-j2\pi(Lr/\lambda)\cos(2\pi/3-\theta)} e^{-j\phi_2} + e^{-j2\pi(Lr/\lambda)\cos(4\pi/3-\theta)} e^{-j\phi_3}) \end{aligned} \tag{2.26}$$

The OPD of the i th aperture to the j th aperture is defined as following:

$$\phi_{ij} = \phi_i - \phi_j \tag{2.27}$$

Simplifying Equation 2.26 results in:

$$\begin{aligned} &I_{Interference} = 3 + 2\cos(\sqrt{3}\cos(\pi/6+\theta)2\pi Lr/\lambda + \phi_{12}) \\ &+2\cos(\sqrt{3}\cos(\pi/6-\theta)2\pi Lr/\lambda + \phi_{13}) + 2\cos(\sqrt{3}\sin(\theta)2\pi Lr/\lambda + \phi_{23}) \end{aligned} \tag{2.28}$$

Equation 2.28 is plotted in Figure 2.18 incrementing the phase of the first aperture by 0.1λ with respect to the second and the third apertures. θ is set to zero. Since color CCD imaging makes use of three filters (Red-Green-Blue), the corresponding operating wavelengths were used to calculate the average intensity pattern (PSF) for three different wavelengths.

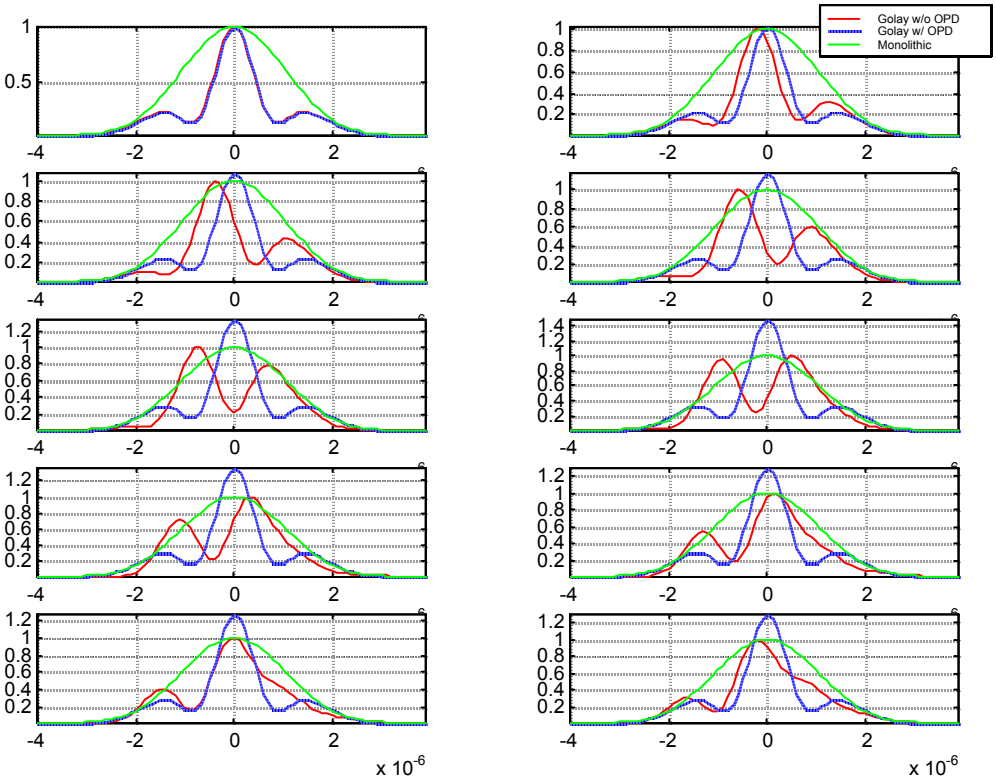

Figure 2.18 2-dimensional PSF plot using Equation Increment 1/10 λ

l/10 λ is suggested as maximum piston (OPD) error allowed at the beam combiner, because this gives approximately more than 90% of the original intensity (Strehl Ratio = 0.9) with minimal degradation in the angular resolution. At 0.9 λ OPD error, the size of the mainlobe on the PSF plot starts resembling that of a monolithic aperture, which means the angular resolution of a sparse imaging array is no better than that of an individual sub-aperture.

Numerical Verification Using MATLAB and ZEMAX

Figure 2.19 shows how the PSF changes when we add OPD error into one of three apertures. As the piston error increases, two major deviations develop over the envelope of the PSF. First, the main envelope shifts in the direction of the piston error. The resultant direction of the envelope shift is the vector sum of phase (piston) error directions weighted by

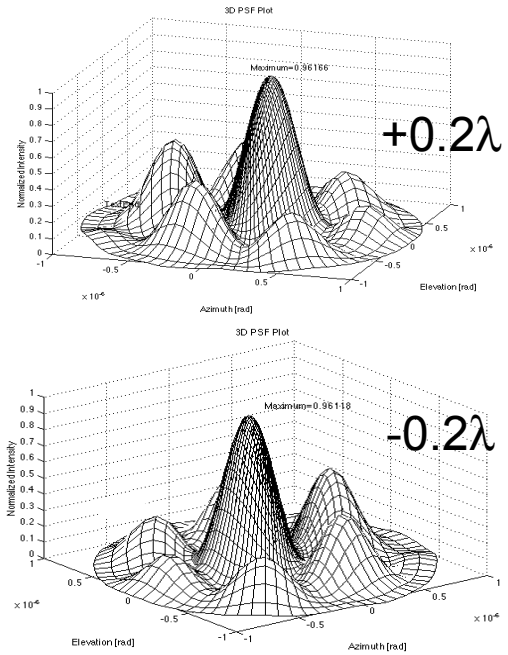

Figure 2.19 3D PSF plot of Golay-3 array with a piston error of +/- 0.2 λ with respect to other apertures

the amount of error. Secondly, the peak intensity gets reduced compared to the normal PSF without any piston errors resulting in a reduced Strehl Ratio (SR). The size of the mainlobe also expands showing a degraded angular resolution (See Figure 2.20).

Our piston error tolerance is derived from the observations made above. When a piston error is 0.1 λ, the peak intensity is 98% of the normal intensity. The beam combining piston error tolerance = 0.1λ = 55nm.

2.4.2 Tip/Tilt Errors

Finite Element Modeling

The approach employed here to analyze tilt errors is to further segment each aperture into smaller elements. We can imagine a three aperture golay array consisting of numerous tiny apertures as shown in Figure 2.21.

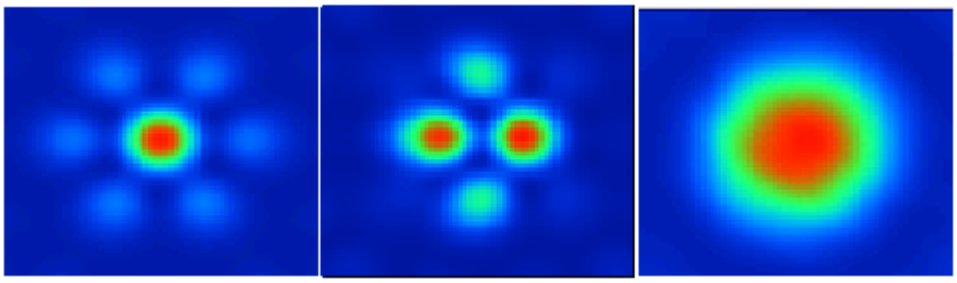

Figure 2.20 PSF plot of Golay-3 array with zero OPD, 0.5 λ OPD , and 1.0 λ OPD, from the left to the right.

The following assumptions are made:

(1) Tilt errors are very small.

(2) Each finite element model is considered as a circular aperture with equal diameters even though it is rectangular. This assumption become more reasonable as we increase the number of elements.

The point spread function is calculated by summing up the interference from all of the finite elements. The phase difference at the central point due to tilt errors are added to the interference term of Equation 2.23. We can find the detrimental effects of tilt errors as shown in Figure 2.22. The maximum peak intensity is reduced to 64% of its original value without any tilt errors. By reading the normalized SR values of the PSF plots under the influence of tilt errors, the maximum allowable tilt error at the beam combining section is determined. The normalized SR values are tabulated in Table 2.1 on page 60. This FEM method predicts that the tilt tolerance between each beam entering the beam combiner should be less than 20 μ degrees (0.072 arcsec = 0.35 μrad).

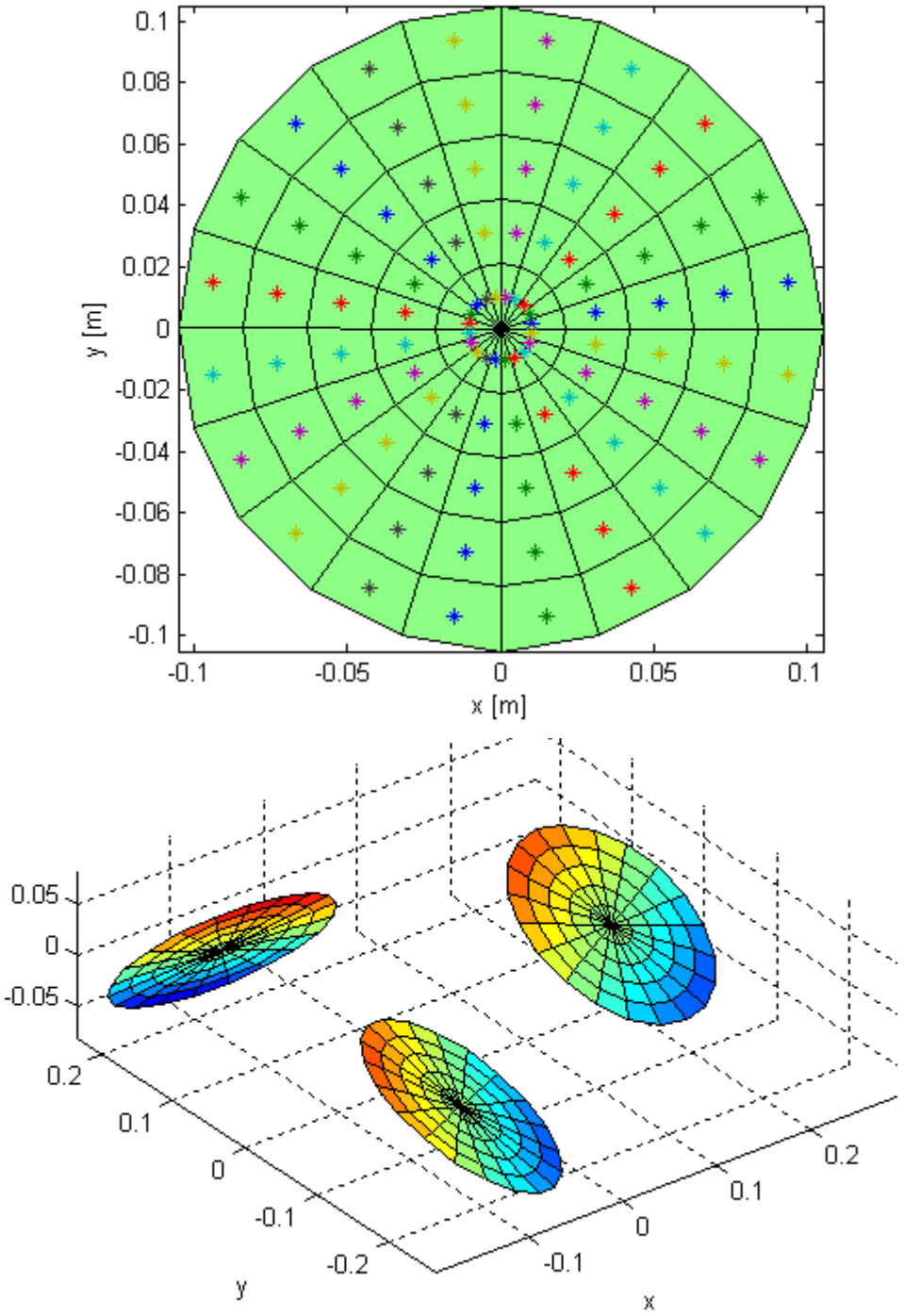

Figure 2.21 The single aperture of D=0.21 m is segmented into a FEM model with 100 elements. The "*" point at the middle of each element indicates the central point, and the phase error of each element is calculated at the central point.

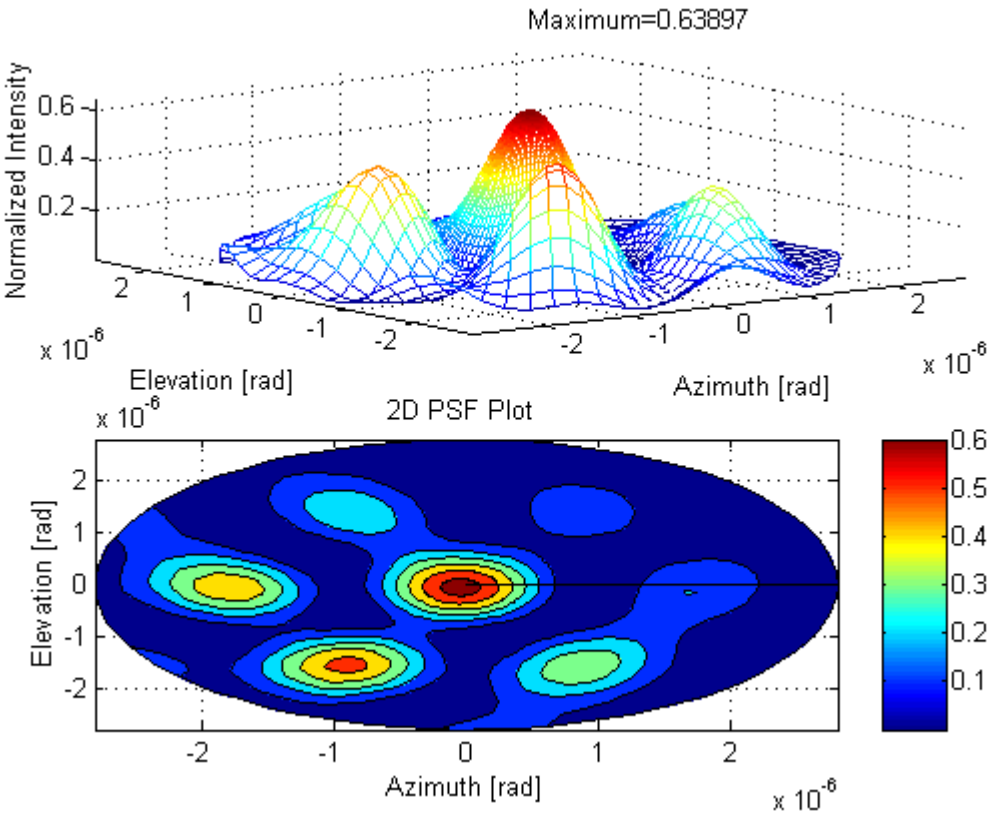

Figure 2.22 PSF plot under the following tilt errors: Aperture 1: X, Y Tilt =0, Aperture 2: X tilt=1.0e-4 degrees, Ytilt=0, Aperture 3: Xtilt=0,Ytilt= -1.0e-4 degrees.

2.4.3 Pupil Mapping Error

If coherent phased imaging is to be achieved over any significant field-of-view (FOV), the pupil mapping process must be performed such that the exit pupil is an exact (scaled) replica of the entrance pupil[Faucherre, 1989;Harvey, 1985;De Hainaut, 1988]. This constraint is commonly called the golden rule of beam combining. There are two error sources contributing to incorrect pupil mapping. The first type of error is a shear error, also commonly called a lateral pupil mapping error. Shearing errors come from the incorrect subaperture image locations across the beam combiner's entrance pupil plane. The second

TABLE 2.1 Strehl Ratio variations under the tip/tilt errors of ARGOS

	Aperture 1		Aperture 2		Aperture 3	
SR	X Tilt [Deg]	Y Tilt [Deg]	X Tilt [Deg]	Y Tilt [Deg]	X Tilt [Deg]	Y Tilt [Deg]
0.99996	5.00E-07	0	5.00E-07	0	5.00E-07	0
0.98689	1.00E-05	0	1.00E-05	0	1.00E-05	0
0.94852	2.00E-05	0	2.00E-05	0	2.00E-05	0
0.88772	3.00E-05	0	3.00E-05	0	3.00E-05	0
0.99996	0	5.00E-07	0	5.00E-07	0	5.00E-07
0.98689	0	1.00E-05	0	1.00E-05	0	1.00E-05
0.94852	0	2.00E-05	0	2.00E-05	0	2.00E-05
0.88772	0	3.00E-05	0	3.00E-05	0	3.00E-05
0.99993	5.00E-07	5.00E-07	5.00E-07	5.00E-07	5.00E-07	5.00E-07
0.9997	1.00E-06	1.00E-06	1.00E-06	1.00E-06	1.00E-06	1.00E-06
0.9933	5.00E-06	5.00E-06	5.00E-06	5.00E-06	5.00E-06	5.00E-06
0.97394	1.00E-05	1.00E-05	1.00E-05	1.00E-05	1.00E-05	1.00E-05
0.89958	2.00E-05	2.00E-05	2.00E-05	2.00E-05	2.00E-05	2.00E-05
0.78755	3.00E-05	3.00E-05	3.00E-05	3.00E-05	3.00E-05	3.00E-05
0.9439	2.00E-05	0	-2.00E-05	0	-2.00E-05	0

source of incorrect pupil mapping is a magnification error. Sub-apertures need to be afocal telescopes, producing a collimated beam with a certain magnification (compression) ratio. This magnification ratio must be precisely controlled up to a required tolerance value. In this thesis, an analysis of pupil mapping errors based on [Faucherre, 1989] is developed taking both shearing error and sub-aperture magnification error into consideration.

A one dimensional, two aperture sparse interferometric array is considered here as shown in Figure 2.23. D is the diameter of a sub-aperture while d is the compressed exit beam size of a sub-aperture. B is the baseline length between apertures while b is the distance between compressed beams when they enter the beam combiner. α is a field angle of the incoming beam to the telescope array, and β is the corresponding field angle to the beam combiner. The golden rule of beam combining can be stated as follows:

$$m_a = \frac{D}{d} = \frac{B}{b} = m_s \tag{2.29}$$

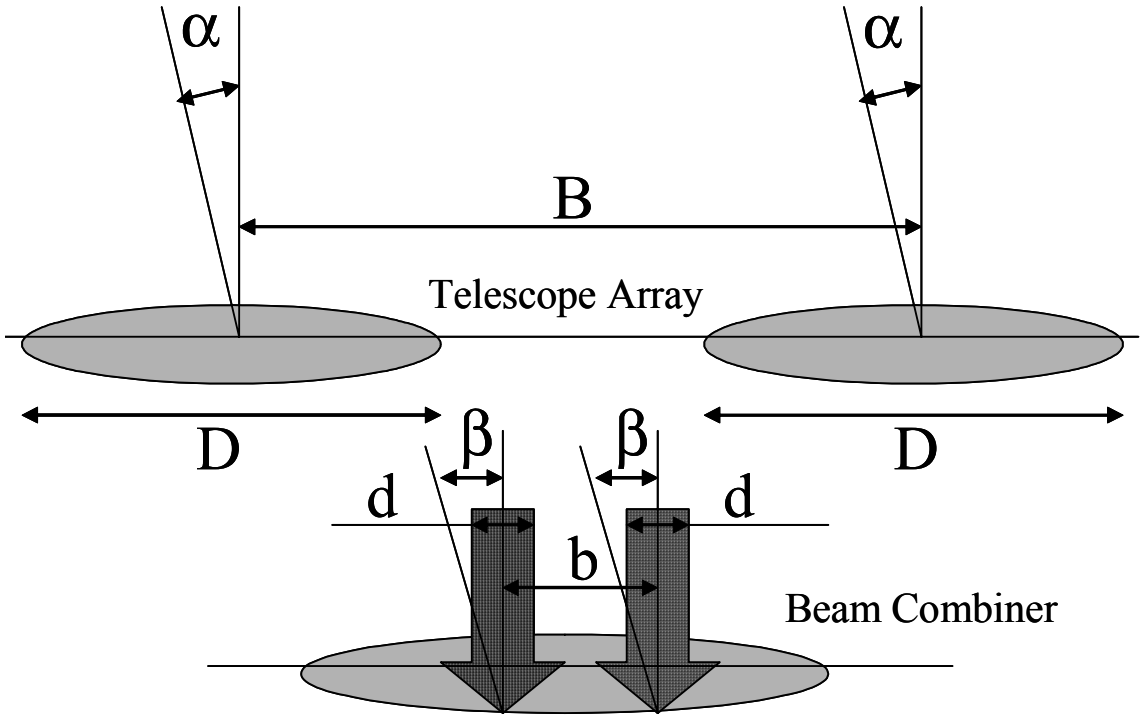

Figure 2.23 Graphical setup for two aperture interferometric array to analyze pupil mapping

where m_a is the aperture magnification factor (D/d), and m_s is the baseline magnification factor (B/b).

From the geometry of Figure 2.23, the net piston errors between input and exit beams due to the incorrect pupil mapping is:

$$OPD_{net} = \left| B\sin\alpha - b\sin\beta \right| = \left| B\sin\alpha - \frac{B}{m_s}\sin(m_a\alpha) \right| \tag{2.30}$$

According to the discussion in Section 2.3.1, 1/10λ phasing is desired to meet the SR and angular resolution requirements. Thus, equating Equation 2.30 with 1/10λ, using an assumption that we can ignore the sine functions for small α, results in:

$$B\alpha\left|1-\frac{m_a}{m_s}\right|=\frac{\lambda}{10} \tag{2.31}$$

Shear Error with Correct Magnification

Firstly, a calculation of shear error tolerance is performed with an assumption that there is no magnification error (sub-telescopes are strictly afocal with the exactly same magnification). Then, the correct magnification is m_a=D/d=B/(b+Δb). The incorrect mapping m_s is still B/b. Inserting these into Equation 2.31 results in:

$$\alpha\left|B-bm_a\right|=b\alpha\left|\frac{B}{b}-\frac{B}{b+\Delta b}\right|=\alpha\frac{B\Delta b}{b+\Delta b}=\frac{\lambda}{10} \tag{2.32}$$

Simplifying for Δb, gives:

$$\Delta b=\frac{\lambda}{10m_a\alpha} \tag{2.33}$$

Equation 2.33 predicts the important relationship between the field of view (α is half of the field angle) and the magnification factor if the "no magnification error" assumption holds. Figure 2.24 shows a graph of tolerable lateral pupil error vs. half of the FOV angle. We can suppress the FOV or decrease the magnification ratio in order to have less stringent shear error tolerance. Since the magnification (compression) of the ARGOS sub-aperture is 10 (210 mm to 21 mm collimated beam), and our full-angle FOV is around 3 arc min, more than 12 microns are allowed for shear error at the beam combiner's entrance pupil.

Incorrect Shear with Incorrect Magnification

The assumptions of no magnification error used for Equation 2.33 is inadequate since perfectly replicating any sub-aperture is impossible in terms of manufacturability. There usually exists some performance window specified by optics manufacturers. The objective of

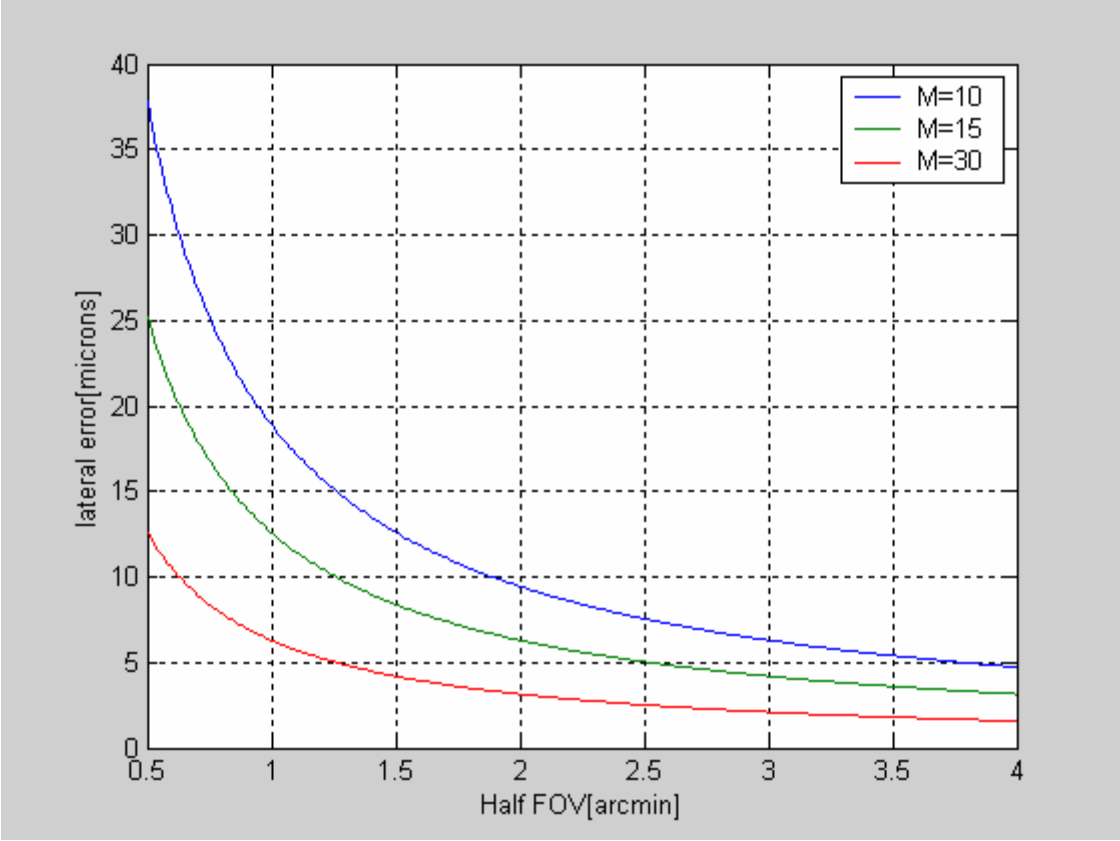

Figure 2.24 FOV vs. tolerable shear error for different magnification factors

this calculation is to find out how precise the magnification tolerance level must be in order to achieve coherent beam combining. If the magnification tolerance is too stringent to be manufactured, methods of relaxing this tolerance will be explored.

For both incorrect m_a (=D/d) and incorrect m_s (=B/b), the correct magnification ratios are defined as follows:

$$m_a^{correct} = m_a + \Delta m_a = \frac{B}{b + \Delta b} = m_s^{correct} \tag{2.34}$$

Inserting these results into Equation 2.31, gives:

$$\alpha b\left|\frac{B}{b}-m_a\right|=\alpha b\left|\frac{B}{b}-\frac{B}{b+\Delta b}+\Delta m_a\right|=\alpha\left|\frac{\Delta bB}{b+\Delta b}+\Delta m_a b\right|=\frac{\lambda}{10} \tag{2.35}$$

We can remove b by using Equation 2.34:

$$\alpha\left|\Delta b m_a^{\ correct}+\Delta m_a\left(\frac{B}{m_a^{\ correct}}-\Delta b\right)\right|=\frac{\lambda}{10} \tag{2.36}$$

Observing that the term inside the above equation is always positive and setting α=FOV/2, $m_a^{correct}=m$ and $B = \sqrt{3}L$ for a Golay-3 array leads to:

$$FOV\left(m\Delta l+\frac{\Delta mL}{m}-\Delta m\Delta l\right)=\frac{\lambda}{5\sqrt{3}} \tag{2.37}$$

From Equation 2.37, we can find the FOV as a function of magnification (m) and pupil mapping tolerances (Δl and Δm):

$$FOV=\frac{\lambda}{5\sqrt{3}\left(m\Delta l+\frac{\Delta mL}{m}-\Delta m\Delta l\right)} \tag{2.38}$$

We can also represent the shear error tolerance Δl as a function of FOV, magnification (m) and magnification tolerance (Δm):

$$\Delta l=\frac{\lambda}{5\sqrt{3}FOV(m-\Delta m)}-\frac{\Delta mL}{m^2-m\Delta m} \tag{2.39}$$

These results are graphically plotted in Figure 2.25. It shows a FOV contour plot as a function of shear and magnification tolerances. In the previous section, 12 μm is suggested for shear error tolerance when we assume there is no magnification error. However, 12 μm shear error cannot produce the FOV requirement of ARGOS (3 arcmin) for any range of magnification error in Figure 2.25. We can tighten the shear error tolerance to

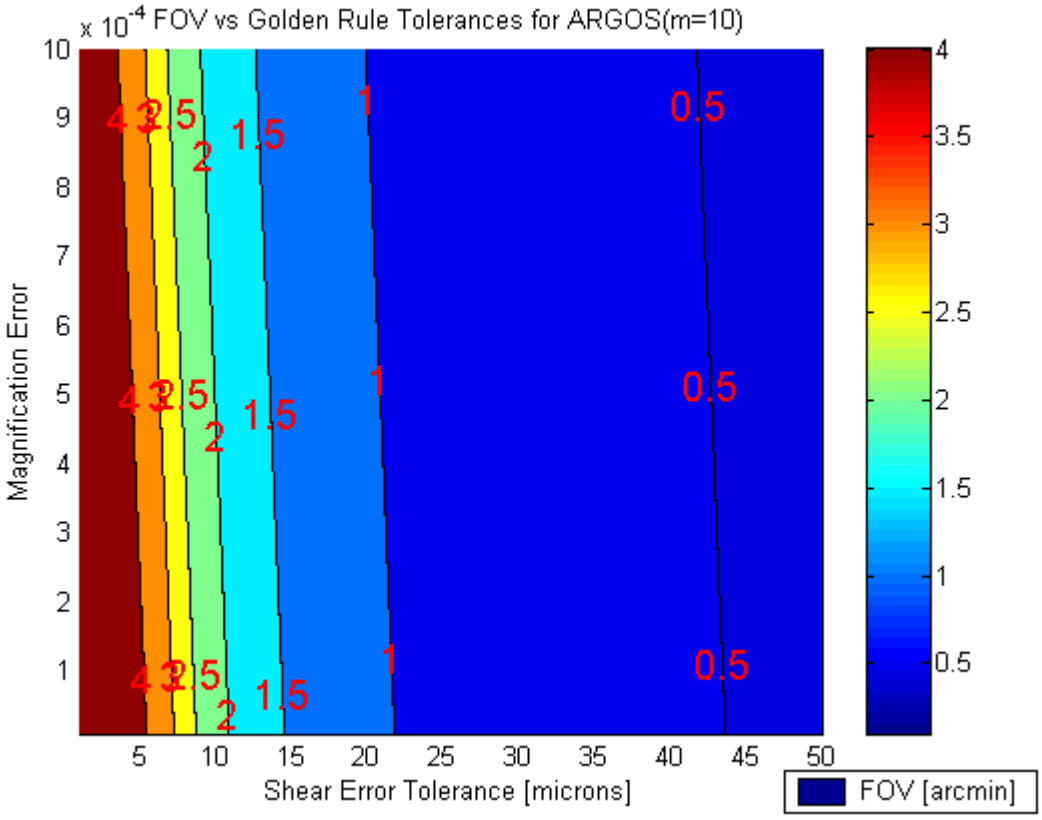

Figure 2.25 FOV vs. Pupil mapping tolerances for ARGOS (m=10) with different FOVs

meet the FOV requirement or we can relax the FOV requirement by shrinking the region of interest in the whole FOV. Therefore, the pupil mapping process is the primary limiting factor deciding the reasonable Field-of-View (FOV) of a sparse aperture interferometric array.

The ARGOS sub-telescope collimators are designed with a tolerance of 0.0095. The size of outgoing beam from a collimator depends on the optical tolerance values of lens design parameters such as surface curvature, thickness and the index number of the glass material. These tolerance values were tailored to satisfy a 0.01mm tolerance of the collimated beam size (10.5 mm radius). 0.0095 is then calculated by (10.51-10.5)/10.5=0.0095. 1/

1000 magnification tolerance requirement is usually considered too expensive to manufacture.

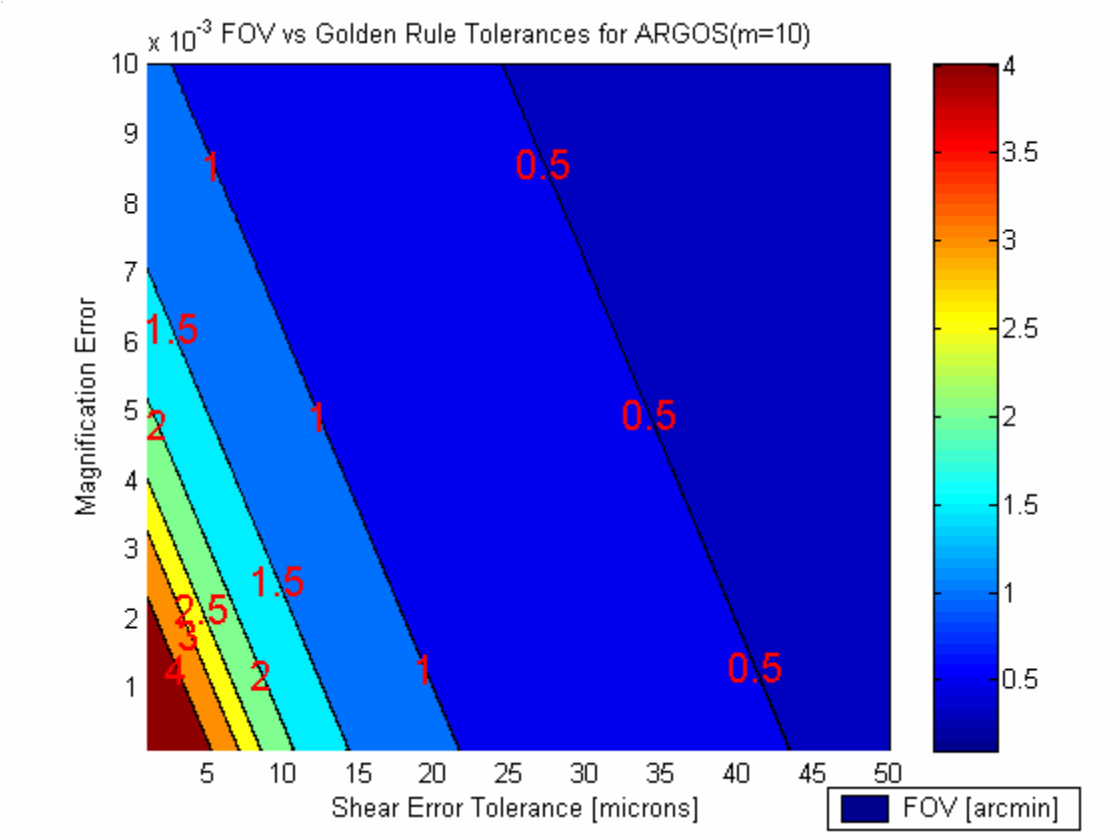

Figure 2.26 FOV vs. Pupil mapping tolerances for ARGOS with achievable magnification tolerance

Figure 2.26 shows another plot of Equation 2.38 with a manufacturable range of magnification errors (0.001-0.01) as compared to Figure 2.25 (magnification error 0.0001-0.001). If we want 12 μm shear tolerance, a manufactured magnification tolerance of the ARGOS sub-telescopes (0.0095) results in a FOV smaller than 1 arcmin. The ability to adjust the focus of a sub-aperture makes it possible to achieve larger FOV imaging. Fortunately, the ARGOS sub-telescopes have a focusing knob which can control the distance between the

primary mirror and the secondary mirror, thereby controlling the size of the beam more precisely.

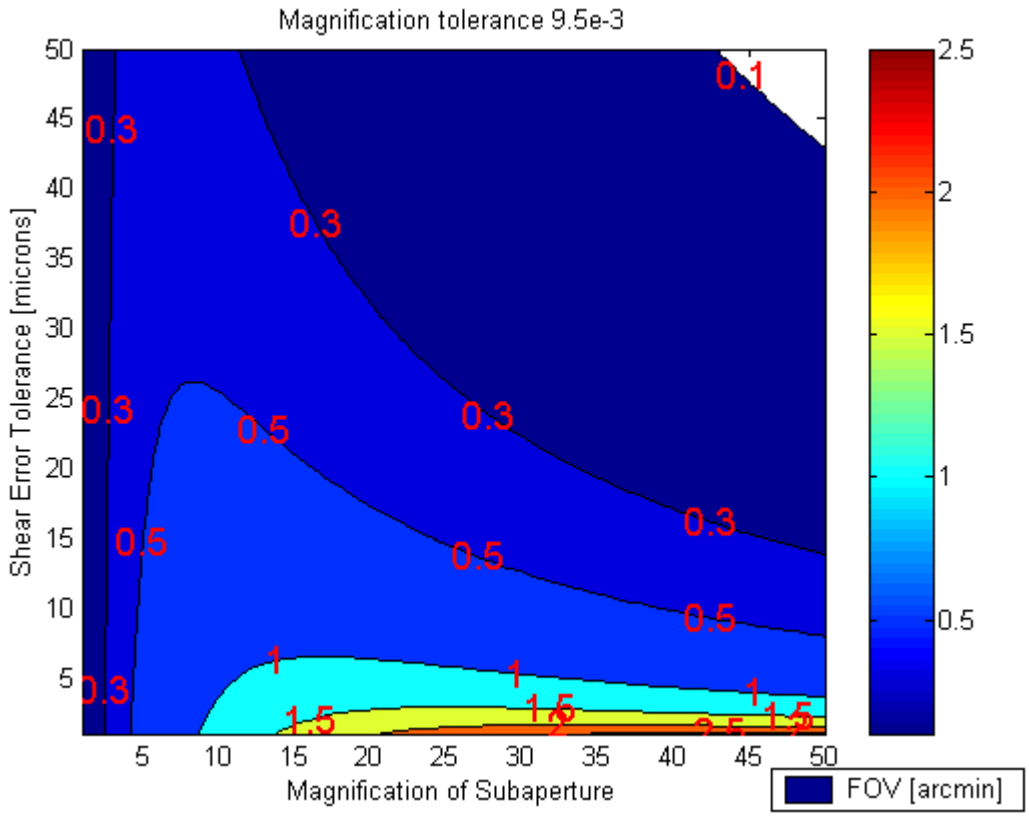

Figure 2.27 Magnification vs. shear tolerance with magnification error =0.0095

Figure 2.27 shows how the magnification of a sub-aperture affects the shearing tolerance value of a sparse aperture imaging system. The magnification tolerance of the ARGOS sub-apertures (0.0095) is chosen because this value is proven to be manufacturable while building the ARGOS testbed. This plot implies that sub-aperture magnification can be tuned to maximize allowable shear error (lateral pupil mapping error) thereby reducing control complexity. For a magnification of 10, we can increase the shear tolerance value

sufficiently high up to 25 µm at the expense of the reduced FOV. For astronomical observations, this FOV can be large enough to satisfy mission requirements.

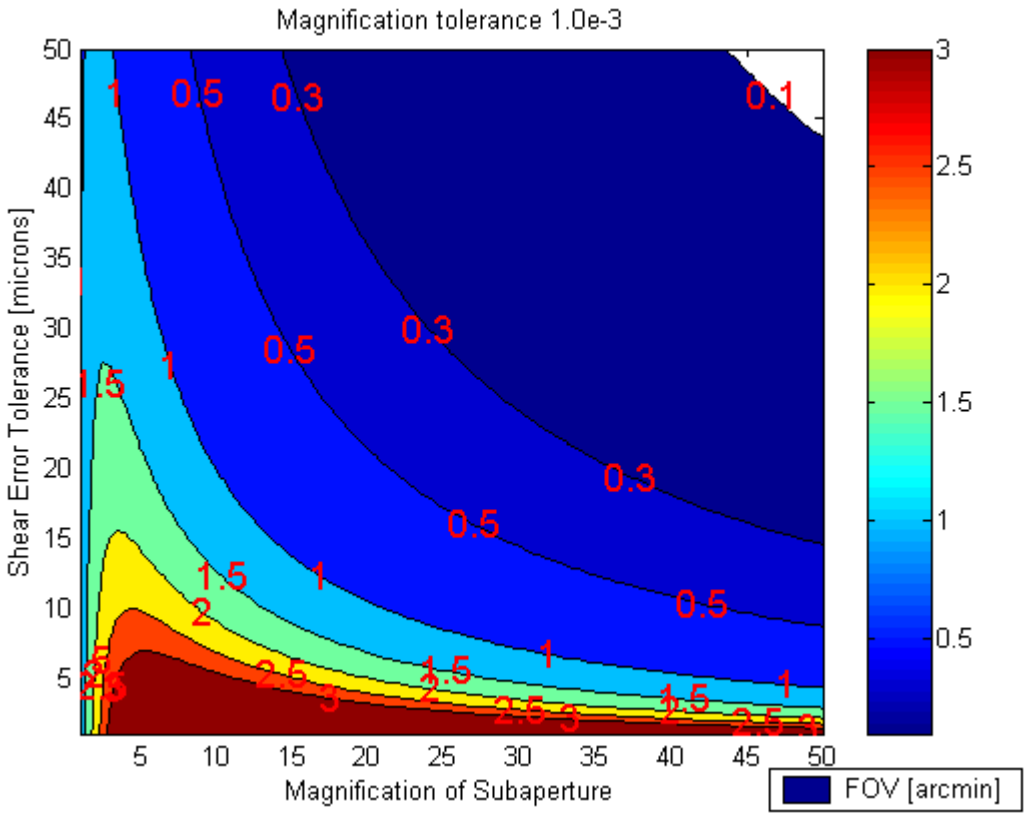

Figure 2.28 Magnification vs. shear tolerance with magnification error =0.001

Figure 2.28 depicts the relationship between magnification and shear tolerance with a more expensive magnification tolerance (0.001) than Figure 2.27. If a sub-aperture of the system has the ability to control the size of the beam precisely, like the ARGOS sub-apertures do, a larger FOV is achievable with the same magnification ratio and shear tolerance. This figure indicates that ARGOS can achieve a coherent imaging FOV of more than 1.5 arcmin with 12 µm shear tolerance and a magnification of 10.

2.4.4 Wavefront Error Budget

Once we calculate the allowable beam combining errors, the wavefront error (WFE) budget is constructed as shown in the SOCS framework (See Figure 2.2 on page 34). An error budget is a way of accounting for all the contributors to system performance error. The error budget defines the maximum error which can be introduced during each step of the design, manufacture, assembly and operations. An additional margin should be maintained as a precaution (see Figure 2.29).

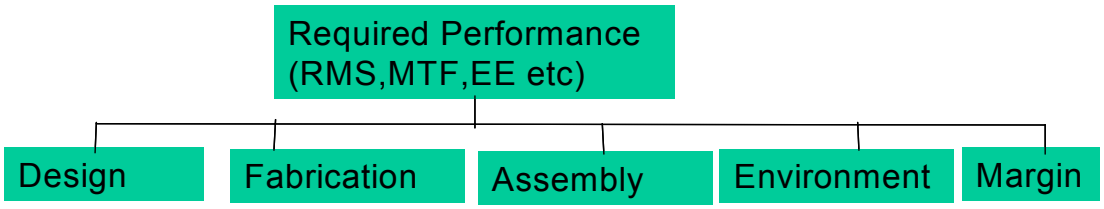

Figure 2.29 Error budget tree for a general optical system

Sources of fabrication errors include incorrect radius of curvature, incorrect element thickness, incorrect surface shape, and curvature center offset from the mechanical center. The optical materials are also a source of error (e.g. incorrect index of refraction). Sources of error in assembly include optical elements offset from the mechanical axis, elements improperly tilted relative to the optical axis, and elements having the wrong orientation. Another source of error is the result of environmental factors, including temperature, humidity and pressure, present at both time of assembly and in field operation. This sort of error includes thermal expansion/contraction of materials, thermally induced changes in the refractive indices, alignment sensitivites introduced by system shock and vibration, and mechanical stresses. In addition, optical system designs have residual design errors.

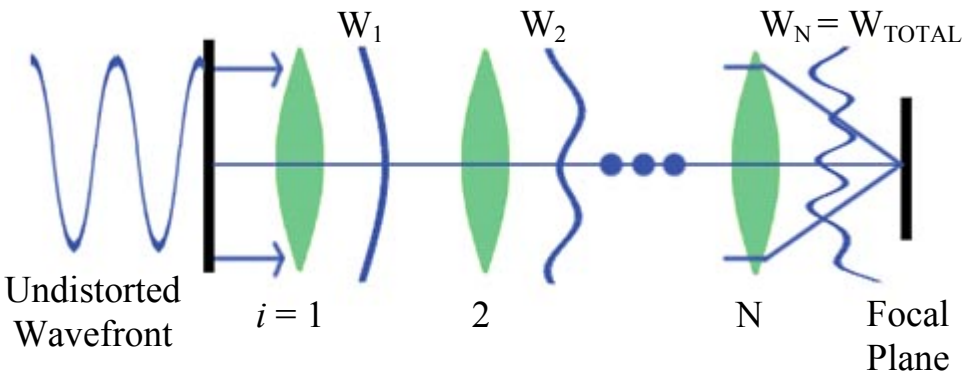

Figure 2.30 Wavefront error propagation

The RMS (Root-Mean-Square) wavefront error in the entire optical train will depend on the types and numbers of mirrors and lenses used. Wavefront error cannot be controlled; it is a result from distortions produced when light bounces off a mirror or travels through a lens. Figure 2.30 shows how these distortions increase as the wavefront travels through the optical train. Wi is the resulting wavefront after each lens or mirror

The total RMS wavefront error of the optical train can be determined from the individual wavefront errors for each optical component. The individual RMS wavefront errors can be added using a Root-Sum-Square (RSS) because the errors are independent of each other (See Equation 2.40).

$$\sigma_{W_{TOTAL}} = \sqrt{\sum_{i=1}^{N} \sigma_{W_i}^2} \tag{2.40}$$

Figure 2.31 shows the WFE budget tree developed in the early design stage for ARGOS. The Strehl Ratio requirement of 0.8 (diffraction-limited) equals 0.075λ RMS WFE. The

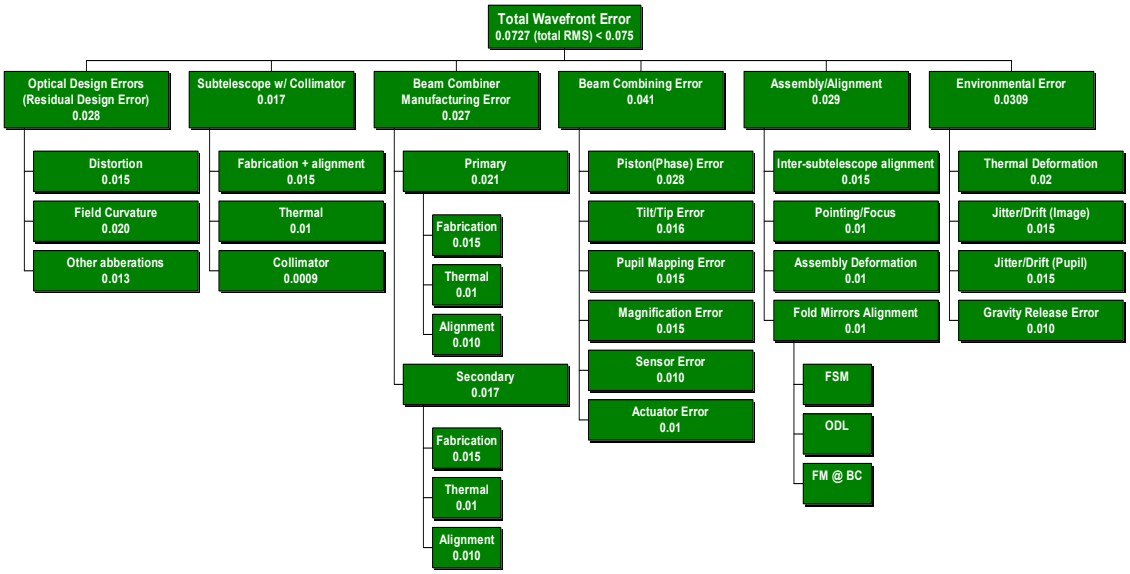

Figure 2.31 The ARGOS WFE budget tree for 0.8 Strehl Ratio (0.075λ RMS WFE)

RSS sum of independently contributing RMS wavefront errors should be less than 0.075λ to obtain a diffraction-limited image. After designing and fabricating each optical component, such as sub-aperture and beam combiner, the RMS wavefront errors are predicted based on the residual design errors by an optical design software, and by actual fabrication tolerances. Allowable beam combining errors are also allocated into the WFE budget. For example, λ/10 phasing errors can be converted to 0.028λ RMS wavefront errors (See Equation 2.14: RMS OPD=P-V OPD/3.5). The remaining RMS wavefront errors can be allocated to account for structural misalignments and environmental errors.

2.5 Chapter Summary

The Sparse-Aperture Optics/Control System (SOCS) design/implementation framework was introduced to facilitate identification and flow-down procedures of design parameters thereby achieving an optimum cost-effective design.

The SOCS framwork begins with an analysis on the optical performance requirements such as Strehl Ratio, Angular Resolution, and Point Spread Function. The Strehl Ratio requirement defines the overal optical performance of the system in terms of the RMS wavefront errors propagating throughout the system. The Strehl Ratio forms a basis on the construction of a wavefront error budget tree.

For imaging extended objects with an instant continuous u-v coverage, the Modulation Transfer Function (MTF) of an image is a better image evaluation criterion than the Point Spread Function. The inevitable contrast loss in the mid spatial frequency region on the MTF plot should be minimized, and the practical cut-off frequency of the MTF defines the angular resolution of a sparse aperture imaging system. Step 2 of the SOCS framework is to determine a proper array configuration that meets the optical performance requirements, especially the angular resolution requirement.

There are three primary beam combining errors that need to be controlled within certain tolerance values for a sparse interferometric array in order to achive phased coherent beam combining. The beam combining errors are the piston errors, the tip/tilt errors and the pupil mapping errors. As the piston errors between the individual beams increase, two major deviations develop over the PSF envelope. First, the PSF mainlobe shifts in the direction of the piston error. Secondly, the peak intensity becomes reduced compared to the normal PSF without any piston errors (The Strehl Ratio decreases). The piston error tolerance is set to 0.1λ or 55nm to have the minimum deviations. The tip/tilt errors between the apertures result in the piston difference as well. A tip/tilt tolerance of 0.35 μrad is chosen to achieve coherent beam combining. If coherent imaging is to be achieved over any significant FOV, the pupil mapping process must be performed such that the exit pupil is an exact scaled replica of the entrance pupil. Previously, 12μm was suggested for the shear error tolerance using an assumption of no magnification error. However, 12μm shear error cannot produce the FOV requirement of ARGOS (3 arcmin) for any range of magnification error as predicted in the previous plots. We can tighten shear error tolerance to meet the FOV requirement or we can relax the FOV requirement by shrinking the

region of interest in the whole FOV. Therefore, the pupil mapping process is the primary limiting factor deciding the reasonable FOV of a sparse aperture interferometric array.

Once the allowable beam combining errors (Step 3 of the SOCS framework) are calculated, the wavefront error budget tree is constructed to correctly predict the performance of the final system. It is also used to keep track of the wavefront errors in design and manufacture of each optical component satisfying the optical performance requirements.

Chapter 3

DESCRIPTION OF ARGOS TESTBED

This chapter focuses on the overall anatomy of the MIT Adaptive Reconnaissance Golay-3 Optical Satellite (ARGOS). Most of this chapter is excerpted from the ARGOS design documents [16.684 CDIO; 16.685 CDIO; 16.686 CDIO]. Even though this thesis emphasizes the optics and control of a sparse aperture imaging satellite, an understanding of a whole sparse aperture spacecraft system is essential in order to grasp the importance of the system engineering philosophy presented throughout this thesis. The conventional subsystems of a spacecraft, such as attitude control system (ACS), structure, avionics, power, as well as other miscellaneous subsystems are presented in this chapter while the design of a optical payload of a spacecraft, sparse aperture array is described in detail in Chapter 4.

3.1 ARGOS Overview

3.1.1 Project Objective

The objective of the Adaptive Reconnaissance Golay-3 Optical Satellite (ARGOS) project is to ***demonstrate the practicality of a modular architecture for space-based optical systems***. In order to understand what is expected from ARGOS, we have broken down our objective into its key components.

First, the word ***demonstrate*** implies that ARGOS will operate in a mode representative of a real-world application. The telescope must be able to capture an image of a real target,

such as the International Space Station (ISS) or a celestial body. Furthermore, the satellite must be capable of remote operation; it should receive commands from a ground station that is not physically connected to the satellite.

Practicality implies that our design competes with the quality to cost ratio of current technology. ARGOS's angular resolution as a function of cost must be comparable to current systems. The design must also have an ease of manufacturability comparable to current systems.

Modular refers to both the satellite architecture and the optics. Modular architecture implies assembling the system out of modules (identical, similar or dissimilar) that facilitate fabrication, integration, and testing. The design should maximize simplicity of interfaces and strive for standardization of components. To achieve this standardization and to hold down manufacturing costs, ARGOS will maximize usage of commercial off-the-shelf (COTS) items. Modular optics generate image data from similar sub-apertures as opposed to a single monolithic system. Active optics control must then be able to coherently combine the light from the separate apertures.

Space-based implies that the ARGOS system must exhibit the functionality of a satellite. It must be able to track a slewing object. Moreover, the satellite must be self-contained, which entails power restrictions, communications, contamination protection, and time critical data transfer.

The motivation for the ARGOS project is the problem currently facing astronomers as discussed in Chapter 1. At this time, large monolithic telescopes such as the Hubble Space Telescope are used to capture detailed images of remote areas of space. Due to size limitations imposed by the capacity of current launch vehicles and the high cost associated with building such large-scale telescopes, advancement in this technology is no longer practical.

One proposed alternative is a design combining several smaller telescopes into a modular satellite that will provide superior quality to current systems. This modular architecture would not only address cost and size limitations, but would also provide easy accessibility to components for replacement or future upgrades. The ARGOS project focuses on demonstrating that a telescope using a modular architecture is a practical solution.

3.1.2 Overview of Mission Requirements

In order to address the concerns of cost and size limitations, the National Reconnaissance Office (NRO) invited design proposals that meet the following requirements:

- Reduce the time required to formalize and validate system designs without shrinking the trade space.
- Reduce the cost and schedule associated with the fabrication, integration, and testing of complex space systems.
- Reduce the cost of low-volume runs by using new design and manufacturing methods.
- Develop methods to better identify, assess, and manage the risks of developing and operating technically advanced space systems.
- Develop an optical control system that can also be used to access the real-time data and code for self-diagnosis, fault detection, software reconfiguration and use of adaptive algorithms.

To fulfill the mission statement, the systems engineering requirements have been derived and divided into functional and operational requirements that the ARGOS project must satisfy.

Functional Requirements:

- The angular resolution of the system must be 0.35 arc-seconds or better.
- The telescope must be able to detect light in the range of 400-700 nm (visible light).
- The field of view (FOV) of the system should be approximately 3-10 arc-minutes.
- The telescope must have a practical visual power range of 72X-400X.

- The telescope must be able to detect images brighter than +15 stellar magnitude.
- The system must have a signal to noise ratio of 100.
- The system must automatically provide health status (telemetry) and operations data.
- The system must have a pointing accuracy of +/- 1 arc-min.
- The system must be able to acquire a target within 2 minutes.
- The system must be able to relay information at a rate of 300 Kilobytes/sec.
- The system must be able to operate in both manual and autonomous control modes.

Operational Requirements:

- The system must have a field of regard equal to 60 degrees (full cone).
- The ground station must receive the image captured by the telescope in less than 10 minutes.
- The telescope must be able to capture images at a maximum imaging rate of 20 images/hour.
- The system must be able to be operated remotely by a wireless console from a distance of 20 meters.
- The satellite must be able to operate autonomously for up to 1 continuous hour.

Above all, the mission statement is upheld, which states the ARGOS project must "demonstrate the practicality of a modular architecture for space-based optical systems." A more in-depth, complete discussion of the requirements, as set forth by the customer and analyzed by the ARGOS team, can be found in Appendix A, "Requirements Document."

3.1.3 Final Design

Figure 3.1 highlights the final design of ARGOS. To demonstrate a complete spacecraft in a 1-g environment, the ARGOS system is mounted on a frictionless air-bearing, and has the ability to track fast orbiting satellites like the International Space Station (ISS) as well as point stars. Modular architecture design emphasizes the use of replicated components and quick connections. The system consists of three identical apertures arranged in a

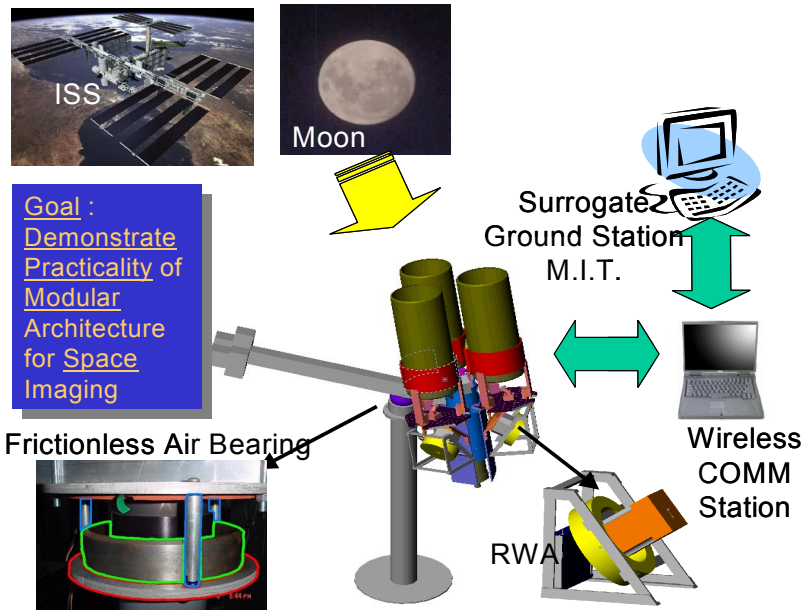

Figure 3.1 Functional and operational objectives of ARGOS

Golay-3 distribution. The light from these telescopes is combined in a center module and transmitted to a Charge-Coupled Device (CCD). Wavefront sensing techniques are explored to mitigate initial misalignment and to feed back real-time aberrations into the optical control loop. The end result is an image as good as the image received from a monolithic telescope using a single aperture. ARGOS operates autonomously and in a self-contained manner while a wireless ground station downloads images and telemetry information.

The ARGOS testbed can be best described in term of six subsystem groups: Passive Optics, Active Optics, Attitude Control System (ACS), Structure, Power-Avionics-Software (PAS), Science-Operations-Communications (SOC).

Passive Optics. Development of the sub-aperture telescope, relay optics, CCD system, and framegrabber avionics designs. Exploration of beam combination methods and designs. Use of a professional optical ray-tracing software.

Active Optics. Design and implementation of optical delay lines (ODLs) and fast steering mirrors (FSMs) for coherent beam combining. Controller and wavefront sensor design and implementation.

Attitude Control System (ACS). Design of three axis slewing and pointing control of the satellite using attitude sensors, rate gyros and reaction wheels. Design and implement momentum desaturation mechanism (propulsion)- active balancing system (ABS) for ARGOS.

Structure. Definition of mechanical interfaces for subsystems, minimization of frame mass, etc. Modeling and measurement of system inertias and model system. Complete CAD and FEM models of system with static, dynamic and thermal loads analysis.

Power, Avionics and Software. Responsible for electrical power system, defining electrical interfaces, optimizing system electrical efficiency, battery hazard control, analog signal conditioning, touch temperature control, analog device drivers, etc. On-board software device drivers, real-time control software operating system, data handling and temporary storage. Development of on-board avionics computer.

Science, Operations and Communications. Creation of the science observation plan that allows the a sparse imaging array to verify that it is meeting requirements. Also, development of the system that allows remote, wireless, and autonomous operation of the satellite from a ground station at MIT.

Passive and Active optics subsystem are discussed in Chapter 4. Other subsystems of the ARGOS testbed are described in the subsequent sections of this chapter.

3.2 Attitude Control System

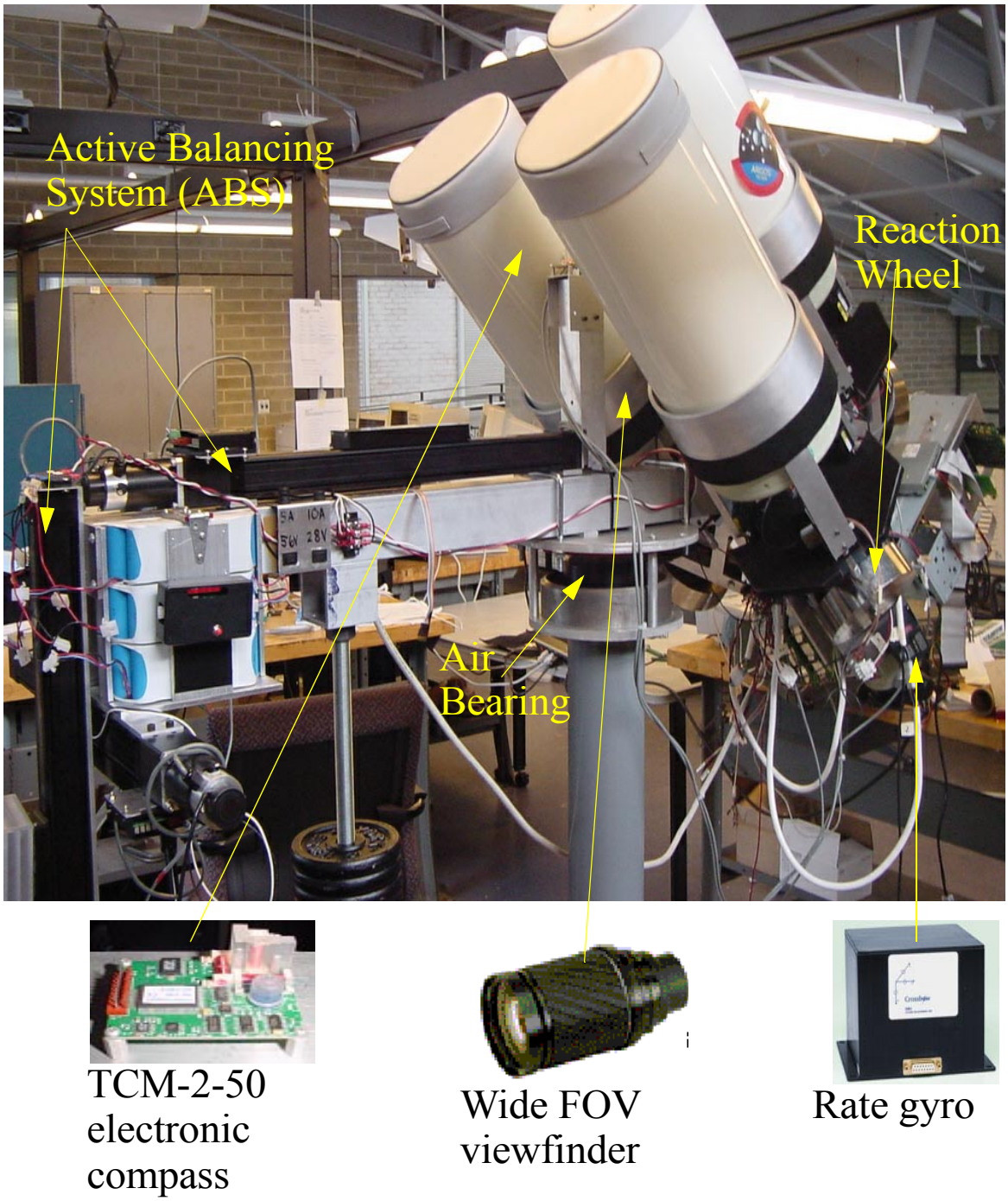

Figure 3.2 The final ARGOS system with the three ACS sensors shown in the bottom

The final ARGOS structure and its major ACS components are shown in Figure 3.2. The Field of View of the CCD is 3 arc-minutes and thus to give us 1/2 arc-minute of margin on either side, the ACS subsystem is required to provide a pointing accuracy of +/- 1 arc-minute. The period of operation of the ARGOS system without human intervention must be 60 minutes or greater, meaning that the ACS system will have to either not saturate its actuators, or have some way of desaturating them within this given time span. The system must be able to slew at a rate of at least 1.5 degrees per second, placing a minimum requirement on the capabilities of the actuators to slew the spacecraft. Due to the nature of the ARGOS system, there will be some offset between center of gravity and the center of rotation, thus the system will need to have sufficient capabilities to overcome this torque (See Section 3.2.2 on page 84).

3.2.1 ACS Sensor Suite

The sensor suite is composed of three integral elements as shown in Figure 3.2. First, the TCM-2-50 electronic compass, with a 3-axis magnetometer, a 2-axis tilt sensor, and facilities to provide temperature information. Two TCM-2's with the ability to provide tilt compensation of 20 degrees and 50 degrees respectively, were both procured so that if one fails, another option exists. Another advantage of procuring two TCM-2's is the opportunity to test the advantages and possible disadvantages of the different levels of tilt compensation.

Inclinometers/Electronic compasses measure the relative angles between the inertial coordinate frame and the body fixed frame. That is, they are used to give relative elevation, roll, and azimuth information between these two coordinate systems. The Inclinometer/ Electronic compass is an essential component of the coarse pointing sensor suite. The TCM-2 was selected as it provided the best sensor functions available and along with the viewfinder will be able to satisfy the requirements levied on the attitude control subsystem.

While working with this sensor in the laboratory it was noticed that local magnetic disturbances were present, thus a method had to be found to mitigate these magnetic disturbances before work could be carried out on this sensor. The electronic compass has internal calibration algorithms for what is known as "hard-iron." This includes permanent local fields like those created by magnets. Unfortunately, things like ferromagnetic metals, such as steel (which the main rod in the ACS testbed is made of) distort the Earth's magnetic field and are considered "soft-iron" disturbances. The algorithms for correcting for soft-iron are too complex to fit on the compass' EPROM, but can be run from a host PC. Since this was not a feasible option, the most intuitive solution was to move the magnetometer away from disturbances and to clean up the local field by making an aluminum pedestal. By placing it on a raised aluminum pedestal away from the ferromagnetic pedestal, the magnetic disturbances were sufficiently attenuated as the read out from the electronic compass was reasonably linear with the true heading in this position. In the future, more sophisticated work will be carried out on the electronic compass to further mitigate the magnetic disturbances.

Second, there is an intermediary sensor, which takes the form of a scope. It is a CCD that provides sufficient overlap with the ACS (Figure 3.3).

Thirdly, there is a 3-axis rate gyroscope. It provides the specifications delineated in the metrics table. Figure 3.2 shows a picture of the Bendix 3-axis rate gyroscope, which was chosen for implementation into the ACS coarse sensor suite. The Bendix rate gyro provides the best resolution available and a satisfactory range for ARGOS's applications. The only disadvantage to choosing the Bendix gyroscope is that it is a mechanical gyro and induces more vibrations on the system than its competitors. However, given the advantages, it was the best option for use in the ACS coarse pointing suite.

During signal to noise testing of the sensors, the rate gyro displayed significant noise disturbances beyond the frequency at which data was being captured; the rate gyro also displayed aliasing effects. In order to filter out these disturbances, a variety of variable

frequency filters were used that collectively failed to filter out the disturbances in all three rate gyroscope directions. Thus a filter was built for testing purposes, which was able to filter out the noise and aliasing to a certain degree. In the final system, rate gyro filters will be added to an ACS protoboard and added to the system.

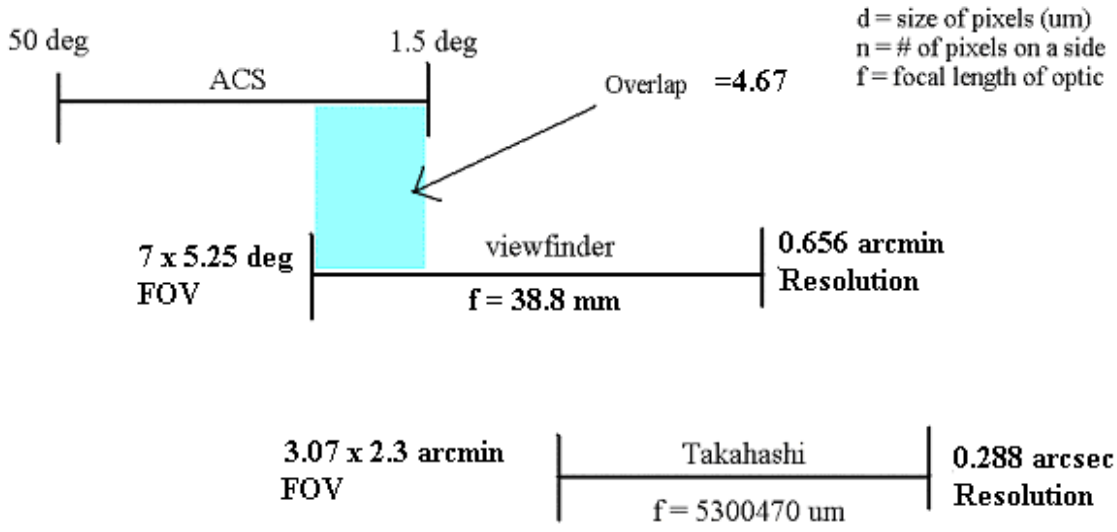

Figure 3.3 Multi-staged ACS Sensors

3.2.2 Active Balancing System

Due to the nature of the air bearing system chosen to simulate the space-based operation of ARGOS, the center of gravity and the center of rotation of the body will not necessarily be at the same position. The offset between their positions will impart a gravitational torque on the spacecraft, which will need to be overcome by the reaction wheels, both increasing their torque requirements as well as significantly increasing the angular momentum storage required by the reaction wheels, as this torque will be integrated over the period of operation of ARGOS.

The torque causes the wheels to increase in speed according to the equation (3.1).

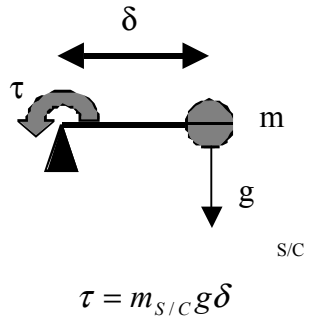

Figure 3.4 Schematic of Center of Rotation, Center of Gravity Offset, and Gravitational Torque

$$\Delta\dot{\theta}_{wheel} = \frac{m_{s/c}\, g\, T_{desat}}{I_{wheel}} \delta \tag{3.1}$$

$\Delta\dot{\theta}$,the change in wheel speed before desaturation is required, is set by a combination of the limitations on the reaction wheel motor and the degree to which the wheels are balanced and T_{desat} is the time between desaturations and is set as a requirement for the overall ARGOS system. In designing the reaction wheels, it was intended to have the primary drivers be similar to those encountered in a space environment, and as such I_{wheel} should not be made much larger than would otherwise be required to control the dynamics of the spacecraft without having to overcome gravitational torques greatly exceeding those encountered in a space environment. In order to meet these constraints, the offset between the center of gravity and the center of rotation (δ) must be kept to on the order of 1 μm.

To accomplish this, firstly the spacecraft will be carefully statically balanced prior to operation in order to bring the center of rotation and center of gravity to the smallest offset possible. This will be accomplished both through designing the spacecraft's center of gravity to be at the center of rotation, as well as the addition of small ballast masses to reduce any offset that develops between the center of gravity of the spacecraft and center of rota-

tion provided by the air bearing. It is believed that through these static methods offsets on the order of 1 μm can be achieved.

In order to keep the center of gravity within this margin throughout the operating range of ARGOS, which could include small shifts in the structure due to gravitational deformation, etc., a 3-axis active balancing system has been devised that will be able to shift the center of gravity to be within the micron tolerances required. It can also be shifted in the opposite direction from any momentum build-up in the wheels to provide ongoing desaturation on all axis except the vertical, where no gravity torques are present to build-up momentum in the first place.

To accomplish this, a weight is moved back and forth along a single axis in order to provide gravitational offsets as presented in Figure 3.5. Although the effective precision of the overall active balancing needs to be quite tight, the individual elements of the assembly (i.e. the resolution of the sliding part) do not need to be, as the ratio of the mass being moved to the mass of the spacecraft scales the resolution of the moving mass to the change in the center of gravity of the spacecraft, placing a requirement that r = bM/m.

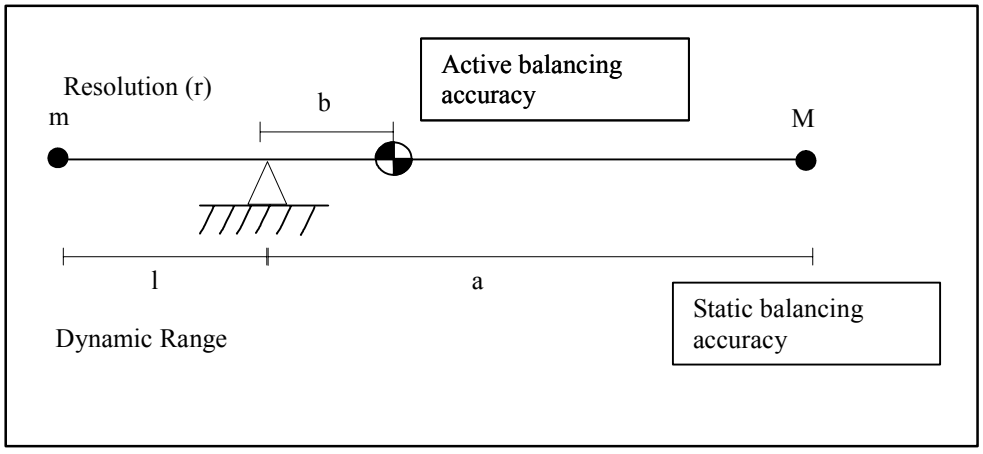

Figure 3.5 : Active Balancing System Schematic

The selected active balancing system design is to use three linear motion slides based upon the custom developed lead screw and fixed servo system. The slides will be positioned on the end of the swing arm away from the telescope, as these do not represent a system that would be included on an actual satellite, and thus can be used to balance the center of gravity initially. Each of the slides will be mounted perpendicular to the other two, such that there are three independent axes of control of the position of the center of gravity.

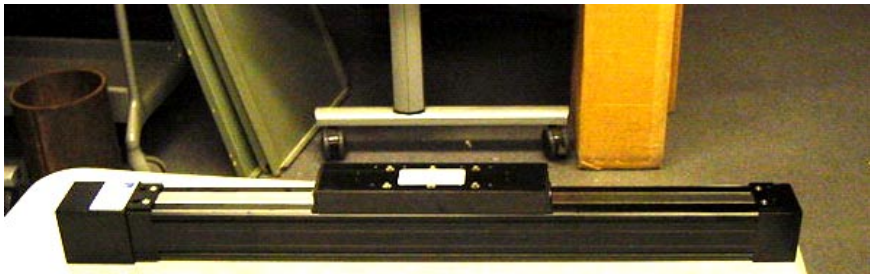

Figure 3.6 Single-axis linear motion slide

Each of these linear motion slides (see Figure 3.6) is composed of a servo connected to a lead screw, which cause a mass to traverse along a track, thus offsetting the center of gravity (CG) of the overall system. When combined with a control system monitoring moment build-up on the reaction wheels, the center of gravity can thus be held to within close tolerances of the center of rotation (CR), and prevent the premature saturation of the reaction wheels.

The length of the lead screw travel (l), the linear precision of the servo-lead screw combination (r), and the mass traversing the rod (m) are selected based upon the total spacecraft (less active balancing system traverse) mass (M), static balancing CG-CR offset (a), and target active balancing CG-CR tolerance (b), as presented in Figure 3.5.

The following design equations are then derived from the resulting geometry:

$$l = \frac{aM}{m} \tag{3.2}$$

$$r = \frac{bM}{m} \tag{3.3}$$

These determine the length of lead screw and precision of the lead screw-servo motor combination required by the selected design. In order to achieve the above stated constraints, the requirements are as follows:

a = 1mm
b = 0.001mm
M = 230kg

The system of each of the chosen linear slide/servo motor combinations in the design has the following characteristics:

l = 350 mm
r = 0.1 mm
m = 1 kg

3.2.3 Reaction Wheels

The most demanding operation to be performed by the reaction wheels is in accelerating the spacecraft and then controlling it to track a fast moving object, such as the International Space Station (ISS). A simplified depiction of this operation is presented in Figure 3.7, with the spacecraft accelerating, tracking Station, and then decelerating, while leaving margins on either side of the full limits of the air bearing.

This operation leads to the following design equations for the reaction wheel system:

$$\tau = \frac{1}{2}\frac{I_{s/c}\dot{\phi}_{track}^2}{\phi_{accel}} \tag{3.4}$$

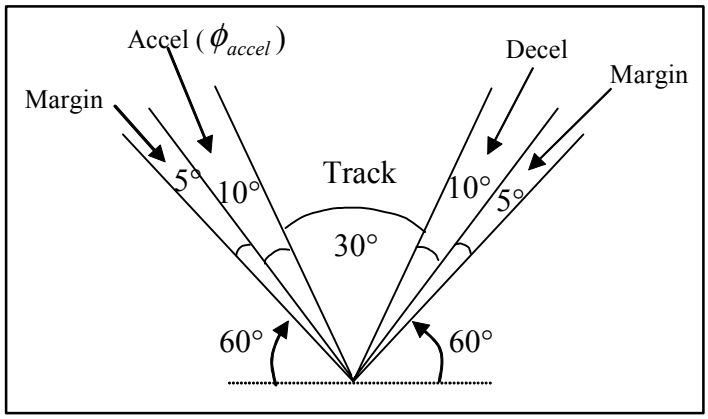

Figure 3.7 ISS Tracking Operation

Torque required to accelerate the spacecraft up to the tracking speed within the angle available. This torque leads directly to the selection of the reaction wheel motor.

$$I_{wheel} = I_{s/c} \quad \frac{\dot{\phi}_{track}}{\Delta\dot{\theta}_{accel}} \tag{3.5}$$

Required wheel moment of inertia given a tracking speed, the moment of inertia of the spacecraft and the desired change in speed of the wheels, based upon conservation of angular momentum. This moment of inertia goes to determine the design of the flywheels themselves.

Taking into account the configuration of ARGOS, these lead to a torque requirement of 0.25 Nm for the motors and a moment of inertia for the wheels of 0.025 kgm^2 to be placed on the design.

After determining that Commercial Off The Shelf (COTS) reaction wheels would be too expensive, and that the spare MACE wheels were inadequate from a momentum perspective, it was decided to investigate developing our own set of reaction wheels for the Attitude Control System. The system is composed of three reaction wheel modules, each with a 7" steel flywheel, an MCG IB34004 motor with built in encoder, and a power amplifier

with a velocity control loop. Each reaction wheel module is placed in a separate sub-aperture, facing outwards such that they are perpendicular to each other. Each module is capable of providing a continuous torque of up to 0.5 Nm and is capable of operating in a speed range from 0 to 3000 RPM.

The wheel is designed such that it will wrap around the motor, thus minimizing the overall length of the reaction wheel system. The height of the wheel is 2", the outside diameter is 7", the inside diameter is 5", and there is 1/4" flange on the top of the wheel to provide rigidity. The wheel is mounted to the motor with the use of a Transtorque coupling.

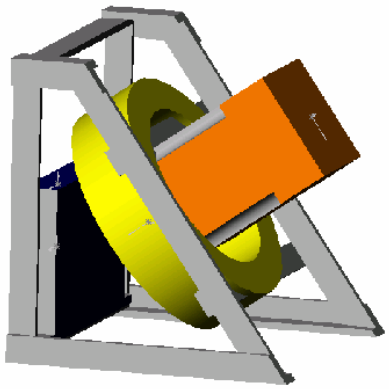

Figure 3.8 Reaction wheel mounting method

3.2.4 General Control System Design

Figure 3.9 gives a summary of the theoretical control design of the ACS subsystem. Through the above control method the attitude of the satellite can be deciphered and controlled. Initially the ARGOS satellite is at some arbitrary position, then the Science Operations and Communications subsystem provides reference information as to the position and behavior of the satellite by providing the ACS subsystem with the International Space Station's azimuth, elevation, range, azimuth rate and elevation rate. The ACS subsystem then converts this information into the body frame of ARGOS and then converts the input

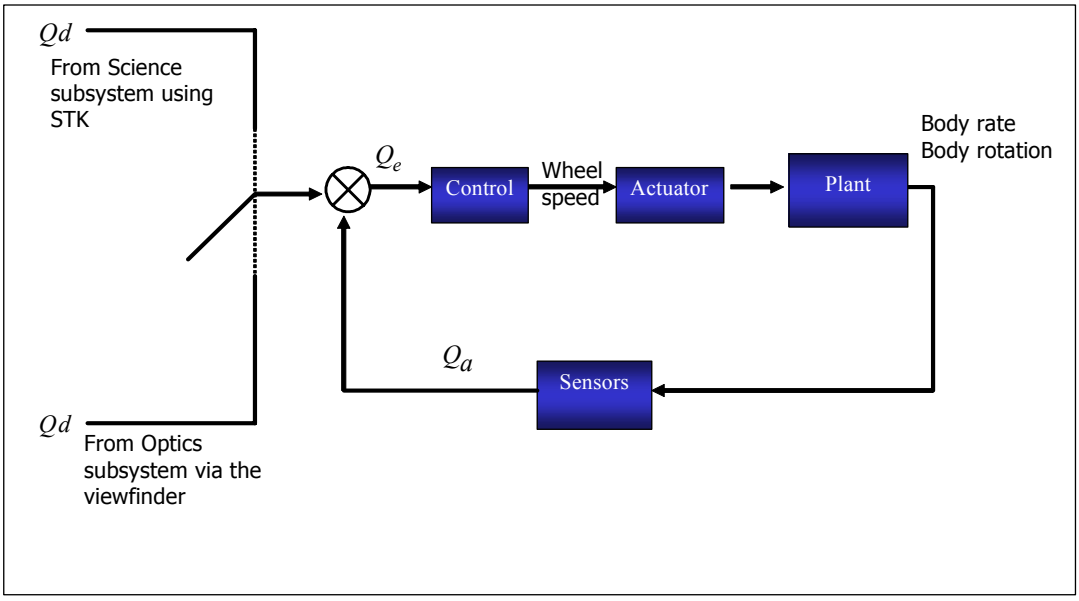

Figure 3.9 General Control System Design

information into quaternion form. At the same time, two of the sensors being used, the rate gyroscope and electronic compass, are providing information as to the actual attitude of the satellite, this information is similarly run through a function that transforms it into the body frame if necessary and then converts it to quaternion form. When the target is within the field of view of the viewfinder, the viewfinder takes over from the Science subsystem providing the ACS subsystem with the desired attitude of ARGOS. With this information the error in ARGOS's actual attitude can be computed and based on the desired and actual attitude information, how much the ARGOS system would need to rotate from its current body frame to the desired body frame would be known. The error quaternion is passed through an attitude controller, which exhibits proportional, integral and derivative control; it is based on a non-linear control design. The output from the attitude controller is wheel speed and this is fed through an actuator system that outputs torque. This torque is then fed through the Attitude Control plant (the physical system) after which the body rate and body rotation of ARGOS would be known. This information is then fed into the system's sensors.

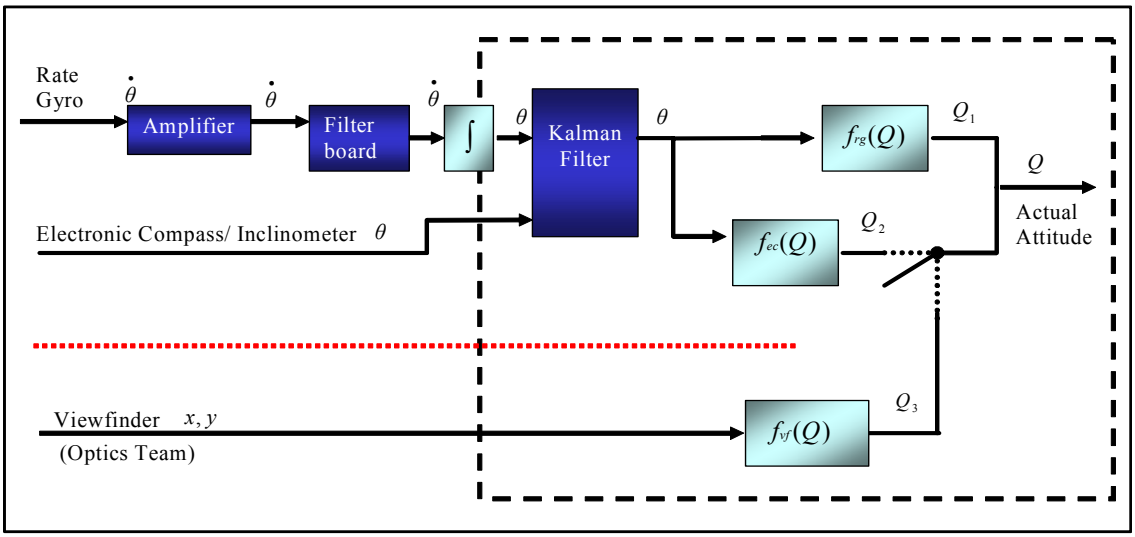

Figure 3.10 Sensor Input Diagram

All the input information into our system is being converted into quaternions, as under these conditions of large angle rotations, quaternions give you the most optimal solutions and are actually being used quite widely in the aerospace field today for large angle applications. Also, other popular methods of attitude definition such as Euler Angles have singularity problems at specific angles, the use of quaternions erases this singularity problem.

Figure 3.10 details how the sensor information is incorporated into the attitude control design. It may be divided into an analogue and a digital section (captured within the white dashed box). It may also be divided into two modes, which are separated in the diagram shown above by the red dotted line. In the first mode, the two main sensors, the rate gyroscope and the electronic compass, communicate angle and rate information to the system. The input from the rate gyroscope is first passed through an amplifier to amplify the signal. This amplified signal is then fed through the ACS filter board to remove any excessive noise and aliasing effects. This signal is then fed through an integrator, which both provides the rotation angle and acts as a stabilizing filter. The electronic compass inputs attitude angle θ, which are fed into a Kalman Filter along with the integrated rate gyro signal.

The Kalman filter is used to provide the best representation of the actual system attitude by combining the input from the different sensors in the most optimal way, because for example, the inclinometer input is best at low frequencies while rate gyro input is best at high frequencies, thus a mixing filter such as the Kalman filter becomes necessary to output the best combination of the two inputs. The Kalman filter outputs a combined integrated signal, which is then manipulated such that the filtered and integrated rate signal can be fed through a function, $f_{rg}(Q)$ that converts it into quaternion form (the rate gyro's information is already in the body frame of our satellite and is therefore simply converted to quaternion form) giving Q1. The filtered electronic compass input is transformed into ARGOS's body frame and converted into quaternion form through the function $f_{ec}(Q)$, this function provides an attitude description in the form Q2. Once the ISS is within the ACS's field of view, a trade off is made from the electronic compass to the viewfinder. This moves the system into the second mode. A switch is used to perform the trade-off in going from mode 1 to mode 2. The optics subsystem relays through the viewfinder the position of the ISS in (x,y) Cartesian coordinates. This viewfinder input is again transformed into ARGOS's body frame and converted into quaternion form through the function $f_{vf}(Q)$, providing Q3. Thus in the second mode you only have rate gyro and viewfinder input.

Figure 3.11 depicts the motor actuator controller. The actual ARGOS attitude from Figure 3.10 is fed through the attitude controller and a notch filter. The purpose of the notch filter is to filter out specific bending modes that were corrupting the obtained signal. After the actual attitude is fed through the attitude controller and notch filter, the desired wheel speed is outputted. The wheel speed is inputted into the actuator system as a voltage. The wheel speed error is fed into a Proportional, Integral and Derivative controller, which is then fed into a power amplifier. The motor exerts a torque on the ARGOS system and the flywheel. The angular position of the wheel is outputted by an encoder attached to the motor, the signal of which is then differentiated and fed-back to determine the wheel speed error.

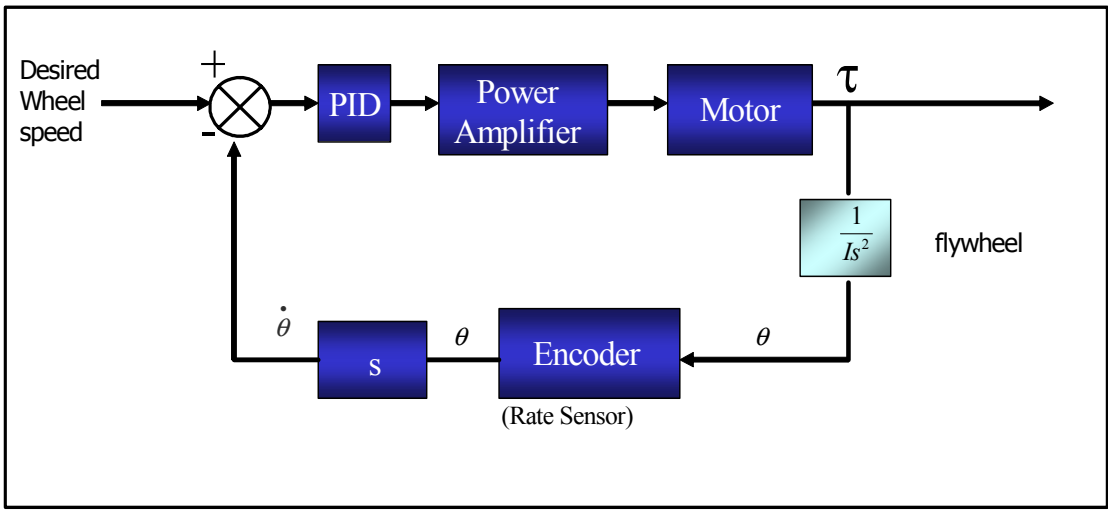

Figure 3.11 Motor Controller Design

The control system for the Active Balancing System will measure the total angular momentum of the ARGOS system through the rate gyro and wheel speed feedback, and knowledge of the moment of inertia of each. The goal of the ABS is to keep this total angular momentum at zero. While a detailed control system is still under development at this stage, the ABS will be actuated such as to provide torques to bring the angular momentum to zero.

During the preliminary design phase (PDP), tests conducted on the ACS testbed revealed a few high frequency issues related to the reaction wheels and the rate gyro. The rate gyroscope's output was significantly corrupted by high frequency noise disturbances, which were superimposed on the desired rate signal. Also present in the output were aliasing effects. Testing with the Origins reaction wheels on the ACS testbed revealed that high frequency signals damaged the reaction wheels. Thus, an ACS filter board was built for ARGOS to filter out these high frequency signals and provide the corrective gains or the option for corrective gains for the rate gyros, tachometers, and the reaction wheels. The ACS filter board is depicted in detain in the ARGOS design documents[16.686 CDIO].

Attitude Controller Simulation

In order to test the complex attitude controller algorithm, the ACS subsystem built a simulator model on our computer that would verify that the attitude control system is working as expected. The science operations and communications subsystem provides reference information about the ISS behavior from the Satellite Tool Kit (STK) database. For the simulator model, the input is as follows, information for a sample ISS pass was taken and input into the model. Also, the sensor input is modeled as rate gyro input, and a torque constraint amounting to a saturation of 0.3 Nm is also added. In addition, zero mean white noise of 0.1°/s is added to the rate gyro signal to provide a source of disturbance, thus making the simulation more realistic. Figure 3.12 and Figure 3.13 depict a far away and zoomed in view of the angular separation error between the line of sight of the ARGOS system and the line of sight of the ISS respectively. The angular separation error fits well within the accuracy target of 1.5°, this accuracy target is represented by the yellow dotted circle.

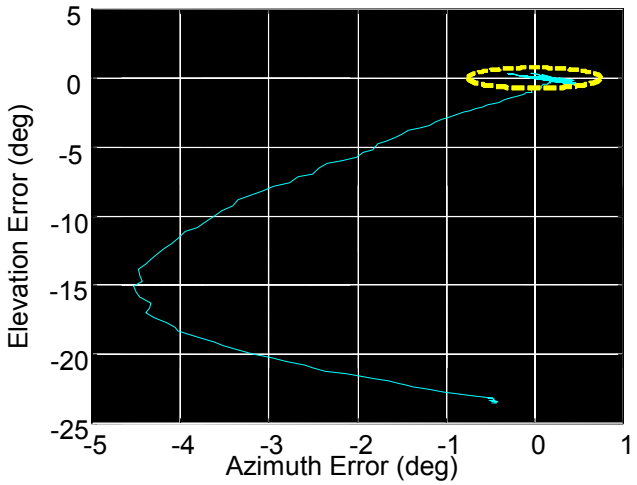

Figure 3.12 Angular separation error between the line of site of ISS and ARGOS

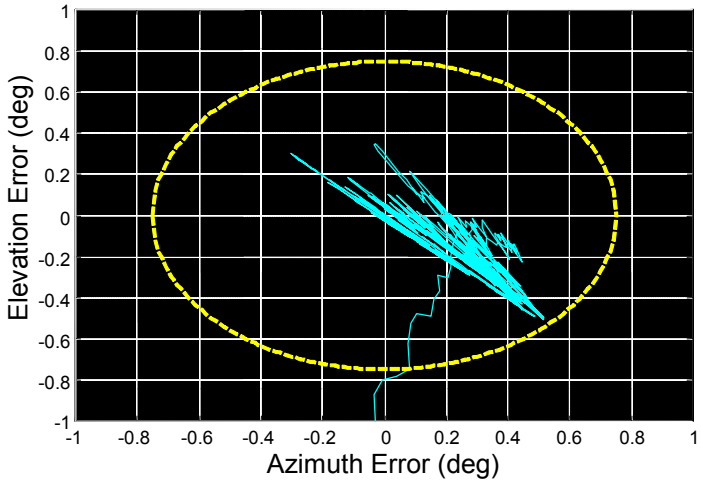

Figure 3.13 Zoomed-out view of angular separation error between the line of site of ISS and ARGOS

3.3 Structure

3.3.1 Aperture Alignment System

The first obstacle that had to be overcome in the development of the aperture modules was the aperture alignment system. This system dictated the design of the rest of the module.

Based on the collar design, there are 3 mounting points for the actuators. One mounting point is located at the base of each leg. The first plan to achieve tip and tilt capability was to use actuators that move each leg straight up and down. The problem with this design is that it does not account for the circular path the telescope will follow as it rotates. If the actuator were to move a straight distance upward, y, there would be a distance, d, between it and the collar leg. There would also be an angular offset equal to the angle that the telescope had rotated. In designing the alignment system, a method for accommodating this translation and rotation had to be devised.

An assumption was made that the aperture collars could be manufactured to provide an alignment tolerance of 1 degree. Based on this maximum of 1 degree offset, the actuators

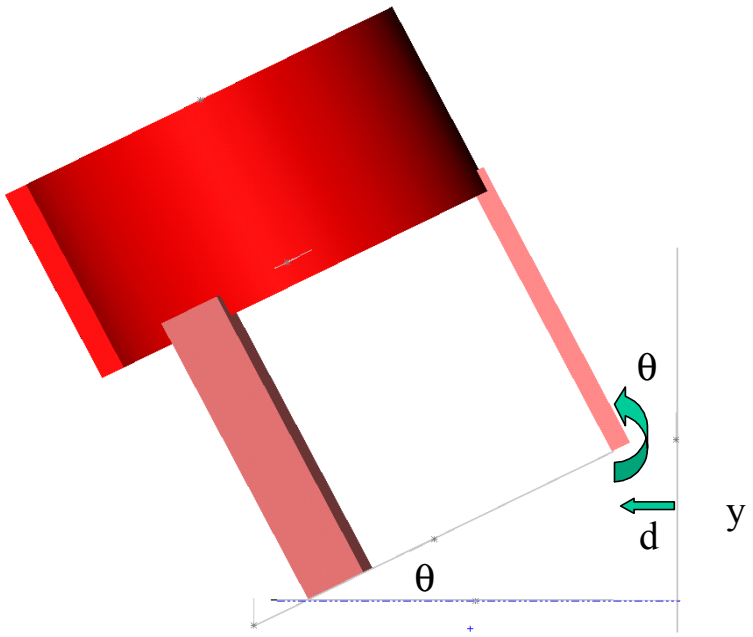

Figure 3.14 Maximum Alignment Requirements: θ =1 deg, d=30 µm, y=3.39 mm
Resolution Requirements: θ=15 arc sec, y=15 µm

will need to have a minimum range of 3.39mm. and will need to accommodate for a 30 micron deflection. The actuators will also need to have a resolution of 15 microns based on the 15 arc sec alignment requirement.

Figure 3.15 shows deflections seen from a 500 N load applied radially inward at the bottom of one of the legs. The deflections are not drawn to scale. The Color coding on the right side of the screen represents the actual deflections seen by the collar. According to the FEM, the 500 N load would cause a 3 micron deflection rather than 30 microns as expected. This told us that our simple cantilevered beam model was too simple and that the stages would have to withstand higher loads for the required deflections. We decided to build the Collar and aperture alignment system to test if the translation stages could withstand these higher loads.

To test the alignment capabilities of the translation stage system, a laser pen was attached to one of the telescope assemblies. The laser was aimed at a target with calibrated lines on

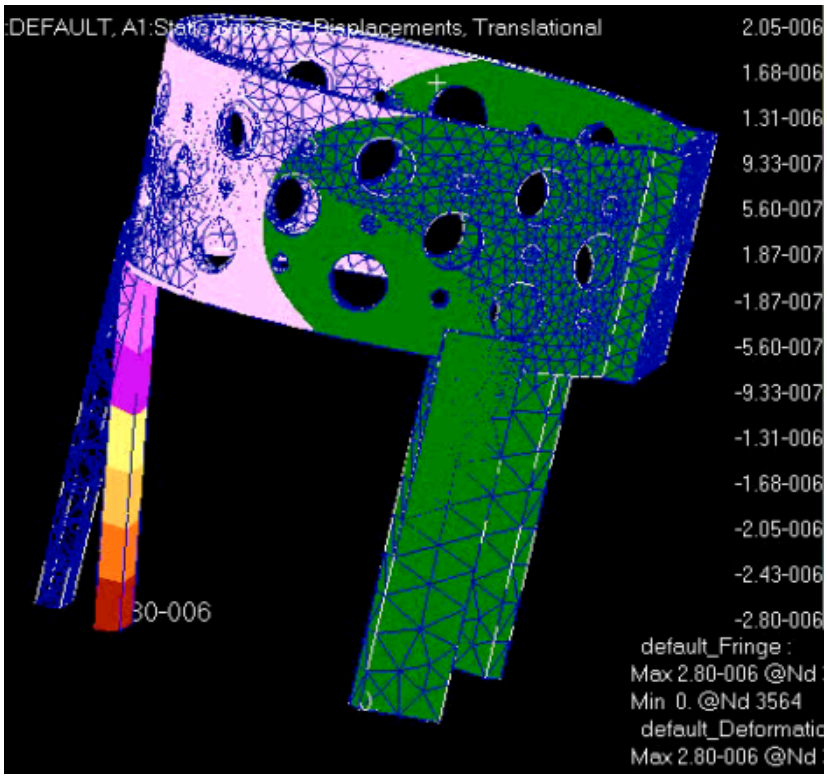

Figure 3.15 FEM Analysis of aperture collar

it. The translation stages were adjusted to their limits and the distance traveled by the laser point was measured. The distance from the center of rotation of the telescope to the target was also measured. Using these two values, the alignment capabilities of the translation stage system was calculated to be 3 degrees.

The translation stage aperture alignment system meets all of the requirements. Each stage has a resolution of 10mm, which beats the 15-mm requirement. The system also allows for a maximum alignment of 3 degrees, which beats the 1-degree requirement. Additional springs were added to the translation stages to prevent the apertures from tipping during operations.

3.3.2 Other Structure Requirements

Modularity

A major requirement of this project is modularity. Modularity has been defined to include three main things. The first is the use of replicated components that simplify the design and manufacturing process. These replicated components should be able to serve a greater function when connected. Secondly, a modular system should have quick connections. These connections should be simple, easily accessible, and detachable. Finally, the modules should have high-density packing. The satellite should be able to separate into modules that allow for compact packing. This will allow for the most efficient use of space in a launch vehicle or in transport to a testing location.

Segregation of optics from bus subsystems

A requirement was set that the bus subsystems be isolated from the optics. Issues such as vibrational disturbances, heat contamination, and electromagnetic interference raised concerns for the optics team. Therefore, the requirement was set that the bus subsystems be placed as far away from the optics as possible.

Derived Requirements

First, it is determined that the central combiner telescope must be located below the central plane of the satellite. This requirement leads to the need for a swing arm so that the air-bearing pedestal does not interfere with the satellite. Second, the optics has placed a requirement that the sub-apertures be aligned within 15 arc seconds. This requirement created the need for a manual aperture alignment system.

The general structure consists of 3 aperture modules and 1 combiner module. The 3 aperture modules attach to the central combiner module to form the satellite. The satellite's center section can then be attached to the swing arm to simulate space conditions. Since this is a ground system, it was determined that certain non-flight components such as batteries and the static and active balancing systems could be placed on the opposite side of

the swing arm. These items will provide a counterbalance to equalize the weight on the swing arm, while still maintaining a valid simulation of a space system.

3.3.3 Final Design

Aperture Module

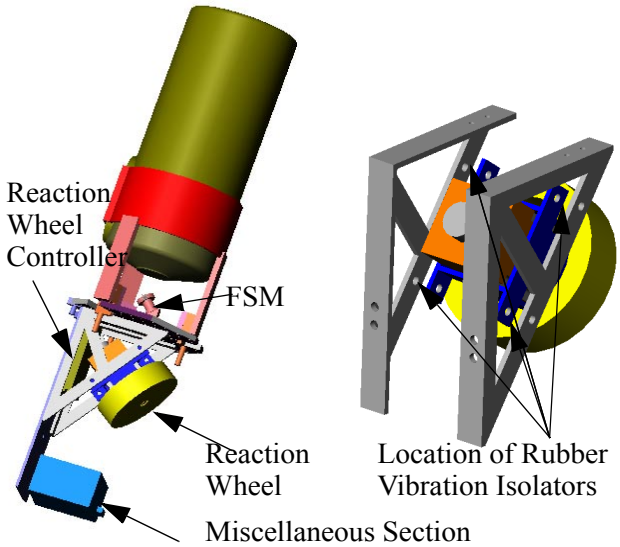

Figure 3.16 Aperture module (left) and RWA module (right)

In order to mount the telescope, an aluminum aperture collar was designed with three legs attached to it for aperture alignment. The original mounting points of the telescope were used and clearance was allowed between the collar and the rest of the telescope as to not interfere with the optics. The collar was designed on SolidWorks and the drawings were given to MIT's Central Machine Shop for manufacturing.

Reaction Wheel Mount

The main challenge in designing the reaction wheel mounts was determining an adequate method of suppressing the vibrations caused by slight imbalances in the wheels. Since a solid metal attachment would translate most of the vibrations, a variety of rubber vibration control mounts were examined. The mounts we chose have a tapped hole to accept a screw on one end of the rubber and a screw of the same size protruding on the other end.

Center Combiner Module

The fourth module of ARGOS is known as the Center Combiner Module (CCM). The CCM holds the Combiner Telescope, the Pyramidal Mirror, the View Finder and the CCD. A series of tip/tilt stages provides rotational control in all axes of freedom and translational control parallel to the central axis. Three clamps that are tightened with ball-bearing tipped setscrews hold the Combiner Telescope. The ball bearings allow the set screws to push the clamps radially inward towards the telescope without rotating the clamps.

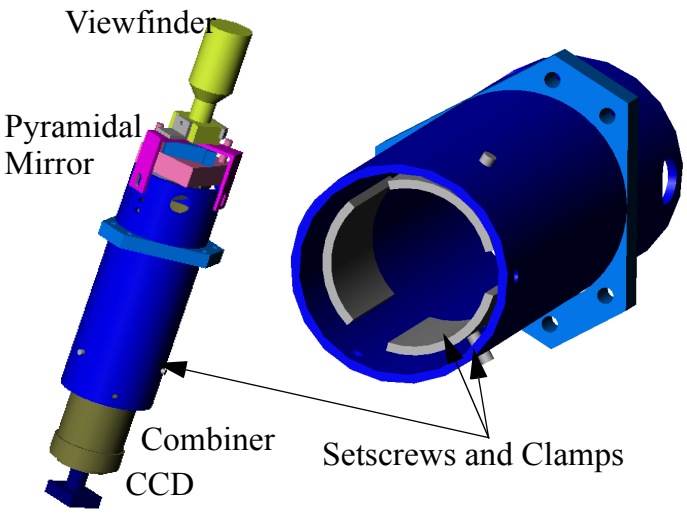

Figure 3.17 Center Combiner Module

Module Interfacing

ARGOS is assembled by attaching the three Aperture Modules to the Center Combiner Module. Each Aperture Module has two locating pins and a through hole for a screw. The Center Combiner Module contains two holes for the pins to drop in for each aperture as well as a tapped hole at the bottom so that the modules may be tightened into place.

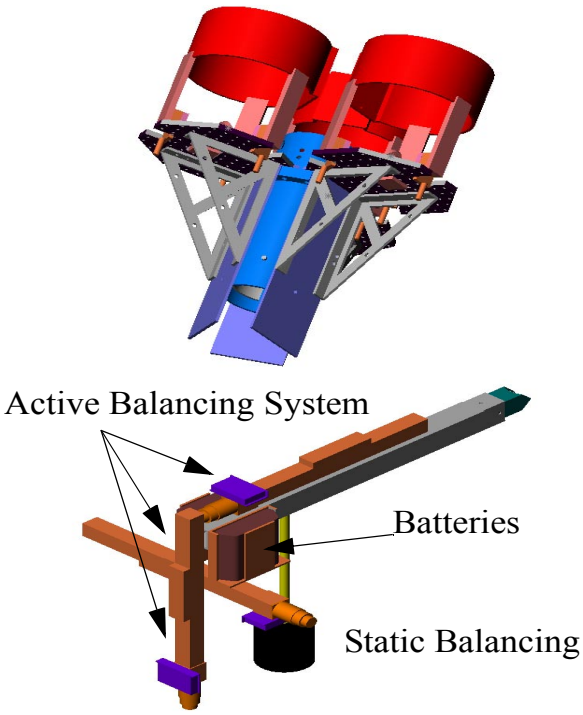

Figure 3.18 Assembled aperture mode and swing arm design

Swing Arm

In order to build a ground version of this satellite and have it float on an air bearing, a swing arm had to be used. The presence of gravity also created the need for things such as the static and active balancing systems to control the location of the center of mass of the spacecraft. Since these systems would not be found on the flight version of ARGOS, they were placed on the opposite side of the swing arm to counterbalance it on the air bearing. The batteries were also placed on the far side of the swing arm since a different power system including solar panels would be used in the flight version of the spacecraft.

Fully Assembly Satellite

Figure 3.19 shows the fully assembled satellite mounted to the swing arm and air bearing. This represents the configuration of the satellite during normal operations. The satellite will be positioned along the swing arm so that it is as close to the air bearing as possible

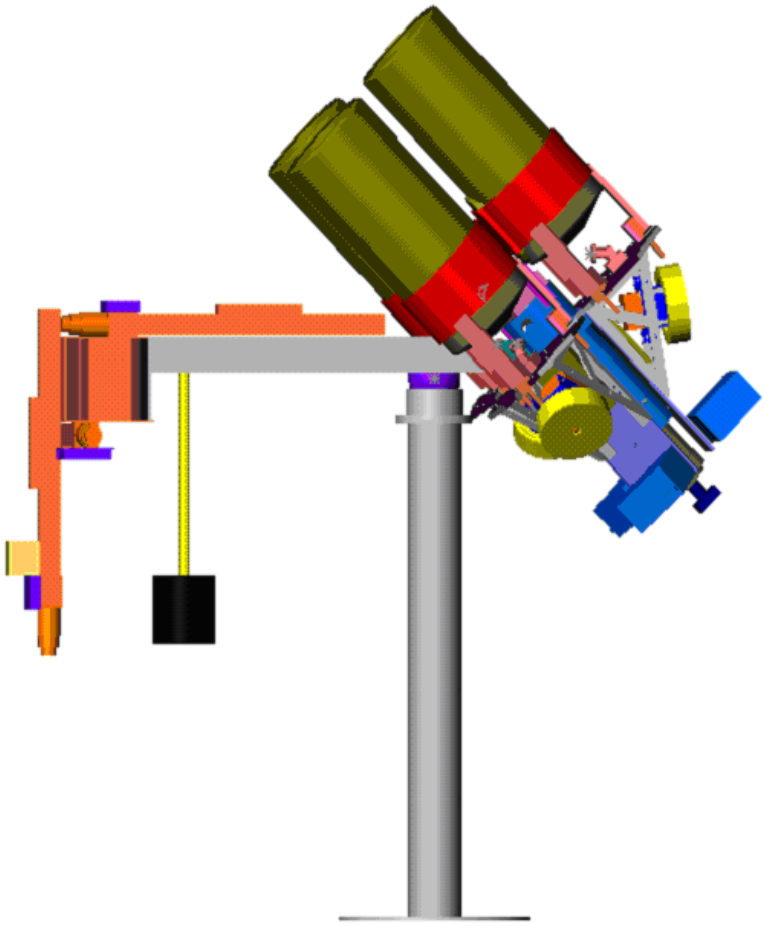

Figure 3.19 Fully Assembled Satellite

while allowing full rotation and a balanced system. This will allow for the lowest possible moments of inertia.

3.4 Power

This section describing the design of the power distribution system will use four requirements related with power subsystem as an outline.

3.4.1 Continuous autonomous operation for up to one hour:

(Refer to Requirement 7.2.5 in Appendix A)

Since the general architecture for the power system has already been specified in the trade analysis section, the first step in defining the power system design is compiling a list of powered components with specifications (voltage, amperage, typical power required, peak power required, and duty cycle). Table 3.1 gives the final estimates of the various power requirements for all the necessary components. This information is what is used to estimate the battery capacity and type of regulation that is necessary.

TABLE 3.1 Power System Requirement

Subsystem	Component	Typical Power (W)	Peak Power (W)	Volts	Amps
Passive Optics	Framegrabber Card	5	5	PC power	PC Power
Active Optics	FSM Amplifier x 9	13.5	18	12	PC Power
ACS	Reaction Wheel Motors	26	70	56	
	RWA/ABS Power Amps	5	100	28	
	Rate Gyro Filters	1.2	1.2	+/- 12	
	Active Balancing Controller	4.23	5	+/- 12, 5	
	Rate Gyros x 3	15		28	
	Inclinometer/ Magnetometer	~0.0875	0.1	+ 5 DC regulated 6-18 DC unreg.	standard mode: 15-20 mA; low power: 7-13 mA; sleep: 2.5 mA
PAS	Avionics (motherboard + DSP board)	97	120	3.3 & +/- 5, +/- 12	
SOP	Wireless LAN Card	5	5	PC Power	PC Power

This equation is used for determining the battery capacity[Wertz, 1999]:

$$C_r = \frac{T_e P_e}{(DOD) N n} \tag{3.6}$$

Te is the amount of time the battery must be discharging, Pe is the total average power draw, DOD is the depth of discharge, N is the number of batteries, and n is the transmission efficiency. The design at PDR created two estimates for capacity, one as a worst case and a second with more realistic duty cycles. The worst case scenario assumed 100% duty cycle for all powered components, while the best guess scenario was calculated with the optics at a 50% duty cycle and the reaction wheels drawing maximum power 20% of the time and drawing quarter power otherwise (the worst case Pe was 520.15 W, while the best guess was 248.14 W). Since then there have been many changes in the power requirements. The reaction wheels have been purchased and assembled and given a more realistic duty cycle (83.3% - maintain wheel speed [~25 W], 16.7% - max wheel torque [~70 W]). The result was a much lower estimate for required power. Also, the depth of discharge was changed from 0.5 to 1 to allow for the complete discharging of the batteries. The last important change was the new approach to voltage regulation using just the PC power supply. On the other hand, the power estimate increased since many of the system components are being powered through the computer, and the power supply is about 65% efficient.

Before calculating the battery capacity, it is necessary to look at the general layout and the varying loads on the different busses. Figure 3.20 shows the basic layout with the 28 V bus and the 56 V bus (Refer to Figure 2.5.1.6 for a breakout of what is included in "Everything Else"). Figure 2.5.1.2 shows the respective loads on the two busses.

For both the 28V bus and the 56 V bus, Average Power estimates are used when possible,and Max Power estimates when necessary. Batteries A and B both have to support the computer (taking into account its inefficiency), the other 28V components, and the reaction wheels: 217.55 W + 20 W + 26 W = 263.55 W (131.775 W each since they are in par-

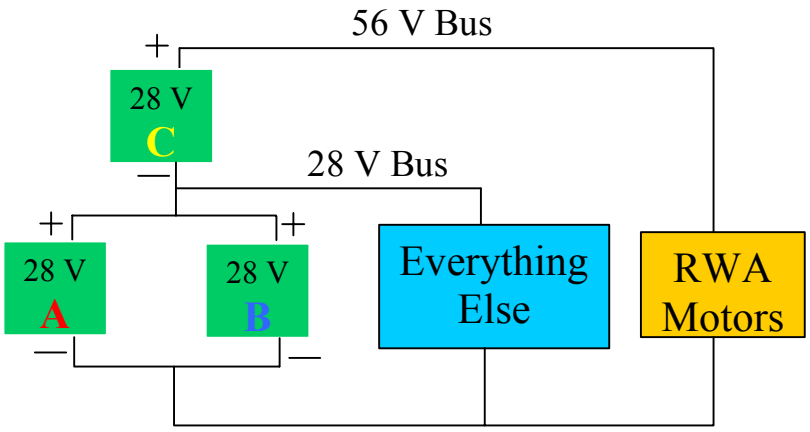

Figure 3.20 Schematic of Power Supply

TABLE 3.2 Loads on 56V bus and 28V bus

Bus	56V Bus	26V Bus
Loads	26W (RWA Motors)	130.53W (raw power thru PC) 20W (other 28V components)

allel). Battery C only has to support the reaction wheels: 26 W. Given that all batteries need to operate for an hour and that they are all 28V, these numbers become:

Battery A and B - 131.8 W (4.7 A-hr)

Battery C - 26 W (0.93 A-hr)

By adding a 25% margin, we have reached our battery design target (2 5.9 A-hr, and 1 1.6 A-hr batteries). According to the trade analysis, it was necessary to match these target designs with what is available COTS and economical. It is for this reason we chose three 6.5 A-hr batteries instead. To proceed any further with the battery design, it becomes necessary to take a closer look at the requirement that we provide continuous operation for an hour.

In order for us to see the International Space Station (ISS), we must be in shadow (i.e. The sun has set some time ago) and the ISS must be illuminated. If the ISS were to pass straight through the zenith, it would take about 10 minutes to travel from horizon to horizon. The best possible case for maximum viewing time of the ISS is two times a night, ten minutes long and an hour and a half in between (refer to Figure 3.21). In determining how many batteries and chargers we need, we looked closely at our operational requirements as well as our needs for general testing.

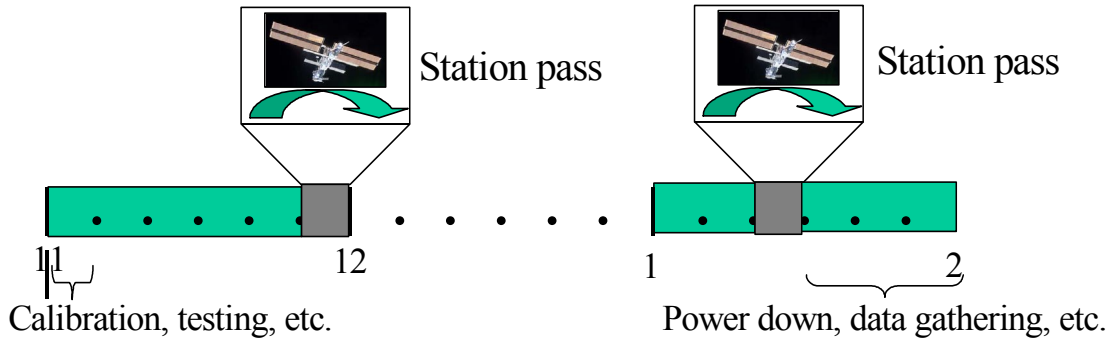

Figure 3.21 ISS Tracking and Power System

The operational requirement of one hour of self-power was derived from the need to operate while tracking station, as well as during preliminary calibrations and tests. By designing according to our best case scenario, our operational requirement should be about 2 hours of powered control within about a 3 hour period. Since this does not allow much time for recharging (without spending exorbitant amounts of money on chargers), two sets of charged batteries must be available on that day. "Battery C" in Figure 3.20 will have more than enough capacity to last for two hours of operation, so we only need to buy 5 28V batteries instead of 6 (2 full sets).

As for general testing, the only added requirement is that both sets of batteries should be ready to be used again the next day (batteries must be able to be recharge over night - requirement related to number of chargers).

One important change brought about by the search for battery chargers was that designing and making 28V chargers was not very cost effective at all. In order to avoid this, the 28V batteries will actually be composed of two 14V cells in series so that we can use 14V chargers. So, the total number of batteries needed is 2 x 5 = 10. Since the chargers can charge a fully discharged battery in about 5-5.5 hours, there can two full charging sessions overnight if necessary. So, the total number of chargers needed is 5 + 1(extra) = 6.

The batteries and chargers were purchased from Rose Electronics (see Figure 3.22). The batteries are 14 V, 6.5 A-hr cells comprised of 11 Panasonic HHR650D cells in series. They come assembled and shrink-wrapped with connectors, poly-switch, and thermistors. A thermistor is a thermal resistor that is used to measure battery temperature. A poly-switch acts as a reusable fuse, switching off the power when the current exceeds the limit and resetting. The chargers charge at 1400 mAh. They are what are called "smart chargers" because they sense battery capacity and temperature and do not overcharge or undercharge.

3.4.2 Simple and Standard Interfaces:

(Refer to Requirement 5.3.1.1 in Appendix A)

This general project requirement applies specifically to the power system in that all components should be COTS and have an interface that reduces the amount of necessary design. One of the modular elements of this project is to have a standard data/power interface on each of the three apertures. This allows for easy maneuverability, quick connect capability, and it perpetuates the modularity concept.

There are many barrier blocks distributed around the satellite to allow access to the different power busses. For example, there is an eight-contact barrier block on each aperture to

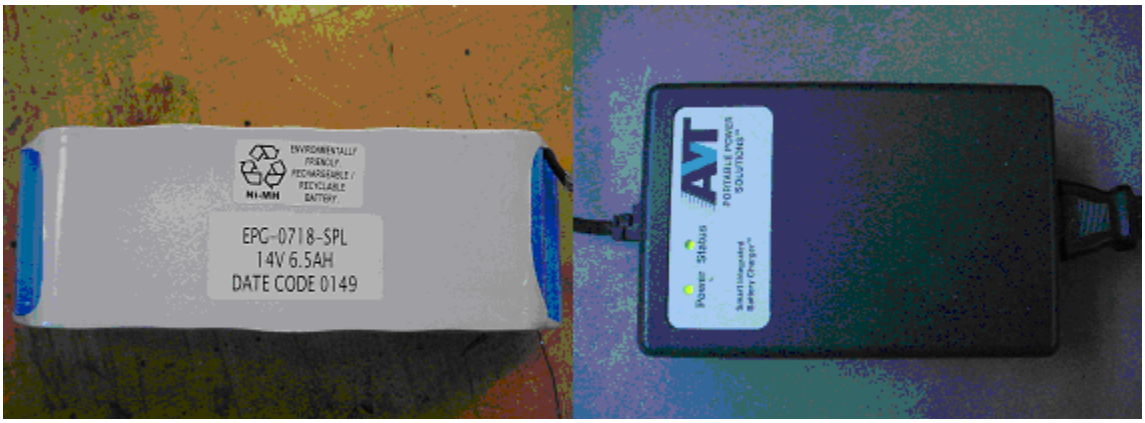

Figure 3.22 ARGOS battery pack and charger

allow access to the 56V, 28V, +12V, -12V, +5V, -5V, 3.3V, and GND busses for all components that are mounted there. With this standard power interface on each aperture, it doesn't matter where the powered items are mounted. This also allows for easy expandability if we want to add more powered components in the future since all this requires is connecting its power cord to the barrier block with spade lugs on the appropriate voltage bus.

We put many connectors throughout the wiring system (standard Molex), keeping in mind the emphasis on modularity and standard interfaces. There is a connector separating the batteries from the rest of the satellite (the two sides of the swing arm) and connectors between each aperture. There are no power lines between apertures that do not have simple connectors for easy assembly/disassembly. All the power lines going from the barrier blocks to the components have connectors as well.

3.4.3 Automatic Health Status (Telemetry) Data Reports:

(Refer to Requirement 7.1.7 in Appendix A)

It is important that we know the remaining capacity of the batteries on the satellite so that we can lock everything down to swap them before they go dead. One of the most accurate ways to do this is by using a gas gauge chip (Texas Instruments bq2014h), an IC that

directly measures the amount of charge leaving a cell. They are configured to apply to specific batteries with different characteristics relating to chemistry, discharge characteristics, capacity, etc. They use this information and self-discharge data to compensate when calculating remaining capacity. One of the easy ways to display this capacity information is through the use of the gas gauge's 5 LED drivers. Battery temperature, voltage, current, and capacity can be outputted digitally through an ADC at 15 bit resolution (serial communication via a 2 wire SMBus protocol).

To avoid the complications associated with adding data lines from each battery to the computer to provide digital telemetry, we decided to use the 5 LED drivers to display battery telemetry visually. The chip operates on normal TTL voltages (+5V power). The /DISP pin (Display control input) is used to control when the LEDs turn on and show the current battery capacity. When pulled low, the LCOM pin (LED common output) becomes an open-drain output for the LEDs which are connected to pins 2-6.

The output on these pins determines whether or not its respective LED lights up, thereby displaying the battery capacity in 20% increments. Pins 2-6 are also the program pins that are used to tell the gas gauge chip the starting value for the battery capacity until the chip "learns" a more accurate capacity through subsequent charges and discharges. This pins are programmed by connecting them to ground or power through soft pull-up or pull-down resistors or by leaving them "floating."

The SR pin (sense resistor input) is used to measure the voltage drop across a small sense resistor (0.05 Ohm). This data is integrated over time in order to get charge/discharge information.

The SB pin (secondary battery input) is used to set the EDV, or end-of-discharge voltage, where we want the gas gauge chip to display an "empty state" on the LEDs (lowest LED blinks rapidly). Our empty state is constrained by our lowest allowably bus voltage for the reaction wheels, 48V. Since, each gas gauge will be attached to and powered by a 14V battery, our end-of-discharge voltage is 48/4 = 12V. We used voltage dividing resistors to get

the voltage on the SB pin to equal the internally hardwired thresholds when the host battery voltage reaches 12V.

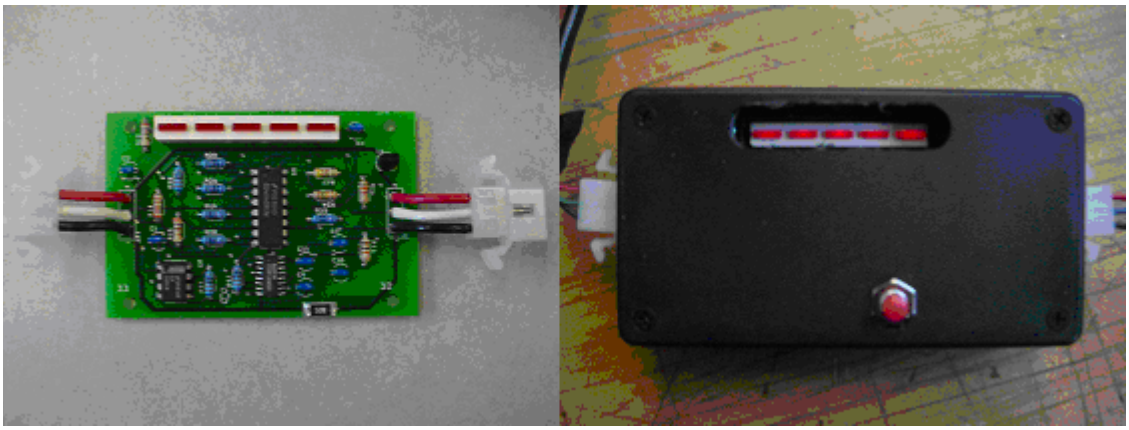

Figure 3.23 ARGOS power telemetry circuit and the case with LED

The RBI pin (register backup input) provides a backup power supply to the gas gauge if disconnected form the 14V battery so that information "learned" about the battery is not lost. But, since we intend to have these chips always connected to the batteries, a backup supply was not necessary.

The DONE pin (charge complete input) is supposed to be pulled high when a charging cycle is complete so that the gas gauge knows to update its full capacity estimate with the last measured discharge (assuming it was a full discharge of the battery). This is connected to a normally-open momentary push-button switch that is pressed whenever a battery is recharged.

So far, we have the gas gauge itself, LEDs, as well as various resistors and capacitors. To step down the voltage from 14V to the TTL levels required by the IC, we used a LM317L voltage regulator (adds another chip plus some resistors/capacitors to set the output volt-

age). We also had to add a LMC555 (astable oscillator/timer) and a CD4040 (12-bit ripple counter) to produce a square wave with a period of about 10 seconds. This was necessary because the /DISP pin needs to be brought low every time you wish to see the LED output. If you leave this pin low, the LEDs stay on for four seconds and then turn off until the next rising and falling edge on /DISP. So now this circuit has two more IC's plus some more resistors/capacitors to set the oscillation frequency.

This entire circuit, including power connectors can be seen in Figure 3.23. The layout was drawn in OrCad Capture and then ported to OrCad layout where each component was given a footprint and the traces were laid. The entire board is about 2.5" x 4" and has a top and bottom layer of trace. All of the traces are 10 mils, except for the power and ground traces which are 30 mils. Some of the constraints on the design were that we could only use two layers (cost goes up exponentially per layer), there shouldn't be any 90 degree turns in the traces, there are no "ground loops," there is only a single-point ground return, and the resistors and capacitors associated with the gas gauge should be as close as possible to the chip itself (please refer to the appendix for the layout design and trace placement, as well as pinouts for the ICs). They were manufactured by Advanced Circuits for approximately $40 each. Each board is inside a plastic electronics box (with holes for the push-button switch, connectors, and viewing the LEDs; see Figure 3.23) that is attached to the satellite with Velcro for easy swapping.

3.4.4 Automatic Control in response to Ground Commands and Manual Control:

(Refer to Requirement 7.1.11 in Appendix A)

This requirement is more important for the Software subsystem, but it applies to the Power subsystem in a few important ways. First, if we allow for the capability to cut any of the power lines remotely, it should be the ones to the reaction wheels. Anything else wouldn't make sense. Originally, we were planning on using a software controlled power relay to disable the 56V bus. Then we discovered that there is a pin on the reaction wheel power

amps called /INHIBIT that cuts off the power when pulled low. This served as a satisfactory substitute for the relay, although it hasn't been implemented since none of our operational modes requires remote power control of the reaction wheels.

3.4.5 Other Design Points

Before the 28V and 56V busses go to the rest of the satellite, they pass through switches and fuses in series. The switches clearly allow manual control of the power and the fuses are set at 5A and 10A for the 56V and 28V busses, respectively. Before going to the PC power supply on the other sides of the swing-arm, the busses are broken out at a barrier block so that the Active Balancing System can have easy access to the 28V bus. As is shown in Figure 3.24, the power lines then stretch across the swing-arm and connect to the barrier block on one of the apertures. The PC power supply receives its 28V DC and the +/-12V, +/-5V, and 3.3V voltages are spliced out of the cables going to the motherboard and connected to the barrier block to provide the remaining bus voltages.

Most of the wires are 16 gauge (some are 18 and 14) so that wire size isn't the limiting factor for the current capacity of the power distribution system. The entire system is grounded to the structure at exactly one point (0V touches the structure right near the PC power supply). This was done to minimize the effect fluctuations in voltage/current from the variable current draw of the PC power supply have on the rest of the system. A single point ground return is important here to avoid ground loops.

3.5 Avionics

3.5.1 Software

The DSP we bought came with its own Compiler: "Code Composer". This constrains us in using C as our programming language in order to communicate with the on board CPU. It is specifically designed in order to test the DSP.

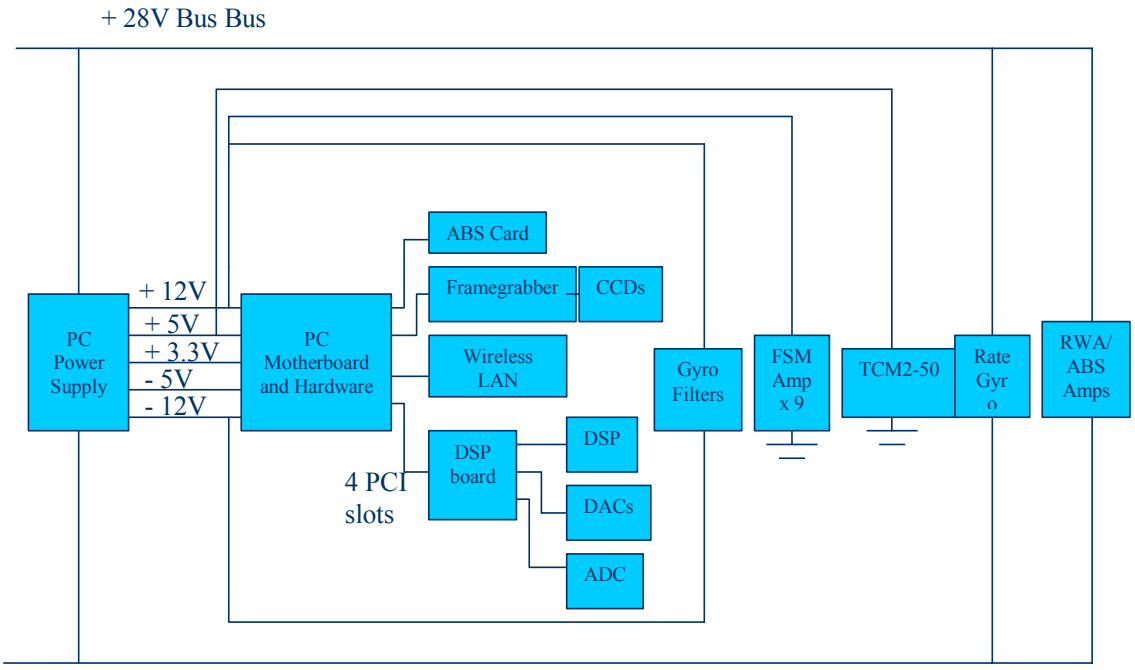

Figure 3.24 28V Bus Power Layout

The objective of the operating system is to schedule, dispatch, and provide intercommunication between the distinct processes. Because multiple processes will be running at the same time, an informed choice needs to be made as to which type of OS will best suit the purposes of the System.

The cyclic executive model in Figure 3.25 was ultimately selected for its ease of implementation, and its extensive usage. This system model is the most commonly used in the aerospace industry especially in complex safety critical systems.

The executive will clock each process, and each process will run in its allotted time. This solves the timing problem, but different complications arise. Because each process executes sequentially, it is possible that one process might fail or take longer than the clock allows for. In this event, the executive would then terminate the process and start the next scheduled task. Another problem is that the process might take less time than allotted, which means the executive does not guarantee optimal response time of the system, or

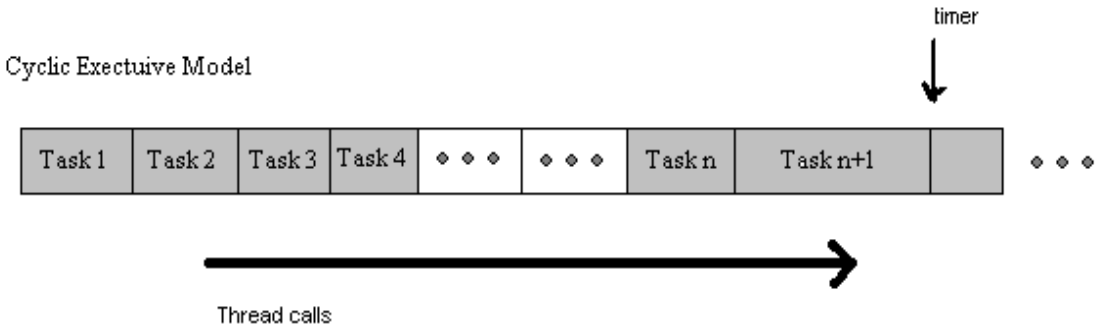

Figure 3.25 Cyclic Executive Model

efficient usage of CPU processing power. Setting a foreground/background type of system solves these problems. Each task will have a certain pre-set priority: those which are vital to the proper operation of the satellite (ACS) will have maximum priority and will therefore be interrupt-driven; those with lesser importance (Telemetry and Health status) will have lower priorities and can be polled. Although each process has its own predetermined schedule, it can be interrupted by a high priority task. Lower priority tasks will then run only when the processor is fully available.

Setting a foreground/background type of system solves these problems. Each task will have a certain pre-set priority: those which are vital to the proper operation of the satellite (ACS) will have maximum priority and will therefore be interrupt-driven; those with lesser importance (Telemetry and Health status) will have lower priorities and can be polled. Although each process has its own predetermined schedule, it can be interrupted by a high priority task. Lower priority tasks will then run only when the processor is fully available.

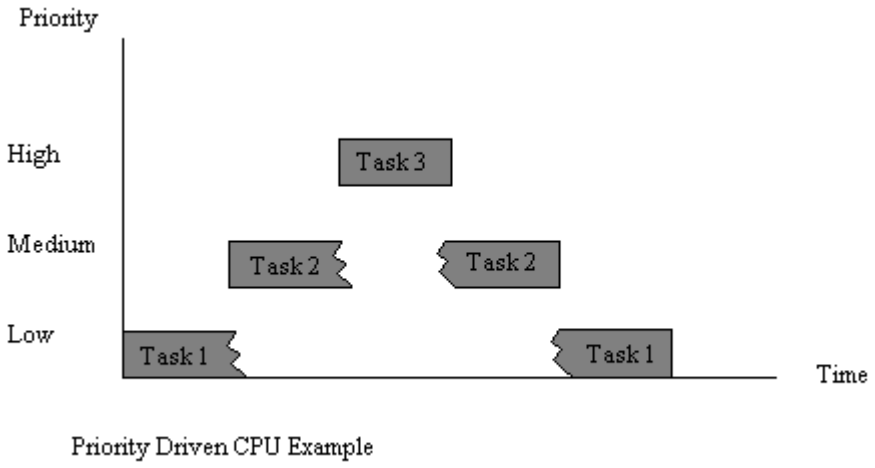

Figure 3.26 Priority Driven CPU Example

To avoid "processor hogging," dynamic priorities can be set so that every time a lower priority task gets pushed back it will be promoted in the priority list. After a number of missed calls the lower priority task will have maximum priority status, which it will then lose once completed.

Figure 3.27 on page 117 shows the GUI control window of the ARGOSVIEW software developed in order to control CCD settings and ACS science input easily. It can select the number of apertures to operate for the FSMs, and set the control mode for the ACS actuators. The text input windows are used to accept the science input (the azimuth and elevation angles of a tracking and imaging target). This GUI window is also used to generate a series of still pictures while tracking fast moving targets like the International Space Station (ISS).

3.5.2 Avionics Hardware

Figure 3.28 contains the ARGOS avionics hardware schematic. The optics systems we have to interface with are in yellow, the ACS systems are in blue, and the Science/Operation/Communications systems are in purple. The number of COTS components that

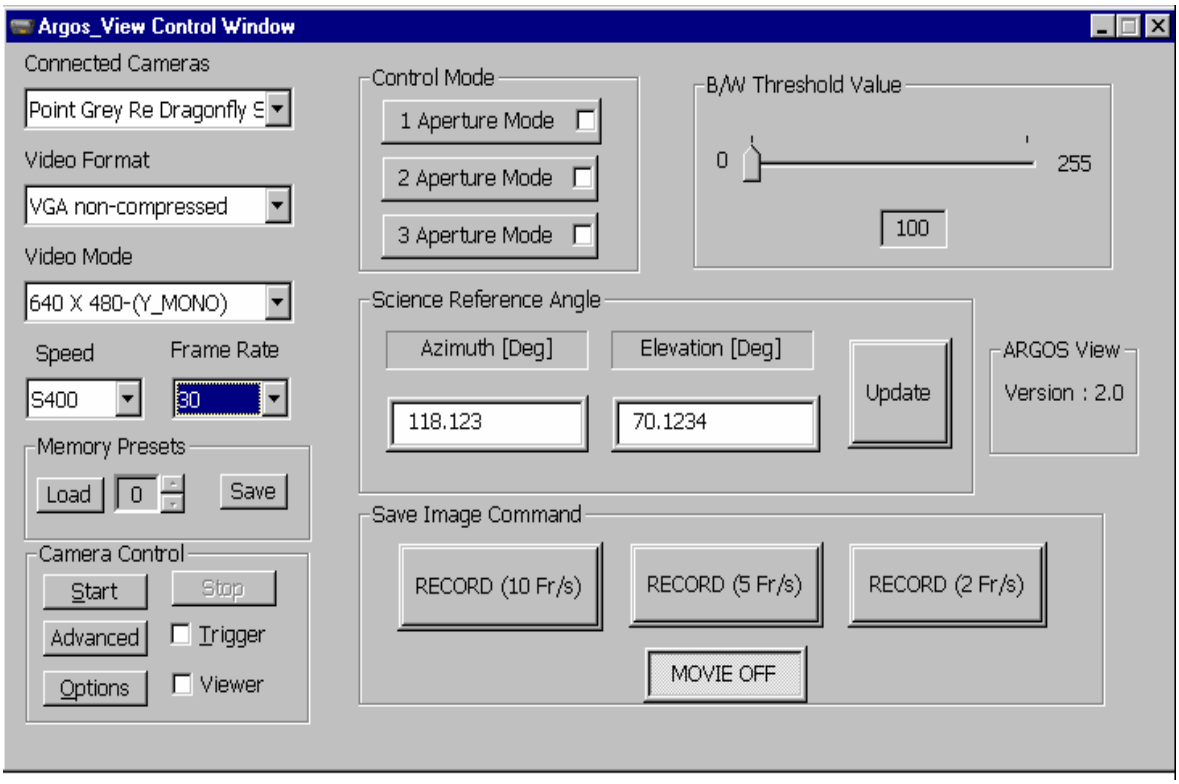

Figure 3.27 ARGOSVIEW- the ARGOS PC GUI controller

require standard PC interfaces has driven our decision to make use of a standard PC motherboard as the base of our avionics system. Sensor readings will be put into the PC's memory to be accessed by the HERON4 DSP when necessary for control purposes.

The HEPC8 houses our HERON4 digital signal processor (DSP) in its first slot. The other three slots are free for expansion modules. To meet our I/O requirements, we are using two HEGD14 8-channel DACs and one HEGD2 8-Channel ADC. The satellite's actuators are connected to the DAC modules, because they must be driven by analog signals. Each fast steering mirror will sit on a set of three piezoelectric actuators that require a signal a voltage signal per actuator. Each ACS wheel will require one signal to control its spin, which in turn will spin the entire satellite. Most of the satellite's ACS sensors are connected to the ADC modules, because they provide analog signals that must be understood by the computer as digital signals. Three tachometers will provide data on how fast each ACS

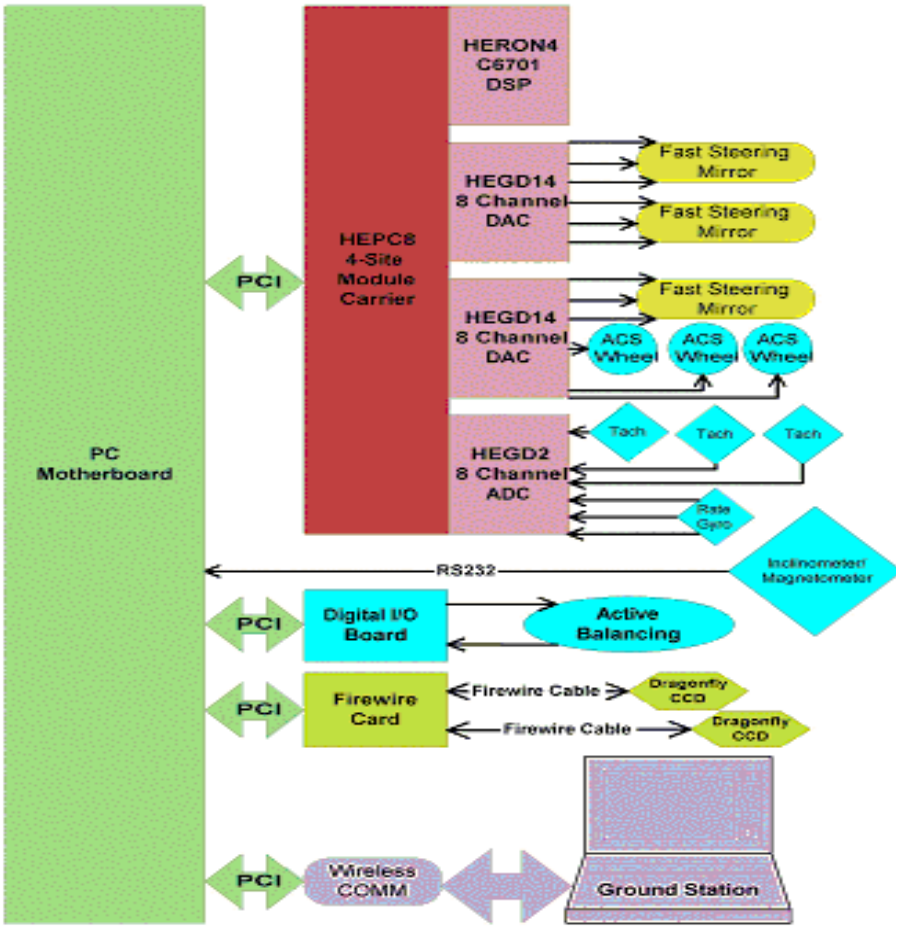

Figure 3.28 Avionics Hardware Schematic

reaction wheel is spinning. A three-axis rate gyro assembly will provide data on how fast the entire satellite as a whole is spinning. The computer will use this data when deciding what signals to send to the reaction wheels to affect the satellite's movement. The remaining ACS sensor is the inclinometer/magnetometer that gives us a data on the satellite's pitch and compass heading. While it does have a choice of analog or digital outputs, it does not fit on our ADC card. Instead, we are connecting it directly to the PC motherboard using a standard RS232 serial port. This may create a problem in the future if these readings cannot be passed from the PC to the DSP fast enough to control the system smoothly, but since it is the only critical ACS sensor on board the PC, we may be able to predict its

readings from the tachometers and rate gyros on board the DSP if this loop frequency needs to be higher than we can manage to deliver. Three other COTS components connect directly to the PC motherboard as well. The active balancing system (ABS) is self-contained within a single specialized I/O board that connects to the motherboard via a standard PCI slot. It will take data from the computer based on other sensors, and send voltages to the ABS actuators to move balancing weights. The main CCD camera and the viewfinder CCD camera will both connect to the same PCI interface card. Finally, the wireless LAN card we are using for remote operation also interfaces with the PCI slot.

To meet the requirement of simultaneous automatic control of various subsystems, ARGOS will be tracking the International Space Station (ISS) as it crosses the night sky. In order to do the image processing necessary to track moving objects with the satellite, we needed to get the most powerful PC we could find. We also needed to load it with as much RAM as we could afford to avoid slow hard drive data writes. Our goal in designing the PC system was to make one that would not need to access a slow, heavy, power hungry hard drive. The combination of an AMD 1.4 GHz Athlon processor on a Shuttle AK31 motherboard will go a long way towards fulfilling this requirement. The AK31 can operate at a front side bus (FSB) frequency of 266 MHz, which helps to alleviate the biggest bottleneck in PC performance - the time between when data is requested from memory and when it is delivered. Also, the AK31 features a highly configurable jumperless BIOS that gives us the opportunity to easily overclock the CPU, FSB, or memory if processes are taking too long.

3.6 Chapter Summary

This capter introduces the ARGOS testbed by focusing on the ACS, Structure, Power, and Avionics subsystems. The objective of the ARGOS project is to demonstrate the practicality of a modular architecture for space-based optical systems. To demonstrate a complete spacecraft in a 1-g environment, the ARGOS system is mounted on a frictionless air-bearing, and has the ability to track fast orbiting satellites like the International Space Station

(ISS) as well as point stars. Modular architecture design emphasizes the use of replicated components and quick connections. The system consists of three identical apertures arranged in a Golay-3 distribution. The light from these telescopes is combined in a center module and transmitted to a Charge-Coupled Device (CCD). Wavefront sensing techniques are explored to mitigate initial misalignment and to feed back real-time aberrations into the optical control loop. The end result is an image as good as the image received from a monolithic telescope using a single aperture. ARGOS operates autonomously and in a self-contained manner while a wireless ground station downloads images and telemetry information. The detailed subsystem designs are explained in this chapter.

Chapter 4

OPTICS COMPONENT DESIGN AND INTEGRATION

This chapter elaborates on trade-off analysis, design and implementation of the actual optics of a sparse aperture imaging array. Chapter 4 corresponds to Step 4 , Step 5, Step 6 and Step 7 of the SOCS framework introduced in Chapter 2.

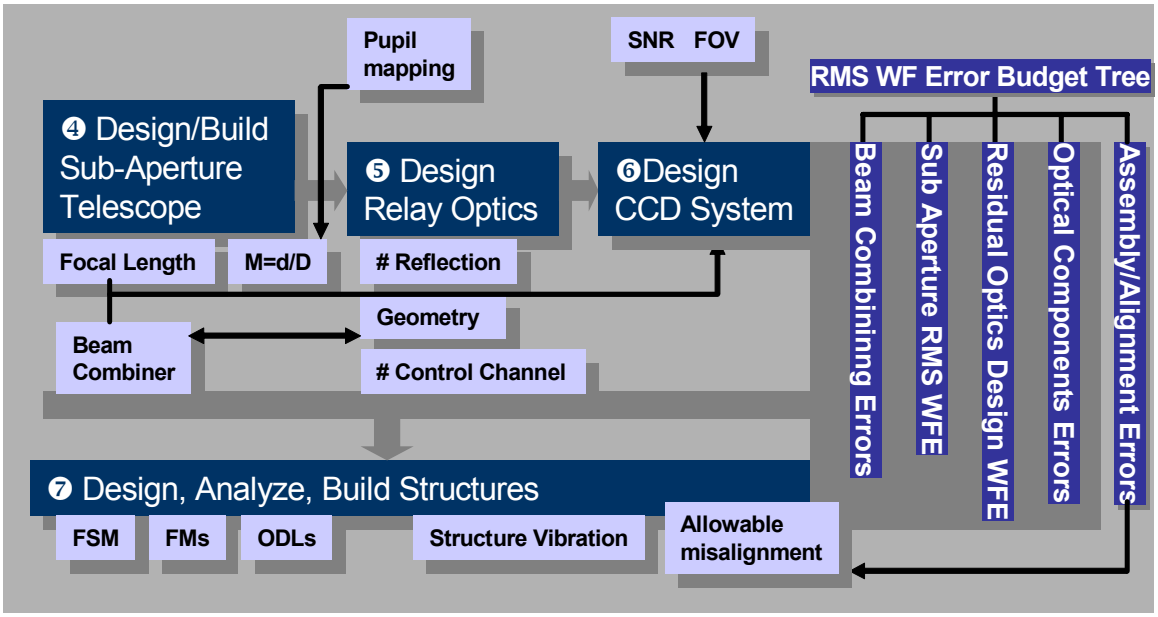

Figure 4.1 Step 4, Step 5, Step 6 and Step 7 of the Sparse aperture Optics/Control System design

Figure 4.1 illustrates the design procedures in this chapter. Once we decide upon the allowable beam combining errors, we can manufacture a telescope array that meets the

specific optical requirements. As discussed in Chapter 2, the Strehl Ratio requirement determines the allocation of wavefront error (WFE) into each contributing factor such as sub-aperture RMS WFE. The series of steps in Figure 4.1 coincide with the optical train that incident light travels through to the arrays (from Step 4, sub-aperture, through Step 6, CCD system).

The current optical layout of ARGOS is shown in Figure 4.2. Light shines in through the

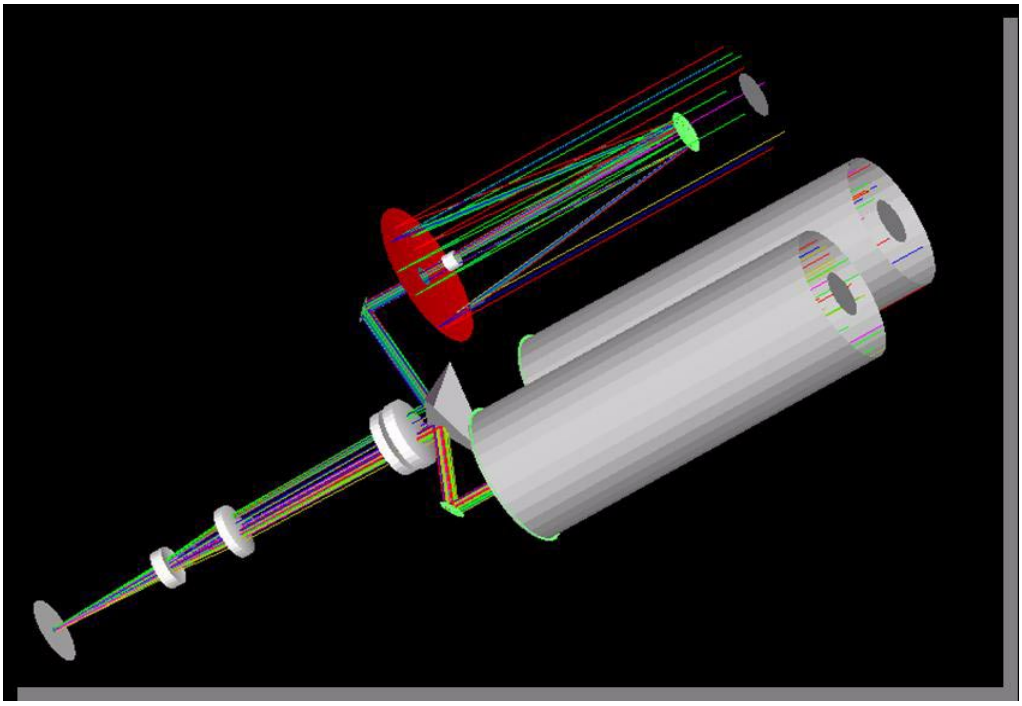

Figure 4.2 Optical layout of ARGOS (Zemax nonsequential modeling)

sub-aperture. The light continues through the telescope until it hits the collimator, which is inside the telescopes' baffle. The light then goes through the collimating lens producing a 21mm diameter beam. The light exits and hits a reflecting mirror mounted onto a three axis Fast Steering Mirror (FSM) that acts as an Optical Delay Line (ODL) as well. The light is then reflected to the pyramidal mirror that is stationary. The light beam then enters

the beam combiner, and is focused onto the CCD. The detailed design procedures are studied in the following sections.

4.1 Sub-Aperture Telescope

4.1.1 Image Aberrations

We can divide image aberrations into two broad categories[Hecht, 2001;Rutten, 1999;Smith, 2000]:

1. Monochromatic aberrations, which may occur in both refracting and reflecting telescopes if only one wavelength is involved.
2. Chromatic aberrations, which occur because the refractive index of glass is different at different wavelengths. This aberration occurs only through refractive surfaces.

Refractive index increases as wavelength decreases; red light is refracted less than blue. The rate of change of refractive index with wavelength is called the dispersion. Optical glass manufacturers usually specify dispersion properties in terms of the Abbe number:

$$V_d = \frac{n_d - 1}{n_F - n_C} \tag{4.1}$$

The F, C, and d are the most often used wavelengths - blue, red, and yellow, respectively, and each n is the corresponding refractive index.

The monochromatic aberrations can be further divided into five primary aberrations: spherical aberration, coma, astigmatism, field curvature, and distortion. These aberrations are called the Seidel aberrations. Only spherical aberration is an on-axis aberration, while the rest of the Seidel aberrations are off-axis aberrations.

Spherical Aberration. Spherical aberration occurs when light rays parallel to the optical axis entering a telescope at different heights come to a focus at different points along the

on-axis. This causes a star to be seen as a blurred disk rather than a sharp point. Most telescopes are designed to eliminate this aberration.

Coma. Coma occurs in an oblique bundle of light when the intersection of the rays is not symmetrical, but is shifted with respect to the axis of the bundle. Off-axis light rays passing through the lens near its edge (i.e. marginal rays) intersect the image surface at different heights compared to those that pass through the center of the aperture. Coma is associated mainly with parabolic reflector telescopes which affect the off-axis images and are more pronounced near the edges of the field of view. The images seen produce a V-shaped appearance (see Figure 4.5). The faster the focal ratio, the more coma that will be seen near the edge, although the center of the field will still be coma-free in well-designed and manufactured instruments.

Astigmatism. Astigmatism is a lens aberration that elongates images which change from a horizontal to a vertical position on opposite sides of best focus. It is generally associated with poorly made optics or collimation errors.

Curvature of Field. Pure curvature of field means that the sharpest image is formed on a curved focal surface rather than a flat focal plane. Field curvature is a field-dependent defocus which changes quadratically with field angle. Field curvature of the individual two-mirror sub-apertures of a sparse aperture imaging array provides a fundamental limit to the field-of-view (FOV)[Harvey, 1985].

Distortion. Distortion is not an image aberration in the normal sense because it influences image scale rather than image sharpness. Distortion is a field-dependent tilt. It causes a displacement of the image point in the Gaussian image plane without loss of quality. Distortion as well as field curvature is a fundamental limiting factor to the FOV of a sparse aperture array made up of two-mirror telescopes. Detailed analysis on the effects of distortion and field curvature can be found in [Harvey, 1985;Faucherre, 1989].

There are two sets of polynomials that have been often used to describe image aberrations. The first is the Seidel polynomial series which evolved from the ray aberrations used by optical designers in imaging systems. The second is the Zernike polynomial set which propagation and optical testing practioners tend to use (e.g. wavefronts of interferometers).

The Seidel polynomial can be expressed mathematically as follows:

$$W = \sum_{i,j,k} W_{ijk} \bar{H}^i \rho^j (\cos\phi)^k \tag{4.2}$$

The subscript ijk in Equation 4.2 is a mnemonic device that ties the coefficient to a specific aberration term in the series. (i=0,j=2,k=0) describes the defocus; (i=0,j=4,k=0), the spherical aberration; (i=1,j=3,k=1), coma; (i=2,j=2,k=2), astigmatism. W_{ijk} is a coefficient independent of the pupil or object coordinate. ρ and ϕ are used to represent the exit pupil in the polar coordinate system.

The Zernike polynomials are defined as:

$$W = \sum_{i} Z_i R_i(\rho) G_i(\phi) \tag{4.3}$$

The functions, R_i and G_i for the first eight Zernike terms are listed in Table 4.1.

The first eight Zernike polynomials are plotted in Figure 4.3. Given Zernikes, the Seidel

TABLE 4.1 The first eight Zernike polynomials

	X Tilt	Y Tilt	Defocus	SA	0 deg Astig	45 deg Astig	X Coma	Y Coma
R	ρ	ρ	$2\rho^2 - 1$	$6\rho^4 - 6\rho^2 + 1$	ρ^2	ρ^2	$3\rho^3 - 2\rho$	$3\rho^3 - 2\rho$
G	$\cos\phi$	$\sin\phi$	1	1	$\cos 2\phi$	$\sin 2\phi$	$\cos\phi$	$\sin\phi$

coefficient magnitudes can be generated from the first eight terms. For example, Seidel aberration is 6 times its Zernike counterpart[Geary, 1995].

4.1.2 Two-Mirror Telescope

The addition of a second mirror to the optical design allows the optical engineer to improve the system FOV, increase the system effective focal length within a given package size, or reduce the package size while maintaining a required focal length and performance characteristics. The Classical Cassegrain telescope employs a parabolic primary mirror, and a hyperbolic secondary positioned such that the parabolic and virtual hyperbolic focii coincide. In the configuration, the on-axis image produced at the real hyperbolic focus is perfect, but off-axis performance suffers. The Ritchey-Chretien (RC) telescope employs two hyperboloids, which completely corrects spherical aberration and coma. But RC systems tend to be expensive. A less expensive design than either the Cassegrain or Ritchey-Chretien, the Dall Kirkham uses an ellipsoid primary mirror and a spherical secondary mirror. The paraxial focii of the two mirrors are slightly separated, and spherical aberration is corrected by the ellipse. On-axis performance of Dall Kirkham is quite good, but degrades rapidly off-axis. The Schmidt-Cassegrain Telescope (SCT), very popular for amateur astronomy, employs a thin aspheric lens to reduce coma, astigmatism, and field curvature at the expense of central obstruction and chromatic aberration due to the correcting lens. The SCT systems tend to be very compact and less expensive.

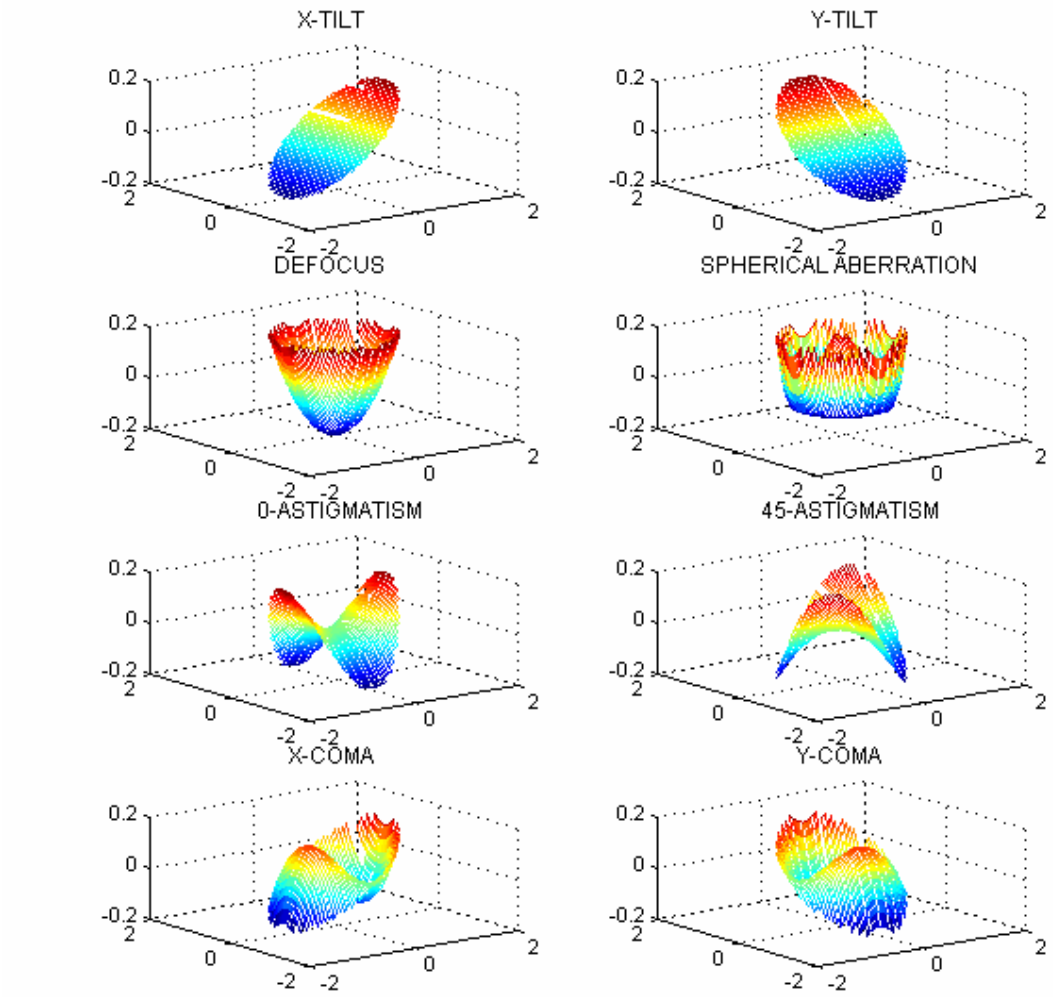

Figure 4.3 The first eight Zernike polynomials

The overall cost of the ARGOS optics system could be significantly reduced by selecting one of the highest precision optics commercially off-the-shelf (COTS) telescope. The Takahashi Mewlon 210, 8-inch Dall-Kirkham telescope is selected as ARGOS sub-aperture (Figure 4.4). It has an elliptical primary mirror followed by a secondary spherical mirror with no corrector lens. Table 4.2 shows the specifications of the Mewlon 210.

Figure 4.4 Takahashi Mewlon-210 , 8 inch Dall-Kirkham telescope

TABLE 4.2 Mewlon-210 specification

Model Name	Mewlon 210
Effective Aperture	210mm
Focal Length	2415mm
Focal Ratio	11.5
Primary Mirror Diameter/ F#	220mm/2.9
Secondary Mirror Diameter/ F#	65mm/4.0
Resolving Power	0.55"
Light Gathering Power	800
Limiting Magnitude	13.4
Tube Length	700mm
Tube Width	244mm

Figure 4.5 depicts the spot diagrams of the ARGOS subaperture, Mewlon-210. It is observed that the coma aberration occurs at off-axis field angles.

The effective focal length of a two-mirror telescope is calculated by

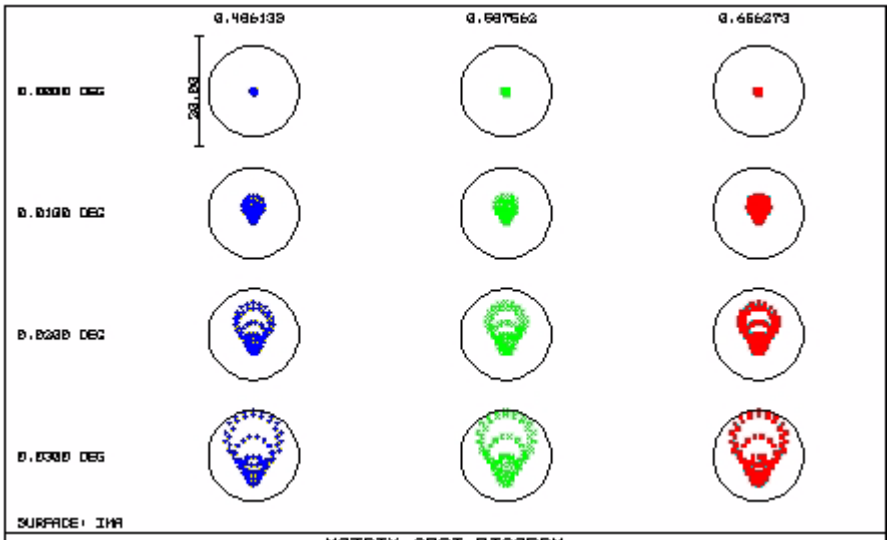

Figure 4.5 Spot diagrams of Mewlon-210, The circles indicate the diffraction-limited airy disk

$$f = \frac{f_1 f_2}{f_1 + f_2 - d} \tag{4.4}$$

where d is the separation between the primary mirror and the secondary, and f_1, f_2 are the focal lengths of the primary and the secondary. The effective focal length of Mewlon-210 is thus 2415mm.

4.1.3 Collimating Lens

Location of Collimating Lens

It is necessary to customize a collimating lens to convert a Dall-Kirkham-type focal telescope to an afocal telescope with a magnification ratio of 10. A magnification of 10 results in 21mm collimated beam. To meet this requirement, a distance of about 25 cm is necessary between the focus and the collimating lens. Since this is a significant length, alternative designs were considered to reduce the size of the optical train. The options include placing a folding mirror before the focus, placing a folding mirror after the focus, placing

the collimating lens after the focus, or placing the collimating lens before the focus. Figure 4.6 displays the possible designs for the relay optics before the ODL.

The following are used for metric evaluation:

- Manufacturability- design and production difficulty
- Vertical length- length of the optics along the axis of the sub-aperture
- Horizontal length- length of the optics along the axis of the sub-aperture's diameter

Table 4.3 shows the final evaluation scores.

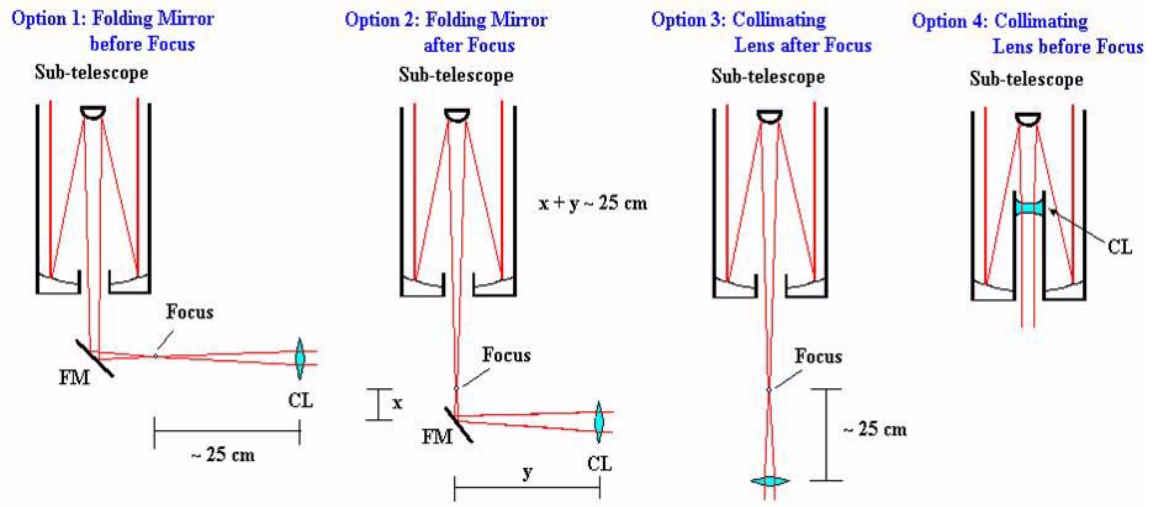

Figure 4.6 Options for location of collimating lens. FM=fold mirror, CL=collimating lens

TABLE 4.3 Evaluation of collimating lens location options

	Weight	Option 1	Option 2	Option 3	Option 4
Manufacturability	2/5	3	3	3	2
Vertical Length	2/5	3.5	3	1	5
Horizontal Length	1/5	1	2	4	5
Total	1	2.8	3	2.4	3.8

Since there is ample space to the sides of the apertures, the horizontal length metric was weighted less, while manufacturability and vertical length were given equal weighting. Based on manufacturability, all the design options were approximately equal. Placing the folding mirror before the focus (Option 1) has an advantage because an attachment exists which fits this design. However, this design would also entail an extending horizontal module that would be difficult to add to the structure. Yet, placing the folding mirror and the collimating lens at the right distance after the focus (Option 2 and 3) is just as equally difficult. Lastly, placing a collimating lens into the baffle tube of the telescope (Option 4) is the most involved process. It would involve designing and manufacturing an attachment to slide up into the baffle and place the lens at the exact position. The advantage of placing the collimating lens before the light is allowed to focus (Option 4), is that it would significantly decrease the horizontal and vertical length of the optics. It turned out that placing the collimating lens into the baffle is possible in order to make the system compact. Figure 4.7 shows the baffle attached to the primary mirror unit.

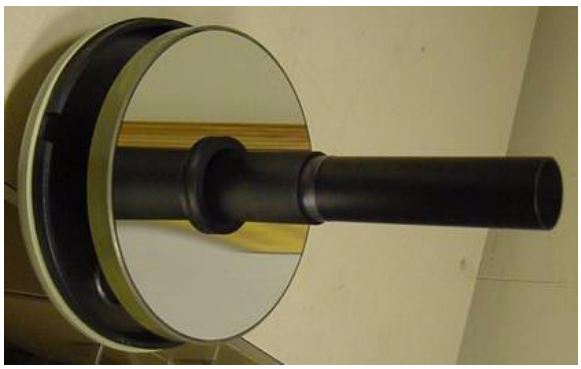

Figure 4.7 Baffle of Mewlon-210

Design of Collimating Lens

The collimating lens went through two rounds of down selecting before deciding what type of lens to use. In the first round, we needed to decide whether to use a cemented dou-

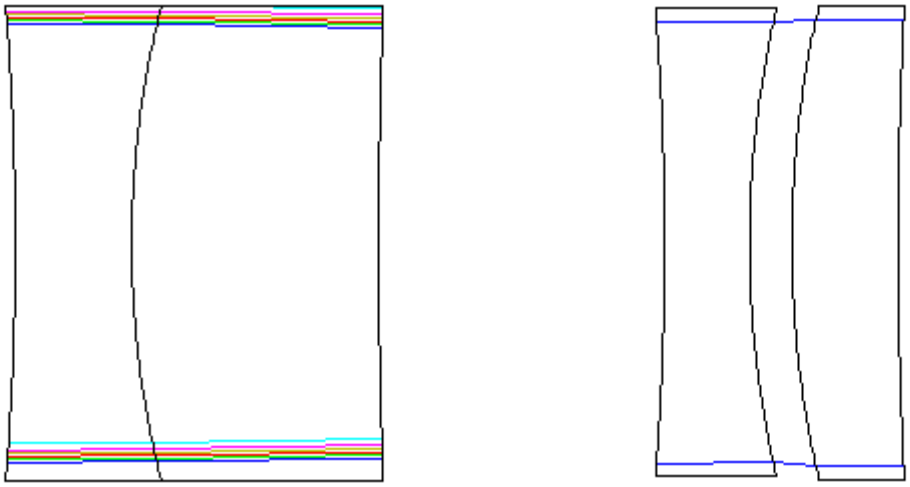

Figure 4.8 Cemented doublet (left) and air-spaced doublet (right)

blet (Fraunhofer cemented), or a regular air spaced doublet. The air spaced doublet is actually significantly more expensive than the cemented doublet. There are several reasons. The cemented doublet has two exposed surfaces that need to be treated with an anti-reflective coating instead of four in the case of the air spaced doublet. The surfaces between the two glasses in the cemented doublet can be polished to a lesser accuracy than those exposed to air since the index of diffraction does not change much from one glass type to the next and therefore wavefront errors are less destructive. A lens cell needs to be designed for the separate lenses and the lenses need to be mounted to very high tolerances. A cemented doublet does not need a lens cell since the two lenses are bonded. Both types of lenses can be designed to perform almost identically, therefore a cemented doublet is chosen to save the cost. In general, for lenses of modest (up to 3- or 4-in) diameter, the cemented form is preferred, primarily because the relationship between the elements (as regards mutual concentricity about the axis and freedom from tilt) can be more accurately maintained in fabrication[Smith, 2000].

A second round of down selecting was done on several different doublets that were optimized extensively by ZEMAX (a ray-tracing software by Focus-Software). The difference

between these doublets is the material they were made of. One drawback of the cemented doublet is that it has bonded glasses, therefore if there is a change of temperature, the doublet may fail. Although a doublet with calcium fluoride (CaF2) performs best in reducing chromatic aberrations, the high Coefficient of Thermal Expansion (CTE) of CaF2 (18.3E-6) forced us to find other glass combination for efficient achromatic doublet design. Smith[Smith, 2000] suggests FK51 (as a crown element) with a KzFS or LaK glass (as a flint). Traditionally the glasses roughly in the range n>1.6, Abbe number>50 as well as n<1.6, Abbe number>55 are considered as crowns, and the others are flints. Our final three designs were:

- FK51/BaK2
  CTE 5.3E(-6), 0.0027λ RMS WFE, some sensitivity to thermal shock
- FPL53/BK7
  CTE 7.1E(-6), 0.001λ RMS WFE, high sensitivity to thermal shock
- BK7/KzFS11
  CTE 0.2E(-6), 0.1λ RMS WFE, low sensitivity to thermal shock

Although the maximum focal shift range can be reduced to 247 microns with FK51-KzFS11, it is not the best choice due to the residual aberrations (RMS wavefront errors predicted by ZEMAX). The final FK51-BaK2 design (See Figure 4.10) achieves 271.6 micron chromatic focal shift range as shown in Figure 4.9.

As dicussed in Chapter 2, the tolerancing values for each lens' optical and geometrical parameters such as radius, thickness or spacing, tilt and decenter of each surface, are calculated based upon the inverse sensivity of the radius of collimating diameter, 10.5mm +/- 0.01mm (0.0095 magnification error). The purpose of tolerance analysis is to determine the amount and type of errors that can be introduced into the built optical system and still have the system perform to requirements. The inverse sensitivity analysis predicted that 0.02% of exposed radii, 0.06% of unexposed radii, 0.35% of center thickness are tolerable to achieve 0.0095 magnification error, and the collimators were fabricated to meet these requirements. A custom mount for the collimator was designed and manufactured, and is permanently placed through the rear of the telescope and into the baffle.

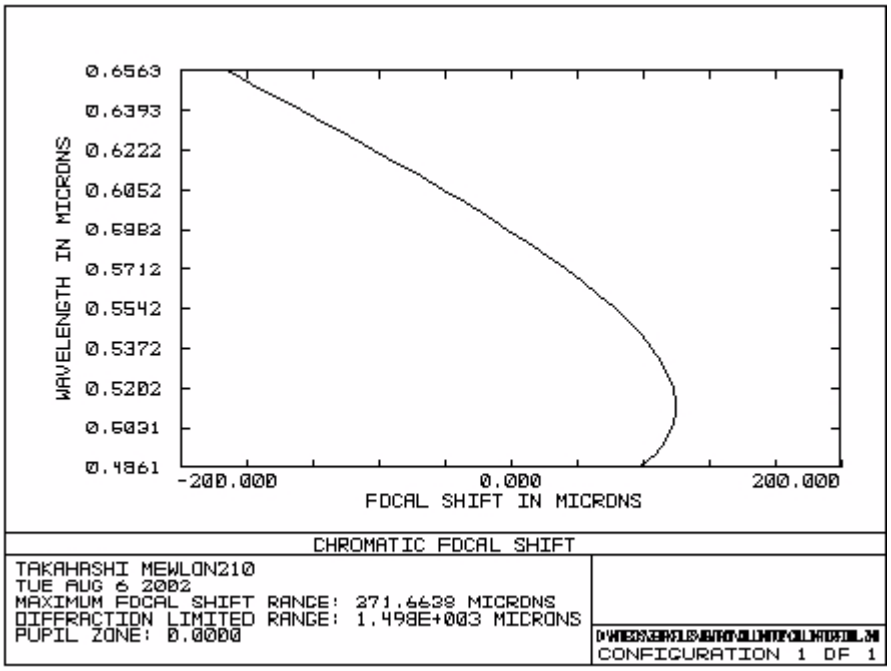

Figure 4.9 Chromatic focal shift of the FK51-BaK2 collimating doublet

The interferograms of the three ARGOS subapertures with the custom collimating doubles installed, are shown in Figure 4.11. From the interferograms we can determine the amount of aberration each sub aperture has by looking at the fringe spacing and linear deviations along a fringe. The distance between fringes represent half waves (λ/2). If there is any optical aberration, we can determine the P-V wavefront errors by reading the linear deviation from the fringes. Figure 4.11 indicates about λ/4.3 Peak-to-Valley (P-V). This corresponds to λ/15 RMS wavefront errors.

4.2 Relay Optics

4.2.1 Optical Delay Line (ODL) Design

An Optical Delay Line (ODL) will be placed in each sub-aperture's optical train to correct for changes in optical path length. Three possible designs for achieving this control are

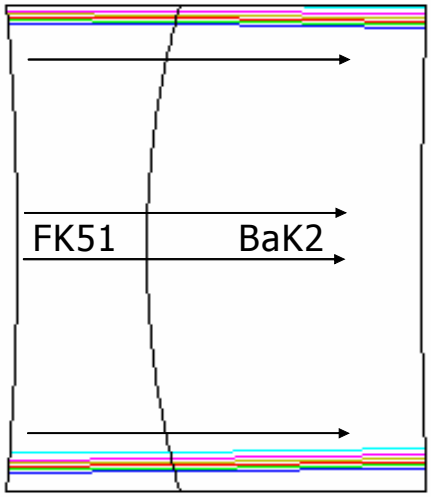

Curvature	Thickness	Glass	Radius
-0.00684092	5.66832270	N-FK51	12.7
0.02126356	12.00000000	N-BAK2	12.7
0.00351668	450.00000000		12.7

Figure 4.10 Final ARGOS collimating doublet. The numbers in mm

Figure 4.11 The real interferograms for the three ARGOS sub-apertures with the collimating lens installed.

identified: Perpendicular Fold Mirrors (FM's), Parallel FM's, and a Carriage (See Figure 4.12).

Option 1 Perpendicular FM's: Two fold mirrors will be placed at 45-degrees so that they are perpendicular to each other. Movement will come form a piezoelectric stack (fine con-

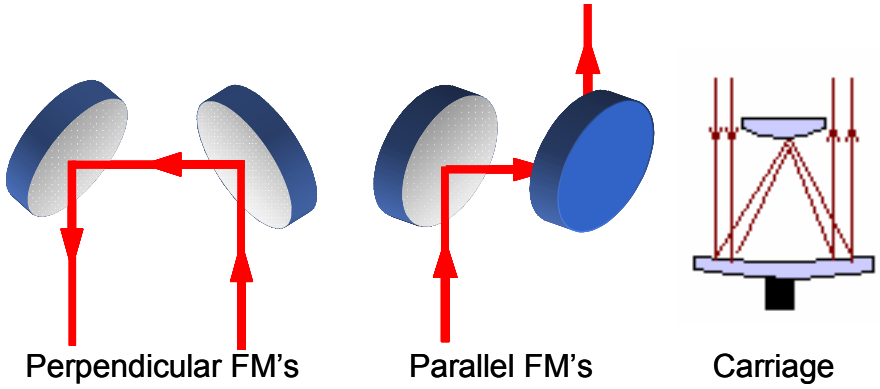

Figure 4.12 ODL designs

trol) and voice coil (coarse control) placed on each mirror so that it is possible to move each fold mirror independently. This independent motion allows the ODL to adjust path length and shear independently (See Figure 4.13).

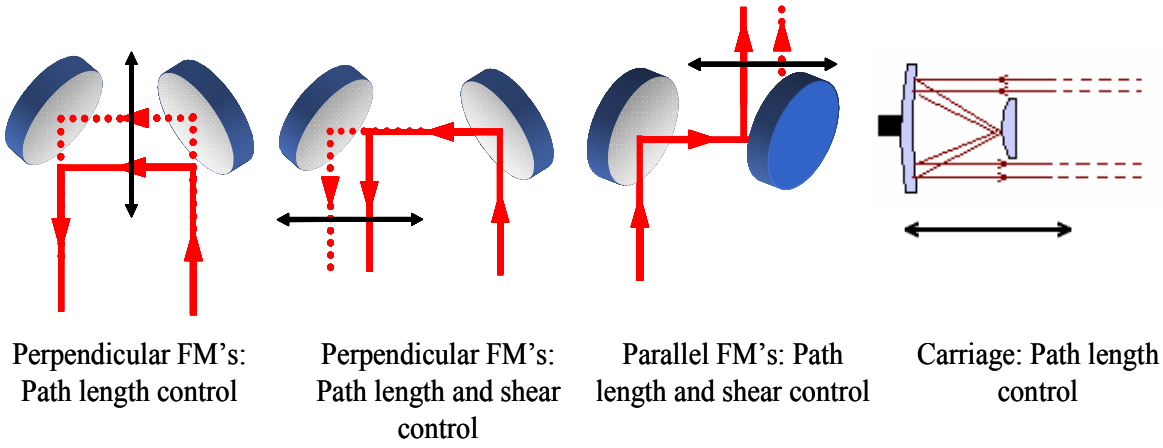

Figure 4.13 ODL control

Option 2 Parallel FM's: Two fold mirrors will be placed at 45-degrees so that they are parallel to each other This option is similar to option 1 in that it makes use of two indepen-

dently controlled fold mirrors. The main difference is that it is not possible to affect path length and shear independently; a change in path length will result in a change is shear.

Option 3 Carriage: A flat mirror will be placed at the focus of a parabolic mirror, and both will be mounted onto a carriage. A voice coil will control the carriage for coarse adjustments in path length. A piezoelectric stack placed behind the flat mirror will be used for fine adjustments.

The parameters used to weigh each of the ODL designs against each other are:

- # Of Reflections: It is very important to minimize the number of reflections in the optical train; a good place to start is the ODL.
- # Of Actuators: This metric reflects how difficult it will be to control a particular ODL design. The more actuators used, the more processing power will be needed to properly control the ODL.
- Size: The size of the ODL should be minimized to allow space for other components.
- Degrees of Freedom: The more degrees of freedom the more useful an ODL will be because it will be able to correct for more errors such as shear and OPD.
- Degrees of independent Control: The metric will show what axis the ODL will be able to control independently.

The number of reflections is critical in order to avoid significant reduction in the optical sensitivity. The sensitivity of a sparse aperture imaging array is expressed in terms of the effective collecting area[Harvey, 1988]:

$$A_{eff} = A_{geometry} R^N \tag{4.5}$$

where N is the number of reflections and R is the mirror reflectance.

This equation is graphically represented in Figure 4.14. The two types of Fizeau interferometry (common secondary type and phased telescope array) may be viable for quasi-monochromatic imaging, however, phased telescope types suffer significant optical sensitivity losses for broadband imaging applications as the number of reflections increases.

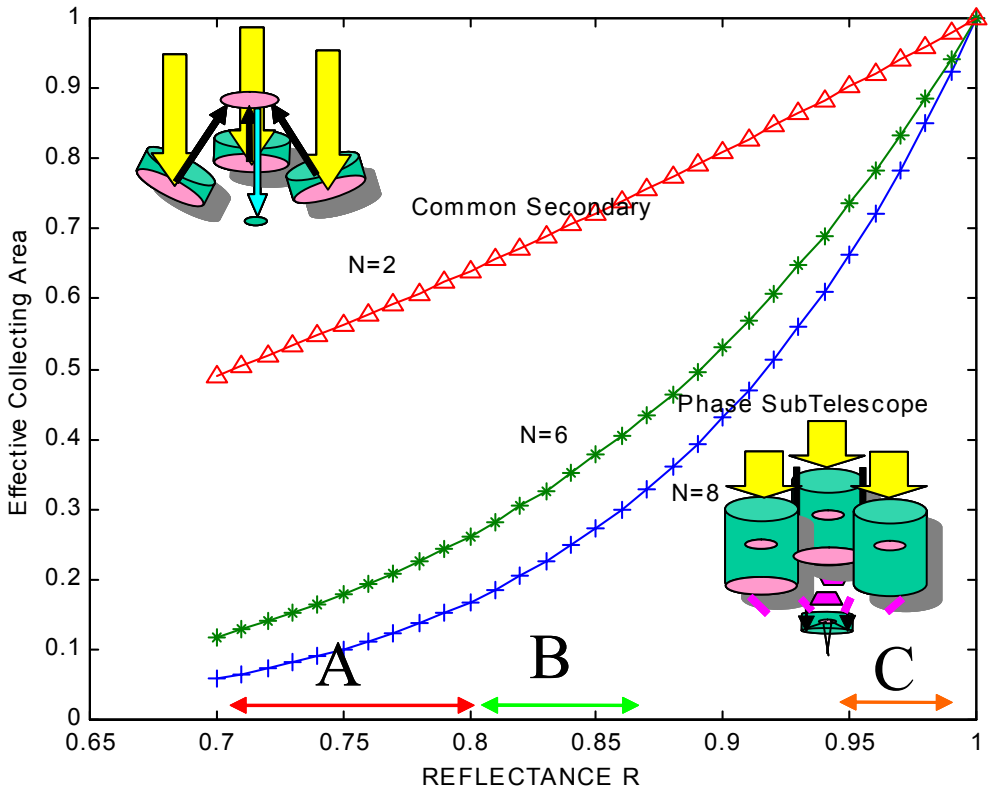

Figure 4.14 Optical sensitivity. A region: UV, B region: visible (color), C region: quasi-monochromatic

The final ARGOS system has four reflections (two for the sub-aperture and two for the FSM/ODL combo and the pyramidal mirror). However, further sensitivity loss is expected in the refractive beam combiner.

ODL Downselect:

Specifications for each ODL are contained in Table 4.4. The downselect table in Table 4.5 contains the actual metrics ranking based on a particular specification. Each of the metrics is weighted based on its importance to the ARGOS project.

TABLE 4.4 Optical Delay Line Specifications

	# Of Reflections	# Of Actuators	Size	Degrees of Freedom	Degrees of independent control
Perpendicular FM's	2	4	Medium	2	2
Parallel FM's	2	4	Medium	2	0
Carriage	3	2	Large	1	1

TABLE 4.5 Optical Delay Line Downselect

	# Of Reflections	**# Of Actuators**	**Size**	**Degrees of Freedom**	**Degrees of Independent control**	**Total (AVG.)**
Weighting	20%	15%	20%	20%	25%	**100%**
Perpendicular FM's	5	2	5	5	5	**4.55**
Parallel FM's	5	2	5	5	1	**3.55**
Carriage	3	4	3	3	3	**3.15**

The Perpendicular and Parallel FM's are similar but differ in the degrees of independent control; parallel placed FM's cannot affect OPD or shear independently. The ODL composed of Perpendicular FM's is the better choice since it is able to affect shear and OPD independently. The ARGOS system employed the parallel FM design since the ODL can be integrated with the FSM as discussed in the following section.

4.2.2 OPD and FSM Coupled Design

When strictly looking at optical delay lines, a perpendicular design seems to offer the most benefits, but further analysis has to be done to see if this design is best for ARGOS. A

FSM will be introduced into the design of the perpendicular and parallel ODL's while the carriage design is going to be thrown out at this point since it received the lowest marks when compared to the other two designs. In order to minimize cost and complexity of the system, the number of actuators is going to be minimized resulting in a slightly different design from above. These designs also take into account the flipping of the image plane.

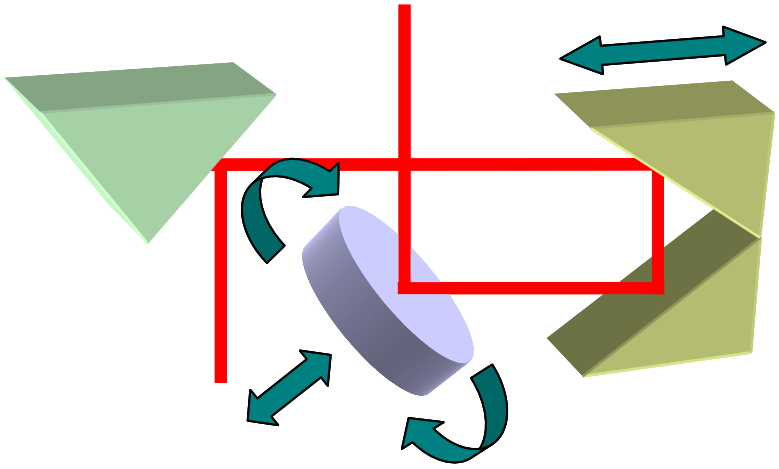

Figure 4.15 Perpendicular ODL deisign coupled with FSM

For the perpendicular design, a multi-axis FSM could be used to generate the required tip/tilt actuations as well as fine optical path difference control (OPD) (See Figure 4.15). FSM's have very fine resolutions so depending on them for fine OPD control will allow us to have a cheaper coarse control for the ODL. Instead of having two 45 deg. mirrors with an actuator attached, it would be possible to still achieve coarse OPD control through only one actuator, a translational stage. A high precision rooftop mirror will replace the two 45 deg. fold mirrors and sit on the translational stage. We can tolerate much more shear error than OPD or tip/tilt error so shear control will be handed off to the center pyramidal mirror that could be controlled manually through micrometer thumbscrews.

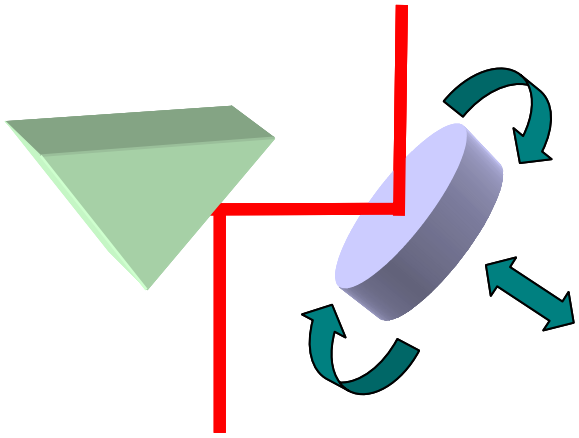

Figure 4.16 Parallel ODL design coupled with FSM

When the parallel ODL design is coupled with a FSM (Figure 4.16), the resulting design is very simple and more cost effective than the previous perpendicular design. This design loses the ability to perform direct coarse OPD control but has other characteristics that are better than the perpendicular design. This design is more compact, which will aid when integrating with the structural design. There is no need for a translational stage or rooftop mirror, which reduces the cost and control complexity, and there is also a greater total reflectance since there are fewer mirrored surfaces for light to bounce off. Fewer mirrored surfaces also reduces the amount of misalignment errors that we will have when mounting them.

In both the perpendicular ODL design and the parallel ODL design, fine OPD control is coupled with shear control so that ΔFine OPD = ΔShear. The effect that a change in fine OPD would have on shear, is not that great and could be ignored for adjustments < 10 microns. This is because we have a much tighter tolerance on piston error (50 nm) than a 12 micron shear error (See Chapter 2). A fine resolution multi-axis FSM (model name: s-315.10) from Physik Instrumente (PI), capable of controlling the tilt/tip as well as piston motion, was selected for the parallel ODL design (see the following section).

4.2.3 Final ODL-FSM design

The selected FSM (see Table 4.8 for its specifications) uses three piezoelectric stacks placed 120 deg. apart to achieve tip/tilt and piston motion. This complicates control for the FSM since these motions are coupled together (See Figure 4.17). The quantities A, B, and C are linear displacements for the corresponding stack.

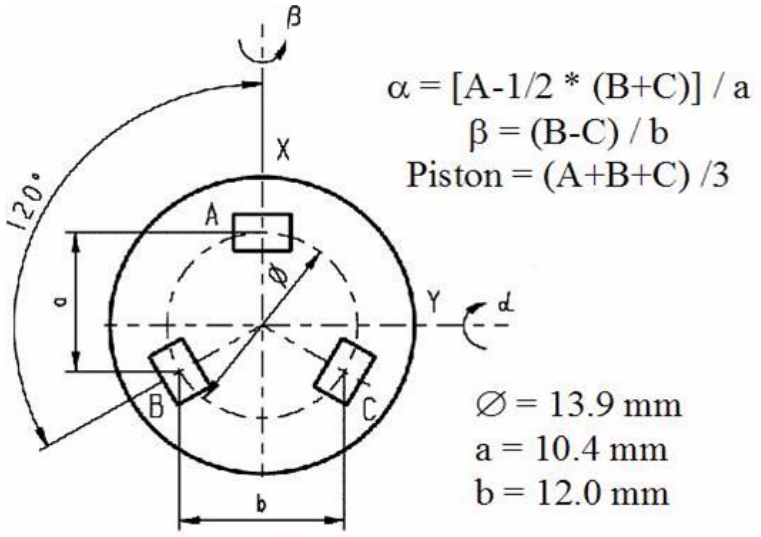

Figure 4.17 FSM control laws from the geometry.

The s-315.10 is the largest multi-axis model that PI offers and it was designed for mirrors up to 25 mm in diameter. This was a problem since we need to use a mirror approximately 35 mm in diameter in order to accommodate the beam size and off axis light (see Table 4.7 for the selected flat mirror specification). Physik Instrumente technicians confirmed that we would be able to use up to a 40mm diameter 10mm thick mirror on the FSM with only a performance decrease in the bandwidth; the resolution of the FSM would be preserved. The bandwidth will now be limited to <100Hz which is higher than the current rate at which we are able to get sensor updates.

Actuator Mounting

The FSM has to be able to compensate for any errors in its mounting. This makes the mount resolution very important. Newport makes high precision mounts that could be used to mount the FSM since they fit into its dynamic range. The advantages of these mounts are the screws it uses. They are high precision 100 threads/inch screws (HPS) and have the ability to be locked in place to minimize disturbances. These screws also have a hex drive which will help when making find adjustments. There is also a stepper motor option that could be installed instead of the HPS to add controllability.

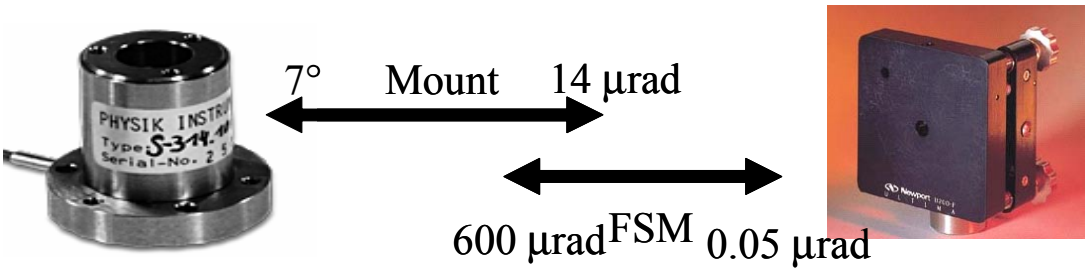

Figure 4.18 FSM and its mount

TABLE 4.6 FSM and FSM mount specifications

Model	Angular Range	Angular Resolution	Linear Range	Linear Resolution
FSM	± 600 µrad	± 0.05 µrad	12 µm	0.2 nm
FSM Mount	± 7 °	± 0.0008 ° (± 14 µrad)	1 cm	1 µm

FSM Amplifier

There were 3 different amplifiers that PI recommended we use to drive the FSM. We chose to go with model E-660.OE. Advantages are that it has the option of being run off

batteries (12V DC), is compact, and is the least expensive. An interface has to be made since it is not a plug and play device. A circuit had to be constructed to place the amplifier in the desired mode. The mode that will be used is the amplifier mode with offset adjustment so that we could create a 50V offset. The purpose of the offset is to have 0V correspond to the center position in the range of the FSM. The circuit used is shown in the figure below.

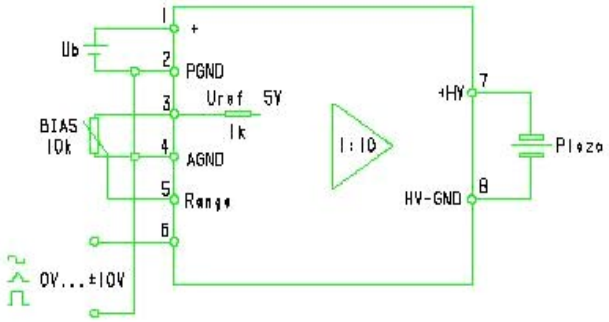

Pin 1 – Operating Input, +12 to +15 VDC
Pin 2 – Operating Voltage GND
Pin 3 – Reference Voltage, +5 V Output
Pin 4 – GND
Pin 5 – Range, 0 to +5 V
Pin 6 – Control Input, 0 to +11 V
Pin 7 – LVPZT Voltage Output, HOT
Pin 8 – LVPZT Voltage Output, GND

Figure 4.19 FSM amplifier circuit

FSM Amplifier Boards

The fast steering mirrors require a 0 to 100 volt input for operation. It is unrealistic for these signals to be sent by the avionics computer. The D/A output of the avionics computer only provides a range from -1 volt to +1 volt. Therefore, this requires an amplifier. Each FSM has its own 10x amplifier, outlined in Figure 4.19 as the large boxes. However, these require an input of -5 to +5 volts to output 0 to 100 volts. Because the signal conditioning is also required with a simple circuit filter, it is used to pre-amplify the signal from the computer by 5x into the amplifiers. This allows for the full range of operation of the FSM with the avionics computer.

Because each FSM requires three signals, three identical boards were manufactured, one for each FSM. Each board has three BNC coaxial connectors for the input of the signals, and three LEMO connectors for the outputs. Each signal goes through a filter that serves

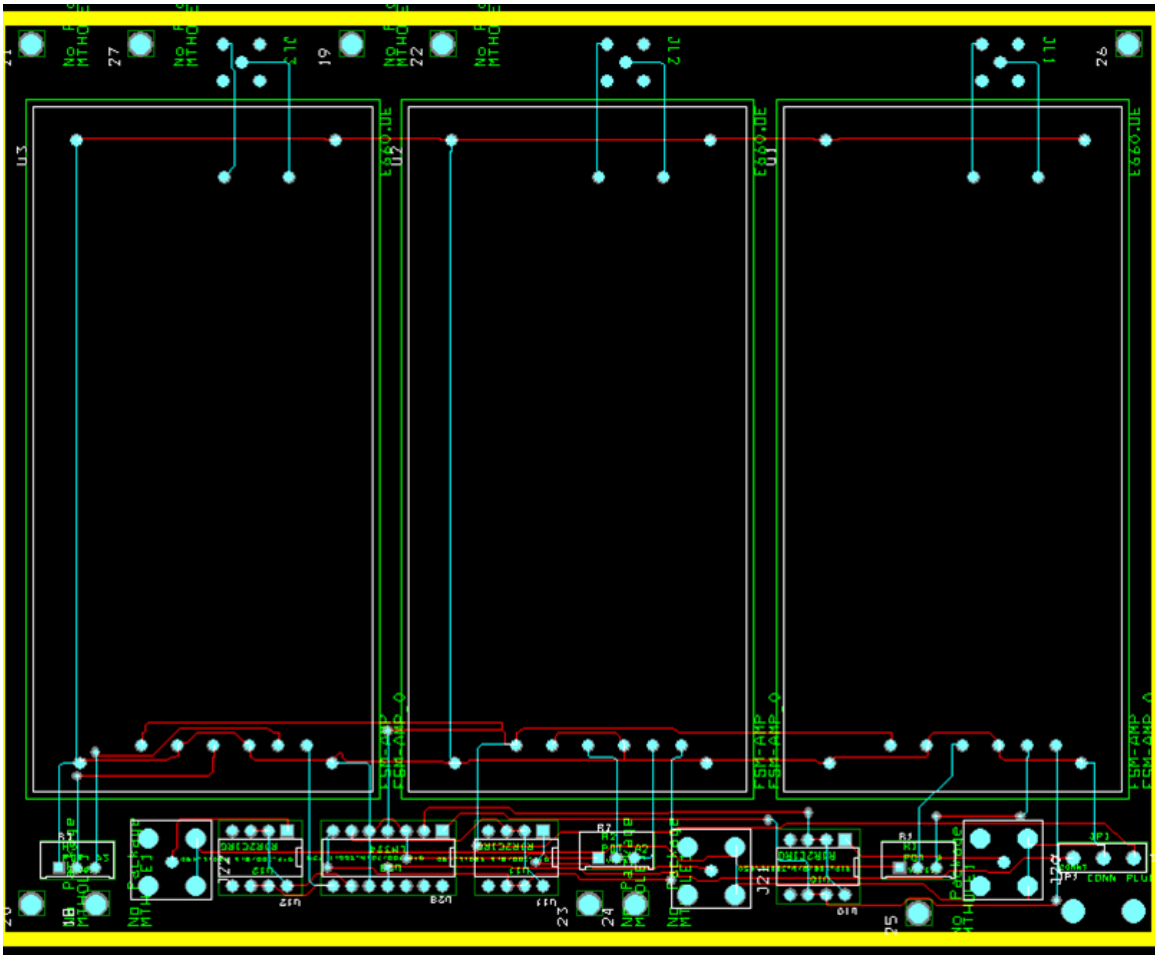

Figure 4.20 Printed circuit board design using Orcad Layout. Three coaxial inputs on the bottom and three LEMO outputs on the top.

as the pre-amplifier. The gain and cut-off frequency of the filter are determined by the two resistors and a capacitor (See the filter section for more information). The filters are characterized by RES 1, RES 2 and CAP 1, which are located on carriers and then are inserted into their sockets. In Figure 4.21, pin one is located on the top right. Pin 1 is along the inside edge of the IC layout. Therefore RES 1 connects pin 1 with pin 8. RES 2 connects pin 2 and pin 7. CAP 1 connects pin 3 and pin 6. Pins 4 and 5 are not connected.

FSM Filter Design

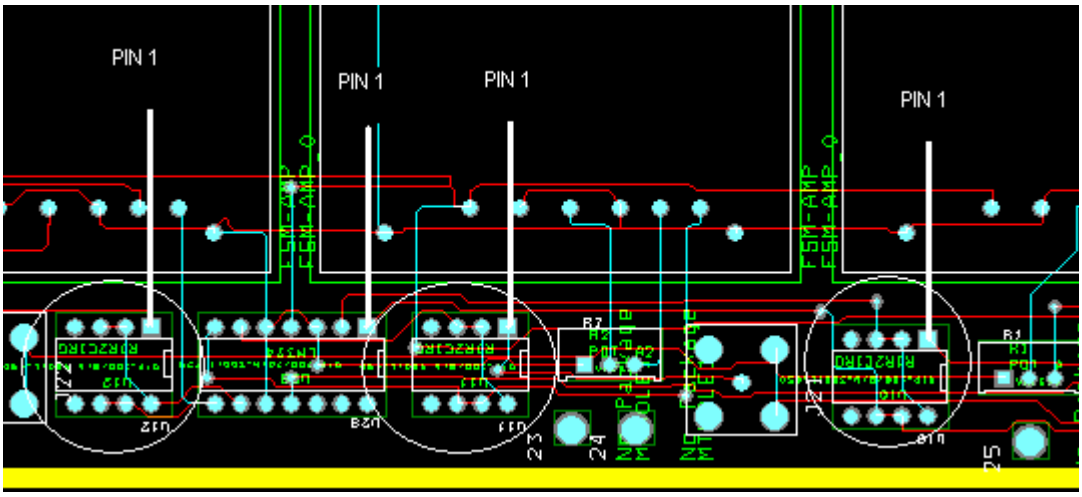

Figure 4.21 Zoom of PCB shows filter locations and orientation.

The input signal to the FSM amplifiers will come from a D to A converter. The converted signal is composed of small steps resembling a staircase. These sharp steps can damage the FSM. A smoothing filter is needed to smooth the steps in the signal. In addition, this filter must amplify the signal to fit the input range of the FSM amplifiers. With the offset of 50V set on the amplifiers, the input range will be -5V to 5V. The D to A converter supplies a signal ranging from -1V to 1V, so a filter with a gain of 5 is required. The cutoff frequency of the filter will be set lower than the resonant frequency of the FSM and flat mirror combo for added security. The specifications for the flat mirror used on the FSM's are included in Table 4.7.

TABLE 4.7 Flat mirror specifications

Manufacturer	Diameter	Thickness	Surface Flatness	Substrate	Coating
Melles Griot	38mm	10mm	λ/10 PV	LEBG	Enhanced Al

The resonant frequency of the FSM and flat mirror combo can then be calculated with the following equations:

$$f_R = \frac{f_0}{\sqrt{\left(1+\frac{I_M}{I_0}\right)}} \tag{4.6}$$

$$I_M = m\left[\left(\frac{3R^2+H^2}{12}\right)+\left(\frac{H}{2}+T\right)^2\right] \tag{4.7}$$

In the above equations m = 25.29 g (mass of mirror), R = 19 mm (radius of mirror), H = 10 mm (thickness of mirror), T = 5 mm (pivot point to platform), I_0 = 150 gmm^2 (moment of inertia of the FSM platform), f_0 = 5.5 kHz (resonance frequency of the FSM platform). The resonant frequency can then be calculated to be f_R = 936.6 Hz.

The diagram and transfer function of the filter circuit used is below.

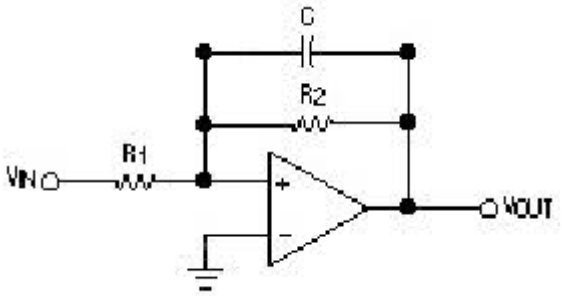

$$G(s) = \frac{-\frac{R_2}{R_1}}{CR_2 s + 1}$$

Figure 4.22 Filter transfer function

The values of R_1 = 2000Ω, R_2 = 10000Ω, and C = 0.33μF were chosen to create the required gain of 5 and a cutoff frequency of f_{cutoff} = 303.03 Hz. This cutoff frequency was chosen since it is well below the resonant frequency of the FSM and flat mirror combo.

4.2.4 Pyramidal Mirror

The pyramidal mirror bends all three beams 45 deg. into the beam combiner. A custom-built pyramidal mirror is chosen due to the cost of making one out of regular mirrors. The main reason for the high cost is that we would need to purchase special thin mirrors that cost $1000+ a piece, and then mount them to an accuracy of +/- 0.001° (+/- 3.6 arcsec). The pyramid cannot be made from mirrors of regular thickness since they constrain the beam diameter.

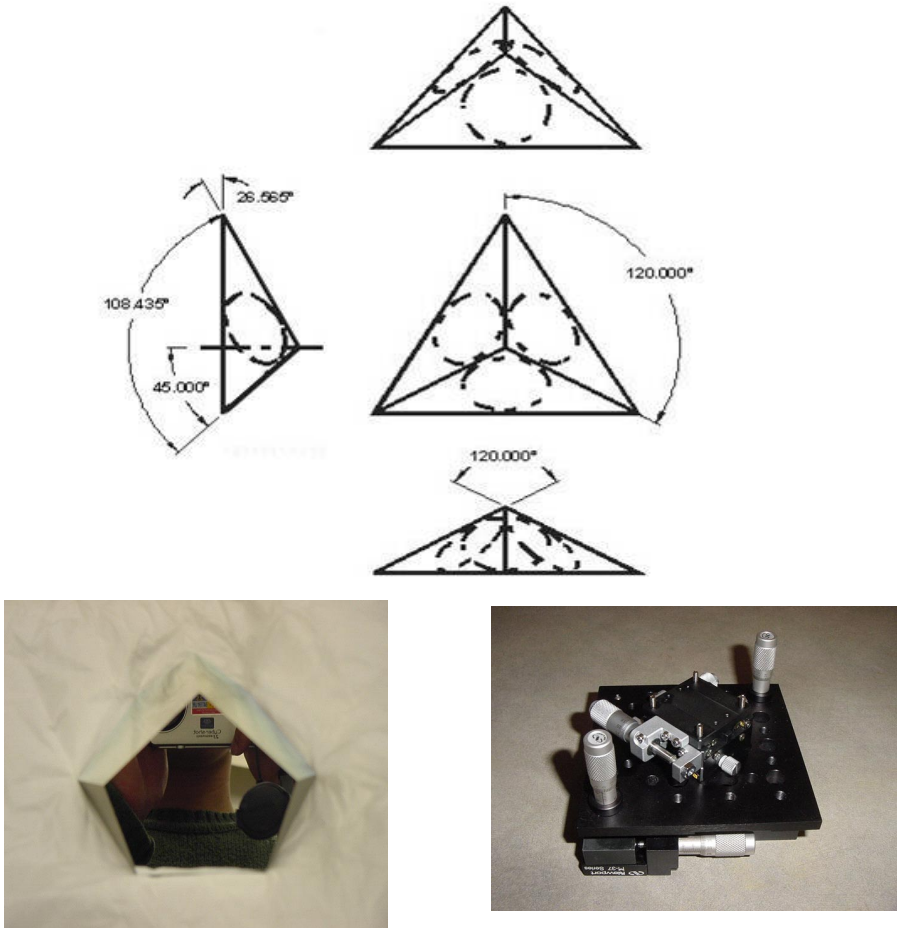

Figure 4.23 Pyramidal mirror and its mount combo

We customized a pyramidal mirror with a surface accuracy of l/10 peak to valley, +/- 3 arcsec angle error, and 50mm clear aperture (see Figure 4.23). The substrate material is BK7 with a coating of AlSiO (aluminum with silicon monoxide). The reflectance will be approximately 90% in the visible range. The two point spread functions shown in Figure 4.24 demonstrate how the FSM can compensate for the +/- 3 arcsec errors in the pyramid. In order to compensate for pyramid errors the FSM has to align itself so that the two reflecting surfaces are parallel.

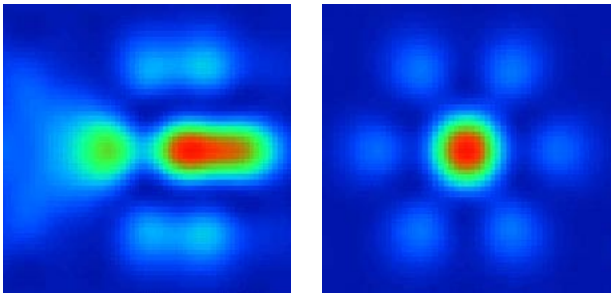

Figure 4.24 The PSF simulation of the ARGOS with 3 arcsec tilt error of the pyramidal mirror (SR=0.444, Left). The PSF with FSM correction (SR=0.960, Right)

Pyramidal Mirror Mounts

TABLE 4.8 Pyramidal mount combo specifications

	Angular Range	Angular Resolution	Linear Range	Linear Resolution
Mount Combo	± 4 °	± 2 arcsec (± 9.6 µrad)	13 mm	3 µm

The pyramidal mount is composed of two stages, one providing all of the angular adjustments and the X-Y translation (see Figure 4.23). The X-Y translation stage is small enough to fit behind the tip/tilt rotation stage and offers the load capacity to hold both the second stage and the mirror. We need to be able to adjust the Z-motion of the pyramidal mirror. A single piston stage could give us this extra degree of freedom, but we do not have the room to add another stage. It would still be possible to adjust the Z-motion

through the screws that connect the two stages to the structure or between the stages themselves. Given that we could turn the screw in 5 to 10 degree increments, it would be possible to achieve a resolution finer than the maximum shear error.

4.3 Beam Combiner

Two options available for the beam combiner are either reflecting or refracting optics. The reflecting beam combiner is compact when compared to a refractor. Unfortunately, the secondary mirror of a Cassegrain telescope would partially block the three incoming beams in any possible configurations in order to obey the golden rule discussed in Chapter 2 as depicted in Figure 4.25. A single parabolic mirror was considered, however the pyramidal mirror would block the focusing beam. Had we used reflecting optics, since nothing is available as COTS, they would have to be custom manufactured. This would have increased the cost significantly. A reflector would also complicate the relay optics significantly since we would not be able to use the pyramidal mirror.

Figure 4.25 Two-mirror (Cassegrain) type beam combiner. The secondary mirror of the beam combining telescope partially blocks the incoming beams.

In contrast, the refracting telescope has many advantages. It allows for very simple relay optics. It is available COTS with high quality optics and is therefore relatively cheap. The FSQ-106N from Takahashi has been purchased (see Figure 4.26). This telescope has significantly less chromatic aberration than other COTS telescopes. This is due to its four element design, two of which are calcium fluoride (CaF2). It has a diameter of 106 mm, and a 530 mm focal length, resulting in a total system focal length of 5300 mm.

Figure 4.26 The refractive beam combiner of the ARGOS testbed

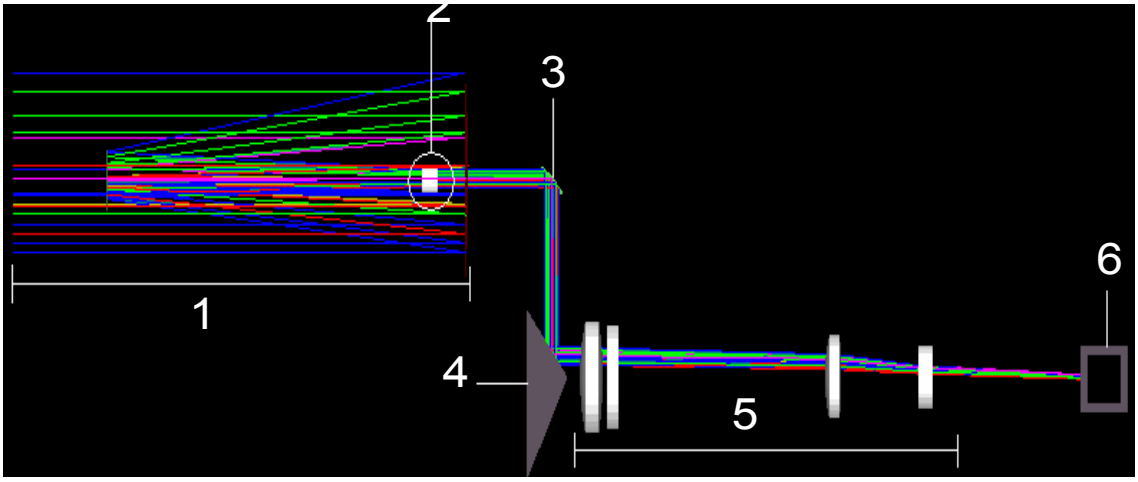

Figure 4.27 The final layout of the ARGOS optical train (only one aperture shown) 1-subaperture, 2- collimating lens, 3-FSM/ODL actuator, 4-pyramidal mirror, 5-beam combiner, 6-CCD

The final optical layout is graphically simulated using Zemax as shown in Figure 4.27.

4.4 Structural Misalignment Tolerancing

As discussed in Section 2.4.4 on page 69, we can assign the RMS wavefront error into each contributing element in the WFE budget tree according to the optics design in the previous sections. The remaining RMS WFE from the requirement can be allocated into the structural misalignment errors or the environmental error. In this section, calculation methods of optics structural misalignment are explained in detail.

4.4.1 Tolerancing Based on OPD Change

The corrective motion of FSMs to compensate tip/tilt errors induces an unwanted optical path-length change. When we control the FSM, we want to compensate the OPD by moving the FSM to Z (piston) direction as well as correcting tip/tilt errors. In order to predict the effects of structural misalignments on the overall OPD change, an OPD tolerancing analysis was performed simulating a variety of misalignment errors in each relay optics component (See Figure 4.28 for definition of the axes).

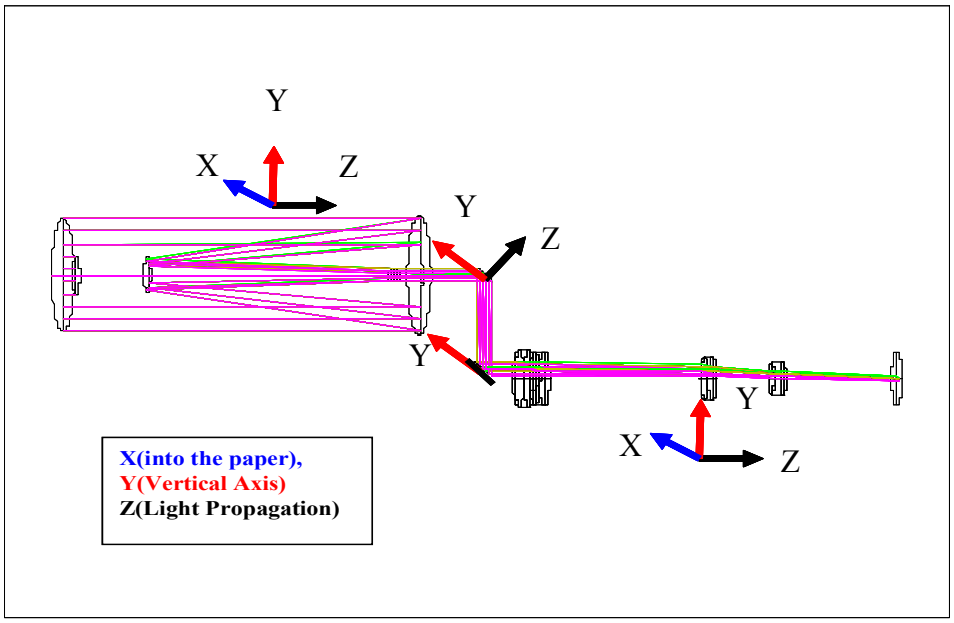

Figure 4.28 OPD tolerancing of a single arm relay optics

The simulated result of this OPD sensitivity analysis is presented in Appendix B. Figure 4.29 shows the seven worst offending errors in this OPD sensitivity analysis. We can see that the overall OPD change is more sensitive to the x-axis tilt and y-axis tilt error of a sub-telescope than the tilt errors of the FSM or the pyramidal mirror (the second Fold Mirror). This implies that it is more important to minimize the structural vibrations of each individual aperture to reduce unwanted OPD aberrations. In general, x-axis tilt induces more OPD errors than y-axis tilt.

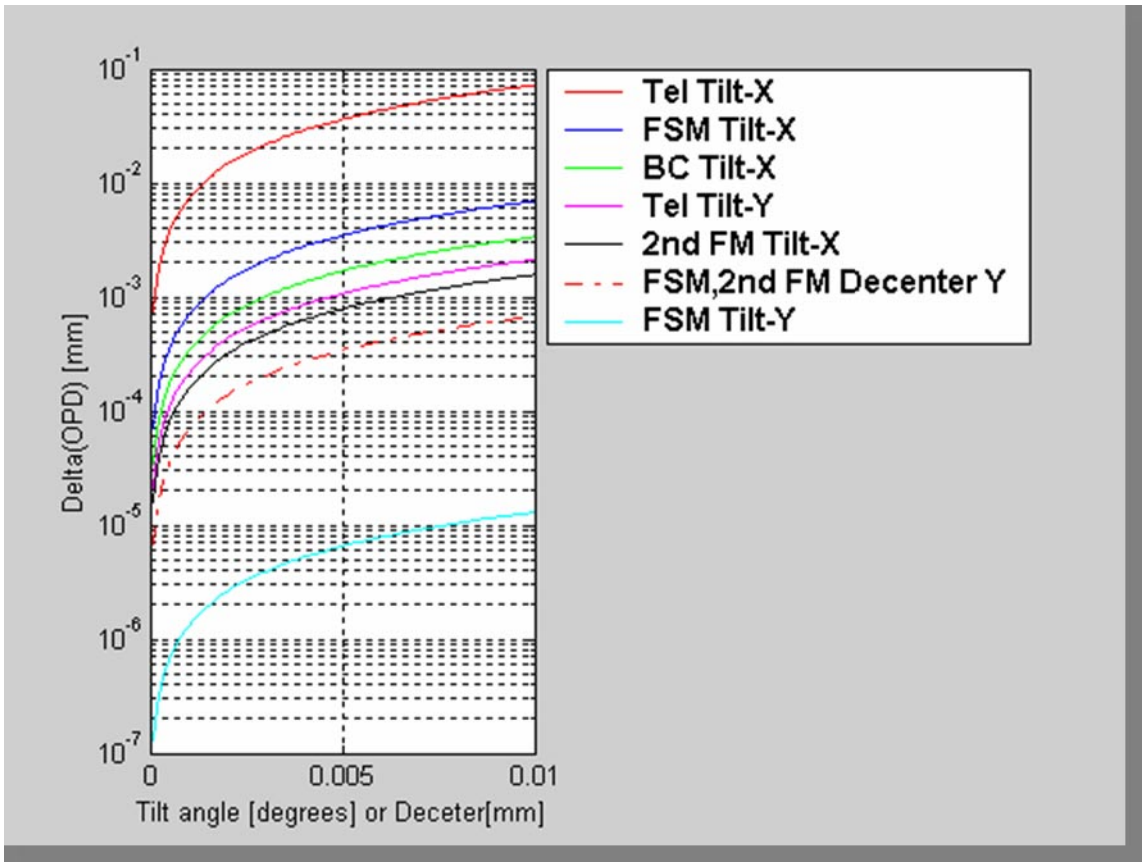

Figure 4.29 OPD Sensitivity analysis of each optics component

4.4.2 Tolerancing Using NSC Ray-Tracing

Using non-sequential component (NSC) ray tracing in ZEMAX, a complete ARGOS optics layout is constructed based on the optical specifications of a subaperture, pyramidal mirror, and the beam combining telescope as shown in Figure 4.2 on page 122. We intentionally perturb the sub-telescope or pyramidal mirror to determine allowable structural misalignments, and we compensate the tilt error by changing the tilt angle of the fold mirror attached to the FSM.

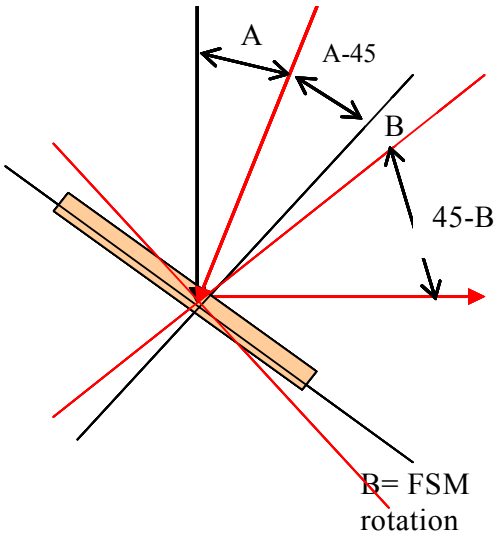

Figure 4.30 Rotation of FSM

In Figure 4.30, angle A is a tilt misalignment of a sub-telescope, angle B is a FSM compensation for that error.

$$45\text{-}A+B = 45\text{-}B \tag{4.8}$$

$$2B=A \tag{4.9}$$

We need to compensate half of the tilt angle of a sub-telescope. However, there is a collimator with a magnification of 10. Thus, any tilt aberration of a sub-telescope is transmitted to a relay optical line as multiplied by 10.

We can conclude:

$$B= 0.5 *A *10 = 5 A \tag{4.10}$$

In reality, FSM compensation of a factor of 5 works well up to 0.0005 degrees of tilt error. Due to off-axis beams, which are larger than 21mm on-axis collimated beam, it was numerically found that a factor of 6.4 works very well up to 0.01 degree level. Table 4.9 lists variations of Strehl Ratio under different sub-aperture tilt angles.

TABLE 4.9 Sub-aperture tip/tilt tolerancing

Telescope Tilt [Deg]	[arcsec]	FSM Comp [Deg] Max	FSM OPD [mm]	Strehl Ratio Aberrated	SR restored
0.0001	0.36	0.034 degree -0.00064	0	0.687	0.982
0.001	3.6	-0.0064	0	0.016	0.979
0.005	18	-0.032	0	0.192	0.907
0.01	36	-0.064	0	0.064	0.604
0.01	36	-0.064	0.0002	0.189	0.859

At 0.01 degrees of tilt of a subaperture, a pure FSM motion cannot restore the SR (Strehl Ratio) above 0.8. But the addition of FSM piston motion can restore the SR value to 0.859. We could achieve a SR of 0.859 (which is above diffraction limited) over 0.01 degrees tilt (See Figure 4.31). But due to a magnification factor of 10, the FSM compensa-

tion exceeded its max range (0.6 mrad=0.034 degree). Since we mounted a FSM onto a precision tip-tilt mount which is capable of several arc-seconds of adjustment (Table 4.6), this static error does not limit the FSM performance. However, it is much safer to have a FSM within a range of eliminating a possible maximum alignment error. 0.005 degrees or 15 arcsec for sub-telescope structural misalignment is suggested.

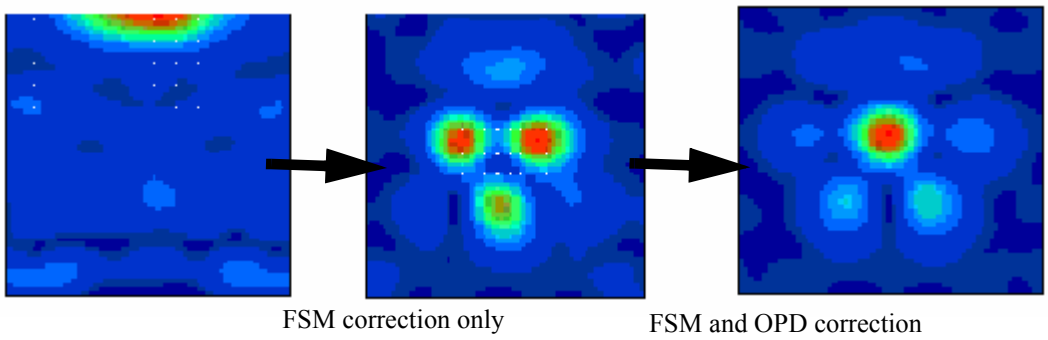

Figure 4.31 0.01 degree tilt error of a sub-aperture (SR=0.064), left, FSM compensation (SR=0.604), middle, OPD correction as well as FSM (SR=0.859), right

By assuming that all other optical components are perfectly aligned and the FSM can compensate all the residual tilt errors, the tilt errors for each surface of the pyramidal mirror are calculated. When the tilt error of the pyramidal mirror unit equals the tilt compensation of a FSM, the aberration loss due to the tilt is completely eliminated. Therefore there is no theoretical tilt tolerance for pyramidal mirror as long as it does not exceed the maximum compensation range (0.01 degrees).

The beam combiner was tilted along its x and y axes while leaving other optical components perfectly aligned (Figure 4.32). This beam combiner misalignment is not correctable by optical actuators like FSMs. However, it turns out that we can tolerate up to 0.2 degrees of tilt error for the beam combiner, which is less stringent than other misalignment tolerances.

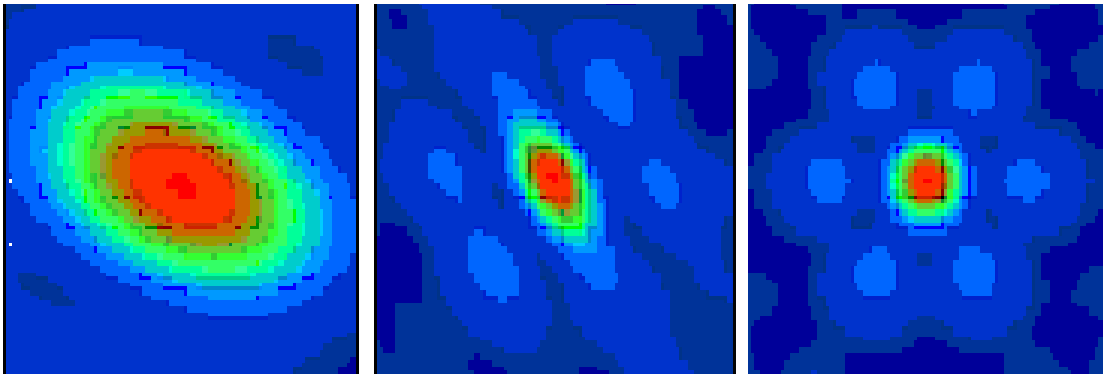

Figure 4.32 The PSF plots when the beam combiner has tilt errors. From left to right, (1) X tilt: 0.2, Y tilt: 0.4 , (2) X: 0.3 Y: 0.3, (3) X: 0.25 Y: 0.25 [degrees]

4.5 CCD System

The optics performance requirements associated with a CCD camera are Signal-to-Noise Ratio (SNR) and Field-Of-View (FOV). It was pointed out that the pupil mapping process is the primary limiting factor deciding the reasonable FOV of a sparse aperture interferometric array (See Section 2.4.3 on page 59). This means that the pupil mapping tolerances become expensive as we increase the FOV. In addition, the off-axis imaging abberations such as distortion and field curvature become dominant as we increase the FOV. Therefore, the CCD system of a sparse aperture imaging system should be carefully designed to meet the optics performance requirements while maintaining the reasonable FOV large enough to capture the science targets. The methods of designing a CCD system are introduced in this section based on the FOV and SNR requirements.

4.5.1 CCD Metrics

The following specifications of a CCD system should be considered to achieve an optimum CCD design.

Quantum Efficiency (QE). QE of a CCD sensor describes its response to different wavelengths of light (See Figure 4.33). Standard front-illuminated sensors, for example, are more sensitive to green, red, and infrared wavelengths (in the 500 to 800 nm range)

than they are to blue wavelengths (400 - 500 nm). Back-illuminated CCDs have exceptional quantum efficiency compared to front-illuminated CCDs.

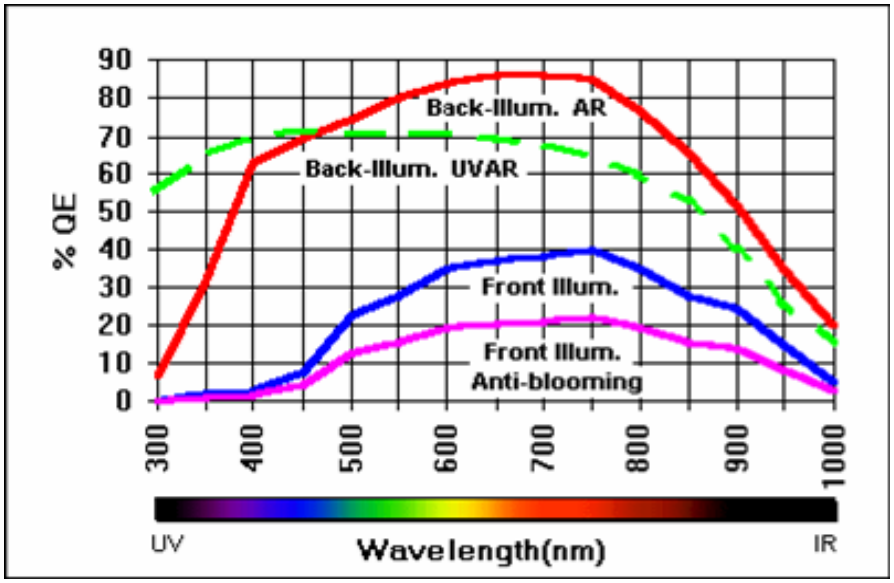

Figure 4.33 Quantum efficiency of CCD systems to different illumination methods. Source: http://www.ccd.com (CCD University)

Anti-Blooming. Anti-blooming helps protect against the objectionable streaks that occur when bright objects saturate the CCD, causing excess charge to bleed down a column of pixels. This feature can, however, produce side effects like increased dark current and reduced sensitivity.

Digitization Parameters. Digitization, also referred to as analog to digital conversion, is the process by which charge from the CCD is translated into a binary form used by the computer. For applications requiring higher speed and less dynamic range (i.e. video), 8- to 12-bit digitization is common. The higher the digital resolution, the slower the frame rate. Well depth, readout noise, and system gain are factors in determining the appropriate digitization.

Frame Rate. The frame rate of a CCD is significantly important to an interferometric array system especially when CCD cameras are employed as the feedback sensor system. For example, ARGOS employs one wide FOV CCD as an intermediary sensor for its attitude control system. The science CCD output is also used to control the FSMs using spot-based wavefront sensing. The bandwidth of the control loop is then limited by the frame rate of a CCD. The frame rate can be calculate by:

$$Frame\_rate = \frac{Data\_rate}{n^2} \tag{4.11}$$

where n is the single-axis pixel format (n=512 for a 512x512 CCD).

The data rate is usually a function of digitization. For example, a high resolution CCD of 14 bit digitization has a data transfer rate of 1.3 MHz. For a 1024x1024 CCD, this results in 1.24 frames/sec. A faster CCD of 8 bit digitization has a 50 MHz data rate, resulting in 47.6 frames/sec.

Sensitivity Parameters. In order to find a proper balance between undersampled images (too few pixels for a target, greater sensitivity, worse resolution) and oversampled images (too many pixels, reduced sensitivity, greater resolution), the CCD system is appropriately designed to match the system focal length. The number of pixels, the pixel size and the noise characteristics are important for this purpose. This will be discussed in detail in the following sections.

4.5.2 CCD Design From FOV Requirement

An optimal CCD size (both the pixel size and the format) depends on the imaging targets and the system effective focal length. Deep-sky imaging requires a sensitive (small pixel size), low-noise camera whereas small arrays with larger pixel size are more suitable for more rapidly changing targets such as planets and satellites.

The required pixel size is determined by the following equation:

$$d = 2.44 \frac{\lambda}{D_{eff}} fQ \tag{4.12}$$

D_{eff} is the effective diameter of the array, f is the system effective focal length and Q is a quality factor. Nyquist sampling criterion tells us that two pixels are generally required to properly record a star's image (3-3.5 arcsec). This corresponds to Q=0.5 with 1.5-2 arcsec per pixel.

The angular resolution per pixel is then calculated from Equation 4.12:

$$\frac{d}{f} = 2.44 \frac{\lambda}{D_{eff}} Q \tag{4.13}$$

A small pixel size as well as a long focal length are required for a fine angular resolution system. The system FOV is calculated by multiplying the angular resolution per pixel with the number of pixels:

$$FOV = \frac{d}{f} n = 2.44 \frac{\lambda}{D_{eff}} Qn \tag{4.14}$$

where n is the number of pixels along the x-axis or y-axis of a CCD matrix.

The ARGOS testbed is designed and built in such a way that it has an ability to track the International Space Station (ISS) (See Figure 4.34). The orbit height of the ISS is around 390km (26 June 2001, Boston), and the approximate length is 52m. The FOV of the ISS is calculated to be 0.4584 arcmin (52m/390km). The ARGOS with coherent phased beam combining, can achieve a 0.35 arcsec angular resolution at the 550nm wavelength. Therefore, the number of pixels needed to picture ISS is 79x79 from Equation 4.14 .

A CCD employing the IEEE-1394 technology is selected as the main science CCD of ARGOS. This CCD can produce 10 bit resolution images at 30 frames per second. The effective focal length of ARGOS from a sub-aperture through the beam combiner is

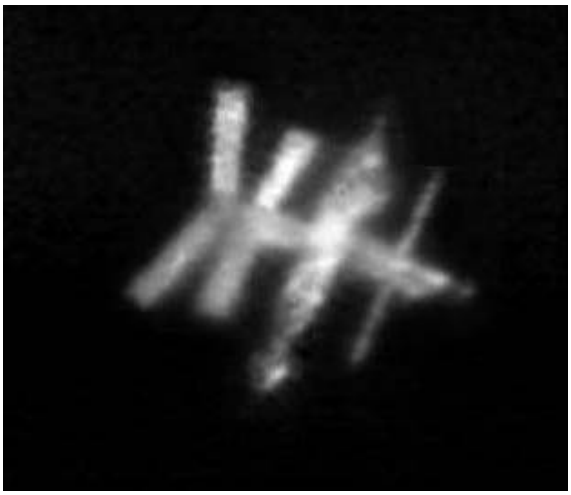

Figure 4.34 ISS image taken by a 12" Schmidt-Cassegrain Telescope at f/30. ARGOS has an effective diameter =0.4 meter so our goal is to achieve a better resolution than this image

5300mm. With a pixel size of 7.4 microns and 640x480 format, the total FOV of ARGOS is 3 arcmin x 2.3 arcmin. In the near future, it is planned to upgrade to a higher frame rate CCD to increase the control-loop bandwidth in the near future.

4.5.3 CCD Design From SNR Requirement

A sparse aperture can cause a substantial depression in the modulation transfer function (MTF) of the system, resulting in a low-contrast and fuzzy raw image. This can be compensated by image reconstruction, such as by using a Wiener-Helstron filter, but at the expense of greater noise sensitivity than for a monolithic aperture [Fienup, 2000]. SNR calculations of sparse aperture imaging systems have previously been done by Fienup and Roddier [Roddier, 1999].

Images acquired by modern CCD cameras may be contaminated by a variety of noise sources. Noise refers to stochastic variations, as opposed to deterministic distortions such as shading or lack of focus. Six noise sources are introduced in this section: photon noise, read-out noise, dark current, KTC noise, amplifier noise, and quantization noise.

Photon Noise

When the physical signal detected by a CCD is based on light, the quantum nature of light plays a significant role. Photon noise is derived by calculating the number of photons received through an imaging system, and is therefore not independent of light source. All matter at any temperature above absolute zero (0 K), emits electromagnectic radiation, commonly called blackbody radiation. The spectral energy distribution of a blackbody is given by Planck's Law[Wertz, 1999]:

$$E(\lambda) = \frac{2\pi hc^2}{\lambda^5} \frac{1}{e^{ch/kT\lambda} - 1} \tag{4.15}$$

where E(λ) is the energy per unit wavelength (also called the spectral irradiance measured in $Wm^{-2}\mu m^{-1}$), λ is the wavelength, h is Planck's constant ($6.6260755 \times 10^{-34}$ Ws^2), T is the absolute temperature of a target, c is the speed of light and k is Boltzmann's constant (1.380658×10^{-23} Ws/K).

The blackbody spectral radiance is calculated by:

$$L(\lambda) = \frac{E(\lambda)}{4\pi} \tag{4.16}$$

The units of L(λ) are typically $Wm^{-2}\mu m^{-1}$/sr, where sr is steradians.

Sometimes, the imaging targets involve reflected radiation from a surface illuminated by the Sun. For example, the thermal emitted radiance of the Earth increases with wavelength, and the reflected radiance from the Earth's surface decreases with wavelength. In this case, the blackbody spectral radiance holds in the long wavelength infrared region (8-14μm), but reflected radiation should be considered for shorter wavelengths (e.g. visible). L(λ) of such a target can be approximated by the astronomical magnitude scale:

$$m_2 - m_1 = 2.5\log(\frac{b_1}{b_2}) \tag{4.17}$$

where m is the astronomical magnitude scale and b is the corresponding spectral radiance. The astronomical magnitudes for various astronomical objects are listed in Table 4.10.

TABLE 4.10 Magnitudes of various targets at brightest

Object	The Sun	The Moon	Venus	Jupiter	Sirius	ISS	Polaris
m	-27	-12.7	-4.6	-2.9	-1.6	-2	2.12

The input power at the entrance to a sparse aperture array is calculated by:

$$P_{in} = \int_{\lambda_1}^{\lambda_2} L(\lambda)d\lambda\left(\frac{\pi D^2}{4}\right)\theta_r{}^2 N = \int_{\lambda_1}^{\lambda_2} E(\lambda)d\lambda\left(\frac{D}{4}\right)^2\left(\frac{1.22\lambda}{D_{eff}}\right)^2 N \tag{4.18}$$

where the integration term integrates E(λ) from Equation 4.15 over the operating wavelengths. N is the number of sub-apertures, D is the diameter of a sub-aperture, and D_{eff} is the effective diameter of a sparse aperture array.

Using Equation 4.18, the number of available photons can be determined as follows:

$$N_p = P_{in}\tau_0 T_i \frac{\lambda}{hc} \tag{4.19}$$

where T_i is the integration time, τ_0 is the optical transmission factor (typically 0.75), c is the speed of light, and h is the Planck constant defined in Equation 4.15.

The number of signal electrons is computed by multiplying N_p with the CCD quantum efficiency:

$$N_{signal} = P_{in}\left(\tau_0 \frac{\lambda}{hc}\mathrm{QE}\right)T_i = \int_{\lambda_1}^{\lambda_2} E(\lambda)d\lambda\left[N\frac{D^2}{D_{eff}{}^2}\right]\left(\frac{1.22\lambda}{4}\right)^2\left(\tau_0 \frac{\lambda}{hc}\mathrm{QE}\right)T_i \qquad (4.20)$$

where QE is the quantum efficiency of a CCD (See Figure 4.33 on page 158). The term inside the square brackets, $N(D^2/D_{eff}^2)$, is commonly called the ***filling factor*** of an interferometric array.

The probability distribution for the average number of photons received by a CCD is known to be Poisson[Brown, 1997]. The standard deviation of the Poisson distribution is the square root of the average value. Accordingly, the total number of photon noise electrons is:

$$N_{PN} = \sqrt{N_{signal}} = \sqrt{\int_{\lambda_1}^{\lambda_2} E(\lambda)d\lambda\left[N\frac{D^2}{D_{eff}{}^2}\right]\left(\frac{1.22\lambda}{4}\right)^2\left(\tau_0 \frac{\lambda}{hc}\mathrm{QE}\right)T_i} \qquad (4.21)$$

Dark Current

Another stochastic source of electrons in a CCD well is thermal energy. Electrons can be released from the CCD material itself through thermal vibration and then, trapped in the CCD well, be indistinguishable from true signal electrons. By cooling the CCD chip it is possible to efficiently reduce the number of thermal electrons that produce thermal noise or dark current. As the integration time increases, the number of thermal electrons increases:

$$N_{DC} = R_{DC}T_i \qquad (4.22)$$

Where R_{DC} is the dark current rate and T_i is the integration time.

Read-Out Noise

Read-out noise (On-chip electronic noise) originates in the process of reading the signal from the sensor through the field effect transistor (FET) of a CCD chip. CCD manufactur-

ers usually specify the number of read-out noise electrons. This noise can become a significant component in the overall SNR at very low signal levels.

KTC Noise

Noise associated with the gate capacitor of an FET is termed KTC noise and can be non-negligible. This noise is independent of the integration time. KTC noise can be almost completely eliminated by proper electronic design that makes use of correlated double sampling and dual-slope integration.

Amplifier Noise

In modern well-designed electronics, amplifier noise is generally negligible. The color CCD produces more amplifier noise for blue wavelengths than for green or red since more amplification is used in the blue color.

Quantization Noise

Quantization noise is inherent in the amplitude quantization process and occurs in the analog-to-digital (A/D) converter. This noise is usually negligible.

SNR Calculation of a Sparse Aperture

Finally, we can calculate the SNR of a sparse aperture array based on the noise characteristics of a CCD system discussed above. In general, photon noise, dark current noise and read-out noise are considered as dominant noise contributors.

$$SNR = \frac{N_{signal}}{\sqrt{N_{PN}^{\ 2} + N_{DC}^{\ 2} + N_{R}^{\ 2}}} \tag{4.23}$$

where N_{signal} is the number of signal electrons in Equation 4.20, N_{PN} is the number of photon noise electrons in Equation 4.21, N_{DC} is the number dark current noise electrons in Equation 4.22, and N_R is the number of read-out noise electrons specified by a manufacturer.

The SNR can be defined again expanding all the equations for noise electrons:

$$SNR = \frac{\int_{\lambda_1}^{\lambda_2} E(\lambda) d\lambda \left[N \frac{D^2}{D_{eff}{}^2} \right] \left(\frac{1.22\lambda}{4} \right)^2 \left(\tau_0 \frac{\lambda}{hc} \mathrm{QE} \right) T_i}{\sqrt{\int_{\lambda_1}^{\lambda_2} E(\lambda) d\lambda \left(N \frac{D^2}{D_{eff}{}^2} \right) \left(\frac{1.22\lambda}{4} \right)^2 \left(\tau_0 \frac{\lambda}{hc} \mathrm{QE} \right) T_i + \left[R_{DC} T_i \right]^2 + N_R{}^2}} \tag{4.24}$$

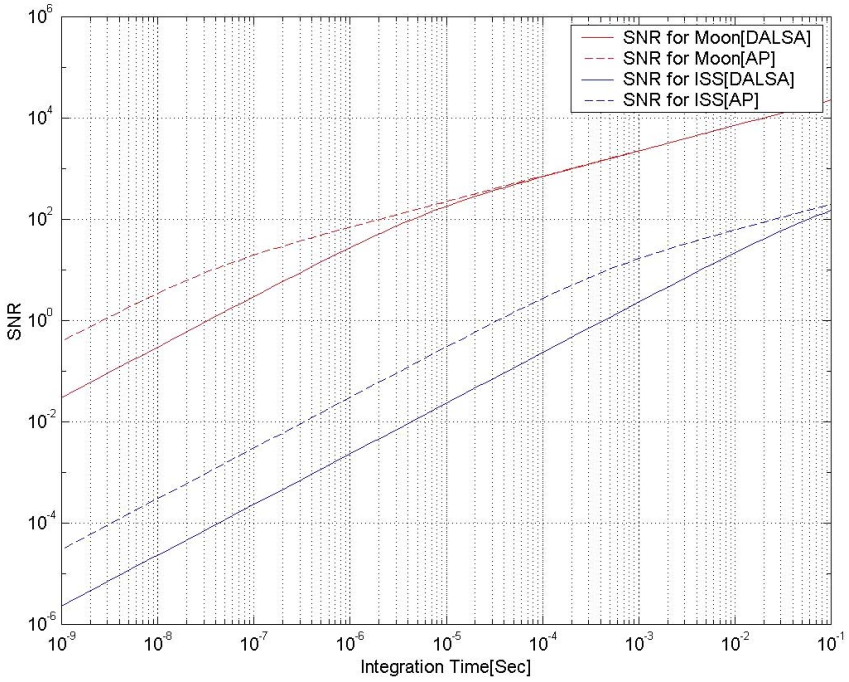

Figure 4.35 SNR plots for two different CCDs: DALSA (low sensitivity with faster frame rate) and AP (high sensitivity with slower frame rate)

The SNR calculations using Equation 4.24 are plotted in Figure 4.35 for two different targets (the ISS and the Moon) also using two different CCDs (one CCD with low sensitivity with faster frame rate, and the other CCD with high sensitivity with slower frame rate).

Equation 4.17 was used to estimate the spectral radiance of the ISS and the Moon since they are reflective objects rather than self-emitting blackbodies at visible wavelengths. The red (upper) lines represent the Moon as the target, and the blue (lower) lines represent the ISS as the target. As seen on the graph, the Moon does not require much integration time due to its brightness. The ISS requires more integration time because it is not as bright. Figure 4.35 predicts that the SNR requirement of 100 may not be achievable for ISS imaging since it needs a lot of integration time, up to 0.1 sec for a rapidly orbiting target.

4.6 Chapter Summary

This chapter elaborates on Steps 4 through 7 of the SOCS framework. The current optical layout of the system is as follows. Light shines in through the sub-aperture. The light continues through the telescope with a 210mm diameter until it hits the collimator which is inside the telescopes' baffle. The light then goes through the collimating lens producing a 21mm diameter beam. The light exits and hits a reflecting mirror mounted onto a three axis FSM that acts as an ODL as well. The light is then reflected to the stationary pyramidal mirror. The light beam then enters the beam combiner, and is focused onto the CCD.The overall cost of the ARGOS optics system could be significantly reduced by selecting one of the highest precision optics commercially off-the-shelf (COTS) telescope. However, it is necessary to customize a collimating lens to convert a Dall-Kirkham-type focal telescope to an afocal telescope with a magnification ratio of 10. The collimating lens is placed into the baffle of the telescope to make the system compact. When the parallel ODL design is coupled with a FSM, the resulting design is very simple and more cost-effective than the perpendicular design. This design cannot perform coarse OPD control, but this design is more compact resulting in easier integration with the structural design. In addition, there is no need for a translational stage or rooftop mirror which reduces the cost and control complexity, and there is also a greater total reflectance since there are fewer mirrored surfaces. Fewer mirrored surfaces also lead to fewer structural mis-alignment errors. The pyramidal mirror turns all three beams 45 deg. into the beam combiner. A cus-

tom pyramidal mirror is chosen due to the cost of making one out of regular mirrors. Two options available for the beam combiner are either reflecting or refracting optics. The reflecting beam combiner is compact when compared to a refractor. Unfortunately, the secondary mirror of a Cassegrain telescope would partially block the three incoming beams in any possible configurations in order to obey the golden rule. The refracting telescope has many advantages. It allows for very simple relay optics. It is available COTS with high quality optics and is therefore relatively inexpensive.

Using the non-sequential ray tracing mode of ZEMAX, a complete ARGOS optics layout is constructed based on the optical specifications of a subaperture, pyramidal mirror, and the beam combining telescope. We intentionally perturb the sub-telescope or pyramidal mirror to determine allowable structural misalignments, and we compensate the tilt error by changing the tilt angle of the fold mirror attached to the FSM. 0.005 degrees or 15 arcsec for sub-telescope structural misalignment is suggested. It is determined that there is no theoretical tilt tolerance for the pyramidal mirror as long as it does not exceed the maximum compensation range (0.01 degrees). The beam combiner was tilted along x and y axes while leaving other optical components perfectly aligned. This beam combiner misalignment is not correctable by optical actuators like FSMs. However, it turns out that we can tolerate up to 0.2 degrees error for the beam combiner; this is less stringent than other misalignment tolerances. The methods of designing a CCD system are introduced in this chapter based on the FOV and SNR requirements.

Chapter 5

WAVEFRONT SENSING AND CONTROL

Previous assessments show that the beam combining problem is the most challenging aspect of sparse aperture arrays. The need for optical control is paramount due to the tight beam combining tolerances. Development of fine wavefront sensors to detect beam combining errors plays a significant role. Extensive studies on this topic were performed for development of the Next Generation Space Telescope (NGST) [Redding, 1998;Lyon, 1999]. This chapter presents a preliminary analysis on the nature of optics sensing and control.

5.1 Wavefront Sensing

A wavefront sensor is an instrument used to measure the optical imaging aberrations that were discussed in Section 4.1.1 on page 123. The Zernike polynomials are often used to represent the wavefront errors of an optical system. In the case of a segmented mirror telescope, the adaptive optics system makes use of the output of a wavefront error sensor in order to eliminate the aberrations due to the atmospheric turbulence or misalignment of each segmented mirror. For a sparse aperture imaging system, measurements of piston errors and tip/tilt errors are sufficient to actuate the optics actuators such as Optical Delay Lines (ODLs) and Fast Steering Mirrors (FSMs). In the presence of the shear errors, the locations of misaligned beams can be adjusted by measuring the X and Y positions on a CCD.

There are two methods of wavefront sensing: direct measurement and indirect measurement. The first is to measure directly the optical path difference (OPD) of an aberrated wavefront in the exit pupil to extract the information on various wavefront errors. There are two ways of a direct wavefront error measurement: radial shear interferometry and point diffraction interferometry [Geary, 1995].

The radial shear interferometer (RSI) is a modified Mach-Zehnder interferometer with two afocal telescopes (one beam expander and the other beam compressor). A wavefront is interfered with expander version of itself. An RSI is employed for the Hubble Space Telescope residing in each Fine Guidance Sensor. The point diffraction interferometer (PDI) is a compact self-referencing interferometer. An object beam is focused onto a pinhole in a neutral density filter. The pinhole diffracts the central portion of the beam, forming a reference beam that travels collinearly with the attenuated object beam.

Instead of measuring the OPD directly, the differential phase between adjacent sampling points in the pupil, and the transverse ray aberrations are measured to estimate the real OPD errors and wavefront errors indirectly. Two most important indirect wavefront sensing techniques are discussed in this chapter: Shack-Hartmann techniques and Phase Diversity techniques. These two sensing methods are fundamentally different and they are competing for a main NGST wavefront error (WFE) sensor.

5.1.1 Shack-Hartmann vs. Phase Diversity

A Shack-Hartmann wavefront sensor is shown in Figure 5.1. The incoming wavefront is broken into an array of spatial samples, called subapertures of the primary aperture, by a two dimensional array of lenslets. The subaperture sampled by each lenslet is brought to a focus at a known distance F behind each array. The lateral position of the focal spot depends on the local tilt of the incoming wavefront; a measurement of all the subaperture spot positions is therefore a measure of the gradient of the incoming wavefront. A two-dimensional integration process called reconstruction can then be employed to estimate the shape of the original wavefront. The incoming wavefront sample is analyzed into spa-

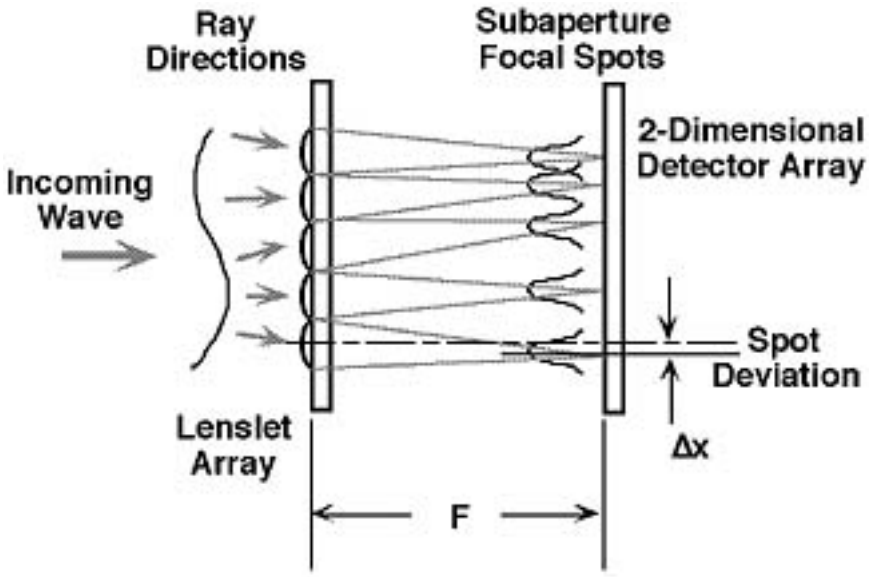

Figure 5.1 Shack-Hartmann sensor of Adaptive Optics Associates (AOA), Cambridge, MA.

tial subapertures by a miniature lens array which creates a pattern of spots on a two-dimensional array [AOA, 2002].

Phase Diversity (PD) is an advanced imaging technique for restoring fine-resolution detail when imaging in the presence of phase aberrations. The incident beam is split into two channels by a beam-splitter: one is focused at the conventional focal plane, the other is intentionally defocussed a known amount and detected by the second CCD (See Figure 5.2). This image pair is used together to estimate both the aberrations and the fine-resolution object common to both images [Paxman, 2000]. One of the advantages of PD is that it can be used to reconstruct an image as well as to estimate wavefront aberrations. Due to the simplicity of Phase Diversity, this wavefront sensing technique can be a candidate for the ARGOS optics system.

One drawback is that the PD method is very computation intensive. There is no way currently to match a frame rate up to 100 frames per second while real-time PD processing of

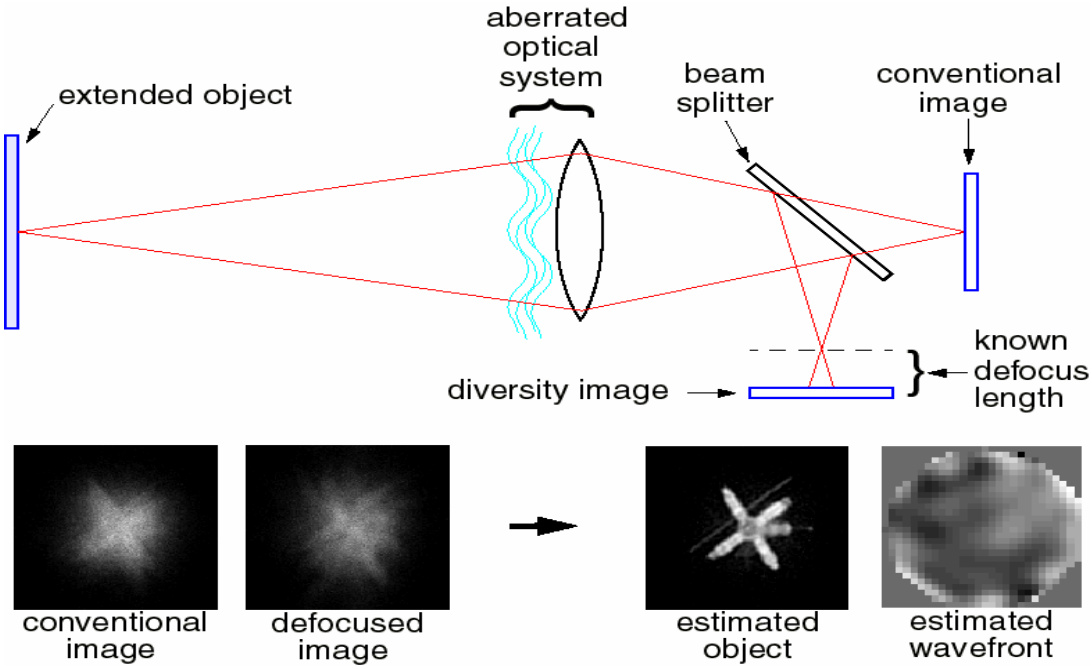

Figure 5.2 Phase Diversity concept [Paxman, 2000]

each frame. A General Regression Neural Network (GRNN) can be used to speed up the calculation of the wavefront errors [Kendrick, 1994].

The capture range of Phase Diversity technique is quite limited. PD is usually regarded as a monochromatic method that will not tell any difference if the piston errors are off by N times 2π. Such errors will however degrade the performance if the telescope operates in broad-band light or at different wavelengths. Accordingly, another complementary wave-front sensor is required.

5.2 Coarse Optics Control of ARGOS

5.2.1 Method of Increasing Image Sampling Rate

The sampling rate of 10 Hz of the previous ARGOS Image processing software using MATLAB was the main cause of the difficulty in centroiding control. The advantages of MATLAB such as powerful image processing and mathematical functions easily implemented are offset by the slow frame rates due to the unnecessary computation time to convert data types for MATLAB. Therefore, a real-time image processing software with a complete C++ language without the use of MATLAB C++ compiler was developed.

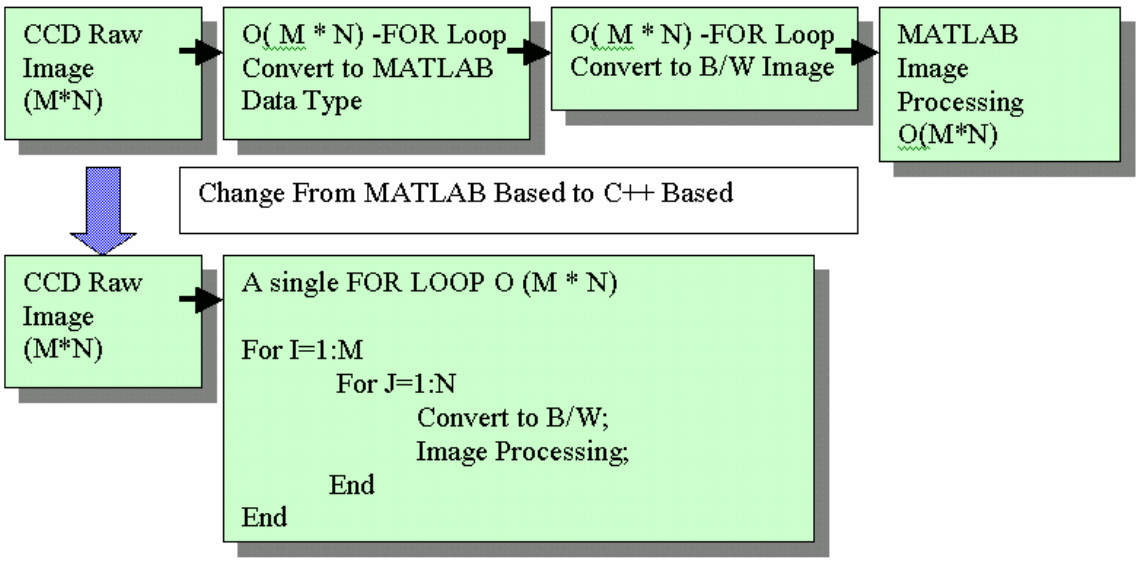

Figure 5.3 Imaging processing loops

As depicted in Figure 5.3, the previous code had two separate for-loops with m*n computation complexity to transfer an image to MATLAB and also to convert an grey-level image to a binary (black and white) image. Additional image processing afterward may have additional complexity, O(M*N) or O(M*N*M*N).

The key difference in the new ARGOS Image processing software is the integration of all the necessary computation in one single for-loop, thus minimizing the computation power. Instead of having separate image processing call functions, the image properties such as centroid, area and locations of edge pixels are calculated while an original gray level image is being converted into a binary image. Currently, the ARGOS image processing software is capable of calculating the image properties at 25-30 frames per second (a raw frame rate of the ARGOS CCDs is 30 frames per second).

5.2.2 Elliptical Spot Based Sensing

Spot-based wavefront sensing is a simple coarse adjustment technique to control the optical actuators until the brightest spot is achieve when a bright, isolated calibration star is being imaged. Elliptical spot based sensing is suggested in this thesis to properly identify the optics actuators without a need to identify each spot using masks.

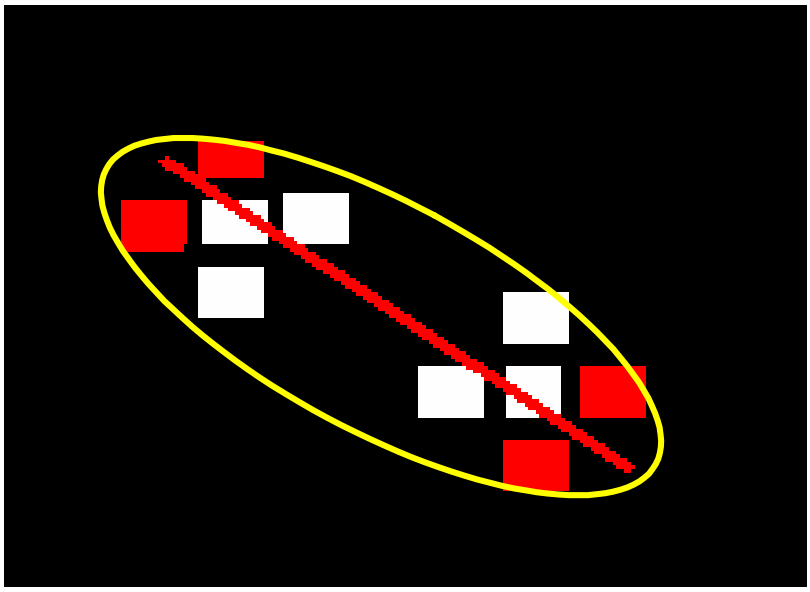

Figure 5.4 Elliptical spot based sensing

The code for controlling the FSM takes as inputs multiple elliptical properties of an image. Their names and definitions are as follows:

argos.centroid – the mass center of all light captured on the CCD
argos.MinXX – the X (column) value of the point with the minimum X value
argos.MinXY – the Y (row) value of the point with the minimum X value
argos.MinYX – the X value of the point with the minimum Y value
argos.MinYY – the Y value of the point with the minimum Y value
argos.MaxXX – the X value of the point with the maximum X value
argos.MaxXY – the Y value of the point with the maximum X value
argos.MaxYX – the X value of the point with the maximum Y value
argos.MaxYY – the Y value of the point with the maximum Y value

After manipulation varying depending on whether the image-processing program is in one-aperture, two-aperture, or three-aperture mode, the code outputs a set of errors of each point from the centroid value.

Two Aperture Mode

In double-aperture mode, the main objective is to move the two points to the mass centroid of the two points as outputted by the CCD. The code utilizes the min and max x and y values to move each point to the centroid. First, the orientation of the two points is found and defined as -1 for negative slope and +1 for positive slope. In the case of orientation = -1, the MinX and MinY values are paired, as well as the MaxX and MaxY, and a coordinate defining each point is derived as the average x and y values of the paired points. For orientation = +1, The MinX and Max Y are paired, as are the MaxX and MinY, and a coordinate defining each point is derived as the average x and y values of the paired points (See Figure 5.5).

When actuating the FSMs, there is a problem in determining which FSM is actuating which point on the CCD, so a control algorithm was derived to determine whether the FSMs were moving in the right direction. The points either move directly toward or directly away from the centroid, and we will find the area of the circle circumscribing the two points and determine whether this value is increasing or decreasing. If the value of the circle is increasing, we flip the signs of the output to the FSMs and maintain the current

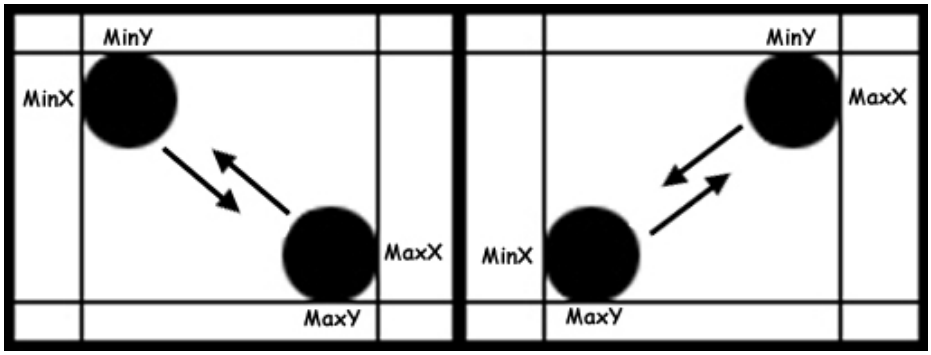

Figure 5.5 MinX, MinY, MaxX, and MaxY values drawn as tangent and moved toward CCD's centroid

movement if the area is decreasing. In order to compensate for momentary jittering, a 10% cushion is placed on the increase of the area of the circle (See Figure 5.6).

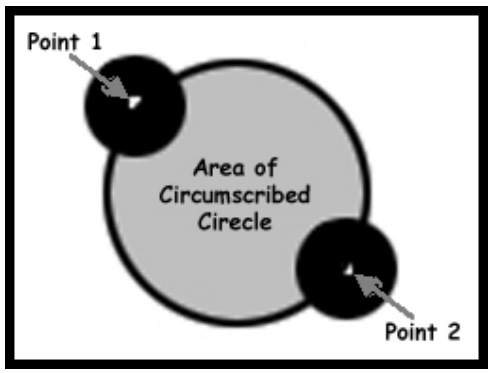

Figure 5.6 Code finds area of circumscribed circle to determine direction of actuation

Three Apertures

Several algorithms have been inspected and one has been chosen as an initial attempt. The degree of complexity of the three-aperture control is much greater if an algorithm similar to the double-aperture control is implemented. The alternate idea is to separate the movement of each FSM into X and Y directions, actuating only in one direction at a time.

Instead of moving each point to a centroid, each point would first be moved to the same column, and then the same row. Since the trouble of determining which point belongs to which FSM still exists, an algorithm independent of the assignments must be implemented. After each actuation of an FSM, the MinX value will be checked. If the value does not change, then another FSM is actuated. If the value decreases, the same FSM is moved, but in the opposite direction. If the value increases, the FSM continues to be actuated in the same direction.

The same procedure is repeated until three cycles go by and there is not change in the MinX value. The whole algorithm is then implemented in the same way for the Y actuation, as shown below. Each FSM is now actuated such that the MinY value decreases until the MinY value no longer changes.

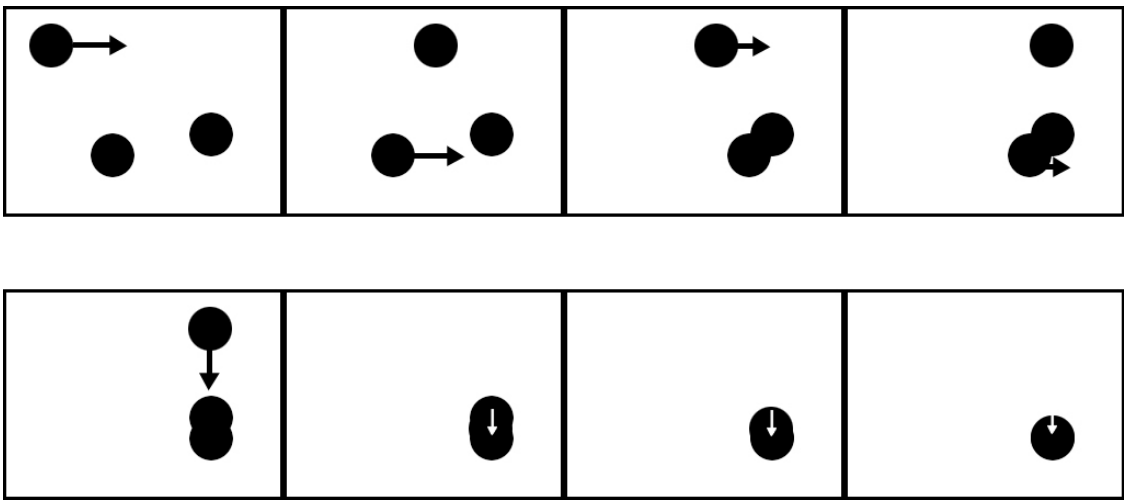

Figure 5.7 : Each FSM is actuated until the MinX value is no longer changed by any FSM (first row), Once the points are vertically aligned, the FSM actuate vertically until one point is achieved (second row).

5.2.3 Controller Design

The elliptical spot-based sensing algorithms were implemented firstly into the dSpace real-time controller employing Matlab-Simulink control blocks as shown in Figure 5.8.

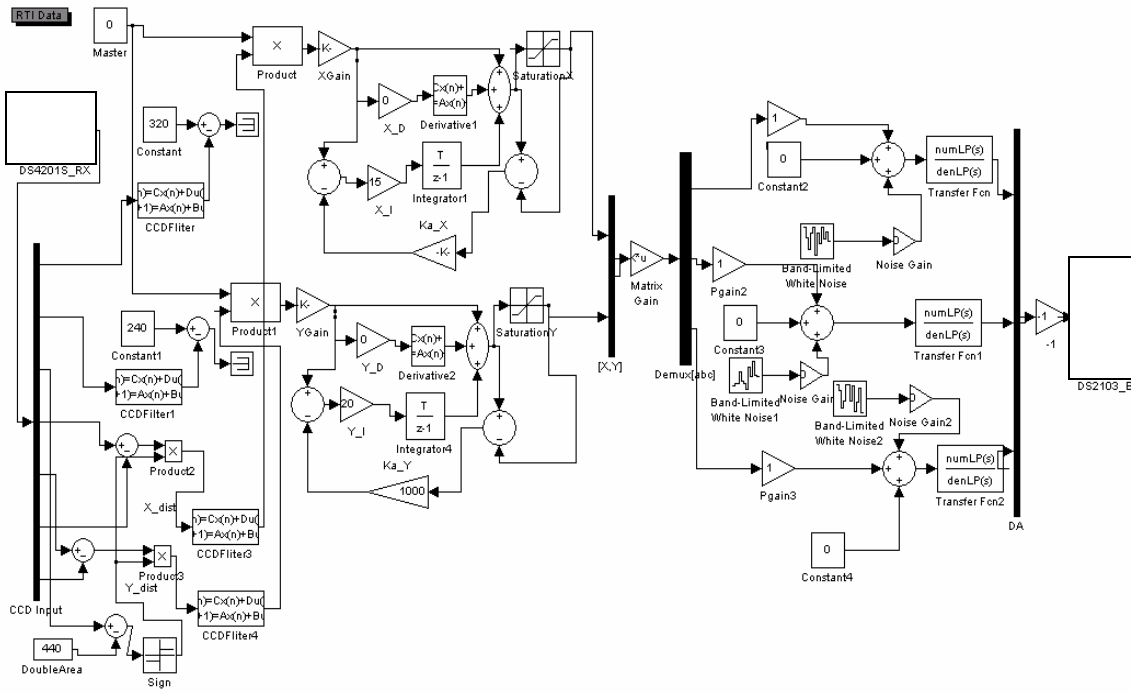

Figure 5.8 Simulink diagram of two-aperture FSM controller

The PID controller is used to actuate each FSM, and the elliptical spot-based sensing determines the desired reference input the controller. Since the dynamic range of the FSMs is limited, there is a possibility that a FSM is saturated. Whenever control saturation happens, we have to stop integrating with the integral control law. Otherwise, the integrator will keep integrating resulting in substantial overshoot or unexpected behaviors of the actuators. Integrator antiwindup with a single nonlinearity is implemented to reduce both the overshoot and the control effort by turning off the integral action as soon as the actuator saturates. It is observed that the frame rate of the CCD system limits the bandwidth of the closed loop. Accordingly, a higher frame-rate CCD is needed to increase the bandwidth of the closed optics control loop.

5.3 Chapter Summary

The direct and indirect wavefront sensing techniques are introduced in this chapter. Phase-diversity techniques is very simple, but computationally expensive. The neural network can be employed to increase the computation speed. Spot-based wavefront sensing is a simple coarse adjustment technique to control the optical actuators until the brightest spot is achieve when a bright, isolated calibration star is being imaged. Elliptical spot based sensing is suggested in this thesis to properly identify the optics actuators without a need to identify each spot using masks. Prior to implementing a fine wavefront sensor, the elliptical spot-based sensing algorithms were implemented for coarse adjustments.

Chapter 6

COST ANALYSIS ON SPARSE APERTURE ARRAY

One of the objectives of this thesis is to apply a cost-effective system engineering approach into building a sparse aperture interferometric array satellite. To this end, the Sparse-aperture Optics and Control System (SOCS) design framework was introduced in Chapter 2, and prior chapters are delineating each step in the SOCS framework. Once we are successful in identifying and deciding design parameters associated with performance and cost, complete life-cycle cost analysis is performed to recommend the most cost-effective design for similar future missions. In this chapter, cost modeling of a sparse interferometric array spacecraft system is discussed.

6.1 Introduction to Cost Analysis

6.1.1 Objective

Cost is an engineering parameter that varies with physical parameters, technology, and management methods [Wertz, 1999]. As the trend of emphasizing cost-effectiveness and minimizing risk in developing space systems prevailing in the industry, the analysis and prediction of space mission cost are becoming increasingly important. This trend is mainly due to the fact that development of a space system often involves huge research and development cost as well as the risk of mission failures. It is often observed that a space system actually ends up costing more than the initial budget. Therefore, the objective of cost analysis becomes clear. Cost analysis is performed in order to derive the most affordable and

the most cost-effective design of a spacecraft system in the early conceptual stage of development or during the actual manufacturing process. Cost modeling is also applied to planning future missions in order to estimate the system cost.

6.1.2 Categories of Life-Cycle Cost

Life-cycle costs of a space mission architecture (i.e. the total mission cost from planning through end-of-life) are broken down into three main phases [Wertz, 1999]. The Research, Development, Test, and Evaluation (RDT&E) phase includes design, analysis, and test of breadboards, brass boards, prototypes and qualification units. Commonly referred to as the nonrecurring phase, RDT&E conventionally includes protoflight units and one-time ground station costs. This phase does not include technology development for system components. The Operation and Maintenance (O&M) phase consists of ongoing operations and maintenance costs, including spacecraft unit replacements and software maintenance. The Implementation and Production (I&P) phase incorporates the cost of producing flight units and launching them.

These life-cycle cost categories can be more intuitively identified as three primary cost categories: the development of the spacecraft payloads and buses, deployment (i.e. launch) of the system, and the operation of the system [Jilla, 2002]. I&P phase includes the first two categories. In this chapter, we are interested in developing a cost model for a sparse aperture payload and a complete system cost of a sparse aperture imaging satellite, based on the actual cost spent on the ARGOS testbed.

The Theoretical First Unit (TFU) is used to represent the first flight-qualified satellite off the line. The ARGOS testbed is considered as TFU. As discussed in Chapter 2, learning curve savings are expected from multiple spacecraft systems and also from a single spacecraft system employing modular architecture like ARGOS. The learning curve savings include cost reductions due to economics of scale, set up time, and human learning as the number of units increase. The total production cost for N units is modeled as [Wertz, 1999]:

$$\text{Production Cost} = TFU \times L \tag{6.1}$$

$$\text{where} \quad L = N^{B} \quad , \quad B = 1 - \frac{\ln\left((100\%)/S\right)}{\ln 2} \quad .$$

The learning curve slope S represents the percentage reduction in cumulative average cost when the number of production units is doubled. For less than 10 units, a 95% learning curve slope is recommended. Between 10 and 50 units, a 90% is appropriate.

6.1.3 Cost Modeling Approach for Sparse Aperture Payload

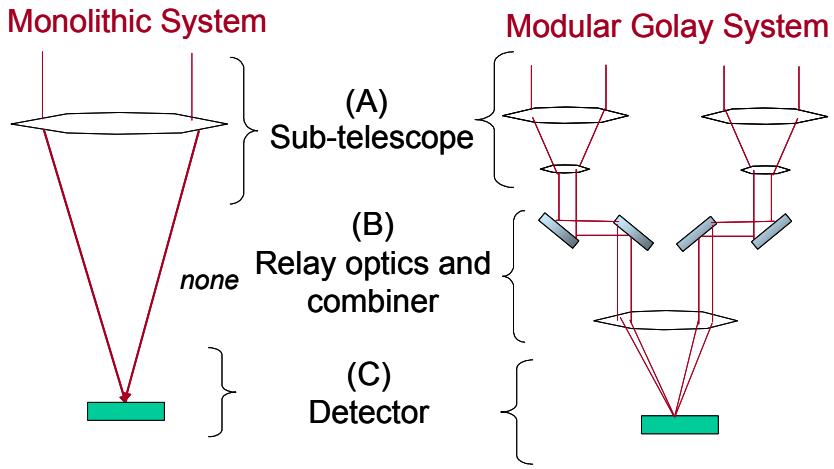

Figure 6.1 Cost modeling approach for sparse apertures

Out of three categories in a spacecraft system's life-cycle costs discussed in Section 6.1.2, cost modeling of the spacecraft payloads and buses for a sparse aperture imaging satellite is developed in this chapter. An emphasis is placed on the impacts of the modular interferometer technology on the system costs. Therefore, the analysis on launch and operation cost is not included in this chapter. Since the motivation of this breakthrough technology, interferometry for a space imaging system, is the cost-reduction in mission development, the objective of cost-modeling is more committed to a comparison analysis between a monolithic aperture and a sparse interferometric array of various configurations.

Figure 6.1 depicts how the cost model of a sparse array payload can be broken down into three cost models to represent a system comparable to that of a monolithic payload. The biggest difference between a monolithic system and a sparse aperture is the existence of the relay optics cost. The payload cost of a sparse array can be stated as:

$$Cost_{SparseArray} = Cost_{Telescope} + Cost_{RelayOptics} + Cost_{CCD} \tag{6.2}$$

The relay optics cost includes a beam combiner, all the optics components in the relay optics train, and the actuators and the avionics for active beam combining control. A cost model of a single telescope is presented in Section 6.3, and a complete system cost modeling considering the payload and the system buses based on the ARGOS is developed in Section 6.4. There are several previous research literatures on cost modeling of a large telescope or a telescope array [Kahan, 1998;Meinel, 1979;Humphries, 1984].

6.2 Telescope Cost Modeling

This section is based on [de Weck, 2001]. Meinel predicted the following scale law:

$$S = 0.37 \cdot D^{2.58} \quad [\text{M\$}]\ (1980) \tag{6.3}$$

This scaling law became one of the motivations to pursue a sparse aperture imaging array as discussed in Chapter 1. The prices of small amateur telescopes with a diameter between 10cm and 80cm are collected and plotted in Figure 1.1 in Chapter 1. To verify the scaling law in Equation 6.3, the parametric estimation method using regression was performed to find the cost estimating relationship (CER) of a telescope scaled to a diameter (see Figure 6.2).

The curve-fitting regression produces the following CER:

$$CER = 28917 D^{2.76} \tag{6.4}$$

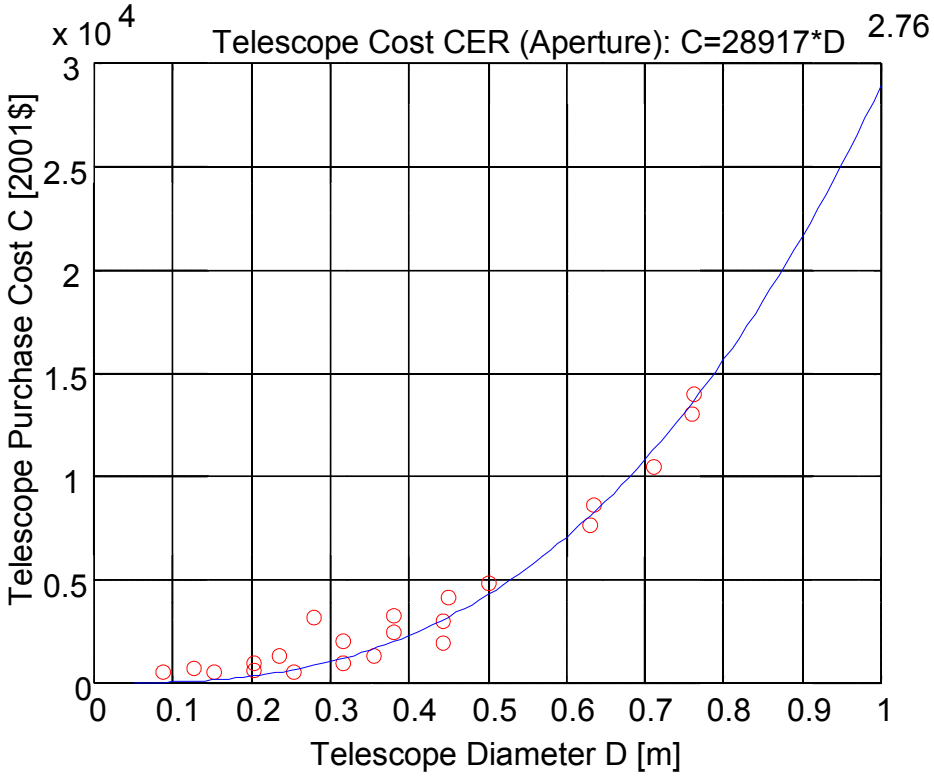

Figure 6.2 Telescope cost CER using small amateur telescopes in Figure 1.1

The exponent of 2.76 is surprisingly close to 2.58 of Meinel's scaling law in Equation 6.3. To further investigate this power scaling law, the CERs from a professional telescope manufactures are compared as shown in Figure 6.3. The CER of a Ritchey-Chretien type telescope is show in Equation 6.5, and the CER of a classical Cassegrain is shown in Equation 6.6:

$$CER_{RC} = 376000 \cdot D^{2.80} \tag{6.5}$$

$$CER_{CC} = 322840 \cdot D^{2.75} \tag{6.6}$$

These CERs are the remarkable results showing almost identical power law across completely different product lines. The scaling law of a monolithic telescope is developed and

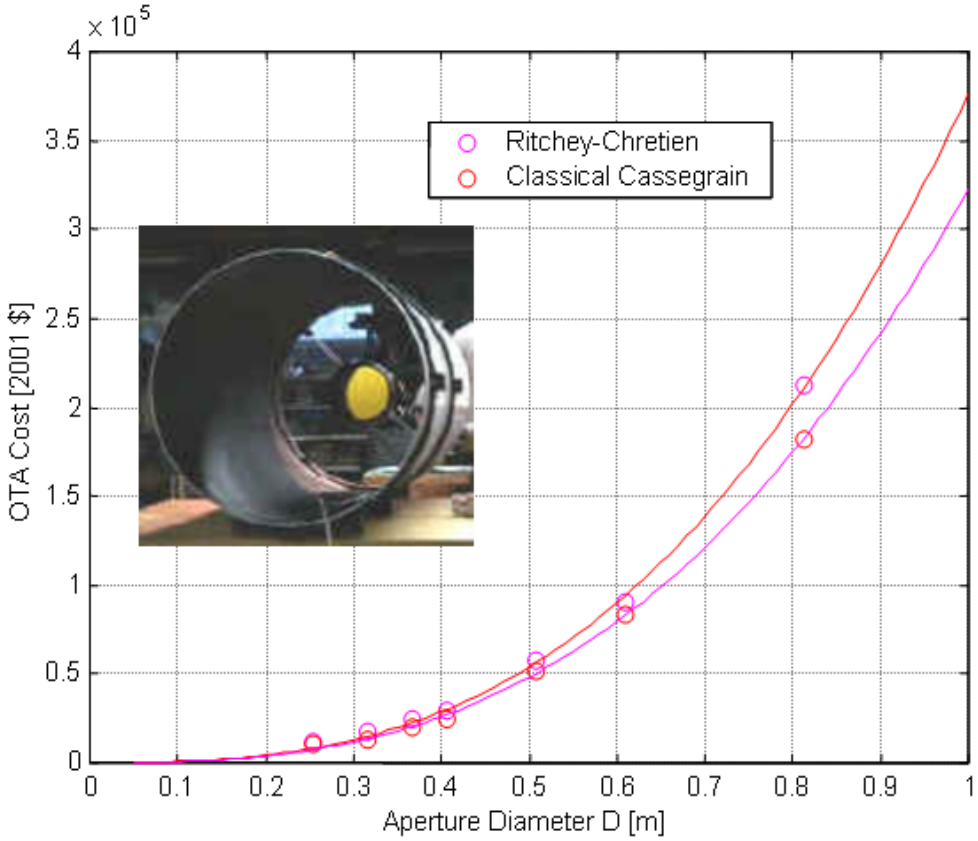

Figure 6.3 Cost of OTA's telescope systems (http:www.opticalguidancesystems.com)

applied to the CERs of a sub-telescope array with N identical apertures using the learning curve saving in Equation 6.1.

$$CER_{\text{Telescope}} = cD^{2.76} \times N^{B} \tag{6.7}$$

where B is the learning curve saving from Equation 6.1.

6.3 Relay Optics Cost Modeling

A different approach is employed in this section to estimate the cost of the relay optics portion of a sparse aperture array. Instead of using statistical data to derive the CER by regression, identifying the theoretical relationships between the design parameters is con-

sidered. From the experience of building the optics control system of the ARGOS testbed, it is observed that the cost of the relay optics including beam combining control depends on the beam combining tolerances such as shearing error and tilt/tip error discussed in Chapter 2. The control difficulty caused by stringent beam combining tolerances defines the complexity of optics control actuators (ODLs and FSMs), and the quality of optics and structures. For example, if we have a tight beam combining requirement, the control actuator and actuator mount with a resolution smaller than this requirement is required.

$$CER_{RelayOptics} \propto Control\_Effort \tag{6.8}$$

Among the three primary beam combining errors (piston error, tip/tilt error and pupil mapping error) discussed in Chapter 2, the piston error requirement itself does not scale with any design parameters such as diameter of aperture or array size. In fact, derivations of tip/tilt errors and pupil mapping errors are based on the requirement of l/10λ phasing. A magnification tolerance of pupil mapping is assumed to be fixed at the manufacturable level. Then, the optics control effort becomes a function of tip/tilt and shearing error tolerances.

$$Control\_Effort = \frac{C_1}{Shear^A} + \frac{C_2}{Tilt^B} + \alpha \tag{6.9}$$

Equation 2.39 in Chapter 2 describes the shear error requirement as a function of FOV, magnification (m) and the array radius (L) - we assume the magnification tolerance (Δm) is fixed.

$$\Delta l = \frac{\lambda}{5\sqrt{3}FOV(m-\Delta m)} - \frac{\Delta mL}{m^2 - m\Delta m} \tag{6.10}$$

FOV can be expressed in terms of the array size

$$FOV = \frac{x}{f_{eff}} n = 2.44 \frac{\lambda}{D_{eff}} Qn \tag{6.11}$$

where x is a size of one pixel, f_{eff} is the effective focal length of the whole system, Q is a quality factor deciding the number of pixels representing one angular resolution element, and n is the number of pixels across a CCD frame.

We can recall the relationship for the effective diameter from Equation 2.20,

$$D_{eff} = 2R_{eff} = R_{uv} = \frac{3L + \sqrt{4D^2 - 3L^2}}{2} \tag{6.12}$$

Plugging this into Equation 6.11 and assuming Q=0.5 (one angular resolution element per pixel) results in:

$$FOV = \frac{2.44\lambda n}{3L + \sqrt{4D^2 - 3L^2}} \tag{6.13}$$

Combining this with Equation 6.10 results in:

$$\Delta l = \frac{3L + \sqrt{4D^2 - 3L^2}}{12.2\sqrt{3}(m - \Delta m)n} - \frac{\Delta m L}{m^2 - m\Delta m} \tag{6.14}$$

We can also derive the tilt error tolerance as a function of a compressed beam size (d=D/m). Simplifying the FEM tilt analysis done in Chapter 2, the maximum allowable OPD error due to the relative tilt angle between two compressed beams with a diameter of d (see Figure 6.4) is calculated. We use l/10λ phasing for coherent beam combining:

$$OPD_{tilt} = \frac{d}{2}\sin(\gamma) \cong \frac{D}{2m}\gamma = \frac{\lambda}{10} \tag{6.15}$$

$$\Delta tilt = \frac{\lambda m}{5D} \tag{6.16}$$

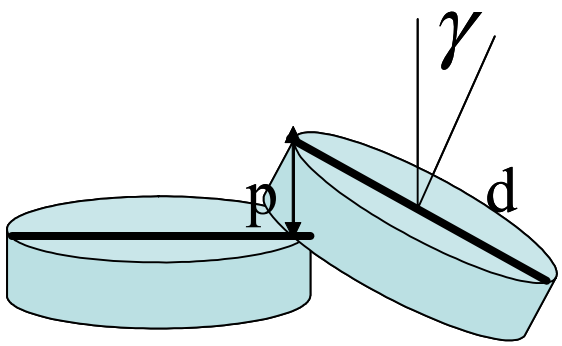

Figure 6.4 Tip/Tilt Error

In Equation 6.9, we assume C_1=1 and C_2=3, based on the fact that one FSM needs three control channels to actively actuate three PZT stacks separated by 120 degrees for tip/tilt control. It was observed while building the ARGOS testbed that more control channels increase the cost. For example, three PZT amplifiers and three D/A channels are required to one single FSM as compared to one per each translational stage for shear or OPD control. The exponents, A, B of Equation 6.9 are assumed to be one indicating the control cost is inversely proportional to the tolerable values of shear error and tip/tilt error.

We can fix the number of pixels across one CCD frame to a certain number at the design stage because we can only select a certain range of CCD format sizes. 512x512 and 1024x1024 CCDs are readily available, and 4096x4096 is considered largest format. Then, the control effort estimate becomes a function of D, (D/L) and m. The ratio of (D/L) has been chosen instead of L because it can depicts the relative size of D and L - how sparse or compact a sparse array is:

$$Control\_Effort = \left[D\frac{3+\sqrt{4(D/L)^2-3}}{12.2\sqrt{3}(m-\Delta m)n(D/L)} - \frac{\Delta mD}{(m^2-m\Delta m)(D/L)} \right]^{-1} + 3\left[\frac{\lambda m}{5D}\right]^{-1} \quad (6.17)$$

We can also represent the control effort estimate as a function of FOV, when the FOV requirement cannot be traded:

$$Control\_Effort = \left[\frac{\lambda}{5\sqrt{3}FOV(m-\Delta m)} - \frac{\Delta mD}{(m^2 - m\Delta m)(D/L)} \right]^{-1} + 3\left[\frac{\lambda m}{5D} \right]^{-1} \qquad (6.18)$$

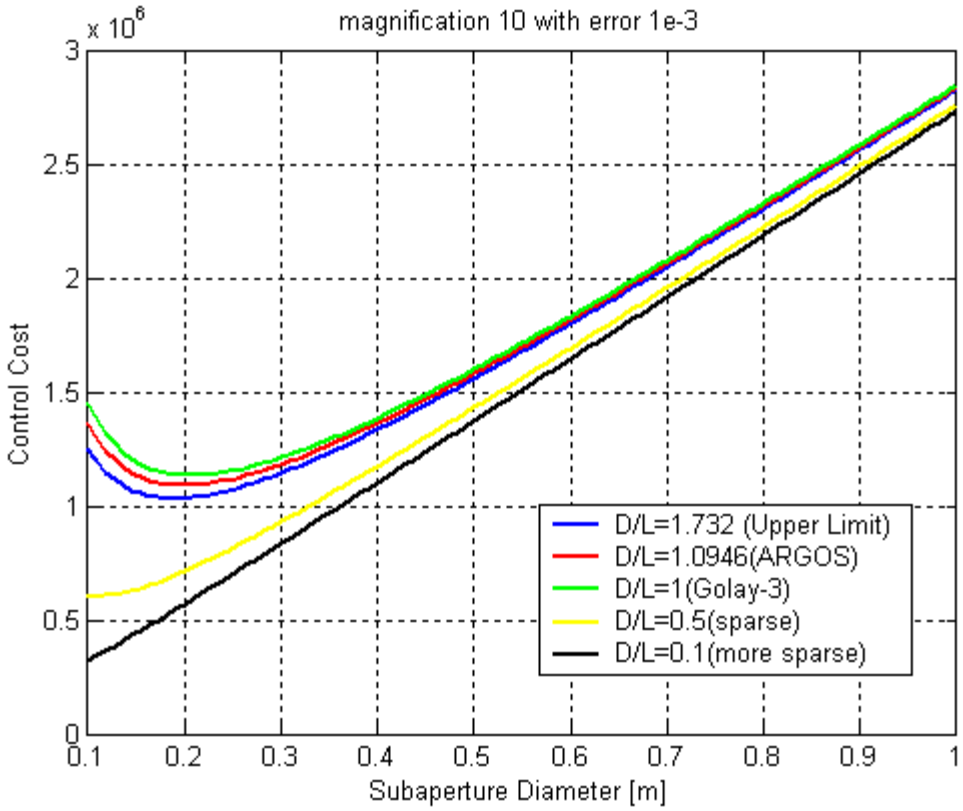

Figure 6.5 Control cost vs. subaperture diameter for different array compactness

Equation 6.17 is plotted in Figure 6.5 with n=1024, magnification =10, and magnification error 1e-3. Five different values of array compactness (D/L) have been selected. The blue line is the upper limit of D/L=1.732=$\sqrt{3}$, in which the individual telescopes touch each others (the most compact array). The red line corresponds to the ARGOS configuration with D=0.21m and L=0.19185m. The green line is the original Golay-3 configuration with D=L. The ratio of 1 is the minimum D/L with which no singular point is expected inside

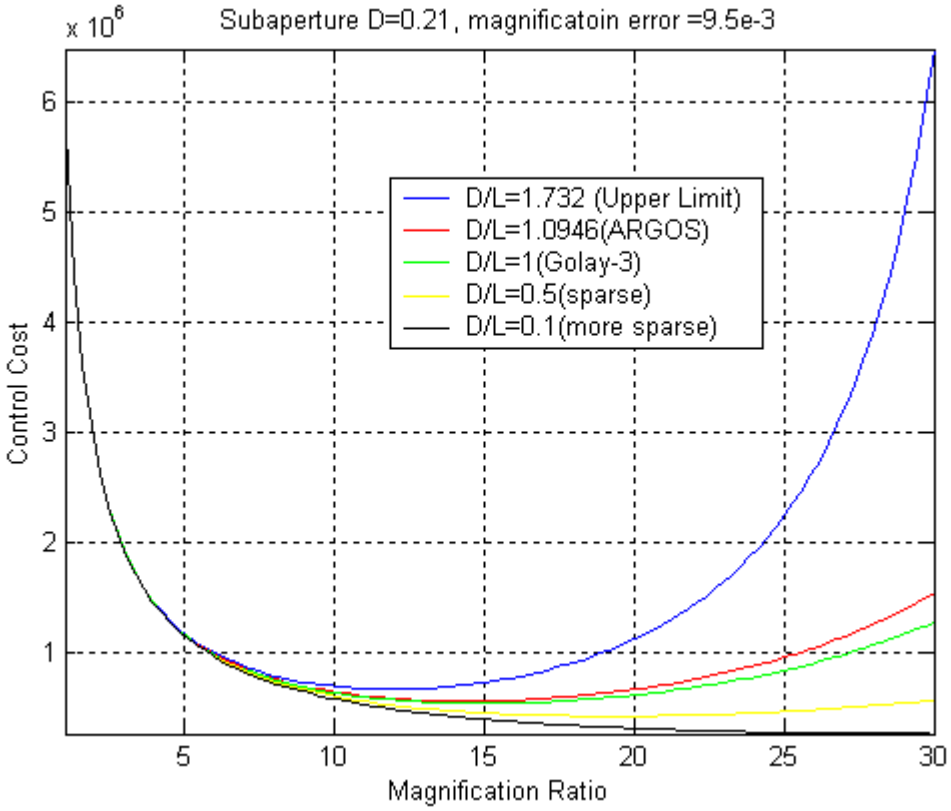

Figure 6.6 Control cost vs. magnification

the MTF envelope as discussed in Chapter 2. The smaller values of D/L were also plotted to observe the control cost trends for longer baseline interferometers like Michelson interferometry. If the squared-root term in the effective diameter equation (Equation 6.12) becomes imaginary, the imaginary parts are ignored in this calculation. This means that the angular resolution of the effective diameter of long baseline interferometer is determined by L only.

For a compact Fizeau type interferometry with D/L greater than 1, we can decrease the control cost by making the array more compact. It is interesting to note that there exists a minimum control cost point for a compact sparse array (D/L>1). This is because shear error dominates at small sub-aperture diameter region while tilt error dominates at large

sub-aperture diameter. We can see that the second part of Equation 6.17 (tilt effect) is linearly proportional to D. As we further increase the array size, the system becomes more sparse, and the minimum control disappear. However we can decrease the control cost by longer baselines.

We can also plot the control cost as a function of magnification as shown in Figure 6.6. As opposed to the previous plot of diameter vs. control cost, tilt error dominates at small magnification while shear error becomes more dominant as the magnification increases. This plot predicts the existence of the minimum control point. This is already predicted in Section 2.4.3 on page 59. Sub-aperture magnification can be tuned to maximize allowable shear error (lateral pupil mapping error) thereby reducing control complexity.

In order to see the effect of array compactness (D/L) on the control cost, Figure 6.7 is plotted. The interesting point is that a smaller sub-aperture does not necessarily result in smaller control cost for a compact sparse array (D/L>1). This observation is also consistent with Figure 6.5, which showed the existence of a sub-aperture size D minimizing the control cost. For longer baseline interferometers (D/L <1), increasing the baseline reduces the control cost.

6.4 Quantitative Life-Cycle System Analysis

This section is based on David Miller's work (the author's advisor). The final cost and mass tables describing each component comprising the ARGOS subsystems are listed in Appendix C.

An analogy-based cost estimating approach is employed to derive the CERs of sparse array spacecraft systems. Based on the detailed subsystem costs of the ARGOS, the CERs of the different configurations such as Golay-6, Golay-12 and the Hex arrays are developed. Nonrecurring and recurring items are identified and the CERs are adjusted for dif-

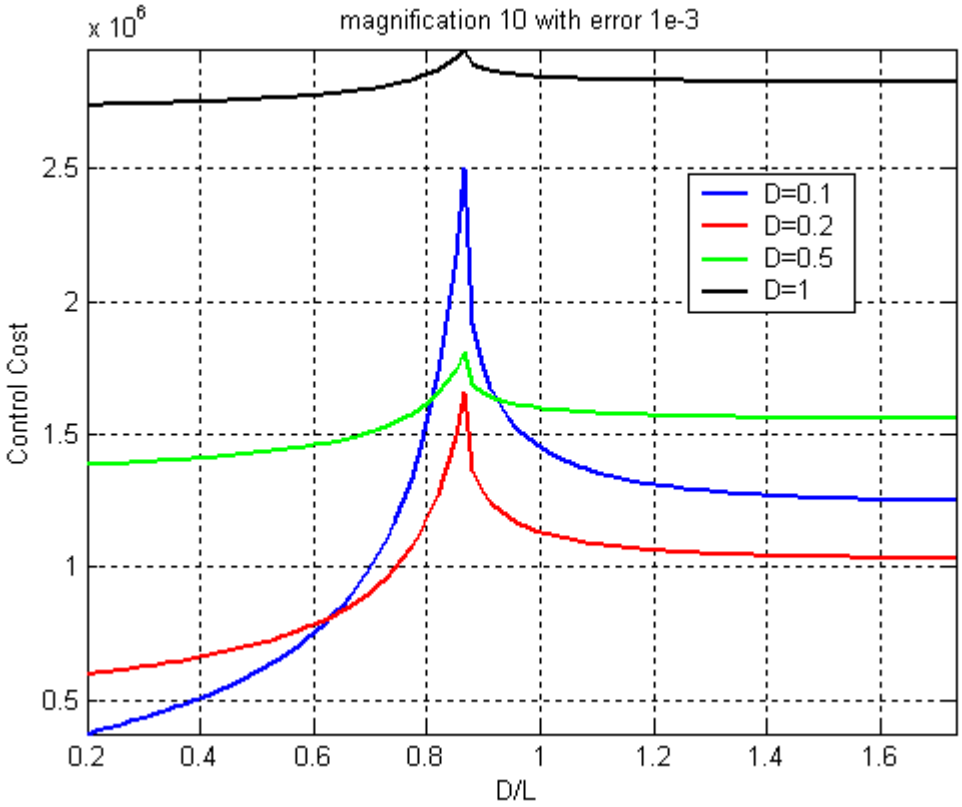

Figure 6.7 Control cost vs. array compactness (D/L)

ferences in size or complexity. Firstly, the scaling law of a monolithic telescope is used to calculate the subaperture diameter (See Section 6.2 on page 184). In order to estimate the Attitude Control System (ACS) cost, regression was performed to derive the relationship between Reaction Wheel Assembly (RWA) mass and momentum capacity from the data collected from RWA manufacturers. The ACS cost scales with the RWA mass assuming the RWA mass dominates the ACS mass. The costs of other subsystems are adjusted by the same method. The labor cost is also taken into consideration by categorizing the subsystem members into management, staff, and engineer levels.

6.4.1 Cost Modeling of ACS

Firstly, the CERs of the ACS subsystem is developed. Reaction wheel mass scales with momentum capacity required. Using the data collected from different Reaction Wheel Assembly (RWA) manufactures, regression was performed to derive the relationship between the mass of RWA and momentum capacity (see Figure 6.8):

$$Kg = 2.49(MomentumCapcity)^{0.41} \tag{6.19}$$

With an assumption that RWA mass dominates the mass of ACS subsystem, the ACS

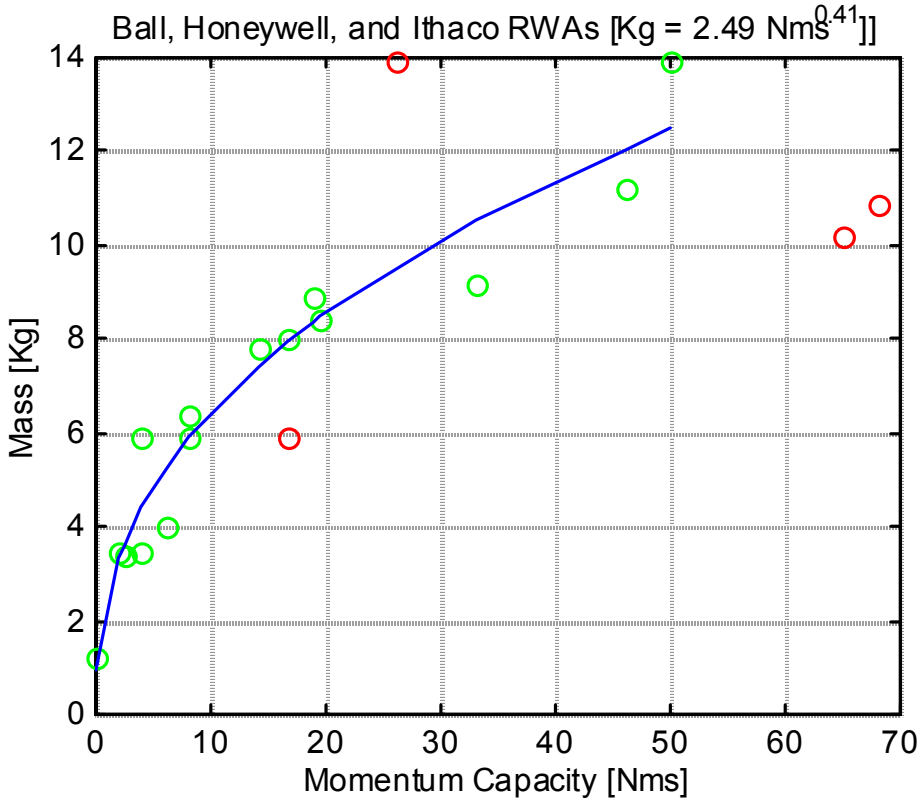

Figure 6.8 Regression curve fitting of momentum Capacity and mass of RWA

CERs is as follows:

$$CER_{ACS} = c_o Kg_{ACS}^{0.8} \tag{6.20}$$

We can scale the equation above using the ARGOS ACS mass and cost. A slew rate of 1.5 degrees per second is assumed in the calculation.

6.4.2 Subsystem Cost Tables

The final cost estimates for a monolithic aperture, a Golay-3 array, a Golay-6 array, a

TABLE 6.1 Cost estimate table for passive optics and active optics sub-systems

Passive Optics

Item	Unit Cost (US$)	Quantity Bought	Actual Cost (US$)	Monolith Quantity	Monolith Cost	Golay-3 Quantity	Golay-3 Cost	Golay-6 Quantity	Golay-6 Cost	Golay-9 Quantity	Golay-9 Cost	Golay-12 Quantity	Golay-12 Cost
Takahashi Telescope (Used)	$2,339	1	$2,339	0	$0	0	$0	0	$0	0	$0	0	$0
Takahashi Telescope	$2,800	2	$5,600	0	$0	3	$8,400	0	$0	0	$0	0	$0
Sub-Aperture (D=0.4169m)	$18,140	0	$0	1	$18,140	0	$0	0	$0	0	$0	0	$0
Sub-Aperture (D=0.09393m)	$377	0	$0	0	$0	0	$0	6	$2,259	0	$0	0	$0
Sub-Aperture (D=0.0618m)	$127	0	$0	0	$0	0	$0	0	$0	9	$1,141	0	$0
Sub-Aperture (D=0.0463m)	$60	0	$0	0	$0	0	$0	0	$0	0	$0	12	$718
Beam Combiner	$3,624	1	$3,624	1	$3,624	1	$3,624	1	$3,624	1	$3,624	1	$3,624
Collimator	$2,300	4	$9,200	0	$0	3	$6,900	6	$13,800	9	$20,700	12	$27,600
Collimator Engineering	$2,500	1	$2,500	0	$0	0	$0	0	$0	0	$0	0	$0
Collimator Mounting	$500	3	$1,500	0	$0	3	$1,500	6	$3,000	9	$4,500	12	$6,000
Pyramidal Mirror	$3,000	1	$3,000	0	$0	1	$3,000	1	$3,000	1	$3,000	1	$3,000
Optical Instruments (Fold Mirrors etc.)	$1,948	1	$1,948	0	$0	1	$1,948	2	$3,896	3	$5,844	4	$7,792
Charged Coupled Device (CCD) Dragonfly	$1,495	3	$4,485	2	$2,990	2	$2,990	2	$2,990	2	$2,990	2	$2,990
Firewire Card	$90	2	$180	2	$180	2	$180	2	$180	2	$180	2	$180
Flock Paper/Adhesive	$106	1	$106	1	$106	1	$106	1	$106	1	$106	1	$106
Compression Ring/Adapter Sleeve	$132	1	$132	1	$132	1	$132	1	$132	1	$132	1	$132
Optical Posts/Shear Plate	$1,617	1	$1,617	0	$0	0	$0	0	$0	0	$0	0	$0
Telephoto Lens	$500	1	$500	1	$500	1	$500	1	$500	1	$500	1	$500
Total		1	$36,730		$25,171		$28,779		$32,986		$42,216		$52,141

Active Optics

Item	Unit Cost (US$)	Quantity Bought	Actual Cost (US$)	Monolith Quantity	Monolith Cost	Golay-3 Quantity	Golay-3 Cost	Golay-6 Quantity	Golay-6 Cost	Golay-9 Quantity	Golay-9 Cost	Golay-12 Quantity	Golay-12 Cost
Fast Steering Mirror (FSM)	$2,575	3	7,725	1	$2,575	3	$7,725	6	$15,450	9	$23,175	12	$30,900
Precision Mount For Combiner	$3,000	1	3,000	0	$0	1	$3,000	1	$3,000	1	$3,000	1	$3,000
1 Channel PZT Amplifier	$515	9	4,635	3	$1,545	9	$4,635	18	$9,270	27	$13,905	36	$18,540
Mirror Mounts w/ High Precision screws	$177	4	708	1	$177	3	$531	6	$1,062	9	$1,593	12	$2,124
Pyramidal Mirror Mount Combo	$1,048	1	1,048	0	$0	1	$1,048	1	$1,048	1	$1,048	1	$1,048
Test PC	$842	1	842	0	$0	0	$0	0	$0	0	$0	0	$0
Optics Electronics	$594	1	594	1	$594	1	$594	1	$594	1	$594	1	$594
Amplifier Boards	$45	6	270	1	$45	3	$135	6	$270	9	$405	12	$540
Clearning Materials	$55	1	55	0	$0	0	$0	0	$0	0	$0	0	$0
Electronic Focuser and Adapter	$694	1	694	1	$694	1	$694	1	$694	1	$694	1	$694
Optics Hardware	$13	1	13	1	$13	1	$13	1	$13	1	$13	1	$13
Large Knobs	$4	10	40	3	$12	9	$36	18	$72	27	$108	36	$144
DAC Channels	$259	12	3,113	3	$778	9	$2,334	18	$4,669	27	$7,003	36	$9,338
Total			22,716		$6,413		$20,725		$36,122		$51,518		$66,914

Golay-9 array, and a Golay 12 array are listed in Table 6.1, Table 6.2 and Table 6.3. The active optics cost is allocated to a monolithic system as well because the FSM can be used

TABLE 6.2 Cost estimate table for the ACS, Structure, Science, Operation, Communications subsystems

Attitide Control System

Item	Unit Cost (US$)	Quantity Bought	Actual Cost (US$)	Monolith Quantity	Monolith Cost	Golay-3 Quantity	Golay-3 Cost	Golay-6 Quantity	Golay-6 Cost	Golay-9 Quantity	Golay-9 Cost	Golay-12 Quantity	Golay-12 Cost
Fly Wheels	$300	3	$900	3	$900	3	$900	3	$900	3	$900	3	$900
Rate Gyros	$3,000	0	$0	1	$3,000	1	$3,000	1	$3,000	1	$3,000	1	$3,000
Motor, Tachometers, Amplifiers	$802	3	$2,406	3	$2,406	3	$2,406	3	$2,406	3	$2,406	3	$2,406
TOM-2-50 (Tilt Inclinometer/Magnetometer)	$769	1	$769	1	$769	1	$769	1	$769	1	$769	1	$769
TOM-2-20 (Tilt Inclinometer/Magnetometer)	$699	1	$699	0	$0	0	$0	0	$0	0	$0	0	$0
Active Balancer	$2,163	3	$6,490	3	$6,490	3	$6,490	3	$6,490	3	$6,490	3	$6,490
Lab Power Supplies	$442	1	$442	0	$0	0	$0	0	$0	0	$0	0	$0
DAC Channels	$259	3	$778	3	$778	3	$778	3	$778	3	$778	3	$778
ADC Channels	$281	6	$1,688	6	$1,688	6	$1,688	6	$1,688	6	$1,688	6	$1,688
Filters for Rate Gyros	$283	1	$283	1	$283	1	$283	1	$283	1	$283	1	$283
Balancing Fly Wheels	$250	0	$0	3	$750	3	$750	3	$750	3	$750	3	$750
Total			$14,455		$17,064		$17,064		$17,064		$17,064		$17,064

Structures

Item	Unit Cost (US$)	Quantity Bought	Actual Cost (US$)	Monolith Quantity	Monolith Cost	Golay-3 Quantity	Golay-3 Cost	Golay-6 Quantity	Golay-6 Cost	Golay-9 Quantity	Golay-9 Cost	Golay-12 Quantity	Golay-12 Cost
Collar	$583	3	$1,750	2	$1,167	3	$1,750	5	$2,917	7	$4,083	9	$5,250
Translation Stages	$234	9	$2,106	0	$0	9	$2,106	18	$4,212	27	$6,318	36	$8,424
Bread Boards	$176	4	$706	1	$176	3	$529	6	$1,058	9	$1,588	12	$2,117
Adapter Plates	$38	10	$380	0	$0	9	$342	18	$684	27	$1,026	36	$1,368
Nuts, Bolts, Tools, Cables, Connections etc.	$378	1	$378	0.5	$189	1	$378	2	$755	3	$1,133	4	$1,510
Model SRA250 Spherical Air Bearing	$12,900	1	$12,900	0	$0	0	$0	0	$0	0	$0	0	$0
Pedestal for Spherical Air Bearing	$980	1	$980	0	$0	0	$0	0	$0	0	$0	0	$0
Air Supply Filter	$1,870	1	$1,870	0	$0	0	$0	0	$0	0	$0	0	$0
Vibration Suppression Mounts	$2	15	$36	12	$29	12	$29	12	$29	12	$29	12	$29
Angle Braces	$199	6	$1,194	0	$0	6	$1,194	12	$2,388	18	$3,582	24	$4,776
Machine Shop	$7,059	1	$7,059	1	$7,059	1	$7,059	1	$7,059	1	$7,059	1	$7,059
Center Structure Assembly	$700	1	$700	1	$700	1	$700	1	$700	1	$700	1	$700
Total			$30,058		$9,320		$14,087		$19,802		$25,518		$31,233

Science, Operations, & Communications

Item	Unit Cost (US$)	Quantity Bought	Actual Cost (US$)	Monolith Quantity	Monolith Cost	Golay-3 Quantity	Golay-3 Cost	Golay-6 Quantity	Golay-6 Cost	Golay-9 Quantity	Golay-9 Cost	Golay-12 Quantity	Golay-12 Cost
WLS LAN PCI Cards 11 Mbps	$230	1	$230	1	$230	1	$230	1	$230	1	$230	1	$230
Wireless Broadband Gateway	$250	1	$250	0	$0	0	$0	0	$0	0	$0	0	$0
Wireless LAN card	$131	1	$131	0	$0	0	$0	0	$0	0	$0	0	$0
Portable Computer	$1,697	1	$1,697	0	$0	0	$0	0	$0	0	$0	0	$0
Total			$2,307		$230		$230		$230		$230		$230

for fine image centroiding control. Among the subsystems, the two optics groups are the major cost driving factor. Even though the passive optics (telescopes and optics supply) subsystem dominates the cost for few sub-apertures, the active optics subsystem (the relay optics, actuators, and WFE sensor) dominates the cost for many sub-apertures.

TABLE 6.3 Cost estimate table for Power, Avionics and Software subsystem and miscellaneous costs

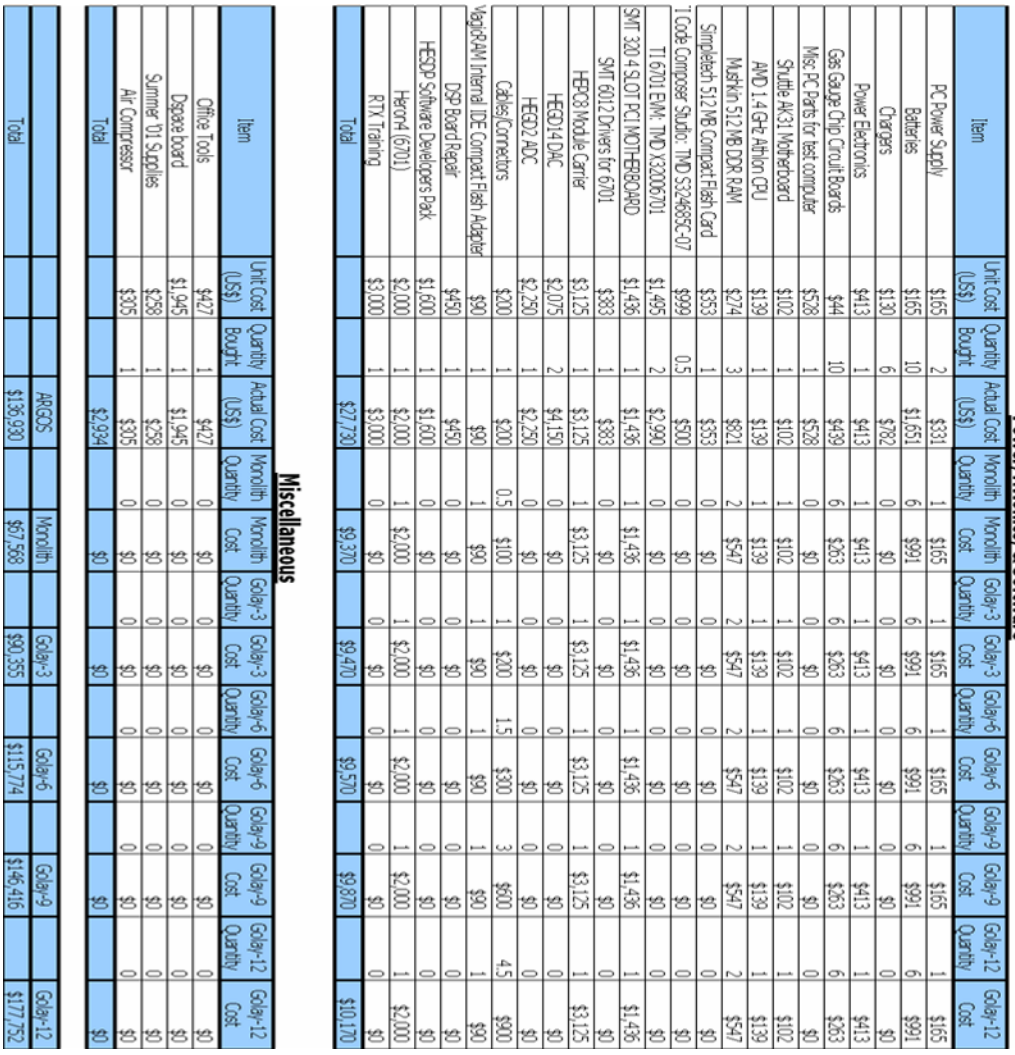

Power, Avionics, & Software

Item	Unit Cost (US$)	Quantity Bought	Actual Cost (US$)	Monolith Quantity	Monolith Cost	Golay-3 Quantity	Golay-3 Cost	Golay-6 Quantity	Golay-6 Cost	Golay-9 Quantity	Golay-9 Cost	Golay-12 Quantity	Golay-12 Cost
PC Power Supply	$165	2	$331	1	$165	1	$165	1	$165	1	$165	1	$165
Batteries	$165	10	$1,651	6	$991	6	$991	6	$991	6	$991	6	$991
Chargers	$130	6	$782	0	$0	0	$0	0	$0	0	$0	0	$0
Power Electronics	$413	1	$413	1	$413	1	$413	1	$413	1	$413	1	$413
Gas Gauge Chip Circuit Boards	$44	10	$439	6	$263	6	$263	6	$263	6	$263	6	$263
Misc PC Parts for test computer	$528	1	$528	0	$0	0	$0	0	$0	0	$0	0	$0
Shuttle AK31 Motherboard	$102	1	$102	1	$102	1	$102	1	$102	1	$102	1	$102
AMD 1.4 GHz Athlon CPU	$139	1	$139	1	$139	1	$139	1	$139	1	$139	1	$139
Mushkin 512 MB DDR RAM	$274	3	$821	2	$547	2	$547	2	$547	2	$547	2	$547
Simpletech 512 MB Compact Flash Card	$353	1	$353	0	$0	0	$0	0	$0	0	$0	0	$0
TI Code Composer Studio: TMDS3246858C-07	$999	0.5	$500	0	$0	0	$0	0	$0	0	$0	0	$0
TI 6701 EVM: TMDX320D6701	$1,495	2	$2,990	0	$0	0	$0	0	$0	0	$0	0	$0
SMT 320 4 SLOT PCI MOTHERBOARD	$1,436	1	$1,436	1	$1,436	1	$1,436	1	$1,436	1	$1,436	1	$1,436
SMT 6012 Drivers for 6701	$383	1	$383	0	$0	0	$0	0	$0	0	$0	0	$0
HEPC8 Module Carrier	$3,125	1	$3,125	1	$3,125	1	$3,125	1	$3,125	1	$3,125	1	$3,125
HEGD14 DAC	$2,075	2	$4,150	0	$0	0	$0	0	$0	0	$0	0	$0
HEGD2 ADC	$2,250	1	$2,250	0	$0	0	$0	0	$0	0	$0	0	$0
Cables/Connectors	$200	1	$200	0.5	$100	1	$200	1.5	$300	3	$600	4.5	$900
VaguRAM Internal IDE Compact Flash Adapter	$90	1	$90	1	$90	1	$90	1	$90	1	$90	1	$90
DSP Board Repair	$450	1	$450	0	$0	0	$0	0	$0	0	$0	0	$0
HEGDP Software Developers Pack	$1,600	1	$1,600	0	$0	0	$0	0	$0	0	$0	0	$0
Heron4 (6701)	$2,000	1	$2,000	1	$2,000	1	$2,000	1	$2,000	1	$2,000	1	$2,000
RTX Training	$3,000	1	$3,000	0	$0	0	$0	0	$0	0	$0	0	$0
Total			$27,730		$9,370		$9,470		$9,570		$9,870		$10,170

Miscellaneous

Item	Unit Cost (US$)	Quantity Bought	Actual Cost (US$)	Monolith Quantity	Monolith Cost	Golay-3 Quantity	Golay-3 Cost	Golay-6 Quantity	Golay-6 Cost	Golay-9 Quantity	Golay-9 Cost	Golay-12 Quantity	Golay-12 Cost
Office Tools	$427	1	$427	0	$0	0	$0	0	$0	0	$0	0	$0
Dspare board	$1,945	1	$1,945	0	$0	0	$0	0	$0	0	$0	0	$0
Summer '01 Supplies	$258	1	$258	0	$0	0	$0	0	$0	0	$0	0	$0
Air Compressor	$305	1	$305	0	$0	0	$0	0	$0	0	$0	0	$0
Total			$2,934		$0		$0		$0		$0		$0

			ARGOS		Monolith		Golay-3		Golay-6		Golay-9		Golay-12
Total			$136,930		$67,568		$90,355		$115,774		$146,416		$177,752

6.4.3 Labor Cost Table

The ARGOS project was developed under the MIT Department of Aeronautics and Astronautics' Conceive-Design-Implement-Operate (CDIO) education initiative. Fifteen undergraduate students took this three-semester-long course to design and implement the ARGOS under the guidance of two faculty members and four teaching assistant staffs. The students are identifed as an engineer level with a salary cap of $50,000, the teaching assistants as a staff level with a $70,000 salary, and the professors as a management level

TABLE 6.4 Labor cost estimates table

Sub-System	ARGOS			Monolith			Golay-3		
	mult	Total	Recurring	mult	Total	Recurring	mult	Total	Recurring
Passive Optics	1	$209,240	$36,990	0.3	$62,772	$11,096.88	1	$209,240	$36,990
Active Optics	1	$138,794	$25,948	0.3	$41,638	$7,784.38	1	$138,794	$25,948
ACS	1	$119,714	$27,560	1	$119,714	$27,560.00	1	$119,714	$27,560
Structures	1	$71,771	$14,354	0.6	$43,063	$8,612.50	1	$71,771	$14,354
PAS	1	$186,980	$37,608	1	$186,980	$37,607.92	1	$186,980	$37,608
SOC	1	$112,316	$24,689	1	$112,316	$24,689.17	1	$112,316	$24,689
Management	1	$81,090	$22,967	1	$81,090	$22,966.67	1	$81,090	$22,967
Total		$919,903	$190,115		$647,572	$140,318		$919,903	$190,115

Sub-System	Golay-6			Golay-9			Golay-12		
	mult	Total	Recurring	mult	Total	Recurring	mult	Total	Recurring
Passive Optics	1.5	$313,859	$55,484	2	$418,479	$73,979	2.5	$523,099	$92,474
Active Optics	2	$277,588	$51,896	3	$416,381	$77,844	4	$555,175	$103,792
ACS	1	$119,714	$27,560	1	$119,714	$27,560	1	$119,714	$27,560
Structures	2	$143,542	$28,708	3	$215,313	$43,063	4	$287,083	$57,417
PAS	1	$186,980	$37,608	1	$186,980	$37,608	1	$186,980	$37,608
SOC	1	$112,316	$24,689	1	$112,316	$24,689	1	$112,316	$24,689
Management	1	$81,090	$22,967	1	$81,090	$22,967	1	$81,090	$22,967
Total		$1,235,088	$248,912		$1,550,272	$307,709		$1,865,456	$366,506

with a $90,000 pay envelope. The amount of the time each team member spent on the six ARGOS subsystems over the course of three semesters are calculated. An overhead wrap of 2.12 is assumed. The labor costs table is shown in Table 6.4. By comparing the labor costs to the hardware costs in the previous section, it is observed that the labor costs dominate the hardware cost.

Figure 6.9 shows the final subsystem costs including both the hardware costs and the labor costs. Even though the passive optics subsystem dominates the cost for few sub-apertures, the active optics subsystem dominates the cost for many sub-apertures.

6.4.4 Results

The cost estimates of different array configurations (See Figure 6.10) as a function of the effective diameter are plotted in Figure 6.11 (the hardware cost only) and Figure 6.12 (both the hardware and the labor costs). Optimum Golay configurations are dependent on the effective diameter. It is observed that the labor costs move the benefits of a sparse

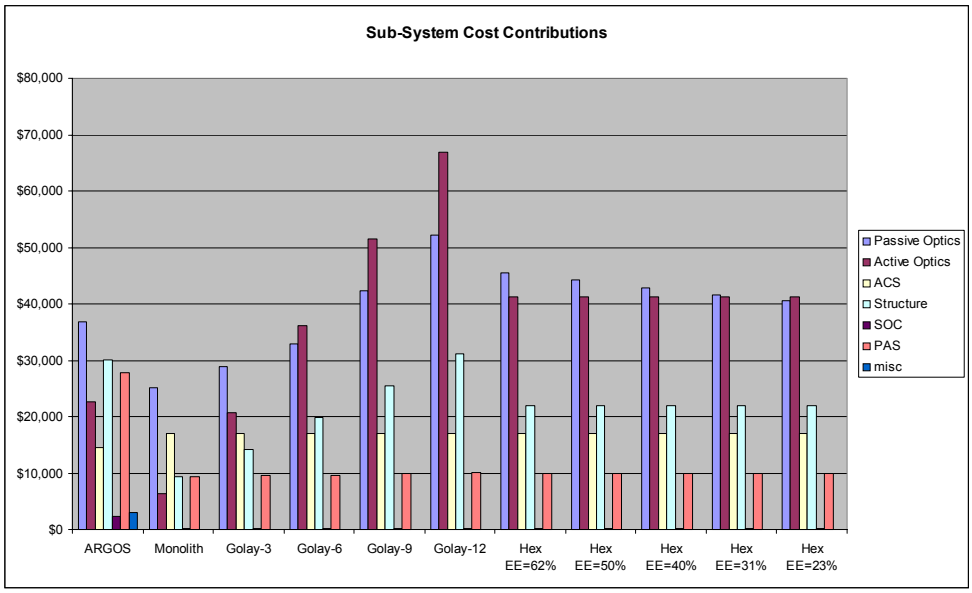

Figure 6.9 Subsystem cost estimates for different array configurations

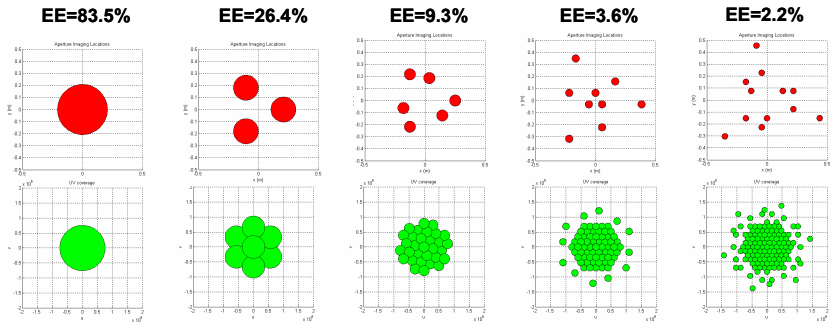

Figure 6.10 Array configurations used for cost estimates- monolith, Golay-3, Golay-6, Golay-9 and Golay-12. EE is a corresponding encircled energy within the mainlobe of a point spread function.

Golay array to the larger effective diameter. While the encircled engergy degrades rapidly as the number of apertures of a Golay array increases, more cost savings are achieved at a larger effective diameter.

The orginal Golay-3 configuration fixes the relationship between the array radius (L) and the aperture diameter (D) - L should equal D. By reducing the array radius (L), a more

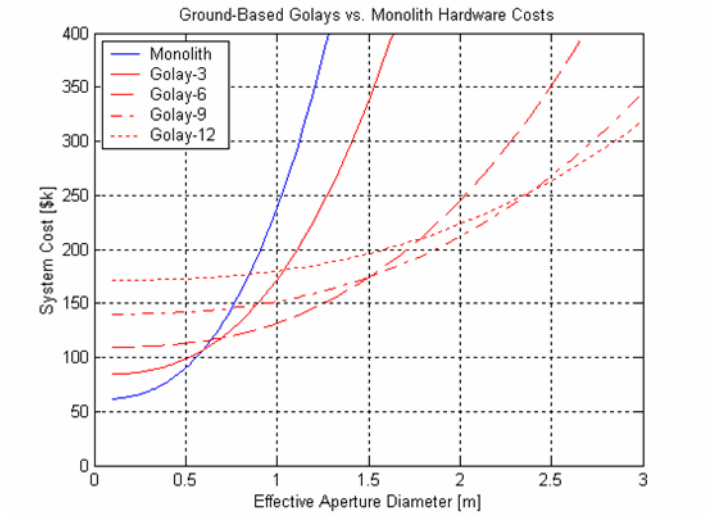

Figure 6.11 Ground-based Golay arrays vs. monolith hardware cost

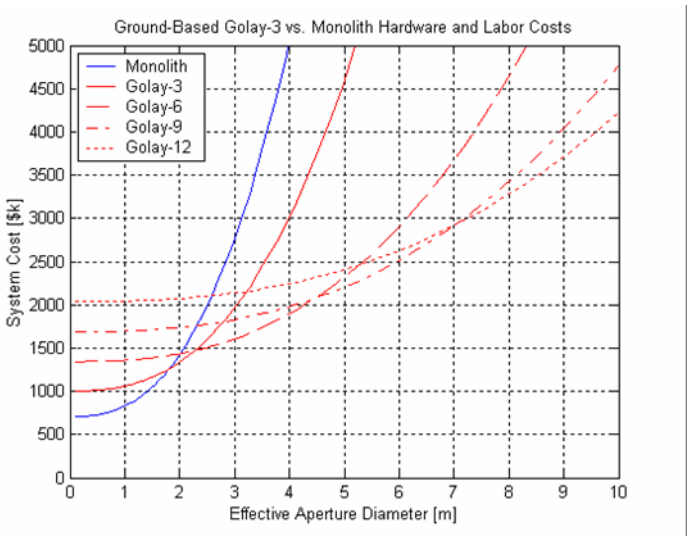

Figure 6.12 Ground based Golay arrays vs. monolith hardware and labor costs

compact array is expected (the final ARGOS array configuration is decided as L=0.19185m and D=0.21m). As simulated in Figure 6.13, a compact Golay-3 array reduces the size of the sidelobes on the PSF plot, thereby improving both the encircled energy and the filling factor (SNR- See the discussions in Chapter 2 and Chapter 4).

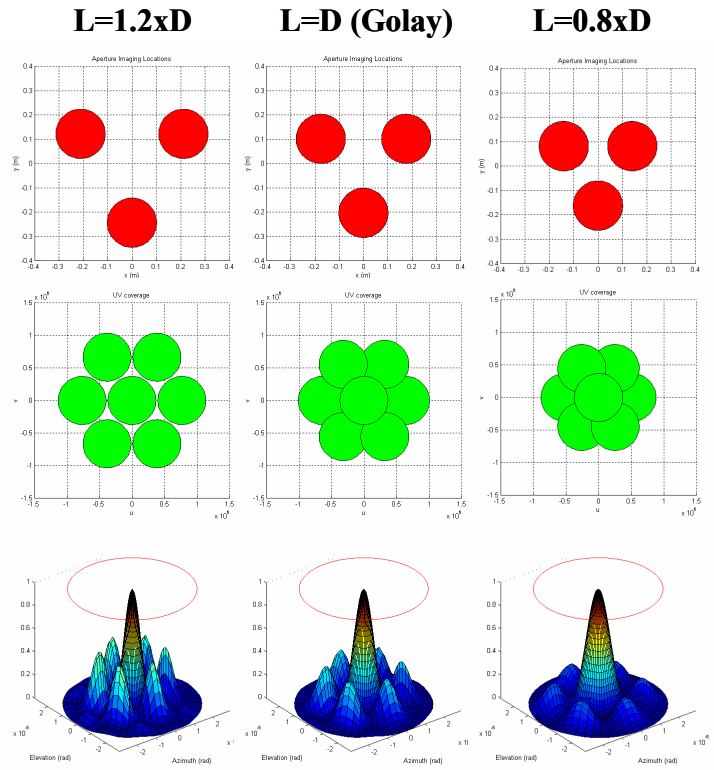

Figure 6.13 Compact Golay-3 arrays with their u-v plots and PSFs.

To see the effects of compactness on a Golay-3 type sparse aperture system, the CERs are developed as a function of effective diameter and array compactness as shown Figure 6.15. Without the complex beam combining part (the relay optics cost in the previous section) of a sparse interferometric array, the telescope cost of monolithic apertures is higher than a sparse array as depicted in Figure 6.14. Therefore, it is the relay optics that dominates the cost of a sparse array system. This cost analysis predicts emergence of a break-even point between monolithic systems and Golays. Past this break-even point, we can build a sparse array system with lower cost than a monolithic aperture system with the same effective diameter.

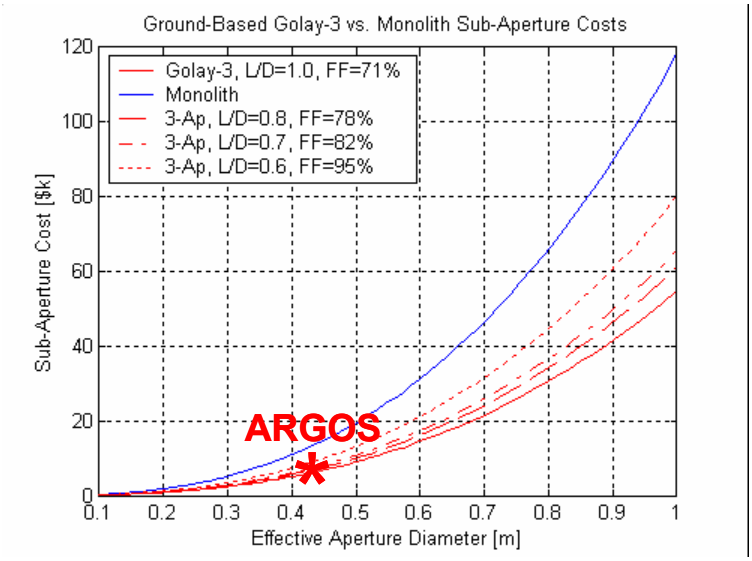

Figure 6.14 Cost of telescopes for three-aperture array

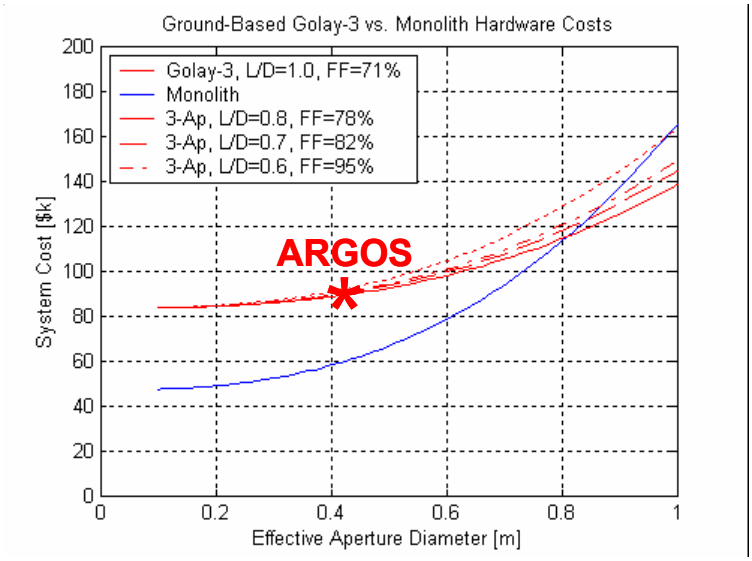

Figure 6.15 15: System cost of three aperture array spacecraft

6.5 Chapter Summary

The three primary cost categories are the development of the spacecraft payloads and buses, deployment (i.e. launch) of the system, and the operation of the system. The cost of the sparse aperture payload can be further broken down into sub-apertures, the relay optics including beam combiner, and the CCD system. In order to derive the cost estimating relation-ships (CERs) of the relay optics portion of a sparse aperture array, identifying the theoretical relationships between the design parameters is considered. From the experience of building the optics control system of the ARGOS testbed, it is observed that the cost of the relay optics including beam combining control depends on the beam combining tolerances such as shearing error and tip/tilt error. The control difficulty caused by stringent beam combining tolerances defines the complexity of optics control actuators (ODLs and FSMs), and the quality of optics and structures.

An analogy-based cost estimating approach is employed to derive the CERs of sparse array spacecraft systems. Based on the detailed subsystem costs of the ARGOS, the CERs of the different configurations are developed. Nonrecurring and recurring items are identified and the CERs are adjusted for differences in size or complexity. The labor cost is also taken into consideration by categorizing the subsystem members into management, staff, and engineer levels. It is observed that the labor costs dominate the hardware cost. Among the subsystems, the two optics groups are the major cost driving factor. Even though passive optics (telescopes and optics supply) dominate the cost for few sub-apertures, active optics subsystem (the relay optics, actuators, and WFE sensor) dominate the cost for many sub-apertures. Without the complex beam combining part (the relay optics cost in the previous section) of a sparse interferometric array, the telescope cost of monolithic apertures is higher than a sparse array. Therefore, it is the relay optics that dominates the cost of a sparse array system. This cost analysis predicts emergence of a break-even point between monolithic systems and Golays. Past this break-even point, we can build a sparse array system with lower cost than a monolithic aperture system with the same effective diameter.

Chapter 7

CONCLUSION

7.1 Thesis Summary

The quest for finer angular resolution in astronomy will inevitably lead to larger apertures. Unfortunately, the primary mirror diameter for space telescopes is limited by the volume and mass constraints of current launch vehicles as well as the scaling laws of manufacturing costs. Efforts are ongoing to break this trend by employing exotic technologies such as deployed segmented mirror telescopes, and sparse aperture optics using interferometry. In order to better understand the technological difficulties involved in designing and building a sparse aperture array, the challenge of building a white light Golay-3 telescope was undertaken. The MIT Adaptive Reconnaissance Golay-3 Optical Satellite (ARGOS) project exploits wide-angle Fizeau interferometer technology with an emphasis on modularity in the optics and spacecraft subsystems.

The objective of the ARGOS project is to demonstrate the practicality of a modular architecture for space-based optical systems. To demonstrate a complete spacecraft in a 1-g environment, the ARGOS system is mounted on a frictionless air-bearing, and has the ability to track fast orbiting satellites like the International Space Station (ISS) as well as point stars. Modular architecture design emphasizes the use of replicated components and quick connections. The system consists of three identical apertures arranged in a Golay-3 distribution. The light from these telescopes is combined in a center module and transmitted to a Charge-Coupled Device (CCD). Wavefront sensing techniques are explored to

mitigate initial misalignment and to feed back real-time aberrations into the optical control loop. The end result is an image as good as the image received from a monolithic telescope using a single aperture. ARGOS operates autonomously and in a self-contained manner while a wireless ground station downloads images and telemetry information.

The Sparse-Aperture Optics/Control System (SOCS) design/implementation framework was introduced to facilitate identification and flow-down procedures of design parameters thereby achieving an optimum cost-effective design.

The SOCS framework begins with an analysis on the optical performance requirements such as Strehl Ratio, Angular Resolution, and Point Spread Function (Step 1). The Strehl Ratio requirement defines the overall optical performance of the system in terms of the RMS wavefront errors propagating throughout the system. The Strehl Ratio forms a basis on the construction of a wavefront error budget tree.

For imaging extended objects with an instant continuous u-v coverage, the Modulation Transfer Function (MTF) of an image is a better image evaluation criterion than the Point Spread Function. The inevitable contrast loss in the mid spatial frequency region on the MTF plot should be minimized, and the practical cut-off frequency of the MTF defines the angular resolution of a sparse aperture imaging system. Step 2 of the SOCS framework is to determine a proper array configuration that meets the optical performance requirements, especially the angular resolution requirement.

There are three primary beam combining errors that need to be controlled within certain tolerance values for a sparse interferometric array in order to achieve phased coherent beam combining. The beam combining errors are the piston errors, the tip/tilt errors and the pupil mapping errors. As the piston errors between the individual beams increase, two major deviations develop over the PSF envelope. First, the PSF mainlobe shifts in the direction of the piston error. Secondly, the peak intensity becomes reduced compared to the normal PSF without any piston errors (The Strehl Ratio decreases). The piston error tolerance is set to 0.1λ or 55nm to have the minimum deviations. The tip/tilt errors

between the apertures result in the piston difference as well. A tip/tilt tolerance of 0.35 μrad is chosen to achieve coherent beam combining. If coherent imaging is to be achieved over any significant FOV, the pupil mapping process must be performed such that the exit pupil is an exact scaled replica of the entrance pupil. Previously, 12μm was suggested for the shear error tolerance using an assumption of no magnification error. However, 12μm shear error cannot produce the FOV requirement of ARGOS (3 arcmin) for any range of magnification error as predicted in the previous plots. We can tighten shear error tolerance to meet the FOV requirement or we can relax the FOV requirement by shrinking the region of interest in the whole FOV. Therefore, the pupil mapping process is the primary limiting factor deciding the reasonable FOV of a sparse aperture interferometric array.

Once the allowable beam combining errors (Step 3 of the SOCS framework) are calculated, the wavefront error budget tree is constructed to correctly predict the performance of the final system. It is also used to keep track of the wavefront errors in design and manufacture of each optical component satisfying the optical performance requirements.

Chapter 4 elaborates on Steps 4 through 7 of the SOCS framework. The current optical layout of the system is as follows. Light shines in through the sub-aperture. The light continues through the telescope with a 210mm diameter until it hits the collimator which is inside the telescopes' baffle. The light then goes through the collimating lens producing a 21mm diameter beam. The light exits and hits a reflecting mirror mounted onto a three axis FSM that acts as an ODL as well. The light is then reflected to the stationary pyramidal mirror. The light beam then enters the beam combiner, and is focused onto the CCD.The overall cost of the ARGOS optics system could be significantly reduced by selecting one of the highest precision optics commercially off-the-shelf (COTS) telescope. However, it is necessary to customize a collimating lens to convert a Dall-Kirkham-type focal telescope to an afocal telescope with a magnification ratio of 10. The collimating lens is placed into the baffle of the telescope to make the system compact. When the parallel ODL design is coupled with a FSM, the resulting design is very simple and more cost-effective than the perpendicular design. This design cannot perform coarse OPD control,

but this design is more compact resulting in easier integration with the structural design. In addition, there is no need for a translational stage or rooftop mirror which reduces the cost and control complexity, and there is also a greater total reflectance since there are fewer mirrored surfaces. Fewer mirrored surfaces also lead to fewer structural mis-alignment errors. The pyramidal mirror turns all three beams 45 degrees into the beam combiner. A custom pyramidal mirror is chosen due to the cost of making one out of regular mirrors. Two options available for the beam combiner are either reflecting or refracting optics. The reflecting beam combiner is compact when compared to a refractor. Unfortunately, the secondary mirror of a Cassegrain telescope would partially block the three incoming beams in any possible configurations in order to obey the golden rule. The refracting telescope has many advantages. It allows for very simple relay optics. It is available COTS with high quality optics and is therefore relatively inexpensive.

Using the non-sequential ray tracing mode of ZEMAX, a complete ARGOS optics layout is constructed based on the optical specifications of a sub-aperture, pyramidal mirror, and the beam combining telescope. We intentionally perturb the sub-telescope or pyramidal mirror to determine allowable structural misalignments, and we compensate the tilt error by changing the tilt angle of the fold mirror attached to the FSM. 0.005 degrees or 15 arc-sec for sub-telescope structural misalignment is suggested. It is determined that there is no theoretical tilt tolerance for the pyramidal mirror as long as it does not exceed the maximum compensation range (0.01 degrees). The beam combiner was tilted along x and y axes while leaving other optical components perfectly aligned. This beam combiner misalignment is not correctable by optical actuators like FSMs. However, it turns out that we can tolerate up to 0.2 degrees error for the beam combiner; this is less stringent than other misalignment tolerances. The methods of designing a CCD system are introduced in Chapter 4 based on the FOV and SNR requirements.

The direct and indirect wavefront sensing techniques are introduced in Chapter 5. Phase Diversity technique is very simple, but computationally expensive. The neural network can be employed to increase the computation speed. Spot-based wavefront sensing is a

simple coarse adjustment technique to control the optical actuators until the brightest spot is achieve when a bright, isolated calibration star is being imaged. Elliptical spot based sensing is suggested in this thesis to properly identify the optics actuators without a need to identify each spot using masks. Prior to implementing a fine wavefront sensor, the elliptical spot-based sensing algorithms were implemented for coarse adjustments.

The three primary cost categories are the development of the spacecraft payloads and buses, deployment (i.e. launch) of the system, and the operation of the system. The cost of the sparse aperture payload can be further broken down into sub-apertures, the relay optics including beam combiner, and the CCD system. In order to derive the cost estimating relation-ships (CERs) of the relay optics portion of a sparse aperture array, identifying the theoretical relationships between the design parameters is considered. From the experience of building the optics control system of the ARGOS testbed, it is observed that the cost of the relay optics including beam combining control depends on the beam combining tolerances such as shearing error and tip/tilt error. The control difficulty caused by stringent beam combining tolerances defines the complexity of optics control actuators (ODLs and FSMs), and the quality of optics and structures.

An analogy-based cost estimating approach is employed to derive the CERs of sparse array spacecraft systems. Based on the detailed subsystem costs of the ARGOS, the CERs of the different configurations are developed. Nonrecurring and recurring items are identified and the CERs are adjusted for differences in size or complexity. The labor cost is also taken into consideration by categorizing the subsystem members into management, staff, and engineer levels. It is observed that the labor costs dominate the hardware cost. Among the subsystems, the two optics groups are the major cost driving factor. Even though passive optics (telescopes and optics supply) dominate the cost for few sub-apertures, active optics subsystem (the relay optics, actuators, and WFE sensor) dominate the cost for many sub-apertures. Without the complex beam combining part (the relay optics cost in the previous section) of a sparse interferometric array, the telescope cost of monolithic apertures is higher than a sparse array. Therefore, it is the relay optics that dominates the cost of a

sparse array system. This cost analysis predicts emergence of a break-even point between monolithic systems and Golays. Past this break-even point, we can build a sparse array system with lower cost than a monolithic aperture system with the same effective diameter.

7.2 Contributions

The following contributions are made by this thesis.

- Theoretical analysis on the characteristics of a sparse aperture array.
- Extensive design procedures of sparse aperture array imaging satellites considering coherent beam combining, modularity, cost-effective system design, and compactness for real flight hardware.
- Design and implementation of the first in-flight sparse aperture array addressing real world problems such as the vibrational coupling between a spacecraft structure and the wavefront errors propagating throughout the whole system.
- Quantitative life-cycle system cost analysis of a sparse aperture array satellite.
- Development of design methodologies in order to correctly flow down the system and science requirements to each design stage for coherent phased beam combining.
- Development of a schematic framework for a sparse interferometric array emphasizing cost-effectiveness by exploring modular architecture in spacecraft systems.

7.3 Recommendations for Future Work

The recommendations for future work are made firstly by the fact that the ACS and optics controllers are still being developed for ISS tracking capability and coherent phased beam combining.

The following work should be completed in order to achieve ISS tracking capability:

- *Complete system identification of the ARGOS structure*
  Modeling of the ARGOS testbed is a key to the success of the ACS control.

It also helps in understanding the vibrational coupling between a spacecraft structure and the wavefront errors propagating throughout the system.

- *Smart passive balancing system for the air-bearing system*
  ARGOS should be sufficiently balanced in order to keep the offsets between the center of gravity (C.G.) and the center of rotation (C.R.) within 1 micron. Calculation of the locations of the C.G. and the C.R. will improve the initial balancing process when the ARGOS testbed is re-assembled (deployment simulation). One suggested method is to place load cells between gaps of the air-bearing structure to measure the incident forces on the air-bearing pedestal. This information is used to locate the C.G. and the C.R.
- *Active balancing system*
  It is recommended that the control loop for the active balancing system be integrated into the main ACS control so that the controller can actively compensate the torque offsets.
- *Control system design for ISS tracking-ACS capability*
  Controller design with staged sensors (the electronic compass for a wide angle, and the centroiding view-finder).

The study in this thesis shows that the beam combining problem is the most challenging aspect of sparse optical arrays. The need for optical control is paramount due to tight beam combining error tolerances. The wavefront sensing/control requirements appear to be a major technology and cost driver. The following can be further examined for successful cohere beam combining.

- *Fine wavefront sensor using Phase Diversity*
  Implementation of the fine wavefront sensor is indispensable for coherent beam combining. Phase Diversity is promising due to its simplicity and compactness. However, Phase Diversity requires a complementary wavefront sensor to detect piston errors off by N times 2π.
- *Application of Neural Networks*
  Neural networks can be employed to increase the computation speed of Phase Diversity. Development of a controller taking the advantages of both conventional model-based controllers and neural networks without a priori model information is one topic to be explored in the future. This control design will have a robust performance for uncertainties in the plant and in the unknown disturbances, and will still have a fast convergence similar to a model-based controller.

REFERENCES

[16.684 CDIO] 16.684 students, ARGOS Adaptive Reconnaissance Golay-3 Optical Satellite Design Document, 16.684 Space Systems Product Development, Ver 1.0, May 2001.

[16.685 CDIO] 16.685 students, ARGOS Adaptive Reconnaissance Golay-3 Optical Satellite Design Document, 16.685 Space Systems Product Development, Ver 2.0, December 2001

[16.686 CDIO] 16.686 students, ARGOS Adaptive Reconnaissance Golay-3 Optical Satellite Design Document, 16.686 Space Systems Product Development, Ver 3.0, May 2002.

[AOA, 2002] Adaptive Optics Associates, Inc. The company homepage. http://www.aoainc.com.

[Bonaccini, 2001] Bonaccini, D., and Byard, P., "LBT Beam Combiner Optical Design Report1", http://medusa.as.arizona.edu/lbtwww/tech/oaa9301.htm, March 2001.

[Brown, 1997] Brown, R.G., and Hwang, P.Y.C, *Introduction to Random Signals and Applied Kalman Filtering*, 3rd edition, John Wiley & Sons, 1997.

[CCD University] CCD University website. http://www.ccd.com.

[Chanan, 1999] Chanan, G. and Troy M., "Strehl Ratio and Modulation Transfer Function For Segmented Mirror Telescopes as Functions of Segmented Phase Error", Applied Optics, Vol. 38 No. 31, November 1999.

[Chung, 2000a] Chung, S.-J. and Miller D.W.,"Design, Implementation and Operation of a Sparse Aperture Imaging Satellite Testbed", 16th AIAA/ASU Conference on Small Satellites, August, 2002.

[Chung, 2000b] Chung, S.-J., Miller D.W., and de Weck, O.L.,"Design and Implementation of Sparse Aperture Imaging Systems", SPIE Astronomical Telescopes and Instrumentation, Waikoloa, Hawaii, August, 2002.

[Colavita, 1999] Colavita, M.M., et al., " The Palomar Testbed Interferometer", The Astrophysical Journal, 510-505-521, January, 1999.

[De Hainaut, 1988] De Hainaut, C.R., "Design of a Wide Field of View Phased Array Telescope", Optical Engineering, Vol. 27 No.9, Setepmber 1988.

[De Hainaut, 1995] De Hainaut, C.R. et al, "Wide Field Performance of a Phased Array

Telescope", Optical Engineering, vol. 34 No.3, March 1995.

[de Weck, 2001] de Weck, O.L., Miller, D.W., Chung, S.-J., and Arnold, J., " Cost Modeling for Modular Optical Imaging System", Research Presentation, November 2001.

[Kong, 1998] Kong, E.M.,"Optimal Trajectories and Orbit Design For Separated Spacecraft Interferometry", S.M Thesis, Department of Aeronautics and Astronautics, Massachusetts Institute of Technology, 1998.

[Faucherre, 1989] Faucherre, M., Merkle, F., and Vakili, F., "Beam Combination in Aperture Synthesis from Space: Field of View Limitations and (u,v) Plane Coverage Optimization", New Technologies for Astronomy, pp 138-145, SPIE vol. 1130, 1989.

[Fender, 1988] Fender, J.S., and Carreras, R.A.,"Demonstration of an Optically Phased Telescope Array", Optical Engineering, Vol. 27 No.9, Setepmber 1988.

[Fienup, 2000] Fienup, J.R., "MTF and Integration Time versus Fill Factor for Sparse-Aperture Imaging Systems", Proceedings in Imaging Technology and Telescopes, Proc.SPIE 4091A-06, July 2000, Sandiego, CA.

[Flores, 1999] Flores, J.L., Paez, G. and Strojnik, M., "Design of a Diluted Aperture by Use of the Practical Cutoff Frequency", Applied Optics, Vol. 38, No. 28, October 1999.

[Franklin, 1997] Franklin, G.F., Powell, J.D., and Workman, M., *Digital Contorl of Dynamic Systems*, 3rd edition, Addison Wesley Longman, Inc., 1998.

[Geary, 1990] Geary, J.M., and O'Neil, B.D., "Polarization effects in Young Systems", Optical Engineering, Vol. 29 No.2, February 1990.

*[*Geary, 1995*]* Geary, J.M., *Introduction to Wavefront Sensors, SPIE Press Vol. TT 18, SPIE Optical Engineering Press, 1995*

[Genest, 1998] Genest, J., Tremblay, P., and Villemaire A., "Throughput of Tilted Interferometers", Applied Optics, Vol. 37 No. 21, July 1998.

[Golay, 1971] Golay, M., "Point Arrays Having Compact Non-redundant Autocorrelations", J.Opt Soc. Am., vol. 61, pp 272, 1971.

[Gonglewski, 1988] Gonglewski, J.D., et al, "System Design of a Wavefront Sensing Package for a Wide Field of View Optical Phased Array", Optical Engineering, Vol. 27 No. 9, September 1988.

[Goodman, 1996] Goodman, J.W., *Introduction to Fourier Optics*, 2nd edition, McGraw-Hill Companies, Inc., 1996.

[Harvey, 1985] Harvey, J.E., Silverglate, P.R., and Wissinger, A.B., "Optical Performance of Synthetic Aperture Telescope Configurations", Southwest Conference in Optics, pp 110-118, SPIE vol. 540, 1985.

[Harvey, 1988] Harvey, J.E., and Rockwell, R.A., "Performance Characteristics of Phased Array and Thinned Aperture Optical Telescopes", Optical Engineering, Vol. 27 No.9, September 1988.

[Hecht, 2001] Hecht E., *Hecht Optics*, 3rd ed., Addison-Wesley, 1998.

[Harvey, 1995] Harvey, J.E., and Ftaclas, C., "Field-of-view Limitations of Phased Telescope Arrays", Applied Optics, Vol. 34, No. 25, September 1995.

[Hege, 1985] Hege, E.K., et al., "Multiple Mirror Telescope as a Phased Array Telescope", Applied Optics, 24(16),2565-2576, 1985.

[Hentz, 1988] Hentz, K.P., "Multiple Beam Combination with Pupil Geometry Maintenance", Optical Engineering, Vol. 27 No. 9, September 1988.

[Hill, 2000] Hill, J.M., and Salinari, P., "The Large Binocular Telescope Project", Astronomical Telescopes and Instrumentation, pp 36-46, Munich, Germany, March 2000.

[Humphries, 1984] Humphries, C.M., Reddish, V.C., Walshaw, D.J., "Cost scaling laws and their origin: design strategy for an optical array telescope", Proceedings of the IAU Colloquium No. 79, April 9-12, 1984.

[Jilla, 2002] Jilla, C.D., "A Multiobjective, Multidisciplinary Design Optimization Methodology for the Conceptual Design of Distributed Satellite Systems", Ph.D. Thesis, Department of Aeronautics and Astronautics, MIT, SSL Report #6-02, 2002.

[Kahan, 1998] Kahan, M.A. and Targrove, J.D., "Cost modeling of large spaceborne optical systems", SPIE Conference on Space Telescopes and Instruments V, Kona, March, 1998.

[Kendrick, 1994] Kendrick R.L., Acton D.S., and Duncan A.L., "Phase-Diversity Wavefront Sensor for Imaging Systems", Applied Optics, Vol. 33 No. 27, September 1994.

[Löfdahl, 1996] Löfdahl, Mats G., "Phase Diversity Wavefront Sensing and Image Restoration Applied to High-Resolution Solar Observations", Doctoral Dissertation 1996, Stockholm Observatory, Stockholm University.

[Loiseau, 1996] Loiseau, S. and Shaklan S., "Optical Design, Modelling and Tolerancing of a Fizeau Interferometer Dedicated to Astrometry", Astronomy and Astrophysics Supplement Series, 117, 167-178, 1996.

[Lyon, 1999] Lyon, R.G., "DCATT Wavefront Sensing and Optical Control Study", Developmental Comparative Active Telescope Testbed Report WFSC-0001, February, 1999.

[Mennesson, 1997] Mennesson, B., and Mariotti, J.M., " Array Configurations for a Space Infrared Nulling Interferometer Dedicated to the Search for Earthlike Extrasolar Planets", ICARUS 128, pp 202-212, 1997.

[Meinel, 1979] Meinel, A.B.,"Cost Scaling Laws Applicable to Very Large Telescopes", SPIE Proceedings Vol. 172, 1979.

[Paxman, 2000] Paxman, R. , "Wavefront Sensing for Deployable-Optic Systems", Wavefront Sensing and Controls 2000 Conference, Kamuela, Hawaii, November 2000.

[Powers, 1997] Powers, M. et al, "Assessment of a Large Aperture Telescope Trade Space and Active Optomechanical Control Architecture", Proceedings of the 1997 IEEE Aerospace Conference, pp 197-229, Feb 1-2, 1997.

[Redding, 1998] Redding, D.C., et al, "Wavefront sensing and control for a Next-Generation Space Telescope", Proc. SPIE Vol. 3356, pp.758-772, 1998.

[Roddier, 1999] Roddier, F., and Ridgway, S., "Filling Factor and Signal-to-Noise Ratios in Optical Interferometric Arrays", The Astronomical Society of the Pacific, III, pp 990-996, August 1999.

[Rousselet-Perraut, 1997] Rousselet-Perraut, K., et al, "Polarization Effects in Aperture Synthesis Arrays", Optical Engineering 36 (4), 980-987, April 1997.

[Rutten, 1999] Rutten, H.G.J. and Van Venrooij, M.A.M, *Telescope Optics*, Willmann-Bell, Inc., 1999.

[Sabatke, 2002] Sabatke, E.M. and Sasian, J.M., "Phase Theory for Multiple Aperture Systems", Optical Engineering 41(3), pp 647-655, March, 2002.

[Scharmer, 2000] Scharmer, G.B, et al, "A Workstation Based Solar/Stellar Adaptive Optics System", SPIE Proceedings, 4007-105, Adaptive Optical Systems Technologies, Wizinowich, ed., Munich, Germany, March 2000.

[Schöller, 2000] Schöller M., Wilhelm, R., and Koehler B., "Modeling the Imaging Process in Optical Stellar Interferometers", Astronomy and Astrophysics Supplement Series 144, 541-552, 2000.

[Smith, 2000] Smith, W.J., *Modern Optical Engineering*, 3rd ed, McGraw-Hill, 2000.

[Voelz, 1988] Voelz, D.G., et al, "Implementation of Optical Path Length and Tilt Control in a Phased Array System", Optical Engineering, Vol. 27 No. 9, September 1988.

*[*Weaver, 1988*]* Weaver L.D, Fender, J.S., and C.R. De Hainaut, "Design Considerations for Multiple Telescope Imaging Array", Optical Engineering, Vol. No.9, September 1988.

[Wertz, 1999] Wertz J.R. and Larson, W.J., *Space Mission Analysis and Design*, 3rd ed., Microcosm Press, 1999,

[Zarifis, 1999] Zarifis, V., et al, " The Multi Aperture Imaging Array", ASP Conf. Series 194, Working on the Fringe: Optical and IR Interferometry from Ground and Space, Unwin and Stachnik, eds, pp. 278, 1999.

[Zemax, 2000] Zemax Optical Design Program User's Guide Version 10.0, Focus Software,inc., 2000

Appendix A

ARGOS REQUIREMENTS DOCUMENT

A.1 Introduction

Astronomers currently use large monolithic telescopes, such as the Hubble Space Telescope (HST), to capture accurate and detailed images of remote areas. Advancing this technology further, however, is no longer feasible due to cost and size limitations. In order to continue improving image quality, other options must be explored and developed.

One alternative design is based on combining several smaller telescopes in a modular satellite that will provide superior quality to current systems. A modular architecture would not only address concerns with cost and size limitations, but would also provide easy accessibility to parts for replacement or future upgrades.

The ARGOS project is focused on demonstrating that a telescope using a modular architecture is a practical solution. After investigating different architectures, the ARGOS project will pursue one design through the assembly and test stage. Although the ultimate use of the ARGOS design is a space-based telescope looking at the Earth from low earth orbit (LEO), for logistical purposes the model will be tested in a simulated space environment that views space from Earth.

A.2 Customer Requirements

In order to address the concerns of cost and size limitations, the NRO invited proposals of designs that meet the following requirements:

2.1 Reduce the time required to formalize and validate system designs without shrinking the trade space.

2.2 Reduce the cost and schedule associated with the fabrication, integration, and testing of complex space systems.

2.3 Reduce the cost of low-volume runs by using new design and manufacturing methods.

2.4 Develop methods to better identify, assess, and manage the risks of developing and operating technically advanced space systems.

2.5 Develop an optical control system that can also be used to access the real-time data and code for self-diagnosis, fault detection, software reconfiguration and use of adaptive algorithms.

A.3 ARGOS Proposed Approach

This section illustrates the ARGOS project's approach to addressing the customer's requirements. The ARGOS project will:

3.1 Elevate mission customization to the module assembly level and capture the cost impacts in a quantitative systems trade analysis.

3.2 Utilize production and test learning curve savings to analyze design.

3.3 Implement design modules that can be used by multiple missions, thereby increasing production volume and associated savings.

3.4 Develop methods to better identify, assess, and manage the risks of developing and operating technically advanced space systems.

3.5 Develop methods to reduce the operational cost of space systems such as self-diagnostics, autonomous operations, fault detection/correction, and remote software-reconfigurable or "virtual" hardware systems.

A.4 Flight Article Description

The ARGOS hardware will have three subapertures arranged in a Golay-3 configuration. The telescope will capture images of celestial objects from an Earth-based testing facility by reorienting and refocusing itself on targets. The satellite will be capable of operating in both autonomous and manual control modes and will continuously send data and telemetry to an Earth-based control center. The design of our satellite will maximize the usage of COTS items. All hardware on board the telescope will be standardized to facilitate the repair and modification of individual components in the future.

A.5 Mission Statement

In order to address the customer requirements, we have condensed the primary points into the following mission statement:

Demonstrate the practicality of a modular architecture for space-based optical systems.

Below, the mission statement is expanded into its key components in order to understand what is expected to result from the ARGOS project.

5.1 Demonstrate implies operating the telescope in a mode representative of a real world application.

> 5.1.1 The telescope must be able to capture a real image (e.g. Planet, International Space Station (ISS), Earth observing, binary systems).
>
> 5.1.2 The satellite must be able to be operated remotely.

5.2 Practicality implies that the design competes with current technology's quality to cost ratio.

5.2.1 The ARGOS project must show that the design's angular resolution as a function of cost is comparable to current systems.

5.2.2 The design must also have an ease of manufacturability comparable to current systems.

5.3 Modular refers to both the architecture and the optics.

5.3.1 Modular architecture implies assembling the system out of modules (identical, similar or dissimilar) that facilitate fabrication, integration, and testing.

5.3.1.1 The design should maximize simplicity of interfaces.

5.3.1.1.1 The design must strive for standardization of its components.

5.3.1.1.2 The satellite must maximize usage of commercial off the shelf (COTS) items.

5.3.2 Modularity in optics entails the generation of imagery data from similar sub-apertures as opposed to a single monolithic system.

5.3.2.1 Active optics control must be able to coherently combine the light from the separate apertures.

5.4 Space based implies that the system must exhibit the functionality of a real satellite.

5.4.1 The satellite must be able to track a slewing object.

5.4.2 The satellite must be self-contained (power restrictions, propellant, communications, contamination protection, time critical data transfer).

A.6 Constraints

The ARGOS program must operate within certain rigid boundaries and ensure that each aspect of the final design meets the following constraints:

6.1 Due to the air bearing:

6.1.1 The satellite must weigh less than 228.95 kg.

6.1.2 The satellite must withstand a 60-degree (full cone) rotation with respect to the vertical axis.

6.2 Due to money:

6.2.1 Entire project cannot exceed USD $150,000.

6.3 Due to time:

6.3.1 Milestones must be achieved by dates outlined in CDIO project plan.

6.4 Due to design:

6.4.1 The design must include a telescope array of a Golay-3 configuration.

A.7 Systems Engineering Requirements

In order to realize the mission statement, systems engineering requirements have been derived and divided into functional and operational requirements that the ARGOS project must satisfy.

7.1 Functional Requirements

7.1.1 The angular resolution of the system must be 0.35 arc-seconds or better. [5.1.1]

7.1.2 The telescope must be able to detect light in the range of 400-700 nm (visible light). [5.1.1]

7.1.3 The field of view (FOV) of the system should be approximately 3-10 arc-minutes. [5.1.1]

7.1.4 The telescope must have a practical visual power range of 72X-400X. [5.1.1]

7.1.5 The telescope must be able to detect images brighter than +15 stellar magnitude. [5.1.1]

7.1.6 The system must have a signal to noise ratio of 100. [5.1.1]

7.1.7 The system must automatically provide health status (telemetry) and operations data. [5.1.2]

7.1.8 The system must have a pointing accuracy of +/- 10 arc-seconds.-relaxed to 1 arcmin. [5.1.1]

7.1.9 The system must be able to acquire a target within 2 minutes. [5.1.1]

7.1.10 The system must be able to relay information at a rate of 300 Kilobytes/sec. [5.1.2]

7.1.11 The system must be able to operate in both manual and autonomous control modes. [5.1.2]

7.2 Operational Requirements

7.2.1 The system must have a field of regard equal to 60 degrees (full cone). [5.1.1]

7.2.2 The ground station must receive the image captured by the telescope in less than 10 minutes. [5.4.2]

7.2.3 The telescope must be able to capture images at a maximum imaging rate of 20 images/hour. [5.1.2]

7.2.4 System must be able to be operated remotely by a wireless console from a distance 20 meters. [5.1.2]

7.2.5 The satellite must be able to operate autonomously for up to 1 continuous hour. [5.4.2]

A.8 Subsystem Requirements

To meet the functional and operational requirements above, each subsystem has been given a set of deliverables that must be accomplished in order to achieve success.

8.1 The Active Optics Subsystem will provide for the following:

8.1.1 Maximum tolerance of 55 nm for phase error. [7.1.1]

8.1.2 Maximum tolerance of 0.025 arc-seconds for tilt error. [7.1.1]

8.1.3 Resolution for piston actuators finer than 5 nm. [7.1.1]

8.1.4 Range for the piston actuator at least 12 microns. [7.1.1]

8.1.5 Resolution of the fast steering mirrors (FSM) must be 0.0025 arc-seconds. [7.1.1]

8.1.6 Range of the FSM must be at least 0.5 degrees. [7.1.1]

8.2 The Passive Optics Subsystem will provide for the following:

8.2.1 Angular resolution for the entire system under ideal conditions is 0.25 arc-seconds. [7.1.1]

8.2.2 Wavelength range of 400-700 nm (visible light). [7.1.2]

8.2.3 Field of view (FOV) for the satellite about 10 arc-minutes. [7.1.3]

8.2.4 The telescope must have a practical visual power range of 72X-400X. [7.1.4]

8.2.5 Capability of capturing an object with stellar magnitude brighter than +15. [7.1.5]

8.2.6 Signal to noise ratio of 100. [7.1.6]

8.2.7 The ratio of effective collecting area and geometric area should be larger than 85% (Aeff=Ageo*R^(n)). [7.1.6]

8.2.8 CCD with a capacity of TBD and a quantum efficiency of TBD. [7.1.6]

8.2.9 Integration time 30 ms to 6 minutes. [7.1.6]

8.2.10 Encircled energy of the mainlobe PSF at least 65%. [7.1.1]

8.2.11 Ensure a frame rate of TBD. [7.2.3]

8.2.12 Ensure a shutter speed of TBD. [5.1.1]

8.2.13 Dedicate more than 1 pixel to angular resolution element, which implies quality factor < 1. [7.1.1]

8.2.14 Quality to cost analysis shows design to be comparable current state of the art systems [5.2.1]

8.3 The Attitude Control Systems Subsystems should provide for the following:

8.3.1 Pointing stability of 0.025 arc-seconds. [7.1.1]

8.3.2 Pointing accuracy of +/- 10 arc-seconds without optics CCD, and one arcmin for ACS system only [7.1.8]

8.3.3 Ability to desaturate system momentum within 45 seconds. [7.1.9, 7.2.5]

8.3.4 Mechanism to determine system attitude within 3 seconds. [7.1.9, 7.2.5]

8.3.5 Period of autonomy should be no less than 60 minutes. [7.2.5]

8.3.6 Maximum slew rate of at least 1.5 degrees per second. [7.1.9]

8.3.7 Sufficient torque to counteract the center of mass-center of rotation off-set. [7.1.9]

8.4 The Structures Subsystems should provide for the following:

8.4.1 Vertical displacement less than 1 mm due to thermal and force loads. [7.1.1]

8.4.2 Angular displacement less than 0.5 degrees for each module. [7.1.1]

8.4.3 Sufficiently small offset between center of mass and center of rotation. [7.1.9]

8.5 The Power, Avionics, and Software Subsystems should provide for the following:

8.5.1 Software that is able to control different subsystems simultaneously. [7.1.11, 7.2.5]

8.5.2 Block diagram of CPU and internal data bus/command structure. [7.2.5]

8.5.3 Prototype power system with simulated loads. [7.2.5]

8.5.4 Diagram of system wiring. [5.3.1]

8.6 The Science, Operations, and Communications Subsystems should provide for the following:

8.6.1 Method to manually control the satellite. [7.1.11]

8.6.2 Telemetry report from the satellite. [7.1.7]

8.6.3 List of potential targets. [5.1.1]

8.6.4 Baud rate of sufficient speed. [7.1.10, 7.2.2]

8.6.5 Onboard storage data size for images between transmissions. [7.2.3]

8.6.6 Map of the bandwidth structure distributed between telemetry and data. [7.1.7]

A.9 Guidelines

9.1 Standard fabrication techniques should be maximized to reduce cost.

9.1.1 Design should use COTS items whenever possible.

9.1.2 Complex components should be outsourced to industrial manufacturers.

9.2 Interacting subsystems should agree upon compatible interfaces.

9.3 The design should facilitate repair and upgrades.

Appendix B

OPD SENSITIVITY ANALYSIS OF OPTICS STRUCTURES

The OPD sensitivity analysis using Zemax tolerancing is performed as discussed in Section 4.4.1 on page 152.

Units are Millimeters. Angles in Degrees
Mode : Sensitivities
Optimization Cycles : Automatic mode
Merit: User defined merit function
Nominal Merit Function (MF) is 1803.04827079
(Optical Pathlength from the entrance pupil of a subtelescope till the entrance pupil of the beam combiner)
Test wavelength: 587.6 nm

Fields: User Defined Angle in degrees

#	X-Field	Y-Field	Weight	VDX	VDY	VCX	VCY
1	0.000E+000	0.000E+000	1.000E+000	0.000	0.000	0.000	0.000
2	0.000E+000	2.500E-002	1.000E+000	0.000	0.000	0.000	0.000
3	2.500E-002	0.000E+000	1.000E+000	0.000	0.000	0.000	0.000
4	0.000E+000	0.000E+000	1.000E+000	0.000	0.000	0.000	0.000
5	0.000E+000	-2.500E-002	1.000E+000	0.000	0.000	0.000	0.000

Sensitivity Analysis:

(1) Sub telescope Tilt X, Tilt Y, Tilt Z(Rotation)

					Minimum				Maximum		
Type	Sf1	Sf2	Sf3	Value	MF	Change	Value	MF	Change
TETX	1	9		-0.010000	1802.98043	-0.067845	0.010000	1803.12041	0.072139
TETY	1	9		-0.010000	1803.05040	0.002126	0.010000	1803.05040	0.002126
TETZ	1	9		-0.010000	1803.04827	0.000000	0.010000	1803.04827	0.000000

(2) FSM (The first FM) Tilt X, Tilt Y, Tilt Z(Rotation)

				Minimum			Maximum		
Type	Sf1	Sf2	Sf3	Value	MF	Change	Value	MF	Change
TETX	11	11		-0.010000	1803.04142	-0.006852	0.010000	1803.05518	0.006908
TETY	11	11		-0.010000	1803.04828	0.000013	0.010000	1803.04828	0.000013
TETZ	11	11		-0.010000	1803.04827	0.000000	0.010000	1803.04827	0.000000

(3) FSM (1st FM) Decenter X, Decenter Y

				Minimum			Maximum		
Type	Sf1	Sf2	Sf3	Value	MF	Change	Value	MF	Change
TEDX	10	10		-0.001000	1803.04827	0.000000	0.001000	1803.04827	0.000000
TEDY	10	10		-0.001000	1803.04759	-0.000681	0.001000	1803.04895	0.000681

(4) Pyramidal FM (2nd FM) Tilt X, Tilt Y, Tilt Z(Rotation)

				Minimum			Maximum		
Type	Sf1	Sf2	Sf3	Value	MF	Change	Value	MF	Change
TETX	14	14		-0.010000	1803.04984	0.001569	0.010000	1803.04671	-0.001561
TETY	14	14		-0.010000	1803.04827	0.000002	0.010000	1803.04827	0.000002
TETZ	14	14		-0.010000	1803.04827	0.000000	0.010000	1803.04827	0.000000

(5) Pyramidal FM (2nd FM) Decenter X, Decenter Y

				Minimum			Maximum		
Type	Sf1	Sf2	Sf3	Value	MF	Change	Value	MF	Change
TEDX	13	13		-0.001000	1803.04827	0.000000	0.001000	1803.04827	0.000000
TEDY	13	13		-0.001000	1803.04759	-0.000681	0.001000	1803.04895	0.000681

(6) Beam Combiner Tilt X, Tilt Y, Tilt Z(Rotation)

				Minimum			Maximum		
Type	Sf1	Sf2	Sf3	Value	MF	Change	Value	MF	Change
TETX	17	24		-0.010000	1803.04491	-0.003361	0.010000	1803.05163	0.003361
TETY	17	24		-0.010000	1803.04827	0.000000	0.010000	1803.04827	0.000000
TETZ	17	24		-0.010000	1803.04827	0.000000	0.010000	1803.04827	0.000000

Worst offenders:

Type	Sf1	Sf2	Sf3	Value	MF	Change
TETX	1	9		0.010000	1803.12041	0.072139
TETX	11	11		0.010000	1803.05518	0.006908
TETX	17	24		0.010000	1803.05163	0.003361
TETY	1	9		-0.010000	1803.05040	0.002126
TETY	1	9		0.010000	1803.05040	0.002126
TETX	14	14		-0.010000	1803.04984	0.001569
TEDY	10	10		0.001000	1803.04895	0.000681
TEDY	13	13		0.001000	1803.04895	0.000681

TETY 11 11 -0.010000 1803.04828 0.000013
TETY 11 11 0.010000 1803.04828 0.000013

Nominal Merit Function : 1803.048271
Estimated change : 0.070498
Estimated Merit Function : 1.80E+003

Merit Statistics:
Mean : 1803.048487
Standard Deviation : 0.015762

Appendix C

ARGOS COST AND MASS TABLE

This is the actual cost spent to develop the ARGOS testbed.

Modular Space Telescope

Sub-System Budget: Cost

Passive Optics

Item	Unit Cost (US$)	Method	Quantity Bought	Anticipatory Cost (US$)	Actual Cost (US$)
Takahashi Telescope (Used)	$2,339.00	Database	1	$2,339.00	$2,339.00
Takahashi Telescope	$2,800.00	Database	2	$5,600.00	$5,600.00
Beam Combiner	$3,623.60		1	$3,623.60	$3,623.60
Collimator	$2,300.00		4	$9,200.00	$9,200.00
Collimator Engineering	$2,500.00		1	$2,500.00	$2,500.00
Collimmator Mounting	$500.00		3	$1,500.00	$1,500.00
Pyramidal Mirror	$3,000.00		1	$3,000.00	$3,000.00
Optical Instruments (Fold Mirrors etc.)	$1,948.00		1	$1,948.00	$1,948.00
Charged Coupled Device (CCD) Dragonfly	$1,495.00		3	$4,485.00	$4,485.00
Firewire Card	$90.00		2	$180.00	$180.00
Flock Paper/Adhesive	$105.70		1	$105.70	$105.70
Compression Ring/Adapter Sleeve	$131.50		1	$131.50	$131.50
Optical Posts/Shear Plate	$1,617.00		1	$1,617.00	$1,617.00
Telephoto Lens	$500.00		1	$500.00	$500.00
Total				$36,729.80	$36,729.80

Color Codes
From database or catologue
Estimations
Not sure/ Don't know

Active Optics

Item	Unit Cost (US$)	Method	Quantity Bought	Anticipatory Cost (US$)	Actual Cost (US$)
Fast Steering Mirror (FSM)	$2,575.00		3	$7,725.00	$7,725.00
Precision Mount For Combiner	$3,000.00		1	$3,000.00	$3,000.00
1 Channel PZT Amplifier	$515.00		9	$4,635.00	$4,635.00
Mirror Mounts w/ High Precision screws	$177.00		4	$708.00	$708.00
Pyramidal Mirror Mount Combo	$1,048.00		1	$1,048.00	$1,048.00
Test PC	$841.67		1	$841.67	$841.67
Optics Electronics	$583.81		1	$583.81	$583.81
Amplifier Boards	$45.00		6	$270.00	$270.00
Cleaning Materials	$54.90		1	$54.90	$54.90
Electronic Focuser and Adapter	$683.90		1	$683.90	$683.90
Optics Hardware	$13.27		1	$13.27	$13.27
Large Knobs	$4.00		10	$40.00	$40.00
DAC Channels	$259.38		12	$3,112.50	$3,112.50
Total				$22,716.05	$22,716.05

Attitide Control System

Item	Unit Cost (US$)	Method	Quantity Bought	Anticipatory Cost (US$)	Actual Cost (US$)
Fly Wheels	$300.00		3	$900.00	$900.00
Rate Gyros	$0.00	SSL	1	$0.00	$0.00
Motor, Tachometers, Amplifiers	$802.00		3	$2,406.00	$2,406.00
TCM-2-50 (Tilt Inclinometer/Magnetometer)	$769.00	www.pnicorp.com	1	$1,500.00	$1,500.00
TCM-2-20 (Tilt Inclinomter/Magnetometer)	$699.00	www.pnicorp.com	1		
Active Balancer	$2,163.33	Catalogue	3	$6,490.00	$6,490.00
Lab/Power Supplies	$442.13		1	$442.13	$442.13
DAC Channels	$259.38		3	$778.14	$778.14
ADC Channels	$281.25		6	$1,687.50	$1,687.50
Filters for Rate Gyros	$283.00		1	$283.00	$283.00
Balancing Fly Wheels	$0.00		1	$0.00	$0.00
Total				$14,486.77	$14,486.77

Structures

Item	Unit Cost (US$)	Method	Quantity Bought	Anticipatory Cost (US$)	Actual Cost (US$)
Collar	$583.33	CMS	3	$1,750.00	$1,750.00
Translation Stages	$234.00		9	$2,106.00	$2,106.00
Bread Boards	$176.40		4	$705.60	$705.60
Adapter Plates	$38.00		10	$380.00	$380.00
Nuts, Bolts, Tools, Cables, Connections etc.	$377.61	?	1	$377.61	$377.61
Model SRA250 Spherical Air Bearing	$12,900.00	Paul Bauer	1	$12,900.00	$12,900.00
Pedestal for Spherical Air Bearing	$980.00	Paul Bauer	1	$980.00	$980.00
Air Supply Filter	$1,870.00	Paul Bauer	1	$1,870.00	$1,870.00
Vibration Suppression Mounts	$2.41		15	$36.20	$36.20
Angle Braces	$199.00		6	$1,194.00	$1,194.00
Machine Shop	$7,059.00		1	$7,059.00	$7,059.00
Center Structure Assembly	$700.00	CMS	1	$700.00	$700.00
Total				$30,058.41	$30,058.41

Science, Operations, & Communications

Item	Unit Cost (US$)	Method	Quantity Bought	Anticipatory Cost (US$)	Actual Cost (US$)
WLS LAN PCI Cards 11 Mbps	$229.99		1	$229.99	$229.99
Wireless Broadband Gateway	$249.99		1	$249.99	$249.99
Wireless LAN card	$130.51		1	$130.51	$130.51
Portable Computer	$1,697.00		1	$1,697.00	$1,697.00
Total				$2,307.49	$2,307.49

Power, Avionics, & Software

Item	Unit Cost (US$)	Method	Quantity Bought	Anticipatory Cost (US$)	Actual Cost (US$)
PC Power Supply	$165.45		2	$330.90	$330.90
Batteries	$165.13		10	$1,651.30	$1,651.30
Chargers	$130.30		6	$781.80	$781.80
Power Electronics	$412.66		1	$412.66	$412.66
Gas Gauge Chip Circuit Boards	$43.88		10	$438.75	$438.75
Misc PC Parts for test computer	$527.67		1	$527.67	$527.67
Shuttle AK31 Motherboard	$102.00		1	$102.00	$102.00
AMD 1.4 GHz Athlon CPU	$138.50		1	$138.50	$138.50
Mushkin 512 MB DDR RAM	$273.50		3	$820.50	$820.50
Simpletech 512 MB Compact Flash Card	$352.99		1	$352.99	$352.99
TI Code Composer Studio: TMD S324685C-07	$999.00	Paul Bauer	0.5	$499.50	$499.50
TI 6701 EVM: TMD X32006701	$1,495.00	Paul Bauer	2	$2,990.00	$2,990.00
SMT 320 4 SLOT PCI MOTHERBOARD	$1,435.50	Paul Bauer	1	$1,435.50	$1,435.50
SMT 6012 Drivers for 6701	$382.50	Paul Bauer	1	$382.50	$382.50
HEPC8 Module Carrier	$3,125.00		1	$3,125.00	$3,125.00
HEGD14 DAC	$2,075.00		2	$4,150.00	$4,150.00
HEGD2 ADC	$2,250.00		1	$2,250.00	$2,250.00
Cables/Connectors	$200.00		1	$200.00	$200.00
MagicRAM Internal IDE Compact Flash Adapter	$90.00		1	$90.00	$90.00
DSP Board Repair	$450.00		1	$450.00	$450.00
HESDP Software Developers Pack	$1,600.00		1	$1,600.00	$1,600.00
Heron4 (6701)	$2,000.00		1	$2,000.00	$2,000.00
RTX Training	$3,000.00		1	$3,000.00	$3,000.00
Total				$27,729.57	$27,729.57

Miscellaneous

Item	Unit Cost (US$)	Method	Quantity Bought	Anticipatory Cost (US$)	Actual Cost (US$)
Office Tools	$426.74		1	$426.74	$426.74
Dspace board	$1,945.00		1	$1,945.00	$1,945.00
Summer '01 Supplies	$257.64		1	$257.64	$257.64
Air Compressor	$304.95	Paul Bauer	1	$304.95	$304.95
Total				$2,934.33	$2,934.33

Modular Space Telescope

Sub-System Budget: Mass

Passive Optics

Item	Unit Mass (Kg)	Method	Quantity Used	Anticipatory Mass (Kg)	Actual Mass (kg)
Takahashi Telescope	8.1	Database	3	24.3	24.3
Beam Combiner	4		1	4	6
Charged Coupled Device (CCD)	1.5	?	1	1.5	0.5
Charged Coupled Device (CCD) (used)	1.5	?	1	1.5	0
Collimator Mounting					
Pyramidal Mirror				7	5
Optical Instruments (Fold Mirrors etc.)					
Firewire Card					
Telephoto Lens				1	0.7
Collimator	0.25		3	0.75	
Total				40.05	36.5

Active Optics

Item	Unit Mass (Kg)	Method	Quantity Used	Anticipatory Mass (Kg)	Actual Mass (kg)
Optical Instruments (Fold Mirrors etc.)	5	?	1	5	
Phase, Beam Tilting Sensing (Quad Cell, A)	0.5	?	3	1.5	
Fast Steering Mirror (FSM)	0.5	Database	3	1.5	
Voice Coil (VC)	0.5	?	3	1.5	
Piezoelectric Translator (PZT)	0.5	?	3	1.5	
1 Channel PZT Amplifier					
Precision Mount For Combiner					
Pyramidal Mirror Mount Combo					
Mirror Mounts w/ High Precision screws					
Total				11	0

Structures

Item	Unit Mass (Kg)	Method	Quantity Used	Anticipatory Mass (Kg)	Actual Mass (kg)
Hardware & Materials	24	?	1	24	24
Nuts, Bolts, Tools, Cables, Connections etc.	4	?	1	4	4
Additional Hardware	15		1	15	
Total				43	28

Science, Operations, & Communications

Item	Unit Mass (Kg)	Method	Quantity Used	Anticipatory Mass (Kg)	Actual Mass (kg)
Wireless LAN	0.5	?	1	0.5	0.5
Total				0.5	0.5

Power, Avionics, & Software

Item	Unit Mass (Kg)	Method	Quantity Used	Anticipatory Mass (Kg)	Actual Mass (kg)
Battery	1.868832	?	6	11.212992	11.212992
PC Power Supply	3	?	1	3	
DAC SMT357	0.2		2	0.4	
ADC SMT356	0.2		1	0.2	
SMT 320 4 SLOT PCI MOTHERBOARD	0.4		1	0.4	
PC Motherboard and Processor	0.5		1	0.5	
SMT 375 6701 TIM Module	0.3		1	0.3	
Cables/Connectors	1.5		1	1.5	
Gas Gauge Chip	0.005		6	0.03	
Wires	2		1	2	
Relays, switches, connectors, etc	0.1		1	0.1	
Total				19.642992	11.212992

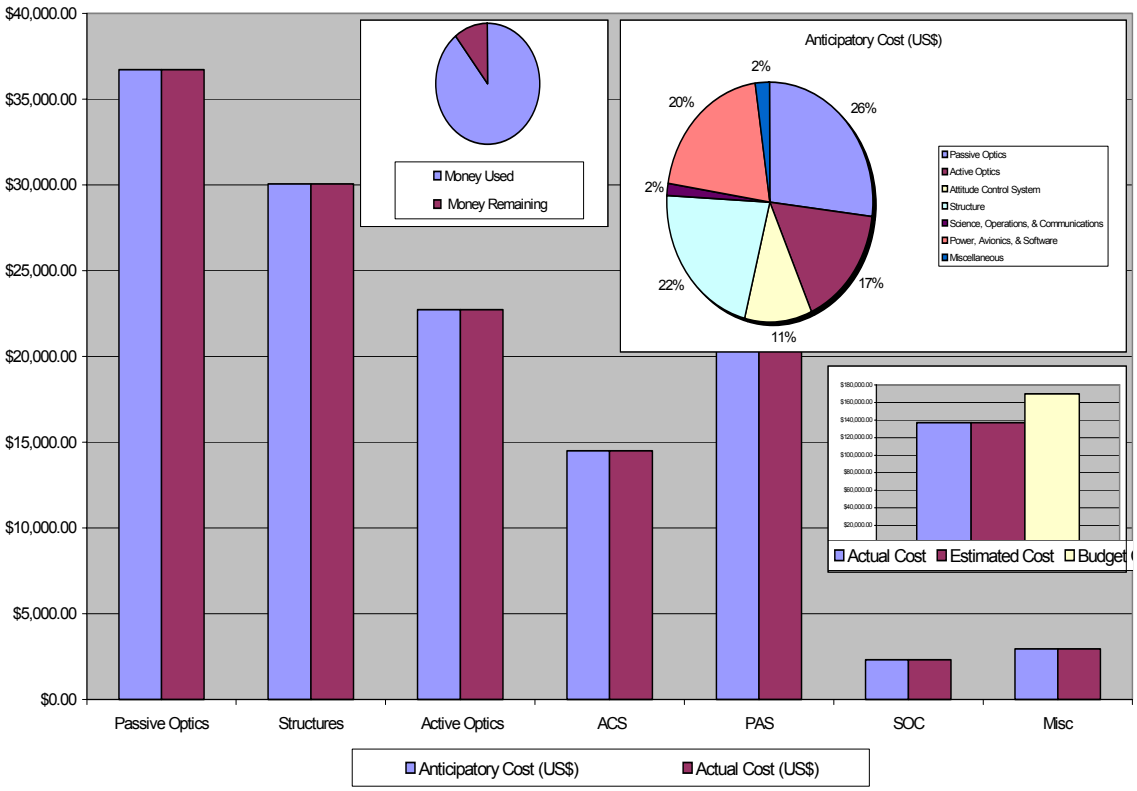
$40,000.00
$35,000.00
$30,000.00
$25,000.00
$20,000.00
$15,000.00
$10,000.00
$5,000.00
$0.00
Passive Optics
Structures
Active Optics
ACS
PAS
SOC
Misc
Anticipatory Cost (US$)
Actual Cost (US$)
Money Used
Money Remaining
Anticipatory Cost (US$)
2%
26%
20%
2%
22%
17%
11%
Passive Optics
Active Optics
Attitude Control System
Structure
Science, Operations, & Communications
Power, Avionics, & Software
Miscellaneous
Actual Cost
Estimated Cost

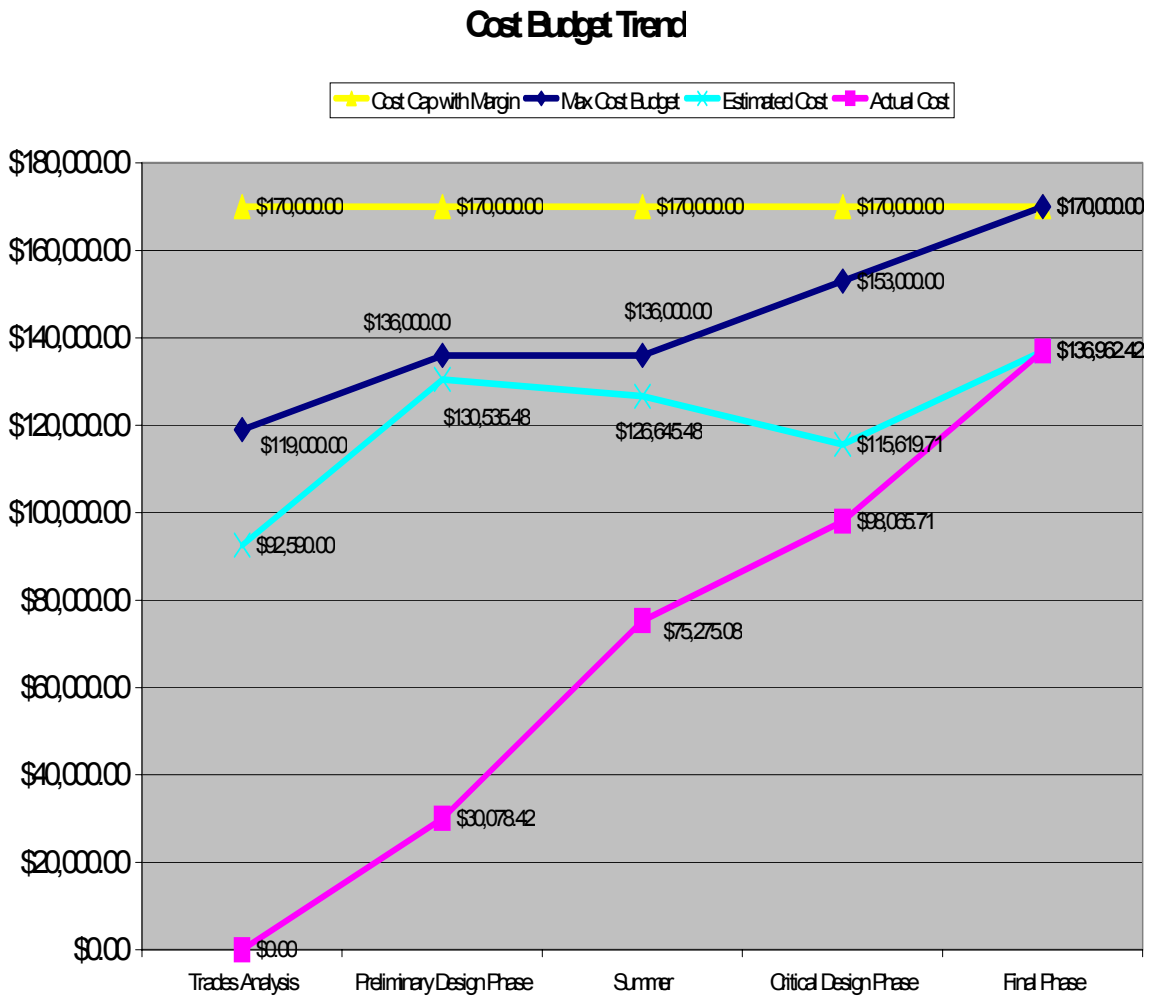
Cost Budget Trend
Cost Cap with Margin
Max Cost Budget
Estimated Cost
Actual Cost
$180,000.00
$160,000.00
$140,000.00
$120,000.00
$100,000.00
$80,000.00
$60,000.00
$40,000.00
$20,000.00
$0.00
$170,000.00
$170,000.00
$170,000.00
$170,000.00
$170,000.00
$119,000.00
$136,000.00
$136,000.00
$153,000.00
$136,962.42
$92,590.00
$130,535.48
$126,645.48
$115,619.71
$98,065.71
$75,275.08
$30,078.42
$0.00
Trades Analysis
Preliminary Design Phase
Summer
Critical Design Phase
Final Phase

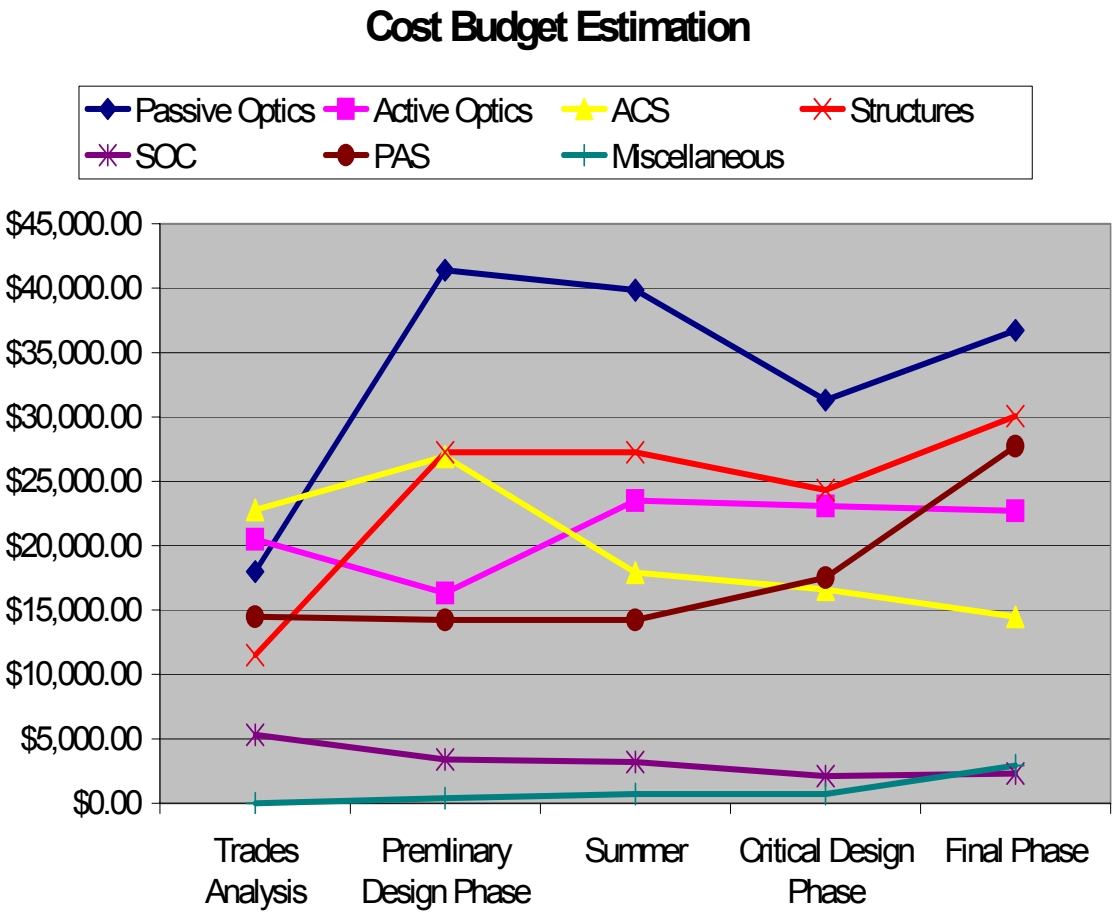
Cost Budget Estimation
Passive Optics
Active Optics
ACS
Structures
SOC
PAS
Miscellaneous
$45,000.00
$40,000.00
$35,000.00
$30,000.00
$25,000.00
$20,000.00
$15,000.00
$10,000.00
$5,000.00
$0.00
Trades Analysis
Premlinary Design Phase
Summer
Critical Design Phase
Final Phase